DEBONDING MECHANISMS OF FIBRE REINFORCED POLYMER STRENGTHENED STEEL MEMBER

By

Ibrisam Akbar

A DISSERTATION

SUBMITTED TO THE SCHOOL OF CIVIL,

ENVIRONMENTAL AND MINING ENGINEERING,

THE UNIVERSITY OF ADELAIDE

FOR THE DEGREE OF

DOCTOR OF PHILOSOPHY

TABLE OF CONTENTS

LIST OF TABLES

LIST OF FIGURES

ABBREVIATIONS AND NOMENCLATURES

τ bond stress
χ curvature
Δ global slip
Δ_s change of slip
δ slip
ε strain
δ_1 slip at maximum bond stress
θ_1 theoretical rotation when full plastic capacity is achieved
θ_2 rotation when moment capacity drops below M_p
$(AE)_p$ axial rigidity of FRP
$(AE)_s$ axial rigidity of steel
$(EA)_c$ axial rigidity of the concrete
$(EA)_p$ axial rigidity of the FRP plate
θ_h plastic rotation
θ_{hm} plastic rotation at maximum moment
τ_{max} maximum bond stress
δ_{max} maximum slip
$\delta_{max,cal}$ calculated maximum slip
$\tau_{max,exp}$ experimental bond stress
$\delta_{max,exp}$ experimental maximum slip
θ_p elastic rotation
ε_p FRP strain
ε_s steel strain
ε_u steel strain at ultimate rotation
ε_{sh} strain hardening
θ_u ultimate rotation
ε_Y yield strain,
A_p area of FRP
B bond force
b width
b_p FRP width
CDC critical diagonal crack
d depth
d_x segment length
E_p Young's Modulus of FRP
E_s Young's Modulus of steel
F force
FRP Fibre Reinforced Polymer
f_{sh} Strain hardening stress
f_y Yield stress
G_f fracture energy

h	height
IC	interfacial crack
J	geometry of the interface debonding failure plane
L_{crit}	critical bond length
L_p	length of embedment
l_p	length of full plastic zone
L_{per}	perimeter length
l_{pf}	length of flange plastic zone
M	moment
M_p	plastic moment
M_{pf}	plastic moment at flange
M_u	ultimate moment
P	load
PE	plate end
P_{IC}	debonding load
$P_{IC,exp}$	experimental interfacial crack load
P_L	load increment
P_{UL}	load decrement
$P_{y.}$	yield load
q	uniform distributed load
R	rotation capacity
t_p	thickness of FRP
t_s	Steel thickness
x_i	distance to inflection point
x_m	distance to plastic moment

ABSTRACT

Applying Fibre Reinforce Polymer (FRP) to steel structures has been proved to be an effective method of strengthening. Experimentally, ageing steel structures such as bridge decks and composite beams which have been strengthened with FRP have shown lifetime extension and enhanced strength. Numerically, different approaches have been carried out to quantify the relationship between FRP and steel members in regard to the observance of the experimental works.

This thesis contributes in term of quantifying the debonding mechanism of FRP strengthened steel members. First, a procedure in the derivation of the bond-slip (τ-σ) relationship is presented by combining the results of the experimental work with a numerical method developed specifically for this purpose. Secondly, the debonding mechanisms of FRP strengthened steel plates due to the yielding of steel is established by experimental and numerical works. Finally, a numerical method was developed to quantify the plate end debonding of a simply supported steel beam.

A total of seventeen pull tests with different types of FRP lengths and adhesives were tested to quantify the (τ-σ) relationship. Another four steel plate tests were carried out to study the debonding mechanism of FRP allowing for the steel to yield. Three different numerical methods were developed to analyse the results obtained experimentally.

STATEMENT OF ORIGINALITY

This work contains no material which has been accepted for the award of any other degree or diploma in any university or other tertiary institution to Ibrisam Akbar, and, to the best of my knowledge and belief, contains no material previously published or written by another person except where due reference has been made in the text.

I give consent to this copy of my thesis, when deposited in the University Library, being made available for loan and photocopying, subject to the provisions of the Copyright Act 1968.

I also give permissions for the digital version of my thesis to be made available on the web, via the University's digital search repository, the Library catalogue, the Australasian Digital Theses Program (ADTP) and also through web search engines, unless permission has been granted by the University to restrict access for a period of time.

Signature :

Name : Ibrisam Akbar

Date : 3/12/2010

ACKNOWLEDGEMENT

In the name of God, Most Gracious, Most Merciful.

The work of research in this thesis was carried out at the University of Adelaide in the Deparment of Civil, Environmental and Mining Engineering under the supervision of Professor Dr. Deric Oehlers, Dr. Ali Mohamed Sadakkathulla and Associate Professor Dr. Abdul Hamid Sheikh.

I am forever thankful to Professor Dr. Deric Oehlers, Dr. Ali Mohamed Sadakkathulla and Associate Professor Dr. Abdul Hamid Sheikh for their excellent guidance, careful supervision and patience throughout this research. They provided me their dedication and contribution which helped me for the completion of this research and publication of the papers. Their commitment in organising the weekly meeting and dedicated supervisions has been cherished with valuable discussions and ideas.

My thank you also goes to the laboratory technicians; especially to Steven Huskinson, David Hale and Ian Cates for their professional advices and dedications throughout the experimental program.

My love to the family; parents Akbar Pura and Isah Parman; wife, Suzilawati Amir Hamzah and children, Iman Ibrisam, Ismail Ibrisam, Sumaiyyah Ibrisam and Isa Ibrisam for their love, encouragement and support throughout the completion of this research. May we all be gathered together in *Jannatul Firdaus*.

Finally, my gratitude to my sponsor and employer, Universiti Teknologi Petronas which provided me their care while completing this work of knowledge.

LIST OF PUBLICATIONS

The following papers were written based on the work presented in this thesis.

1. Ibrisam Akbar, Deric John Oehlers, M.S. Mohamed Ali (2010). "Derivation of the bond-slip characteristics for FRP plated steel members." Journal of Constructional Steel Research, 66(8-9), 1047-1056.

2. Ibrisam Akbar, Deric John Oehlers, M.S. Mohamed Ali (2010). “Partial and Full Interaction Behaviour of FRP Plated Steel Member.” International Conference on Sustainable Building and Infrastucture. Kuala Lumpur.

3. Ibrisam Akbar, Deric John Oehlers, M.S. Mohamed Ali (2010). “Plate end debonding of FRP plated steel member using partial interaction theory.” Journal of the Institution of Engineers Malaysia. Kuala Lumpur. *submitted*

CHAPTER 1: INTRODUCTION

1.1 BACKGROUND

The need to retrofit steel structures such as offshore structures, bridges, and buildings has been apparent this last decade. Conventionally, steel plating was used by cutting out or replacing the deteriorated members, or to attach external plates. It is easy to see the problem since these plates are heavy, bulky and difficult to work on site. The alternative to this is composite material such as Fibre Reinforced Polymer (FRP). FRP is a material of choice in the strengthening and rehabilitation of structures mainly because of its ease of use. The high stiffness-to-weight and strength-to-weight ratios of FRP combined with the superior environmental durability has made them so appealing to be used (Buyukozturk, Gunes et al. 2003). FRP is also thin so it does not infringe upon the headroom requirement compared to other materials (e.g. steel plate) (Colombi and Poggi 2006). Furthermore, FRP is very flexible and can be formed to any shapes – easing the work on site (Zhao and Zhang 2007). Studies were reported regarding the enhancement of the strength of deteriorated steel structures when retrofitted with FRP (Miller, Chajes et al. 2001; Jones and Civjan 2003; Tavakkolizadeh and Saadatmanesh 2003a; Tavakkolizadeh and Saadatmanesh 2003b; Al-Saidy, Klaiber et al. 2005; Deng and Lee 2005a; Deng and Lee 2005b; Colombi and Poggi 2006; Fawzia, Al-Mahaidi et al. 2007; Lam, Cheng et al. 2007). However, debonding of FRP from the steel member must first be addressed in order for the composite action to be fully utilised. The first critical stage is to understand the bond-slip characteristics of FRP plated steel members which is susceptible to the yielding of the steel.

1.2 BOND-SLIP (τ-δ) RELATIONSHIP

The bond-slip relationship plays an important role in charaterising the behaviour of FRP bonded steel members. It can be used to derive the bond strength, the slip, and the effective bond length. Conventionally, the derivation of the bond-slip relationship was carried out experimentally in pull tests. Strain gauges were glued on the FRP plate along the bond length from which the values of the bond stress could be calculated from the strain readings. The slip can be determined by integrating the measured strain distribution along the plate length (Xia and Teng 2005).

A bilinear shape is considered to be a reasonable idealisation of the bond-slip relationship for both concrete and steel members glued with FRP (Yuan, Teng et al. 2004; Xia and Teng 2005; Zhao and Zhang 2007). Figure 1.1 shows the bilinear bond-slip relationship which consists of the maximum bond stress, τ_{max}, the maximum slip, δ_{max} and the slip at the maximum bond stress, δ_1. The area encompassed by the bond-slip relationship is the interfacial fracture energy, G_f.

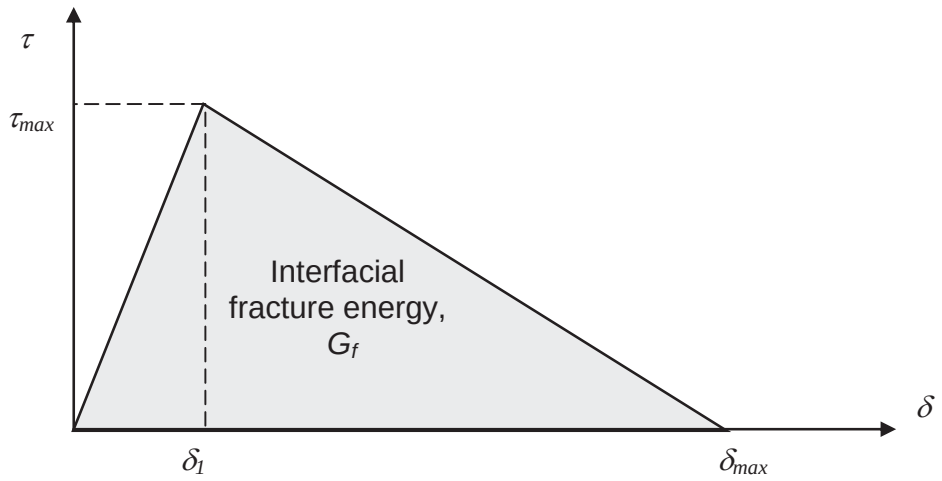

Figure 1.1 Bilinear bond-slip relationship

1.3 DEBONDING FAILURES

Figure 1.2 shows an FRP plated steel beam under the influence of a point load. Debonding can occur at the centre of the beam where steel has yielded toward the plate end. At the plate end, debonding can occur due to failure within the adhesive or failure between the adhesive-adherent interfaces (Al-Emrani and Kliger 2006), also known as plate end debonding. Once debonding occurs, FRP is debonded from the steel member and can no longer act as a strengthening material, hence, must be avoided.

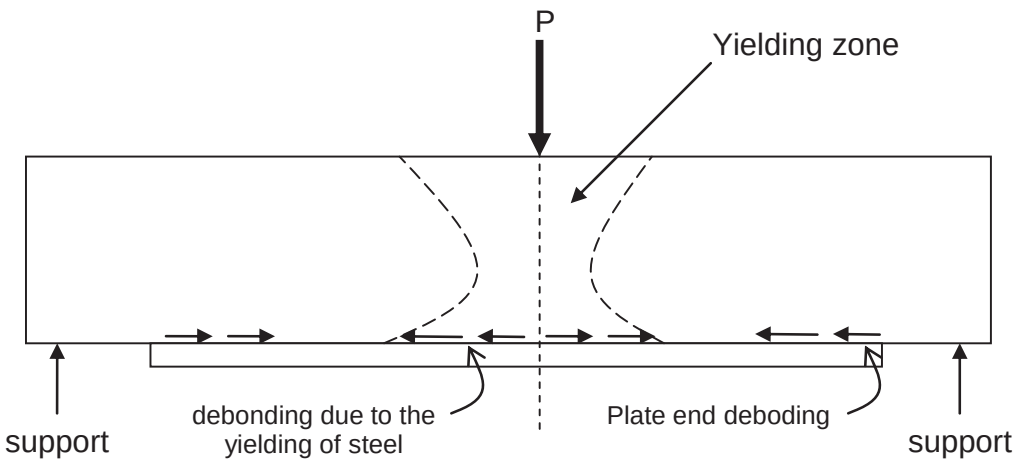

Figure 1.2 Intermediate crack debonding mechanism

1.4 FULL AND PARTIAL INTERACTION THEORY

Consider the case of a composite beam in which the interface slip is totally prevented as in Figure 1.3 (a) such as the case of an FRP plated steel member. The strain of the FRP, ε_p is equal to the strain of the steel, ε_s. Hence, the slip strain, ds/dx, which is the difference of the two strains, ε_p and ε_s is 0. This condition is referred to full interaction. If the interface slip with some degree of friction is allowed to take place at the interface of the FRP and steel as in Figure 1.3 (b), the strains are no longer equal hence the slip strain, is no longer 0. This condition is known as partial interaction.

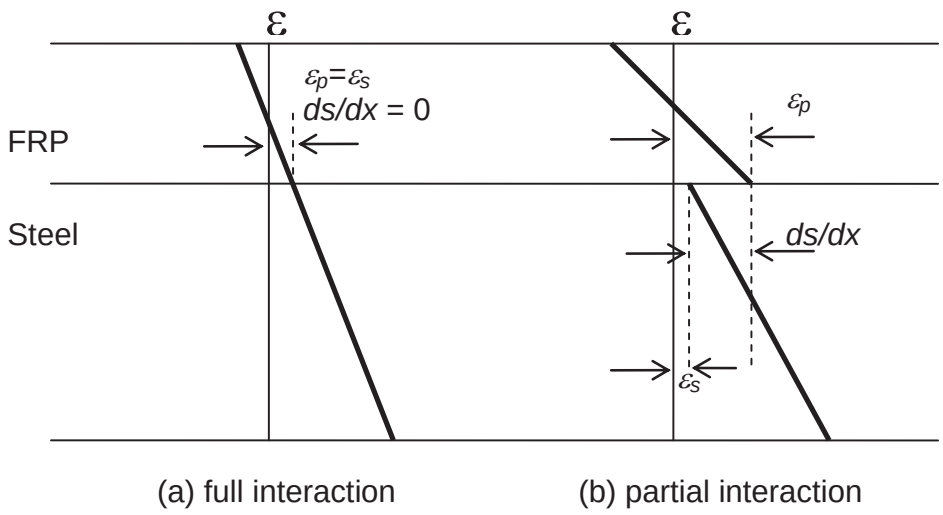

Figure 1.3 Degree of interaction

1.5 SCOPE AND OBJECTIVES

This research will look into the derivation of the bond-slip relationship of FRP plated steel member which is simpler than the conventional method. Debonding mechanism will also be discussed in regard to the yielding of steel and moment curvature response.

1.6 THESIS OUTLINE

The thesis begins with the introduction in Chapter 1 consisting of the general background on the bond-slip relationship, the intermediate crack debonding, full and partial interaction theory and the discussion of the scope and objective of this research. Chapter 2 consist of the literature review forming the basis of this research. Chapter 3 described the experimental work and results of pull tests. A numerical method was developed and described in Chapter 4 and compared to the test results in Chapter 3 in establishing the method of derivation of the bond-slip characteristic of FRP plated steel member. Chapter 5 describes the experimental work and results of FRP plated steel plate where the steel is allowed to yield. Chapter 6 discusses the numerical method developed to understand the debonding mechanism observed in Chapter 5. In Chapter 7, a numerical method is developed to investigate the influence of rotation to the FRP plated steel beam. Finally, conclusions in Chapter 8 discuss all the findings in this research.

CHAPTER 2: LITERATURE REVIEW

2.1 INTRODUCTION

This chapter covers the literature review of the experimental and numerical works related to the derivation of τ-δ relationship of FRP plated steel members. At the end of this chapter, the objective of this research will be clearly stated.

2.2 RESEARCH RELATED TO DEBONDING OF FRP

The reliability of the strengthening of Fibre Reinforced Polymer (FRP) to steel or concrete structures depends on the success of the stress transfer between the FRP plate and steel or concrete element (Sebastian 2003b; Al-Saidy, Klaiber et al. 2005). The stress between the two elements was transferred via shearing and the adhesive as the element that bonds the two materials together becomes an important medium for such action to be successful.

The application of FRP into the strengthening to reinforced concrete (RC) structures has been well documented. The general consensus gained from the research done in FRP-to-concrete is that debonding is the major cause of failure (Buyukozturk, Gunes et al. 2003). These debonding failures can be categorised into intermediate crack (IC), critical diagonal crack (CDC) and plate end (PE) debonding (Oehlers and Seracino 2004). IC debonding is more common when the critical bond length is exceeded and an important form of debonding as it determines the increase of flexural capacity, the reduction in sectional ductility and a required check in design (Seracino, Raizal Saifulnaz et al. 2007). These debonding failures are related to the bond strength between adhesive, FRP and concrete. When the maximum slip is exceeded, debonding will occur. This relationship between bond strength and slip is known as bond-slip behaviour.

Cracks that initiate and propagate and/or yielding of the reinforcement at a discrete level of the reinforcement is closely linked to the debonding failure which

is inherently absent for the case of steel-FRP (Sebastian 2003a). Separation of the RC-FRP member is also related to the fracture of the concrete near the adhesive whereas for steel-FRP, it is due to the fracture of FRP or the adhesive (Sebastian 2003a). Due to the reasons above, direct extrapolation from the RC-FRP cannot be made for steel-FRP.

Debonding of the adhesive layer can occur within or at the interfaces of the materials in the strengthening system (Buyukozturk, Gunes et al. 2003). The bond between FRP and adhesive is the weakest (Sen, Liby et al. 2001) and various approaches were taken to model the behaviour. Models of debonding can be classed into three major categories (Buyukozturk, Gunes et al. 2003); the strength approach, fracture mechanics approach and empirical (and semi-empirical approach).

Strength approach (or also known as stress distribution approach, bond-slip relationship approach or multi layer distribution model (Zhao and Zhang 2007) involves the calculation of the interfacial or bond stress distribution in FRP strengthened members based on elastic material properties (Buyukozturk, Gunes et al. 2003), usually by conducting pull tests (Lu, Teng et al. 2005). The strength approach is popular for its simplicity and number of research was carried out in this form (Chen and Teng 2001; Yuan, Teng et al. 2004; Ali, Oehlers et al. 2006). Fracture mechanics approach is applied due to fact that debonding is essentially a crack propagation promoted by local stress intensities (Buyukozturk, Gunes et al. 2003). Even though it is more complicated, a number of research was carried out to simplify the approach (Deng, Lee et al. 2003; Lenwari, Thepchatri et al. 2006). Empirical and semi empirical approach is an approach where simplified relations on a phenomenological basis were applied to predict failure, thus avoiding the complexity in the other approaches (Buyukozturk, Gunes et al. 2003) which was carried out by several researchers (Ali, Oehlers et al. 2001; Smith and Teng 2002).

2.3 τ-δ RELATIONSHIP

An accurate local bond-slip (τ-δ) model is important in the modeling of FRP-strengthened RC structures (Lu, Teng et al. 2005). Various bond-slip models were suggested and out of these, the experimental results indicated that the bilinear model provides the close approximation (Yuan, Teng et al. 2004) as shown in Figure 2.4. The bilinear model consists of an elastic branch which peaks at τ_{max} and the softening branch up to δ_{max} and the slip at the maximum bond stress, δ_1. The area under the bond-slip curve is the fracture energy, G_f. So long as the values of τ_{max} and δ_{max} are constant, the value of G_f does not change since the area under it does not change. For example, the unilinear relationship has the same value of τ_{max} and δ_{max} which resulted the same area underneath similar to that of the bilinear relationship.

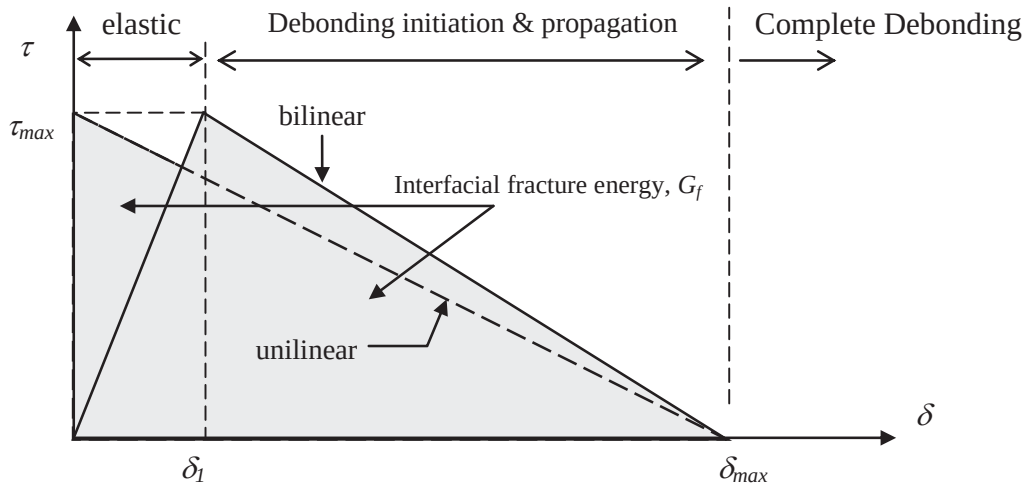

Figure 2.4 Local bond-slip model

2.4 DEBONDING LOAD, P_{IC}

The relationship between the local bilinear bond-slip to the global load displacement behaviour of a pull test was described in length by Yuan et al. (2004). As the load is being applied, the bond stress is increased up to the maximum bond stress, τ_{max} with slip increment up to δ_1 as shown in Figure 2.4. After reaching τ_{max}, the bond stress started to reduce while the slip is still increasing. At this range, debonding starts to initiate and propagate. Complete debonding occurs once δ_{max} is reached and no more bond stress can be taken. It is mathematically described as:

$$f(\delta)=\begin{cases}\dfrac{\tau_{max}}{\delta_1} & \text{When } 0 \le \delta \le \delta_1 \\ \dfrac{\tau_{max}}{\delta_{max}-\delta_1}(\delta_{max}-\delta_1) & \text{When } \delta_1 \le \delta \le \delta_{max} \\ 0 & \text{When } \delta > \delta_{max}\end{cases} \tag{2.1}$$

The bond-slip model was derived from a pull test experiment. The pull test consists of FRP which is applied to a concrete block with a layer of adhesive as in Figure 2.5. As load is incrementally applied, the bond stress resisting the load will start to increase as elastically (state I) as shown in Figure 2.5(a). Debonding will start to occur once the maximum bond stress has been exceeded as shown in Figure 2.5(b). At this point, the elastic-softening stage (state II) begins at the loaded end as shown in Figure 2.5(c) and moves towards the other end. This is when the ultimate load is first attained. The elastic-softening stage will propagate until the critical bond length is achieved (Figure 2.5(d)). Once the critical bond length is achieved, debonding (state III) will occur and τ_{max} moves toward x = 0 (Figure 2.5(e)), where *d* is the debonded length. The zone where the maximum bond stress has reached the other end is shown in Figure 2.5(f). The maximum shear stress at this point begins to decrease with load applied (Figure 2.5(g)).

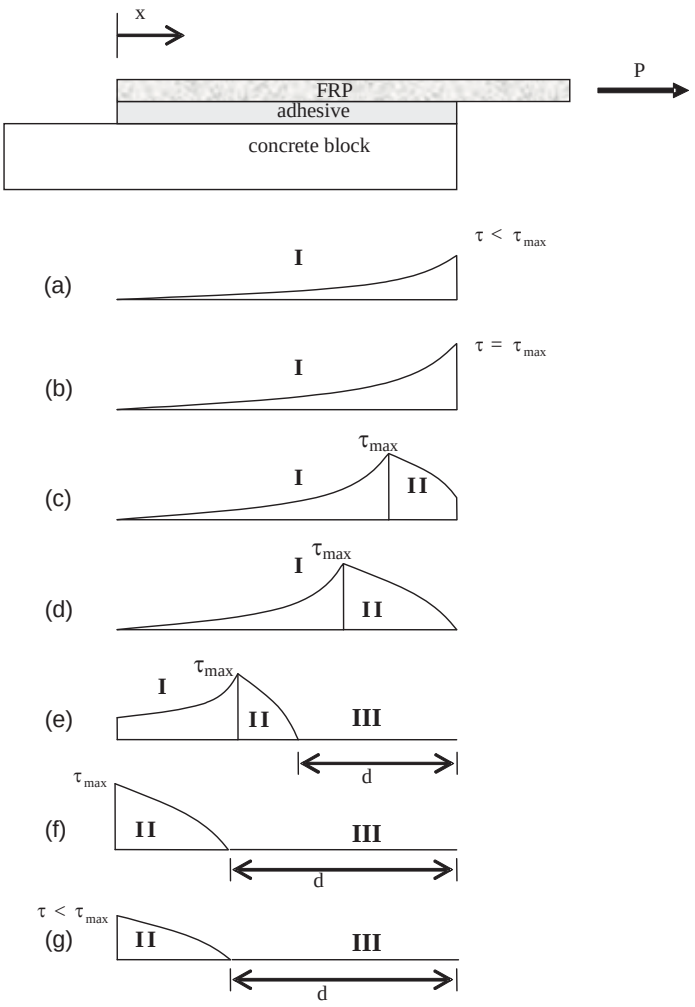

Figure 2.5 Interfacial stress distribution and propagation of debonding for a large bond length.

Figure 2.6 shows a load-displacement (*P-Δ*) curve of a typical pull test. The description of the graph is as follows: Region O-A depicts the elastic stage of loading in Figure 2.4 and the increment of stress in Figure 2.5(b). As the load is increased to the yield point B, the local bond stress begins to soften at the debonding initiation and propagation zone in Figure 2.4 and the start of debonding at the loaded end in Figure 2.5(c). The plateau B-C occurs when there is an increment of displacement without additional load. This is depicted in Figure 2.4 at

the debonding initiation and propagation zone and when the maximum bond stress is reached at the free end to the other end in Figure 2.5 (d) to Figure 2.5(f). Total debonding occurs at point C in Figure 2.6, just as the maximum slip is reached in Figure 2.4 and the reduction of bond stress in Figure 2.5(g). Point D occurs when the peak shear stress reaches the unloaded end and Point D-E simply indicates that the displacement reduces linearly with the load. Generally the complete debonding at point E is generally not obtainable from experiment.

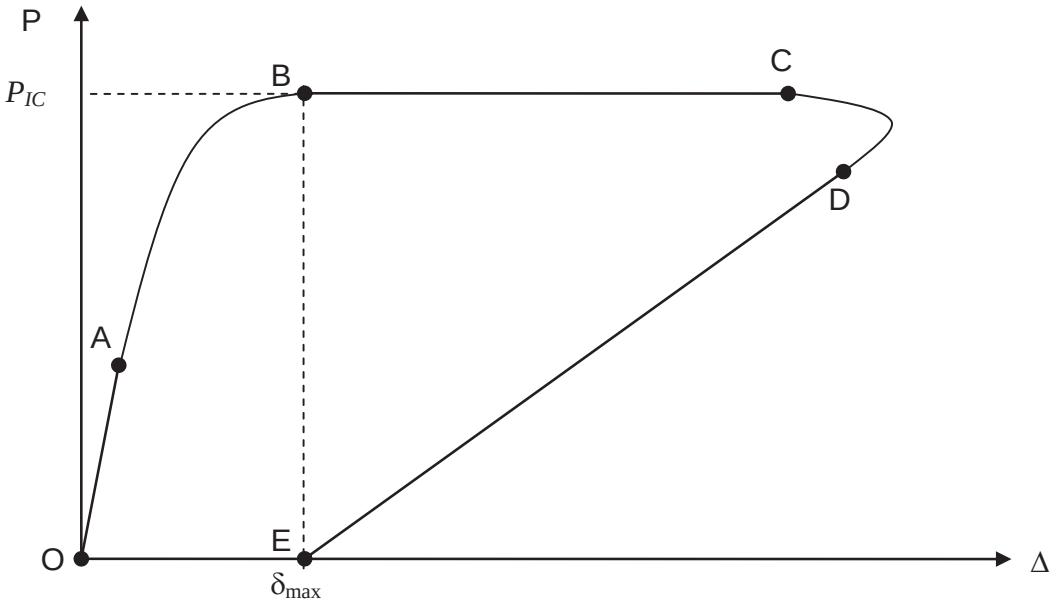

Figure 2.6 Typical theoretical load-displacement curve

From the analytical solution, Yuan et al. (2004) obtained the following expression for debonding load,

$$P_{IC} = b_p \sqrt{\tau_{max} \delta_{max} E_p t_p} \tag{2.2}$$

Where τ_{max} and δ_{max} are the maximum bond-stress and slip of the τ-δ relationship; Ep is the Young's Modulus of the FRP; b_p and t_p are the width and

thickness of the FRP plate respectively. The interfacial fracture energy, G_f is basically the area under the bond-slip curve in Figure 2.4, given by,

$$G_f = \frac{1}{2}\tau_{\max}\delta_{\max} \tag{2.3}$$

The governing ordinary differential equation defining the behaviour of a joint in a FRP-to-concrete pull tests was given by Yuan et al. (2004),

$$\frac{\partial^2 \delta}{\partial x^2} - Jf(\delta) = 0 \tag{2.4}$$

It was reported by Ali et al. (2006) that the bilinear bond-slip model may be idealised by a single descending branch as shown by the broken line in Figure 2.4. The function $\delta(f)$ from the idealised bond-slip model is thus given by,

$$f(\delta) = \frac{\tau_{\max}}{\delta_{\max}}(\delta_{\max} - \delta) \tag{2.5}$$

J in Eq. (2.4) is defined in terms of geometry of the interface debonding failure plane and not the geometry of the plate (compare to Yuan et al. (2004)) and is given as,

$$J = L_{per}\left[\frac{1}{(EA)_p} + \frac{1}{(EA)_c}\right] \tag{2.6}$$

Where $(EA)_p$ and $(EA)_c$ are the axial rigidity of the FRP and concrete respectively. Substituting Eq. (2.4) and (2.5) into Eq. (2.6) and solving the differential equations gives,

$$P_{IC} = \frac{\tau_{\max} L_{per}}{\lambda} \tag{2.7}$$

L_{per} is defined as length of debonding failure plane (in cross section) for externally bonded (EB) plate and near-surface mounted (NSM) plate (Seracino, Raizal Saifulnaz et al. 2007) as shown in Figure 2.7. and defined as,

$$L_{per} = 2d_f + b_f \tag{2.8}$$

Eq. (2.7) is only valid if the bond length is greater than the critical bond length. Assuming that in the pull test, the value of *(EA)* for the concrete or steel is very large relative to $(EA)_p$, as it usually is, the value of L_{crit} as derived from a unilinear bond-slip relationship (Figure 2.4) is given by,

$$L_{crit} = \frac{\pi}{2\lambda} \tag{2.9}$$

and λ is given as,

$$\lambda^2 = \frac{\tau_{\max} L_{per}}{\delta_{\max} (EA)_p} \tag{2.10}$$

Substituting Eq. (2.10) into (2.7) yields,

$$P_{IC} = \sqrt{\tau_{\max} \delta_{\max}} \sqrt{L_{per} (EA)_p} \tag{2.11}$$

Eq. (2.11) is applicable to any plate geometry, provided that the bonded length is more than the critical bond length (Seracino, Raizal Saifulnaz et al. 2007). It is being separated by axial rigidity of the FRP plate $(EA)_p$, the maximum bond stress and slip, $\tau_{max}\delta_{max}$ and the length of debonding failure plane L_{per}. The

value of $\tau_{max}\delta_{max}$ can be directly obtained from the local bond-slip curve as shown in Figure 2.4. The value of P_{IC} can be obtained directly from the P-Δ curve as shown in Figure 2.6. The value of the slip at the point of the maximum bond shear, δ_1, will determine the slope of the global load-slip curve at point O-A (Figure 2.6).

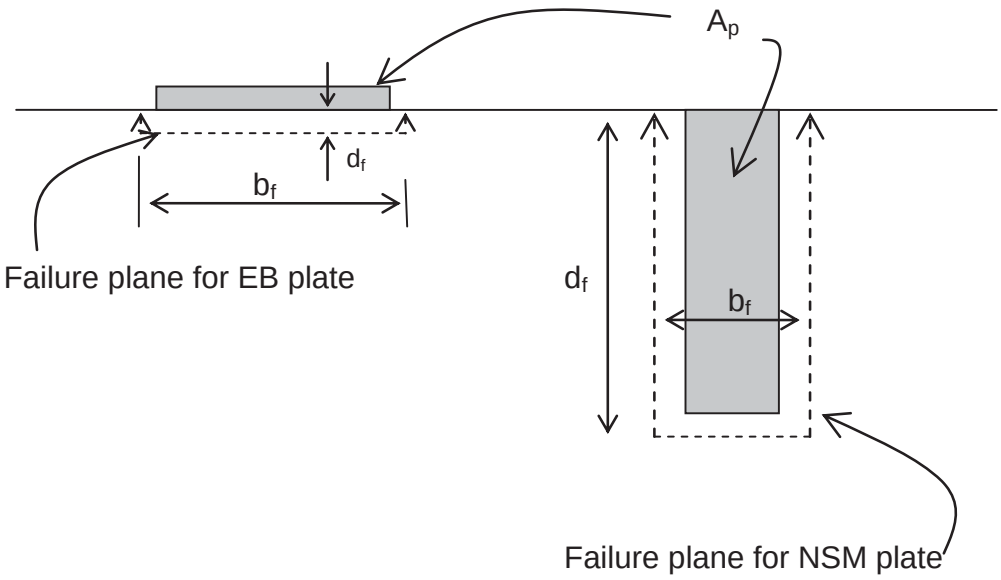

Figure 2.7 Definition of IC debonding failure plane (cross sectional view of plate)

2.5 CRITICAL BOND LENGTH

The critical bond length is similar to development length of steel reinforcement in RC design. Providing bond length less than the critical bond length or development length will not allow the section to achieve its maximum debonding resistance (Haskett, Oehlers et al. 2007). Similarly, extending the bond length beyond the critical bond length will not increase the strength of the cross section even though it will increase ductility (Chen and Teng 2001). Furthermore, the use of Eq. (2.2) and (2.11) in calculating debonding resistance can only be

used for a cross section which has reached its maximum debonding resistance i.e. when critical bond length has been provided. Knowing an estimate of the critical bond length will provide the basis of applying FRP for strengthening.

2.6 BOND TESTING METHODS IN FRP-STEEL

The types of bond tests are categorized into four types for different purposes of studies (Zhao and Zhang 2007):

Type 1: Load indirectly applied to the FRP and the steel plate in a beam
Type 2: Load directly applied to the FRP.
Type 3: Load directly applied to the steel element without any gap
Type 4: Load directly applied to the steel element with a gap

2.6.1 LOAD INDIRECTLY APPLIED TO THE FRP AND THE STEEL PLATE IN BEAM - NOZAKA, SHIELD AND HAJJAR (2005)

The specimen tested by Nozaka, Shield et al. (2005) involves bolting a steel plate to the tensile flange of a beam which is later strengthened with FRP plate as shown in Figure 2.8. The beam was a W14 x 68 section and was 4.3 m long. This particular beam was chosen to ensure that it would not fail by local buckling at the flange when the adhesive reached its maximum tensile strength. By this arrangement, the load experienced by the strengthening system was in a pure bending and should be able to replicates the adhesive shear and peel stresses induced by the load. The slit was intended to represent severe crack in tension flange on a fatigued steel bridge girder in the field and were varied into five configurations. The combination of slit and hole in the beam were created to isolate the tensile force in the FRP strip.

Figure 2.8 Experimental test setup and dimensions (Nozaka, Shield et al. 2005)

The major objective of this research was to determine the critical bond length. An analytical model was developed by adopting the single lap joint specimen as in Figure 2.5. A finite element analysis of the beam was also conducted where for simplicity, the bolted connection between the steel plate and beam was assumed to be perfectly connected i.e. no slip occurred. The experimental results indicated that all 27 specimens had some degree of debonding failure and none exhibited a purely tensile failure on the FRP plate. However, the types of debonding failure i.e. between the interfaces of the adherent and adhesive or cohesive were not reported.

The good correlation between the experimental and analytical results is shown in Figure 2.9 indicates that the single lap joint analytical model is sufficient to simulate the strain distribution in the FRP plate. However, the results are specimen-dependant and the model developed cannot be applied to other types of sections (e.g. steel hollow section) (Zhao and Zhang 2007).

Figure 2.9 Comparison of analytical and experimental test results (Nozaka, Shield et al. 2005)

2.6.2 LOAD DIRECTLY APPLIED TO THE FRP

2.6.2.1 DAMATTY AND ABUSHAGUR (2003)

A research was conducted where a series of tests involving adhesively bonding 20 numbers of 100 mm x 100 mm FRP plates to hollow steel section (HSS) as shown in Figure 2.10 (Damatty and Abushagur 2003). The FRP plate is 19 mm thick x 100 mm width x 110 mm long and bonded to the surface of the HSS for 100 mm in length. Load is applied to the specimen through the thick plate on top of the FRP plates. Load deflection data were recorded and later was converted to values of maximum shear stresses using closed form solution.

There are four types of debonding failure in the tests. The cohesive failures between the adhesive and FRP section were reported in 6 specimens and another 6 specimens experiencing cohesive failures between the adhesive and steel associated with an area of bonding between the steel and the FRP random fibers. Combination of cohesive failure between the adhesive and FRP section and adhesive and steel section were reported in 7 specimens whereas only 1

specimen experiencing cohesive failure between the adhesive and the steel section. This four types of failure modes were specifically cohesive failures and tensile failure of the FRP plate cannot be simulated simply because the tests were all in compression. Futhermore, applying compressive force to the FRP in this test will include compressive failure due to the smaller compression strength (Zhao and Zhang 2007). Finally, FRP is used more in tension rather than in compression.

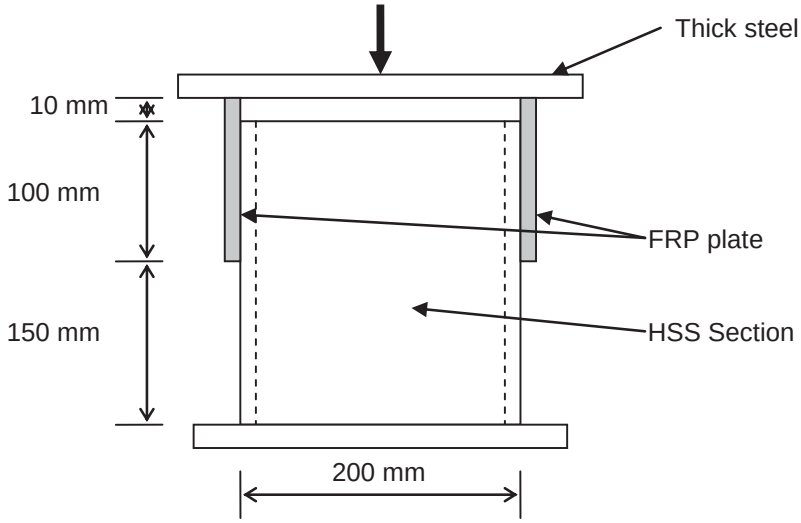

Figure 2.10 Schematic of the conducted shear lap tests (Damatty and Abushagur 2003)

2.6.2.2 XIA AND TENG (2005)

The problem of violent variations in the strain readings in the FRP-concrete experiment can be eliminated if using FRP-steel. Xia and Teng (2005) tested 13 numbers of FRP-to-steel specimens to measures the bond-slip behaviour by varying the adhesive thickness and adhesive types. The test specimens consist of a steel block bonded with FRP plates as shown in Figure 2.11. Strain gauges were attached along the FRP at spacings with a range from 25 mm to 50 mm. The shear stresses along the FRP were calculated from the readings of the strain gauges so they represent the average shear stress upon the

intervals of each strain gauge. Four thicknesses of adhesive were used for each adhesive: 1 mm, 2 mm, 4 mm and 6 mm. The first two thicknesses were realistic and the other two were used to achieve a wide range of adhesive thickness. The FRP plate used in the tests was 350 mm in length, a width of 50 mm, a thickness of 1.2 mm and an elastic modulus of 165 GPa. The specimen details, test results and predictions obtained from the experiment and the adhesive material properties are shown in Appendix A.

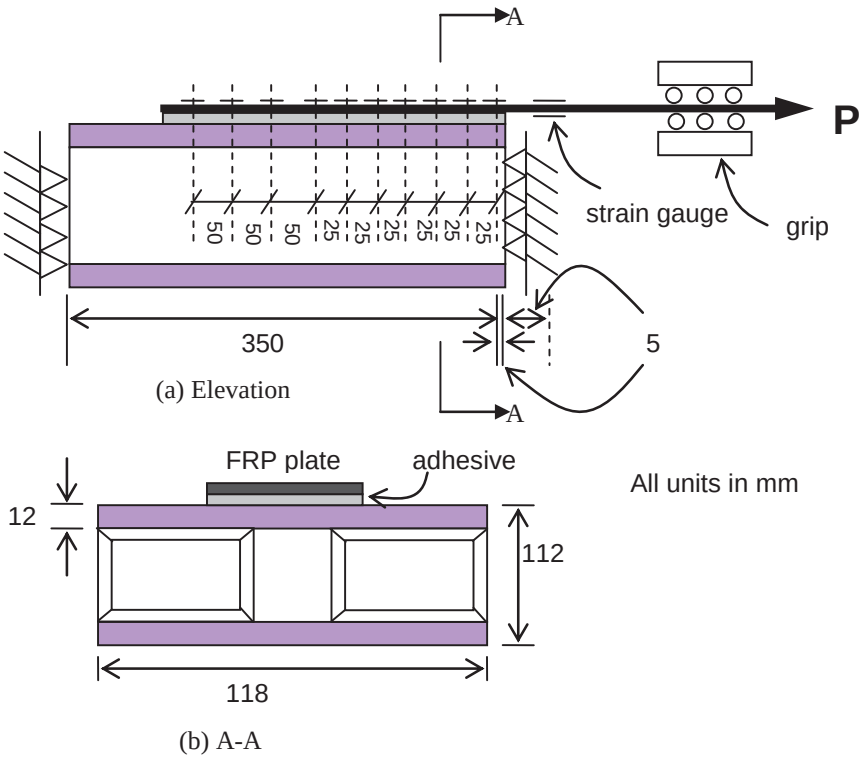

Figure 2.11 Pull test specimen setup from Xia and Teng

A bond-slip model was proposed from this research based on detailed strain measurements as shown in Figure 2.12. The slips of the FRP plate were found by integrating the measured strain distribution along the plate length while the shear stresses were calculated from the readings of strain gauges mounted on the top surface of the FRP plate, so that they represent the average shear

stresses over strain gauge intervals which are smaller than the actual values of the specimen.

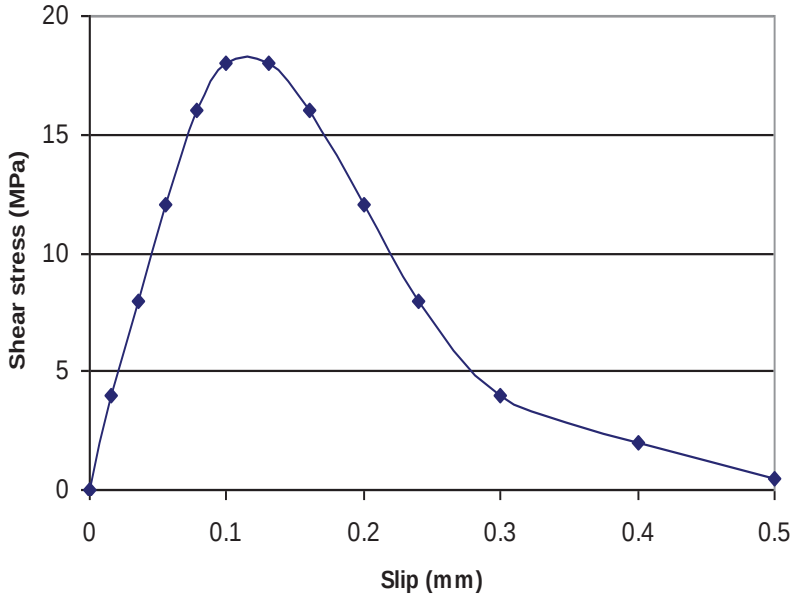

Figure 2.12 Shear stress distribution

2.6.3 LOAD DIRECTLY APPLIED TO THE STEEL ELEMENT WITHOUT A GAP

2.6.3.1 MILLER, CHAJES, MERTZ AND HASTINGS (2001)

Miller et al. (2001) conducted a series of tests to investigate the force transfer between the FRP and steel. The main objective for this experiment was to determine the corresponding critical bond length. Six 914 mm long steel specimens (38 mm wide x 12.7 mm thick) doubly reinforced with FRP plates were loaded in tension. The FRP plate dimensions are 37 mm wide x 5.25 mm thick and 457 mm long, glued on both sides of the steel plate as shown in Figure 2.13. The beveled of 45^0 angle at the FRP end was to reduce adhesive shear and the peel stresses. This method of experimental work is suitable to quantify the force transfer and bond durability in a monotonic load and cyclic load, respectively (Zhao and Zhang 2007).

Figure 2.13 Schematic of bond test specimen (Miller, Chajes et al. 2001)

Eleven foil strain gauges were attached to one side of the FRP plate with another five on the other side as a backup to capture the longitudinal strain development along the bonded length. An increasing tensile load was applied to the test specimens and the strain data were recorded. A 1-dimensional linear-elastic analytical model was also developed. Figure 2.14 shows the comparison between the measured values (CIBA 1 and CIBA 2) and analytical prediction. It was concluded that 98% of the force transfer occurs within the first 100 mm of the end of the FRP plate hence the critical bond length is 100 mm. However, the mode of failures were not reported.

Figure 2.14 Comparison of measured and computed strain along FRP (Miller, Chajes et al. 2001)

2.6.3.2 COLOMBI AND POGGI (2005)

Colombi and Poggi (2006) analysed similar specimens as Miller et al. (2001) to investigate the strengthening applied to steel members to prevent possible damage. The specimen as shown in Figure 2.15 consists of a steel plate of 1200 mm length x 60 mm width x 6 mm thick which is reinforced on both sides by FRP plates of 600 mm length x 60 mm width x 1.4 mm thick. Strain gauges were attached at 169 mm, 199 mm, 229 mm, 259 mm and 289 mm from the middle of the specimen.

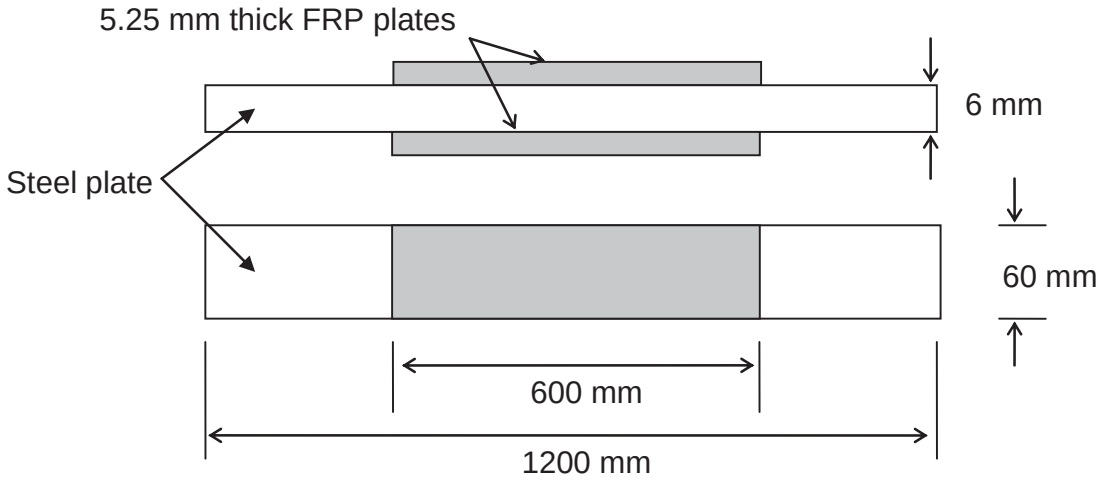

Figure 2.15 Schematic of bond test specimen (Colombi and Poggi 2006)

Using a strength approach, a numerical model was developed to evaluate the static responses of the FRP plated steel member. The following assumptions were applied:

1. Elastic stress-strain relationship for steel, FRP and adhesive.
2. No slippage between the steel and FRP, i.e. perfect bond.
3. Stresses are constant through the adhesive layer thickness i.e. the adhesive layer is thin.

Experimentally, yielding occurs firstly at the part where the steel was not reinforced with FRP which is beneficial since the idea of using FRP is to enhance the strength at the position where FRP is applied. Then yielding propagates towards the reinforced part of the specimens which also causes debonding to occur. Figure 2.16 shows the measured and predicted stress distributions across the bonded length where the critical bond length can be estimated to be 100 mm in length. Since yielding of the steel occured at the plate end induced high strain in comparison to the lower strains of the FRP plate, the mode of failures in all cases were cohesive failure between the adhesive and the steel plate.

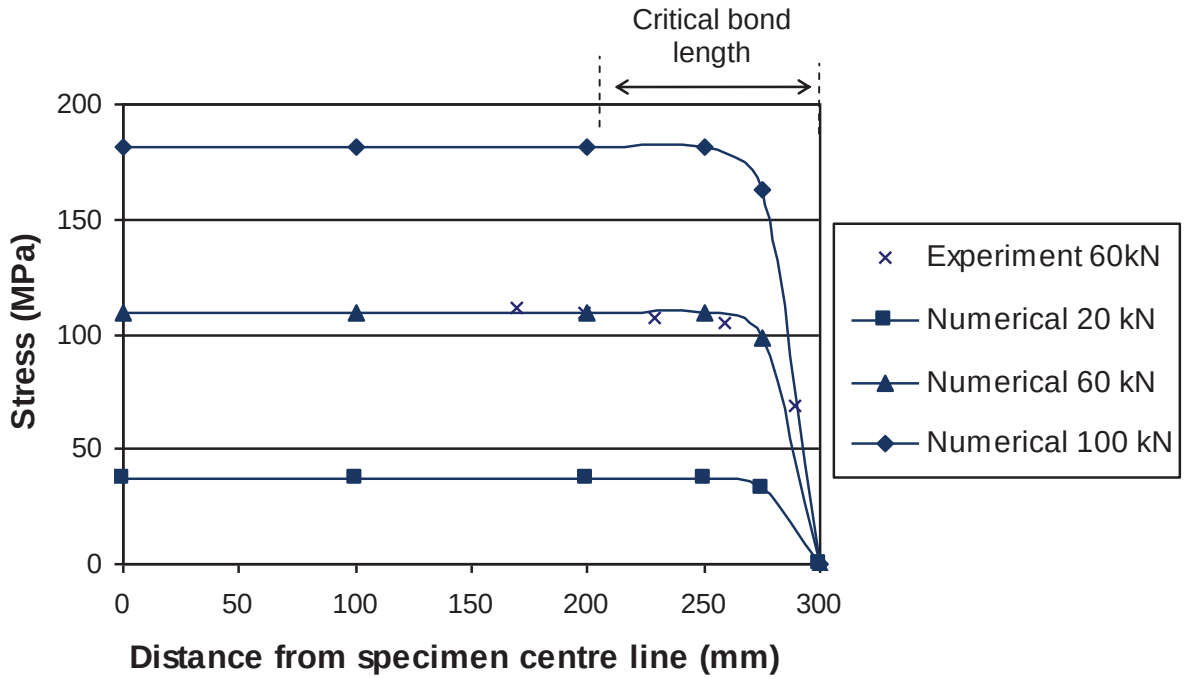

Figure 2.16 Comparison of measured and computed strain along FRP (specimen without a gap) (Colombi and Poggi 2006)

2.6.3.3 AL-EMRANI AND KLIGER (2006)

By considering a steel I-beam glued with FRP in Figure 2.17, Al-Emrani and Kliger (2006) anticipated four possible failure modes when it is loaded in bending:

1. Rupture of the laminate when the maximum axial stress in the FRP reaches its ultimate strength.
2. Debonding failure at the end of the FRP.
3. Debonding failure in the middle of the FRP.
4. Interlaminar failure (delamination) at the end of the FRP.

Figure 2.17 Schematic illustration of the principal load effects in a steel beam glued with FRP (Al-Emrani and Kliger 2006)

To demonstrate the failure modes, the test specimen in Figure 2.18 was developed. The shape of the specimen was chosen so that (Al-Emrani and Kliger 2006):

1. Successive yielding of the steel adherent could be obtained, starting from the middle of the specimen.
2. The fracture modes expected to be obtained in steel beams with bonded FRP (Figure 2.17) could be reproduced.

Figure 2.18 Test specimen for pull test incorporating steel yielding (Al-Emrani and Kliger 2006)

Two types of adhesives were used in the experiments. The material properties for the adhesives which were obtained experimentally using a collar-bone specimen and the measured material properties of the FRP plate are given in Appendix B. By having the specimen in Figure 2.18, steel will first yield at the middle of the specimen which eventually leads to failure. Finite element analysis which was carried out shows that two areas where shear stresses are high occur at the middle of the plate and at the end of the plate (higher load of 150 kN and 184 kN) as shown in Figure 2.19. Comparing the peak shear stresses at 184 kN, it shows that debonding may begin at the middle of the section before debonding at plate end is obtained. High shear stress also existed at the plate end and may also debond first rather than at the middle section since the actual debonding can never be determined first experimentally.

Figure 2.19 Predicted stress variations along the bonded length of Specimen A12 (Al-Emrani and Kliger 2006)

LOAD DIRECTLY APPLIED TO THE STEEL ELEMENT WITH A GAP - COLOMBI AND POGGI (2006)

Double lap joint specimens were produced and tested (Colombi and Poggi 2006) to study the repair to a damaged section. The geometrical properties of each material are the same as in Section 2.6.3.2 except that the steel plate was disconnected at the middle as shown in Figure 2.20. Ten strain gauges were attached at 0, 35, 65, 105, 145, 175, 205, 235, 265 and 295 mm from the middle of the specimen. The strength approach which adopted the same assumptions as in Section 2.6.3.2 was used and is plotted in Figure 2.21. A reasonably good agreement between the numerical analysis and experimental result can be observed. In addition, the critical bond length is about 75 mm. However, they are four possible positions at the gap where debonding may occur making instrumentation for the experiment and observation more difficult.

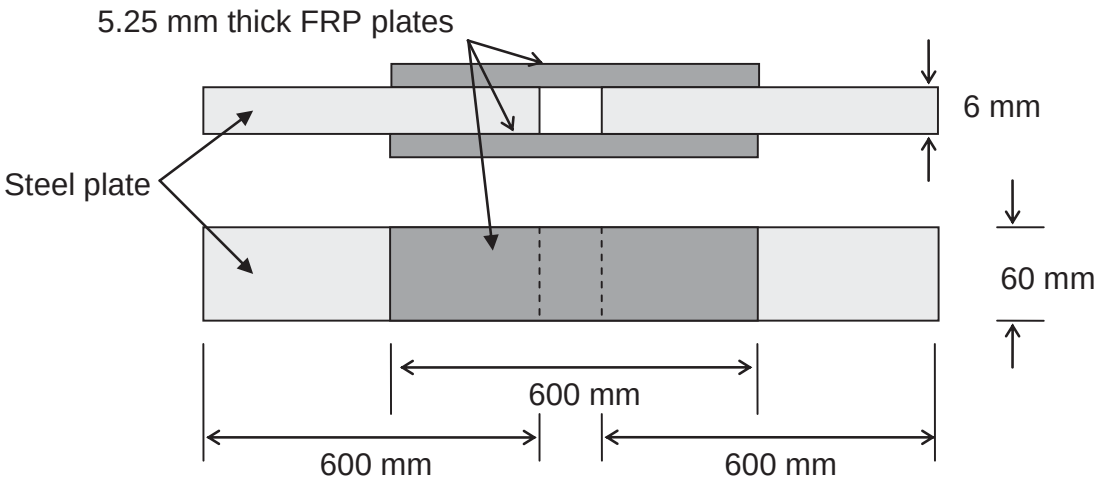

Figure 2.20 Double lap joint specimen (Colombi and Poggi 2006)

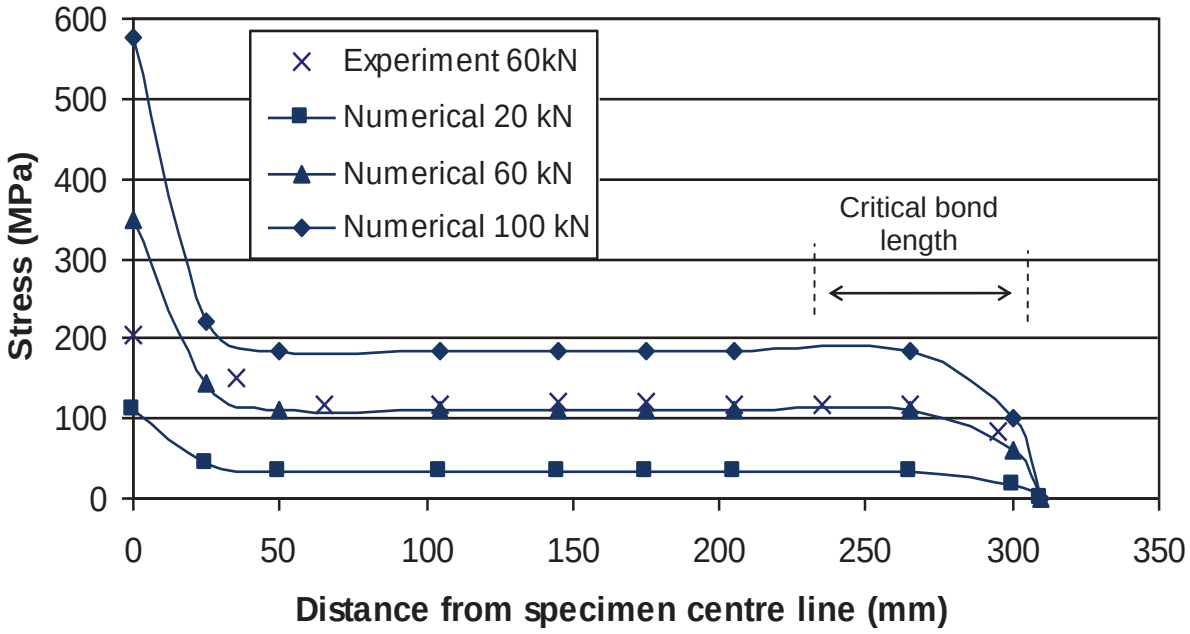

Figure 2.21 Comparison of measured and computes strain along FRP (specimen with a gap) (Colombi and Poggi 2006)

2.7 EXTRACTING THE τ_{max}-δ_{max} RELATIONSHIP

If Eq. (2.11) is going to be used, the values of τ_{max}-δ_{max} must be determined first from experimental or structural mechanics approach. The local bond-slip curves can be determined from (a) axial strains of the FRP plate measured with closely spaced strain gauges or (b) from the *P*-Δ (slip at the loaded end) curves (Lu, Teng et al. 2005). In the first method, the shear stress can be calculated by using difference formula while the corresponding slip can be determined by integrating the measured axial strains of the plate. Although it appears to be simple, this method is not necessarily accurate because the FRP plate when laid on a concrete surface will result in violent variations in the strain reading. For example, a strain gauge that lies on top of a crack in the concrete surface will have a greater strain compared to the other which lies on top of a large aggregate. Even though this can be avoided In steel-FRP system, the strain gauges only give average stresses over the strain gauge length and consequently can miss the peak stresses and as the strain gauges are only placed on the outer surface of the FRP plate, the readings may be affected by local distortion of the plate whilst debonding.

The second is the indirect method, where the local bond-slip curve is determined indirectly by the *P*-Δ curve. In this method, the value of P_{IC} and δ_{max} can be determined from the *P*-Δ curve (Figure 2.6). Using Eq. (2.11), the value of τ_{max} can be determined. The problem with this method was that it was hard to obtain δ_{max} accurately hence, an inaccurate τ_{max}.

2.8 PARTIAL-INTERACTION NUMERICAL METHOD OF BOND-SLIP RELATIONSHIP

Haskett et al. (2007) developed a partial-interaction numerical method which can integrate various τ-δ relationships to simulate a load-slip curve for an FRP-strengthened RC joint with a full critical bond length. The numerical method is particularly useful to simulate the bond-slip relationship of a reinforcement bar which is confined within a concrete member. The following algorithm is used in the development of the partial interaction numerical method (Haskett, Oehlers et al. 2007) as illustrated in Figure 2.22:

- A strain is fixed at the loaded end: $\varepsilon(0)$.
- According to the stress-strain profile of the FRP plate, the load at the loaded end, $P(0)$, is calculated.
- Corresponding to this fixed strain a slip at the loaded end is assumed, $\Delta(0)$.
- The assumed slip at the loaded end corresponds to the local slip over the first segment length. Corresponding to this assumed slip, $\Delta(0)$, the bond stress, $\tau(0)$, acting over the first segment length is calculated according to the local τ–δ relationship assumed.
- The bond force acting over the first segment length is calculated: $B(0)= \tau(0) d_x \pi d_b$ where d_b is the diameter of the FRP plate.
- The load in the FRP plate is calculated at the end of the first segment is $P(1)=P(0)-B(0)$,
- The corresponding strain is calculated: $\varepsilon(1) = \frac{P(1)}{(AE)}$.
- The strain in the concrete at the end of the first segment is calculated : $\varepsilon_c(1) = -\frac{P(1)}{(AE)_c}$.
- The slip strain is calculated: $\frac{ds(0)}{dx} = \varepsilon(0) - \varepsilon_c(0)$

- The change in slip over the first segment length is calculated by integrating the slip strain over the segment length: $\Delta s(0) = \int \frac{ds(0)}{dx} dx$.
- According to the change in slip over the segment length, the slip at the beginning of the second segment is calculated: $\delta(1) = \delta(0) - \Delta s(0)$.
- According to this slip the bond force acting over the second segment is calculated. The process is carried out throughout the bonded length until the boundary condition is achieved. There are two boundary conditions. For fully anchored plates, the boundary condition is $\delta = ds/dx = 0$ and for the not fully anchored plates, that is plates with bond lengths less than L_{crit}, the boundary condition is $\varepsilon_p = 0$ at the free end.

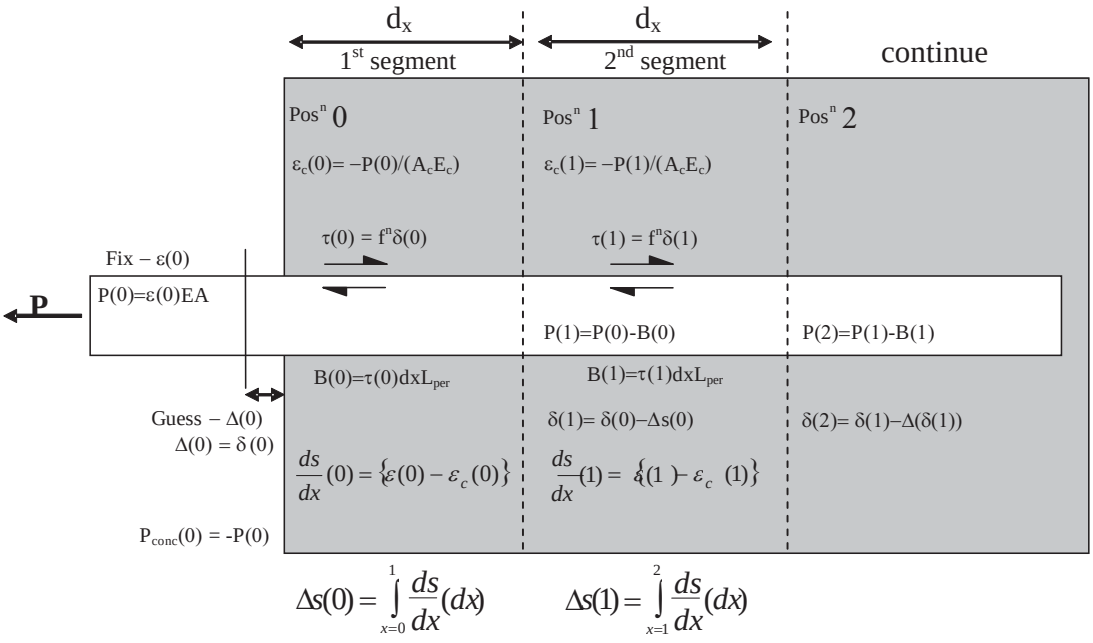

Figure 2.22 Graphical representation of numerical analysis (Haskett, Oehlers et al. 2007)

2.9 CONCLUSIONS

Establishing the τ-δ relationship is important in order to understand the behaviour of FRP plated steel so that debonding may not occur whilst the members are in service. This thesis will address the problem related to the previous research on establishing the τ-δ relationship using a purely empirical approach which may lead to scatter of results as well as underestimating the peak shear. In addition, this thesis will also discuss the debonding mechanism of FRP plated steel members when yielding occurs which is more critically needed when FRP plated beam is considered. In order to achieve these objectives, the aims are:

1. To conduct a series of push-pull test of FRP plated steel members in order to establish the τ-δ relationship. A numerical method will be developed to eliminate experimental errors where applicable.
2. To understand the behaviour of the debonding mechanism of an FRP plated steel member when subjected to the yielding of the steel. A series of tests with dog-bone shaped steel plates and a numerical method will be developed for detailed understanding of the debonding mechanism.
3. To develop a numerical method where the τ-δ relationship and the debonding mechanism when steel yielded are being incorporated into beam problem.

The first test will be a series of pull tests with varying bond lengths and FRP thicknesses as shown in Figure 2.23. This setup is similar with the experiment conducted by Xia and Teng (2005) in Section 2.6.2.2 except that only two strain gauges will be attached on the FRP plate. This experimental work will be combined with numerical analysis to obtain the τ-δ relationship.

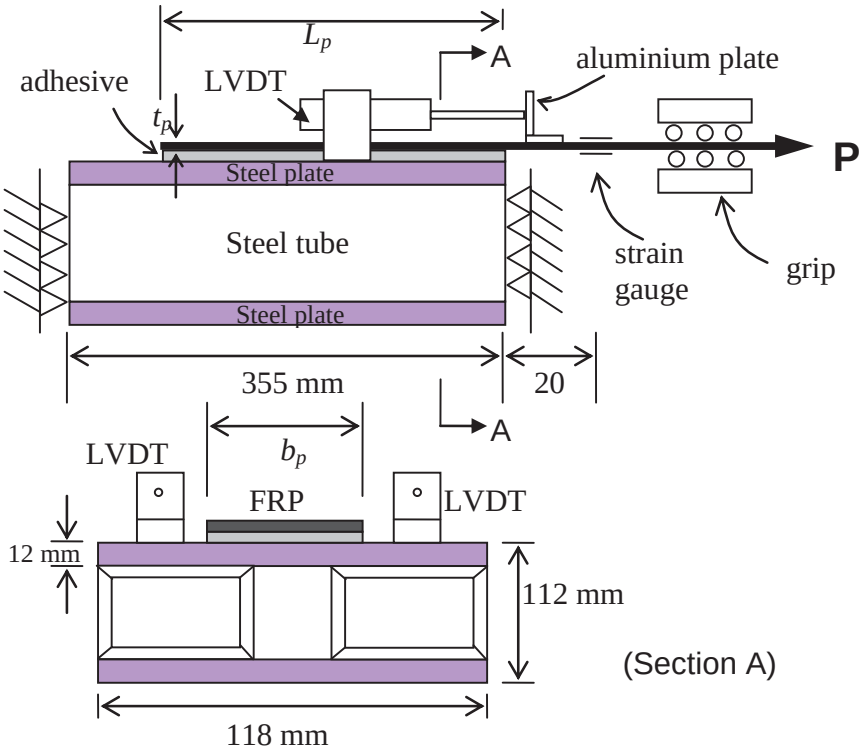

Figure 2.23 Typical pull test setup

The second test will be a series of pull tests with varying bond length and FRP thicknesses as show in Figure 2.24. This setup is similar with the experiment conducted by Al-Emrani and Kliger (2006) in Section 2.6.3.3 with some modifications. This experimental work will be combined with numerical analyses to investigate the debonding mechanism due to steel yielding. Finally a numerical method will be developed to study the debonding mechanism due to beam rotation.

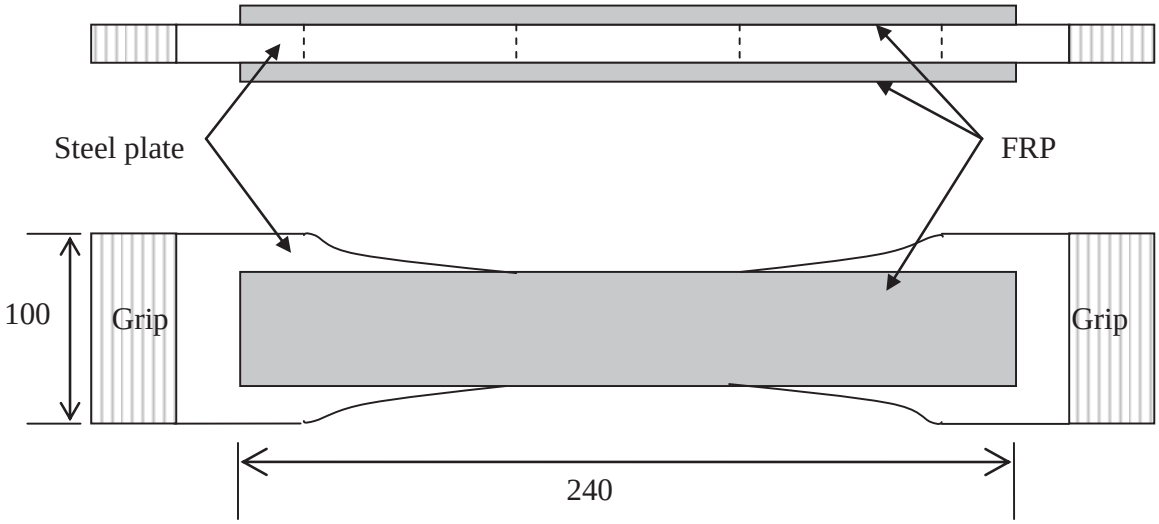

Figure 2.24 Typical pull test with steel yielding setup

CHAPTER 3: PUSH PULL TESTS

INTRODUCTION

This chapter explains the push-pull tests of FRP plates adhesively bonded to a steel block. Pull tests were conducted in order to predict the bond strength and also for developing local bond-slip curves based on strain measurements (Lu, Teng et al. 2005). The main objective of these experiments is to obtain the τ-δ relationship of FRP plated steel using alternative approach compared to what was reported in previous research by Xia and Teng (2005). The next section of this chapter will be the description of the test specimens, test setup, instrumentation and material properties. Then observations from each individual test are described. Finally, summary and conclusion of the whole tests are discussed.

SPECIMENS

Ten FRP plates bonded to steel were tested with varied bonded length. All of the FRP plates were 100 mm of width. The bonded length of the FRP varies at 250 mm (one and two layers of FRP plate), 100 mm and 20 mm. The variation of the bonded length was used to investigate the effect of critical bond length in the experiment. A specimen where critical bond length was exceeded is named as a fully anchored specimen whereas the specimen in which it has not exceeded the critical bond length is named as a not fully anchored specimen. The FRP plate was glued at the centre to the steel block as shown in Figure 3.1. Two types of adhesive, SIKA and CIBA were used in the experiment. The parameters of the ten FRP plates are summarised in Table 3.1. The bonded length was determined using Eqs. (2.9) with initial values of τ_{max}-δ_{max} taken from Xia and Teng (2005).

The steel block was fabricated by welding two 12 mm thick steel plates to two 70 mm x 50 mm rectangular hollow sections with a thickness of 3 mm. The

steel block can be used repeatedly as long as the surface was cleaned appropriately. The surfaces were sandblasted and cleaned with Acetone to remove any particles that may affect the bond between the steel and adhesive. The adhesive was set to 1 mm thick. In order to achieve this, a 1 mm diameter ball bearing was placed along the steel block as spacers (Figure 3.2). After the FRP plate was laid on the steel block, a sufficient force (a weight of 20 kg) must be placed on top of it for a minimum of five hours so that constant thickness of adhesive can be achieved and any excess adhesive extruding out from the FRP plate can be removed (Figure 3.3). The specimen then was left for five days for curing.

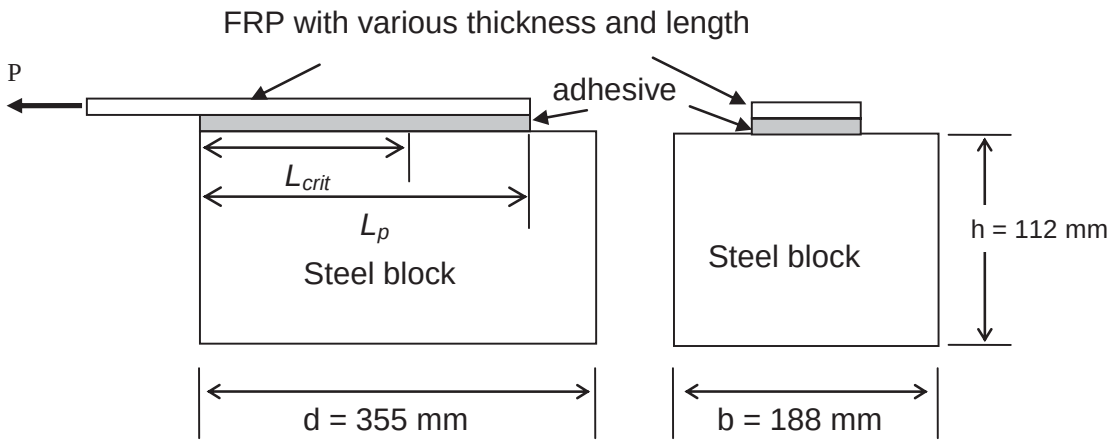

Figure 3.1 Typical pull test setup

Table 3.1 Material and geometric properties of the FRP plate

Test specimen	FRP thickness (mm), t_p	Bonded length (mm), L_p	Young's Modulus (MPa), E_p	Category
SIKA 1	1.2	250	156383	Fully anchored
SIKA 2	2.4	250	160942	Fully anchored
SIKA 3	1.2	100	155743	Fully anchored
SIKA 4	1.2	20	159513	Not fully anchored
SIKA 5	1.2	20	158571	Not fully anchored
CIBA 6	1.2	250	157944	Fully anchored
CIBA 7	2.4	250	160727	Fully anchored
CIBA 8	1.2	100	159209	Fully anchored
CIBA 9	1.2	20	158418	Not fully anchored
CIBA 10	1.2	20	152147	Not fully anchored

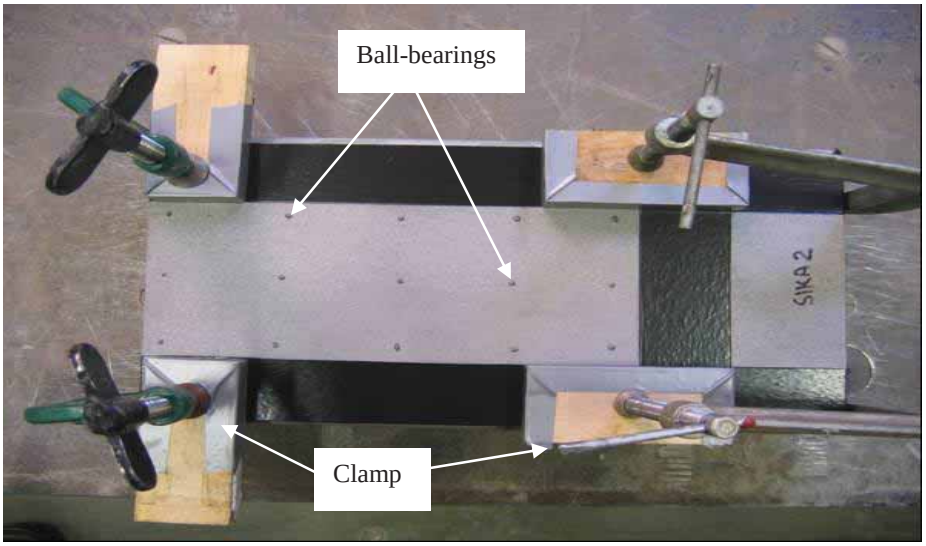

Figure 3.2 Ball bearings set on the steel surface

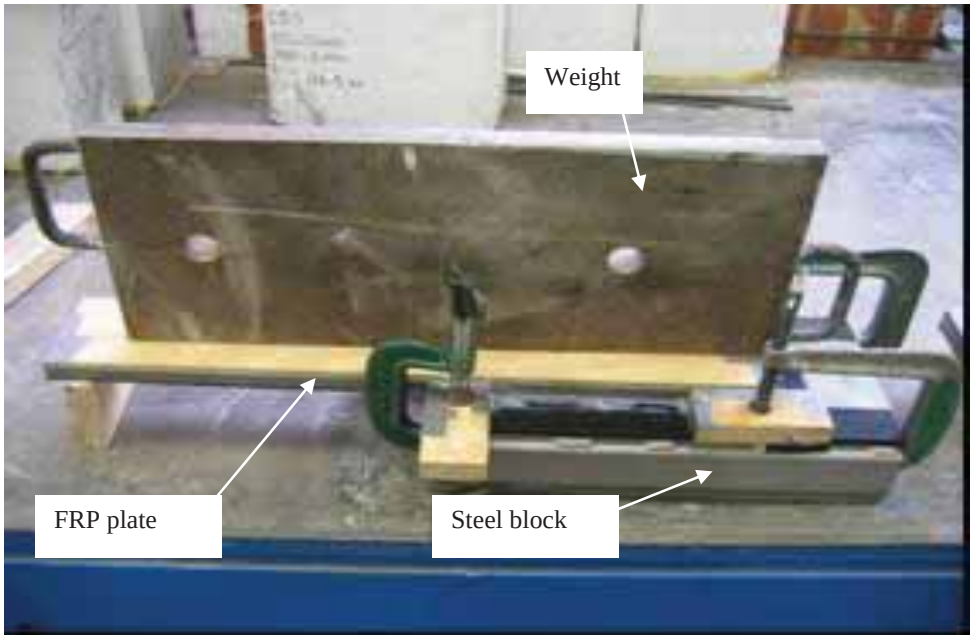

Figure 3.3 Force applied on FRP-to-steel

TEST SETUP

A Universal Testing Machine (UTM) was used for the pull test. The steel block plated with the FRP was placed upward, where the bottom of the steel block was clamped to the UTM to minimize plate bending as shown in Figure 3.4. The loaded end of the steel block was restraint by a steel plate to avoid uplifting (Figure 3.5). An L-shaped aluminium plate was glued on the FRP plate as a restraint for the Linear Variable Differential Transformer (LVDT) as shown in Figure 3.5. The L-shaped aluminium plate pressed the LVDT downward and the slip reading was initialised to 0. When the FRP plate was being pulled out, the L-shaped aluminium plate will be moving outward. The data recorded from the LVDT from this movement is the slip.

An aluminium plate was glued at the end of the FRP plate as shown in Figure 3.6 to provide a firm grip between the UTM machine and the FRP plate. Then the load was applied under load control at linear range. However, as the

specimen reaches its nonlinear region, the speed of the load increment must be slowed down as it reaches debonding so that the data logger is able to capture the strain data i.e. displacement control is applied. This is important so that the data logger is able to capture the test data from the strain gauges and from the LVDTs.

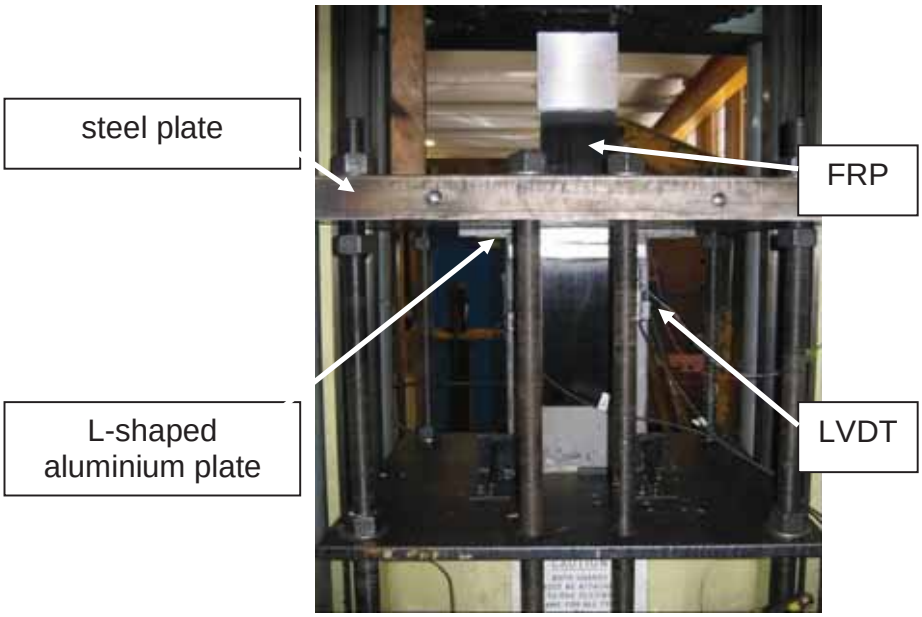

Figure 3.4 Test rig with the specimen

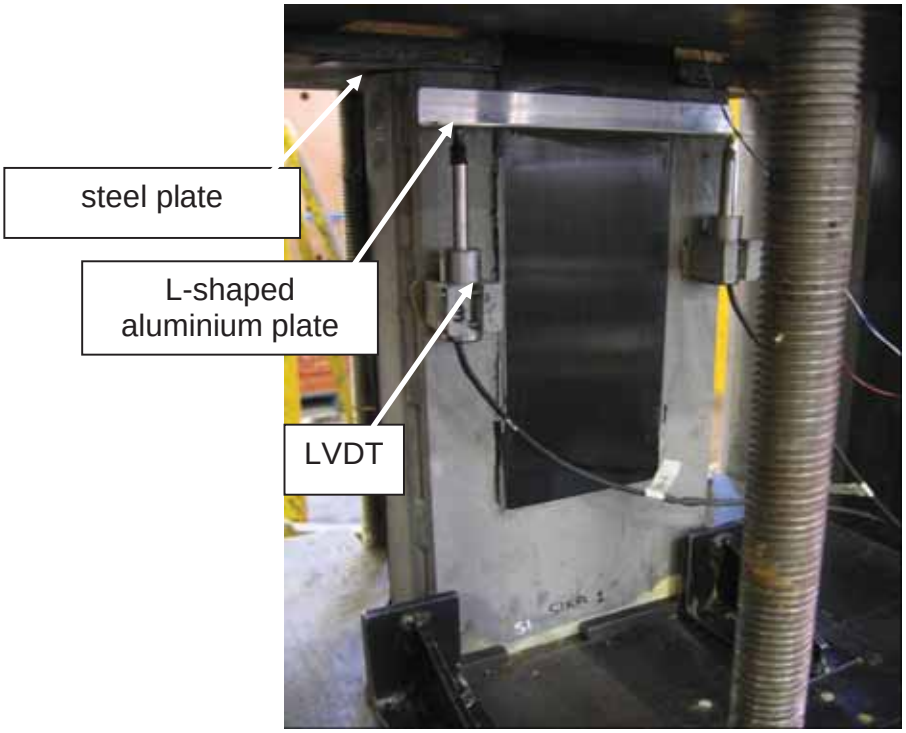

Figure 3.5 Location of steel plate for restraining and aluminium plate for LVDT's restraint.

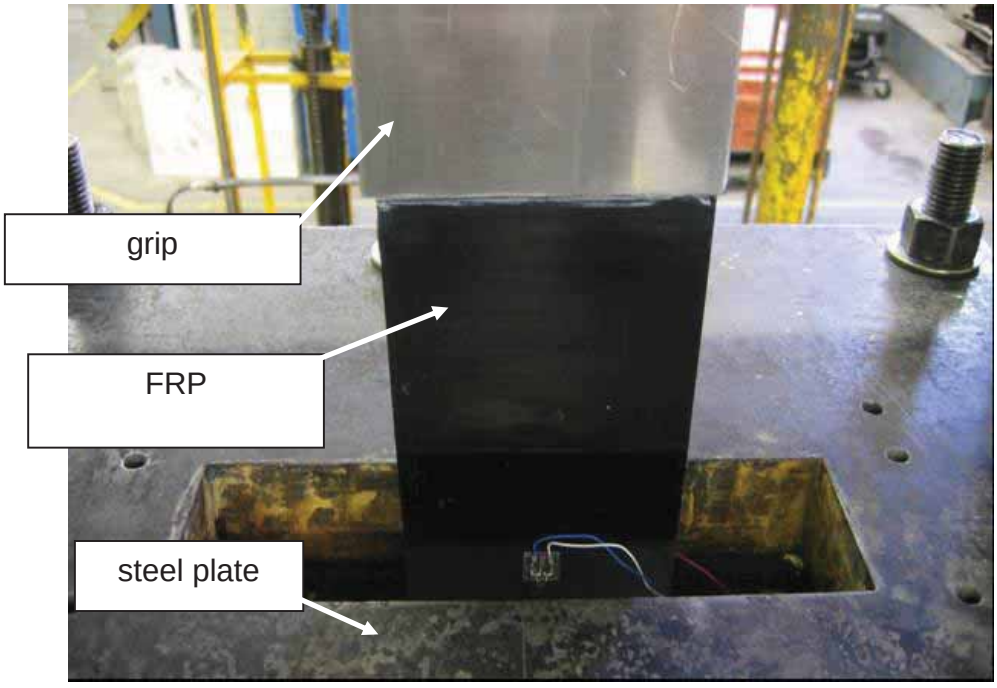

Figure 3.6 Aluminium plate as a grip

INSTRUMENTATION

Two 10 mm strain gauges were glued 20 mm away from the loaded end as shown in Figure 3.7. The purpose of the strain gauges was to provide information on the FRP plate's Young's Modulus from the stress-strain curve that can be derived from the load and strain data. The other purpose of the strain gauges was to detect any bending that may occur on the FRP plate while load was applied. Plate bending was considered to occur when the differences between the top and bottom of the strain gauges were relatively large. Two LVDT (L1 and L2) were set at the loaded end or free end of the specimen as shown in Figure 3.7. The data from the LVDT and strain gauges were connected and recorded by a computer.

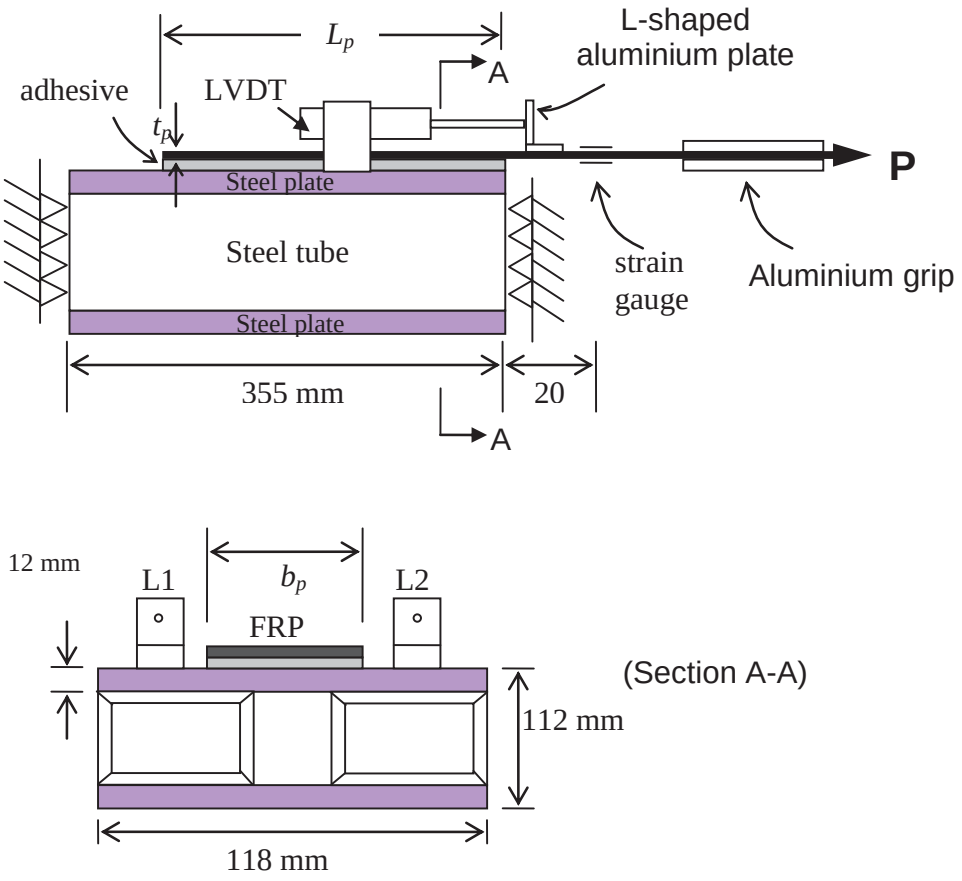

Figure 3.7 Detail instrumentations of the specimen

MATERIAL PROPERTIES

The adhesives used were CIBA and SIKA (A and B as in Xia and Teng (2005)) and the material properties are listed in Table 3.2 which were obtained directly from the dog-bone specimens tested by Xia and Teng (2005). Both of the adhesives consisted of two parts: that must be mixed together. For SIKA, the mixture was in the ratio of 3:1 whereas for CIBA, 1:1. After mixing, there was about 45 minutes for the adhesive to be applied on to the steel block before it became too sticky to be workable. The FRP plates used in the tests had the same values of width (b_p) of 100 mm. The material properties of the adhesives used were determined experimentally (dog bone specimens) and is tabulated in Table 3.2 (Xia and Teng (2005). Using Eq. 2.11, the L_{crit} for CIBA and SIKA specimens are calculated to be at 70 mm.

Table 3.2 Material properties of adhesive

Adhesive	Tensile strength (MPa)	Young's Modulus (MPa)	Ultimate tensile strain (%)	Poisson's ratio
SIKA	20.48	10793	0.1898	0.27
CIBA	22.53	4013	0.5614	0.36

TEST RESULTS OF SIKA SPECIMEN

This section describes the experimental results for specimen glued with SIKA adhesive. Average stress is,

$$\tau_{ave} = \frac{P}{A_p} \tag{3.1}$$

Where P is the applied load and A_p is the cross section at the plate steel interface.

3.6.1 SPECIMEN SIKA 1

This was the first specimen tested. The fibres along the longitudinal direction of the FRP plate were split as shown in Figure 3.8 (a). It was observed that debonding at the adhesive layer occurred at the loaded end before slowly shifting to the interface of adhesive and FRP plate as shown in Figure 3.8 (b). Some of the fibres of the FRP plate were observed to remain glued to the adhesive layer at the free end of the specimen which means that the failure mode was within the adhesive layer. Figure 3.9 shows the P-Δ relationship where there is a clear indication where the first point of IC debonding has been reached at a slip of 0.07 mm. The P_{IC} corresponding to that slip is 73.9 kN. Total debonding of the FRP plate from the steel block occurred at a slip of 0.77 mm.

(a) FRP plate at failure

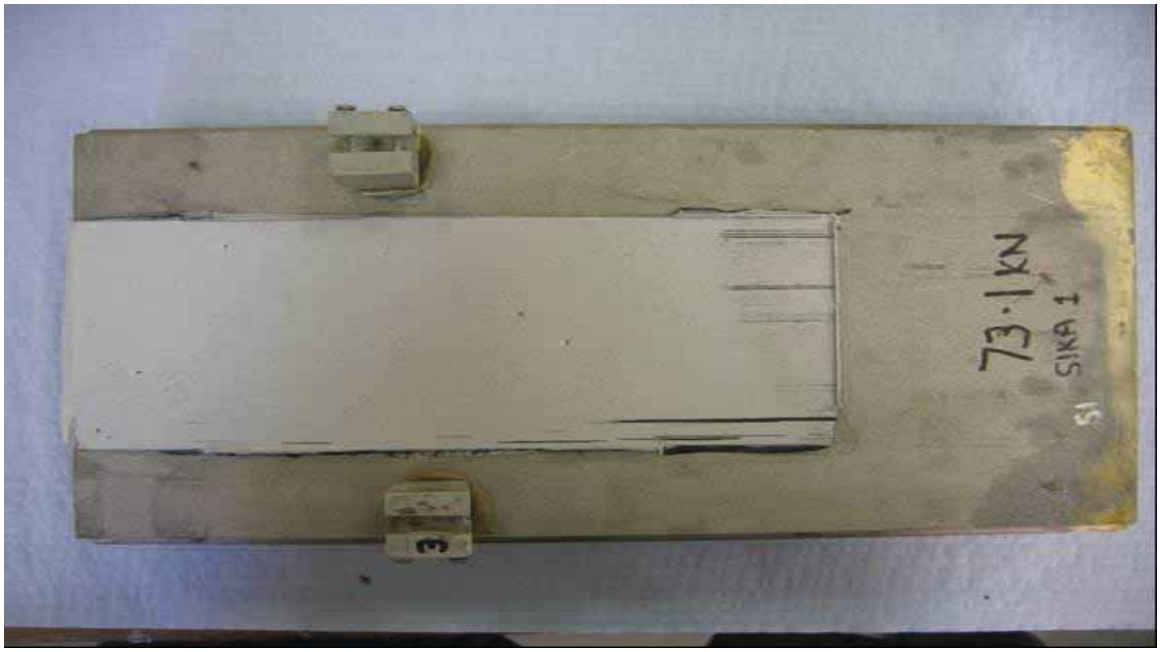

(b) Adhesive layer at failure

Figure 3.8 Failure mode of specimen SIKA 1

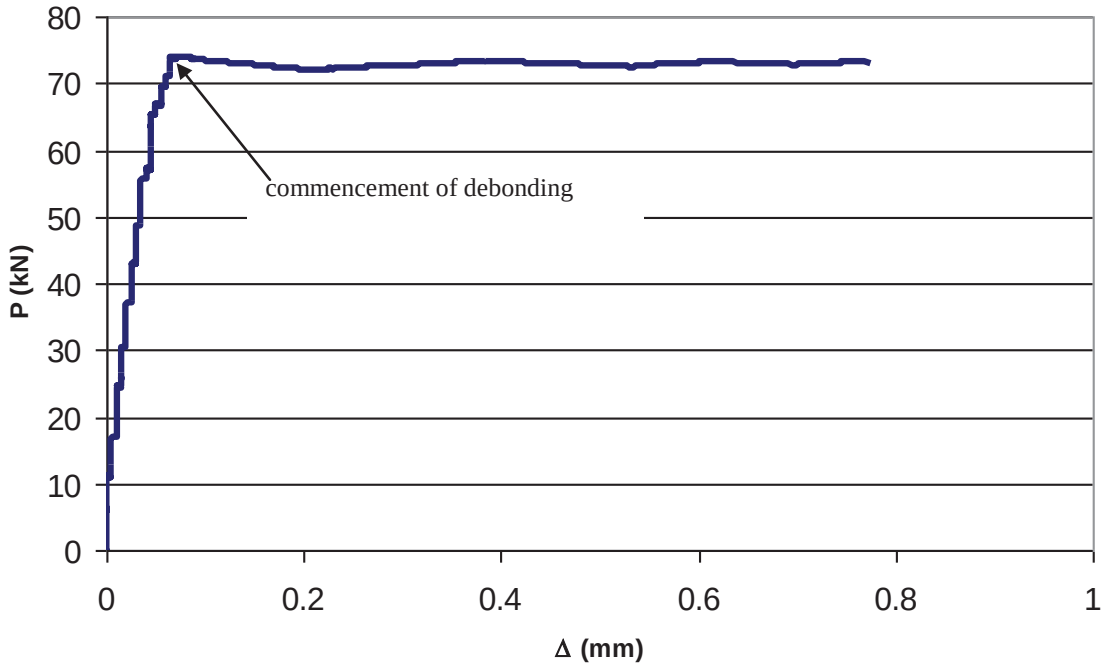

Figure 3.9 Global P-Δ for specimen SIKA 1

3.6.2 SPECIMEN SIKA 2

Specimen SIKA 2 was similar to SIKA 1 except that the thickness of the FRP was doubled. The failure mode was almost the same as SIKA 1 with the fibres along the longitudinal direction of the FRP plate being split as shown in Figure 3.10 (a). However, unlike SIKA 1, there was more of a concentration of FRP plate fibres that remained glued to the adhesive layer at the free end of the specimen (Figure 3.10 (b)). The approximate maximum slip is 0.095 mm with the corresponding P_{IC} of 100.5 kN as shown in Figure 3.11. The higher IC load was expected due to the thicker FRP plate. Total debonding of the FRP plate from the steel block occurred at a slip of 0.4 mm.

(a) FRP plate at failure

(b) Adhesive layer at failure

Figure 3.10 Failure mode of specimen SIKA 2

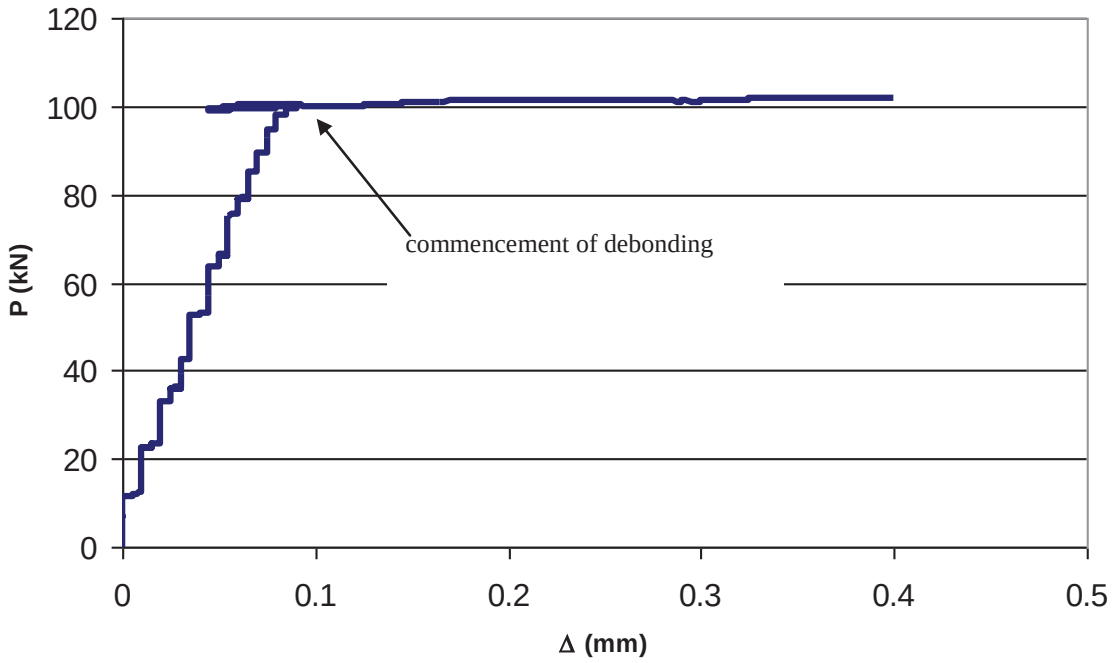

Figure 3.11 Global P-Δ for specimen SIKA 2

3.6.3 SPECIMEN SIKA 3

The failure mode was basically at the adhesive layer (Figure 3.12 (a)) but some of the FRP fibres were still glued to the adhesive layer near to the loaded end. The FRP plate itself split just like the previous specimens SIKA 1 and SIKA 2. A small chunk of the adhesive was split at the corner of the free end as shown in Figure 3.12 (b). Figure 3.13 shows the applied load against slip at the loaded end curve. The slip was 0.055 mm at the P_{IC} of 68.7 kN. The shorter plateau compared to SIKA 1 and SIKA 2 was expected since the bonded length was shorter.

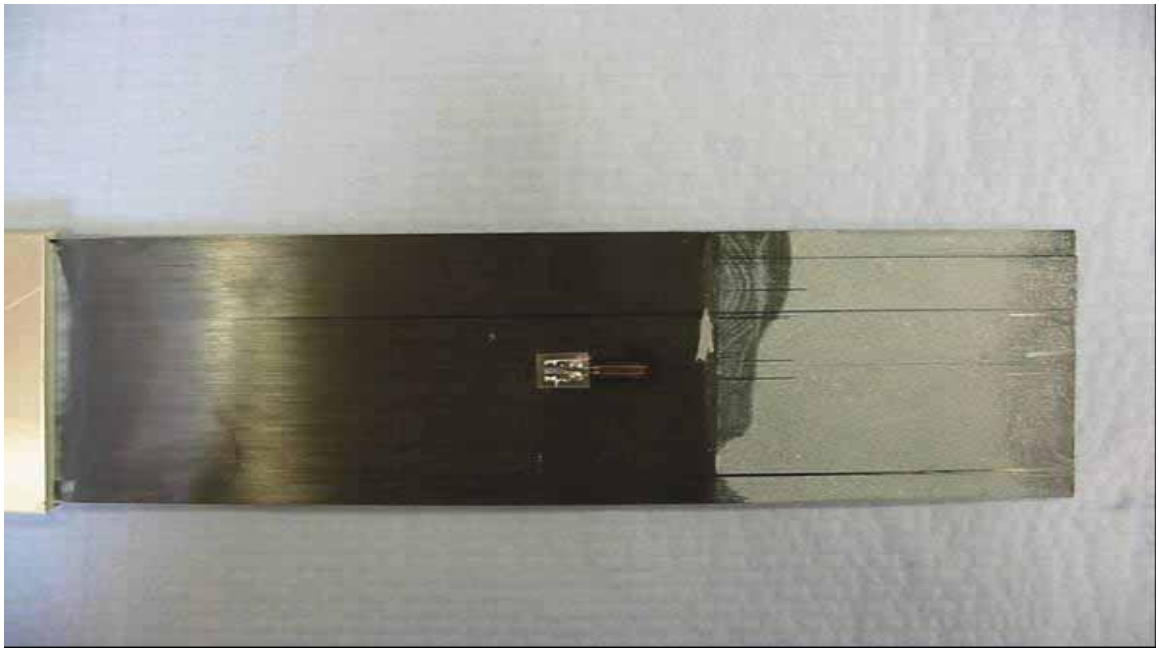

(a) FRP plate at failure

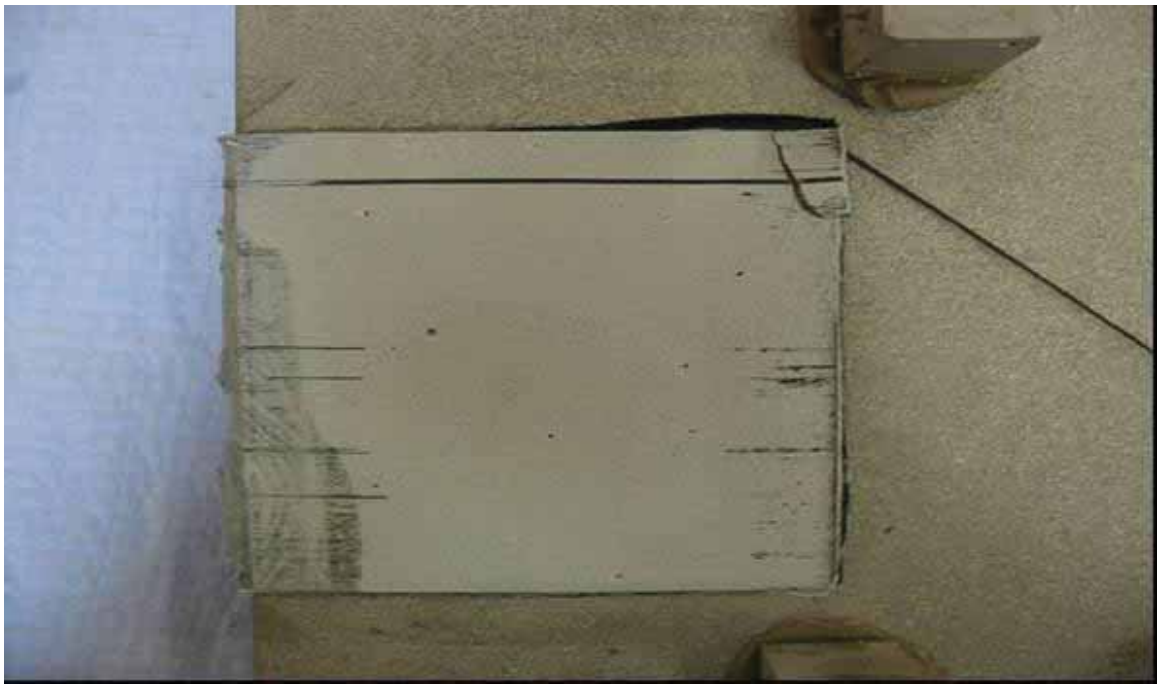

(b) Adhesive layer at failure

Figure 3.12 Failure mode of specimen SIKA 3

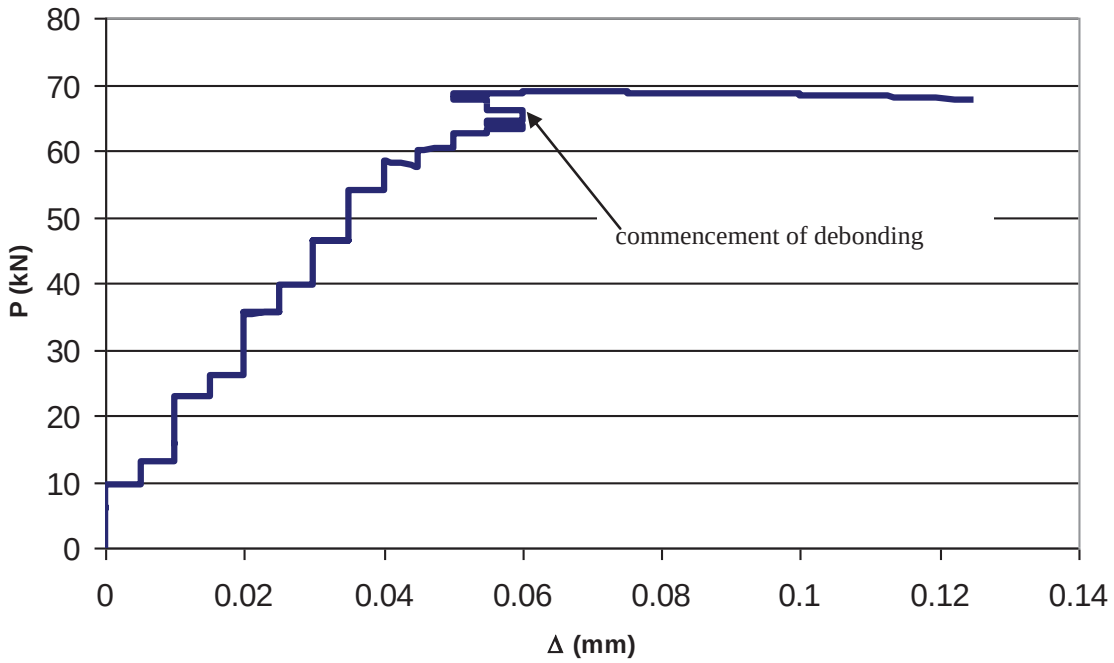

Figure 3.13 Global P-Δ for specimen SIKA 3

3.6.4 SPECIMEN SIKA 4

SIKA 4 was the not fully anchored specimen. The failure mode was between the adhesive and the FRP plate as in Figure 3.14 (a) leaving the chunk of the adhesive attached to the steel block. Some FRP fibre was also glued to the adhesive layer (Figure 3.14 (b)). FRP plate splitting was also observed. The *P-Δ* relationship is shown in Figure 3.15. Since the bond length was less than the critical bond length of 70 mm (Section 3.5), a plateau was not expected. An average shear stress can be calculated as the bond length was very small at 20 mm. From the corresponding failure load of 44.8 kN, the average shear, τ_{ave} was calculated as 22.4 MPa. The zigzag line, instead of an expected smooth line, was observed in the graph was simply because the accuracy of the LVDT was limited to 0.005 mm only.

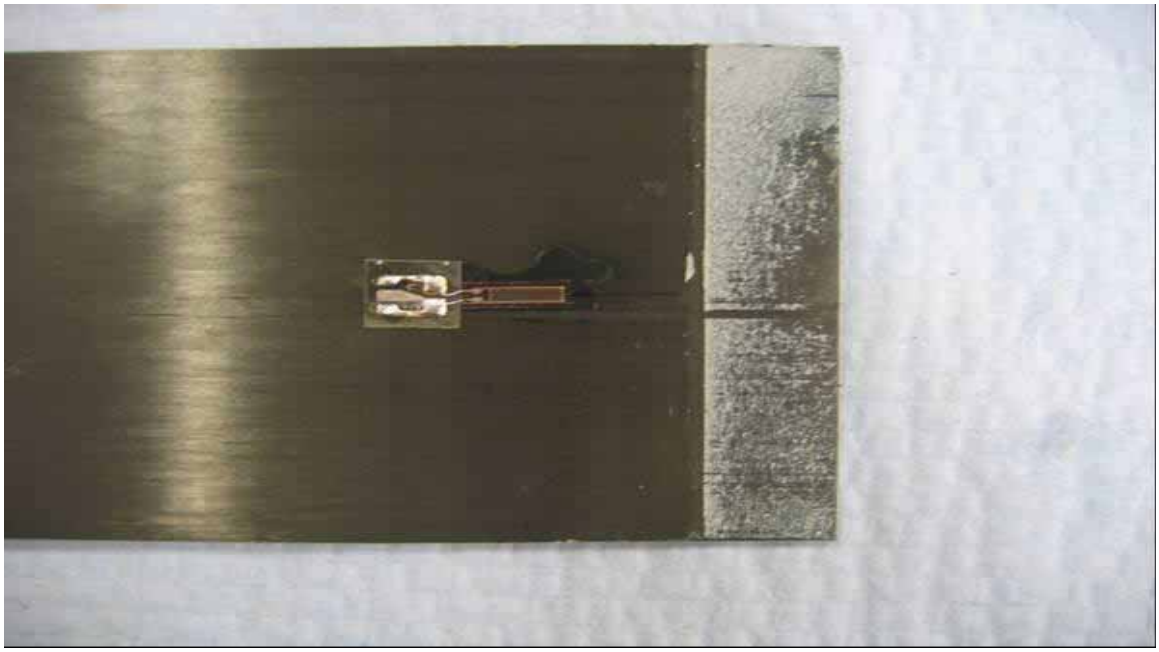

(a) FRP plate at failure

(b) Adhesive layer at failure

Figure 3.14 Failure mode of specimen SIKA 4

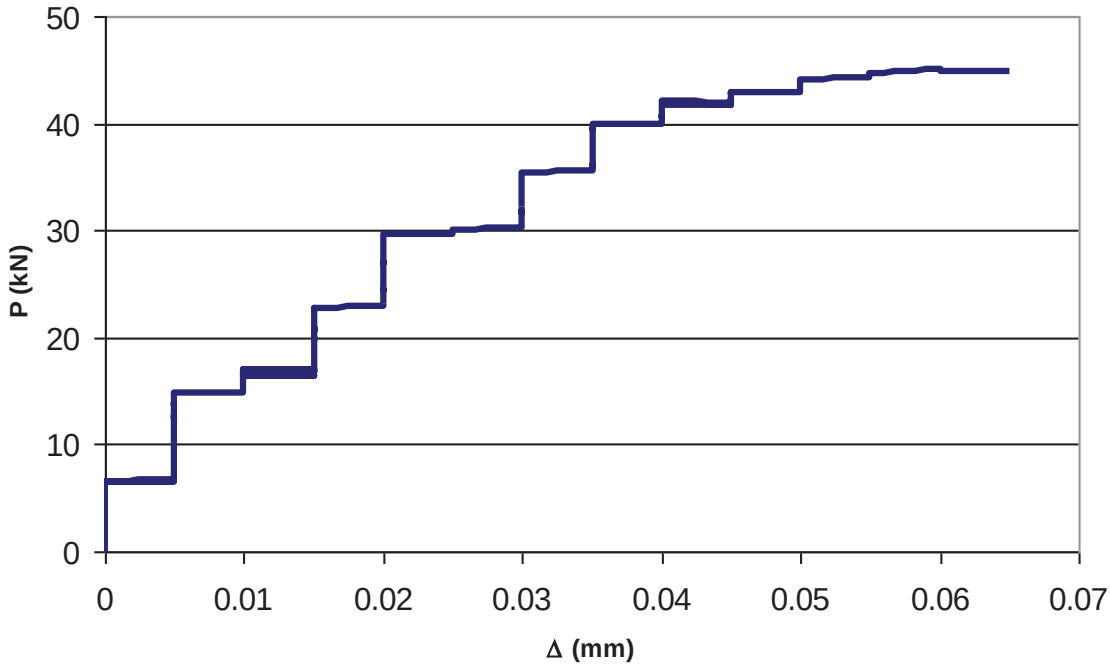

Figure 3.15 Global P-Δ for specimen SIKA 4

3.6.5 SPECIMEN SIKA 5

The specimen was identical to SIKA 4 so the same failure mode was expected. It was observed that some adhesive portion was glued to the FRP plate as shown in Figure 3.16 (a). There was some FRP fibres glued to the adhesive as well (Figure 3.16 (b)). A similar *P-Δ* curve as SIKA 4 was expected as shown in Figure 3.17. The corresponding failure load was 46.8 kN at an end slip of 0.06 mm. The average shear, τ_{ave} was calculated as 23.4 MPa.

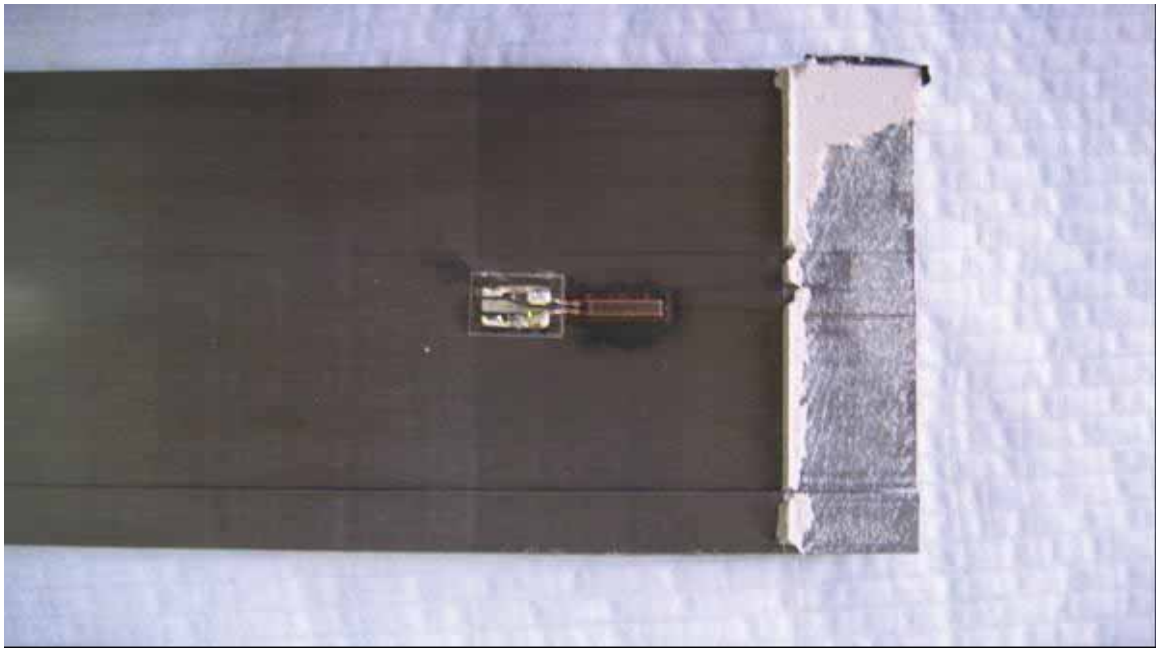

(a) FRP plate at failure

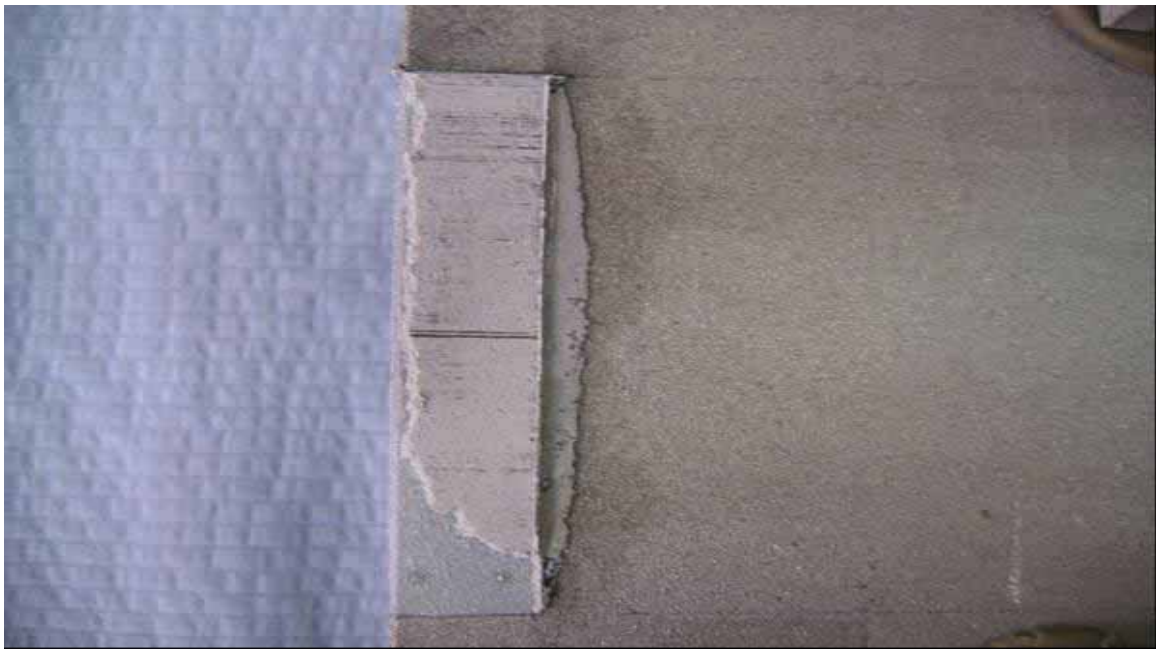

(b) Adhesive layer at failure

Figure 3.16 Failure mode of specimen SIKA 5

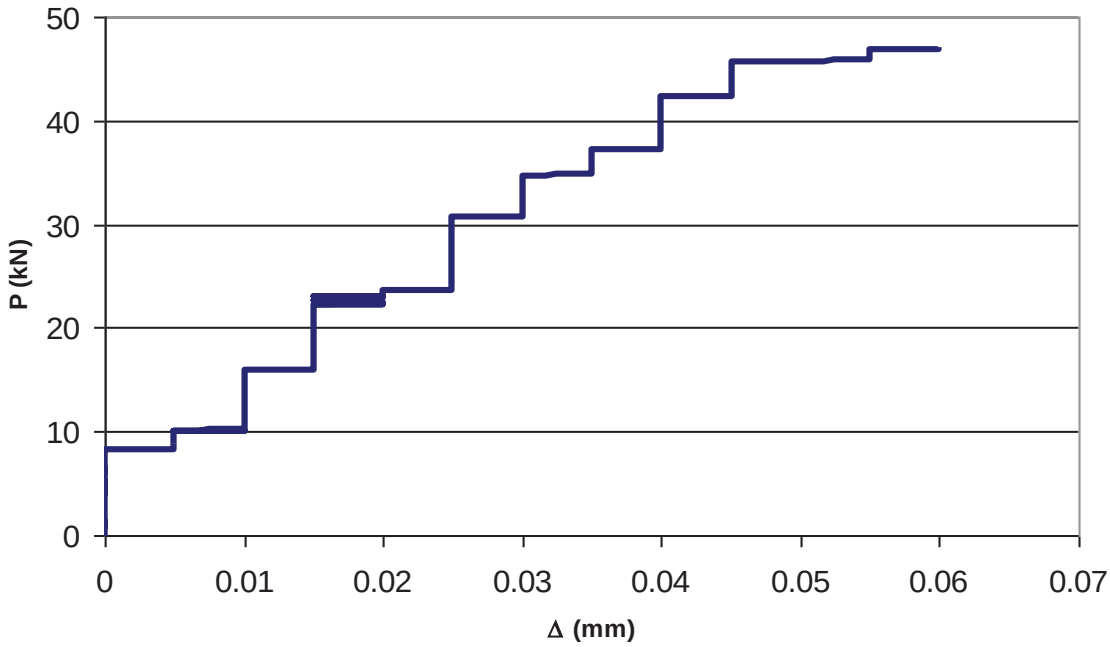

Figure 3.17 Global P-Δ for specimen SIKA 5

3.6.6 SUMMARY ON SIKA SERIES TESTS

The global *P-Δ* responses for FRP bonded steel joints for SIKA adhesive are shown in Figure 3.18. For the fully anchored specimens, SIKA 1, SIKA 2 and SIKA 3, the displacement increased linearly with the load and then extends to a plateau. For a bond length of 100 mm, SIKA 3, the plateau is shorter than 250 mm which means that the total debonding occurred faster in a shorter specimen even though the P_{IC} value is the same since debonding propagated progressively from the loaded end. With the increase of FRP thickness, the value of P_{IC} is higher but it loses its ductility as shown by the shorter plateau.

Pure interfacial debonding, which is the debonding between the adhesive-FRP and adhesive-steel, was not observed which indicates the strong bond capacities of the adhesive to the steel and FRP plate surfaces. The failure mode for the fully anchored specimens (SIKA 1, SIKA 2 and SIKA 3) occurred within the

adhesive layer indicated by a thin layer of adhesive that was attached to the FRP plate after failure.

For the not fully anchored specimens, the value of average bond shear, τ_{ave} was 22.4 MPa and 23.4 MPa. The failure mode was within the adhesive layer similar to the fully anchored specimens.

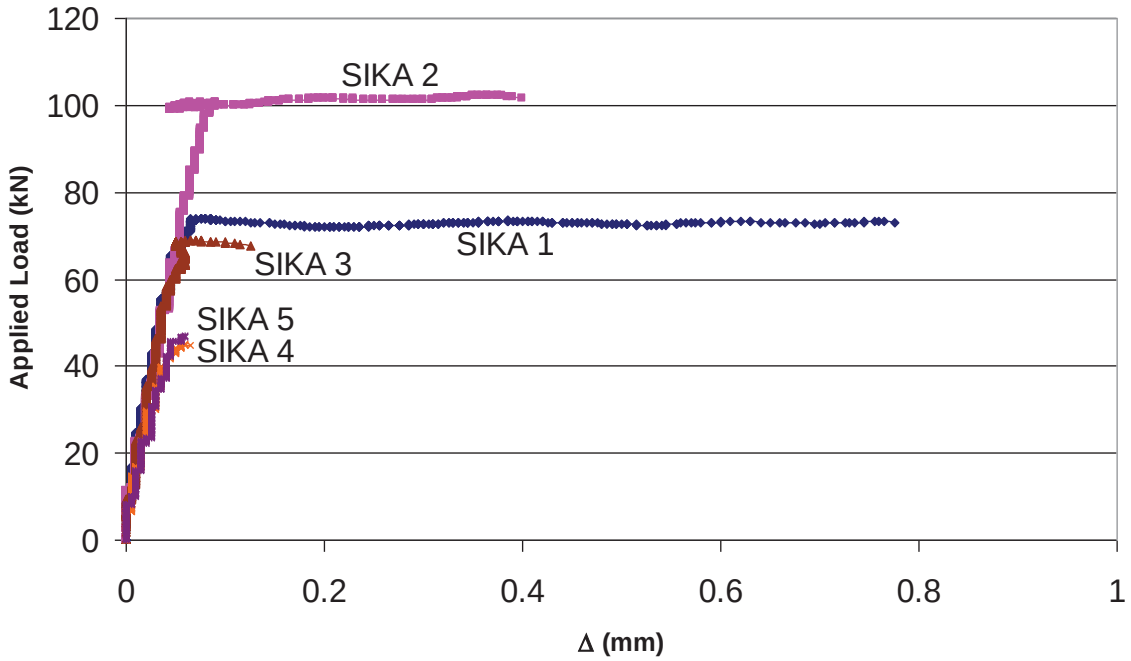

Figure 3.18 Global P-Δ for specimen SIKA series

3.7 TEST RESULTS OF CIBA SPECIMEN

This section describes the experimental results for specimens glued with CIBA adhesive.

3.7.1 SPECIMEN CIBA 6

Figure 3.19 (a) shows the failure mode of specimen CIBA 6 and it can be observed that there are two modes of failure: at the adhesive layer and at interfacial face of the adhesive and FRP layers. At the adhesive layer failure, part of the adhesive remained glued to the FRP layer and similarly part of the FRP fibres remained glued to the adhesive layer (Figure 3.19 (b)). This is in contrast to the failure mode for SIKA 1 where a smooth failure occurred within the adhesive layers.

Figure 3.20 shows the global P-Δ curve of CIBA 6. The P_{IC} value for CIBA 6 is 100.6 kN with the corresponding slip of 0.07 mm. Total debonding occurred when the slip reached 0.40 mm. At the point where the first IC debonding load was achieved, a reduction of slip was observed. This can be attributed to a possible error in the experimental setup which can also be observed, in sample SIKA 2 in Figure 3.11. There are two possible errors related to the decreasing slip as it reached debonding point. First, there might be an eccentricity due to movement of the FRP plate due to the weak grip at the pulling end that pressed the aluminium plate towards the LVDT (instead of moving away). Secondly, the grip on the upper part of the pulling machine may have slide a bit, pulling only half of the FRP plate. The result of this is that one of the LVDT having increased reading while the other decreasing (based on average of two LVDTs). A check with the raw data shows that both of the LVDTs were giving out decreasing slip value, eliminating the second possibility. Furthermore, the slip is too small, even at total debonding. Therefore, a sligtht movement of the grip will appear significant in the graph.

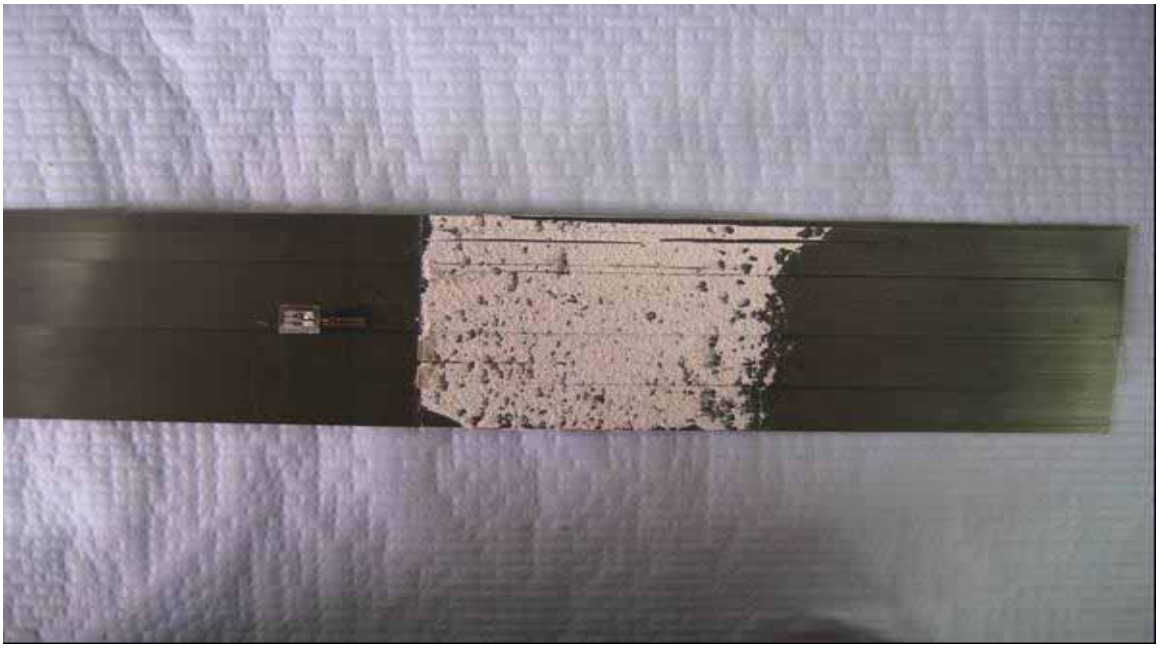

(a) FRP plate at failure

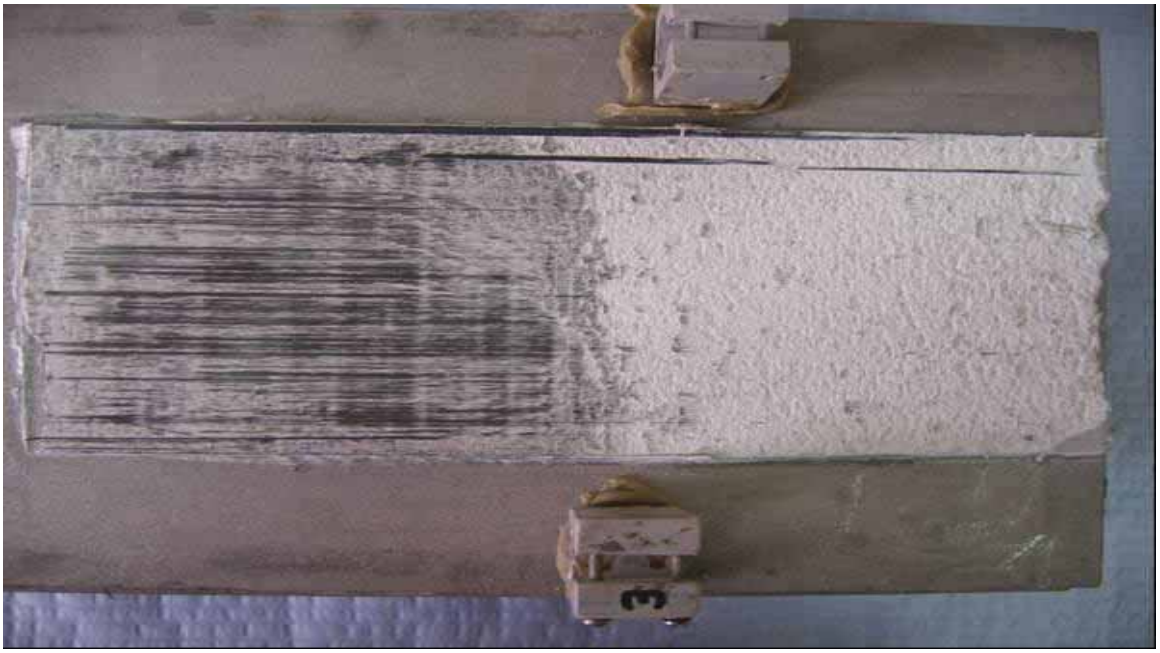

(b) Adhesive layer at failure

Figure 3.19 Failure mode of specimen CIBA 6

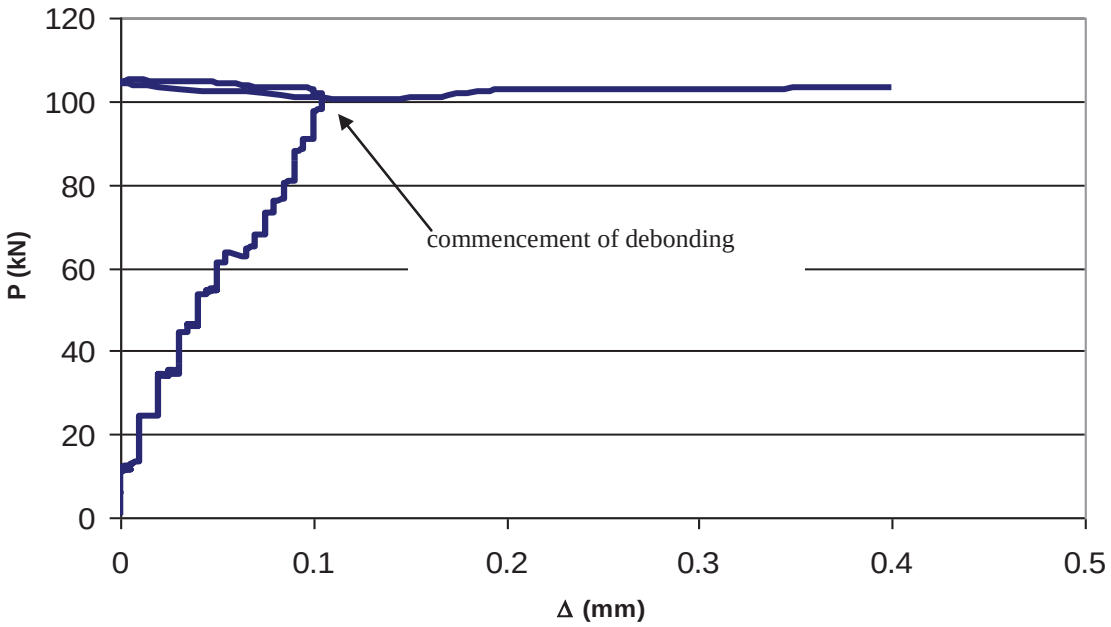

Figure 3.20 Global P-Δ for specimen CIBA 6

3.7.2 SPECIMEN CIBA 7

Figure 3.21 shows the failure mode of sample CIBA 7 which is similar to CIBA 6. Half of the bonded FRP failed on the adhesive layer and the other half failed on the FRP layer. The higher IC debonding load was expected because the layer of the FRP was doubled compared to CIBA 6. The P_{IC} was 152.3 kN and the corresponding slip was 0.17 mm as shown in Figure 3.22. Total debonding occurred when the slip reached 0.45 mm.

(a) FRP plate at failure

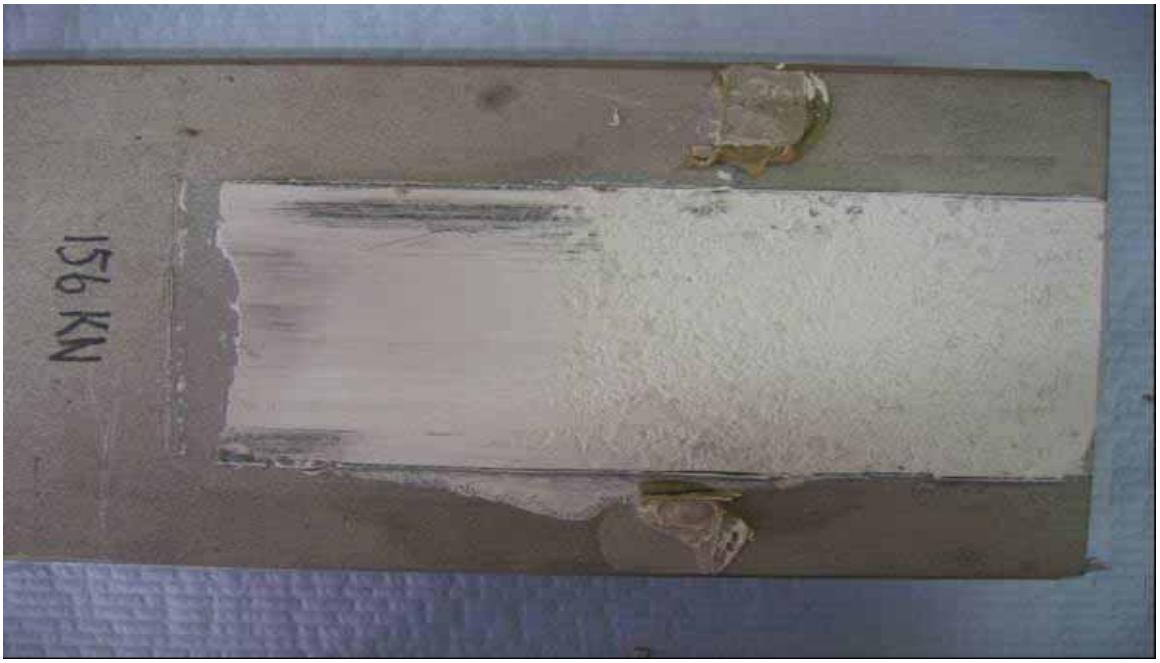

(b) Adhesive layer at failure

Figure 3.21 Failure mode of CIBA 7 specimen

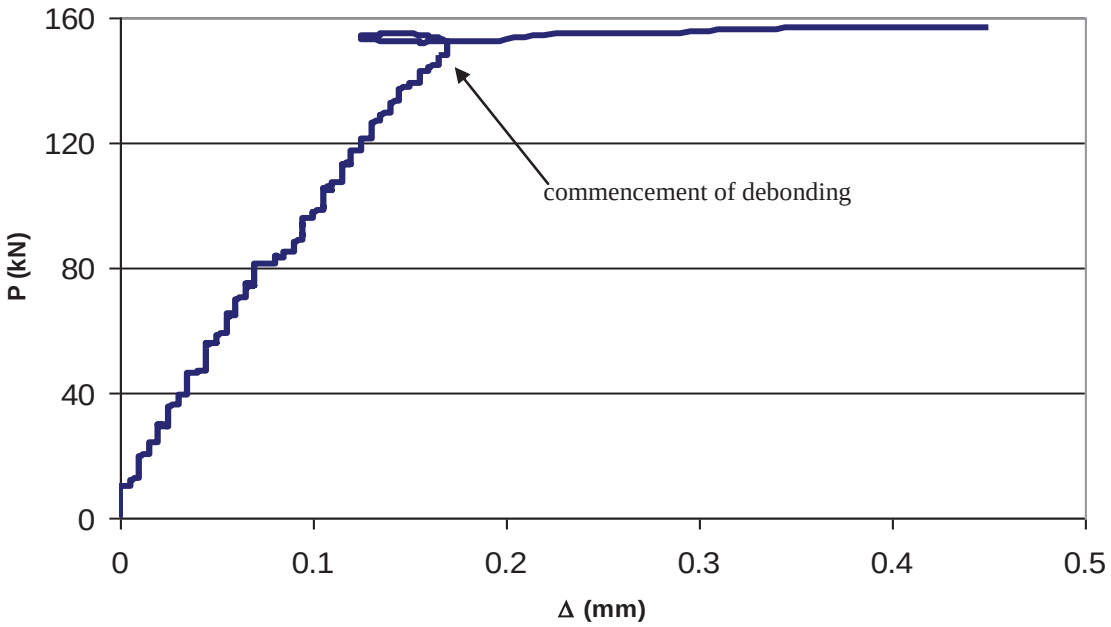

Figure 3.22 Global P-Δ for specimen CIBA 7

3.7.3 SPECIMEN CIBA 8

In this test, the slip data was faulty and did not give a correct reading. The specimen at failure is shown in Figure 3.23. The failure mode is similar to CIBA 6 and CIBA 7 where half of the bonded FRP failed on the adhesive layer and the other half failed on the FRP layer. Figure 3.24 shows the global *P-Δ* curve. At a load of 100 kN, the slip reduced instead of increasing which implied that there was a probable error during the experiment as reported in Section 3.7.1.

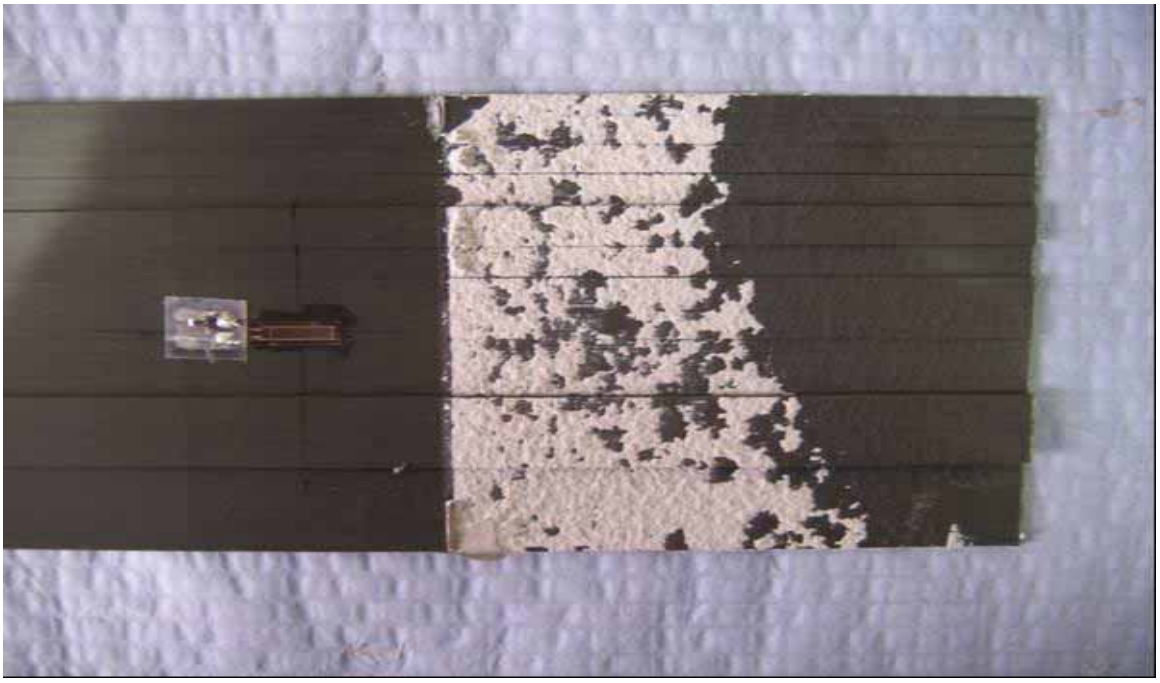

(a) FRP plate at failure

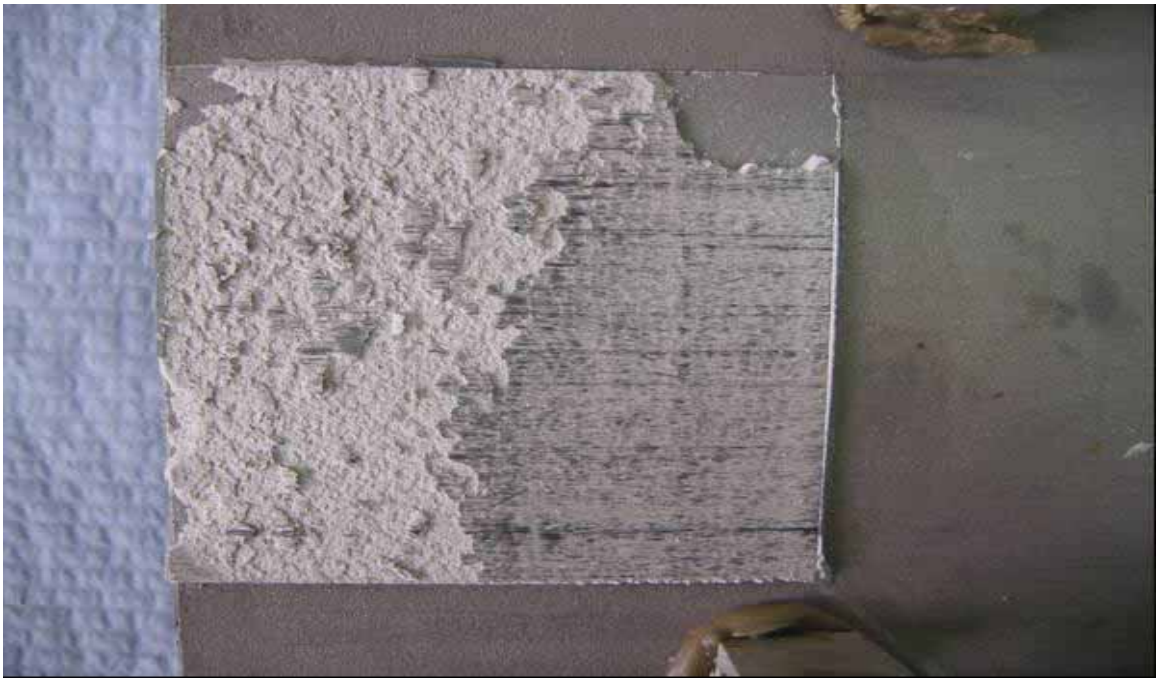

(b) Adhesive layer at failure

Figure 3.23 Failure mode of specimen CIBA 8

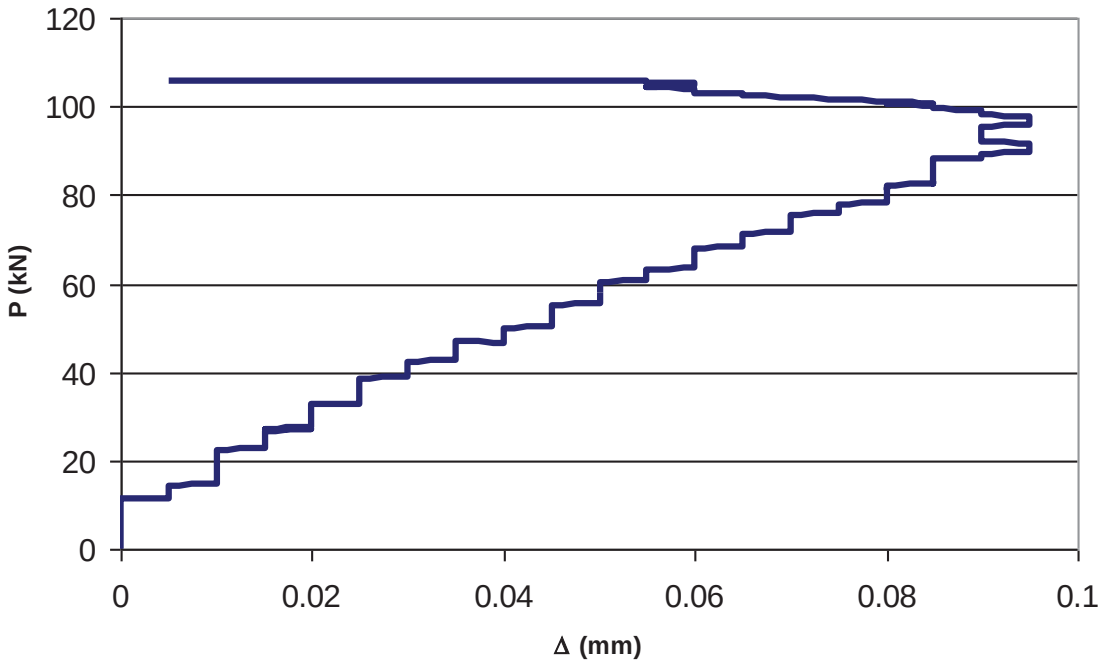

Figure 3.24 Global P-Δ for specimen CIBA 8

3.7.4 SPECIMEN CIBA 9

Figure 3.25 shows the failure mode of sample CIBA 9 where the bond length was 20 mm. The failure mode was within the FRP plate. Figure 3.26 shows the global P-Δ curve. From the corresponding failure load of 44.7 kN, the average shear, τ_{ave} was calculated as 22.4 MPa.

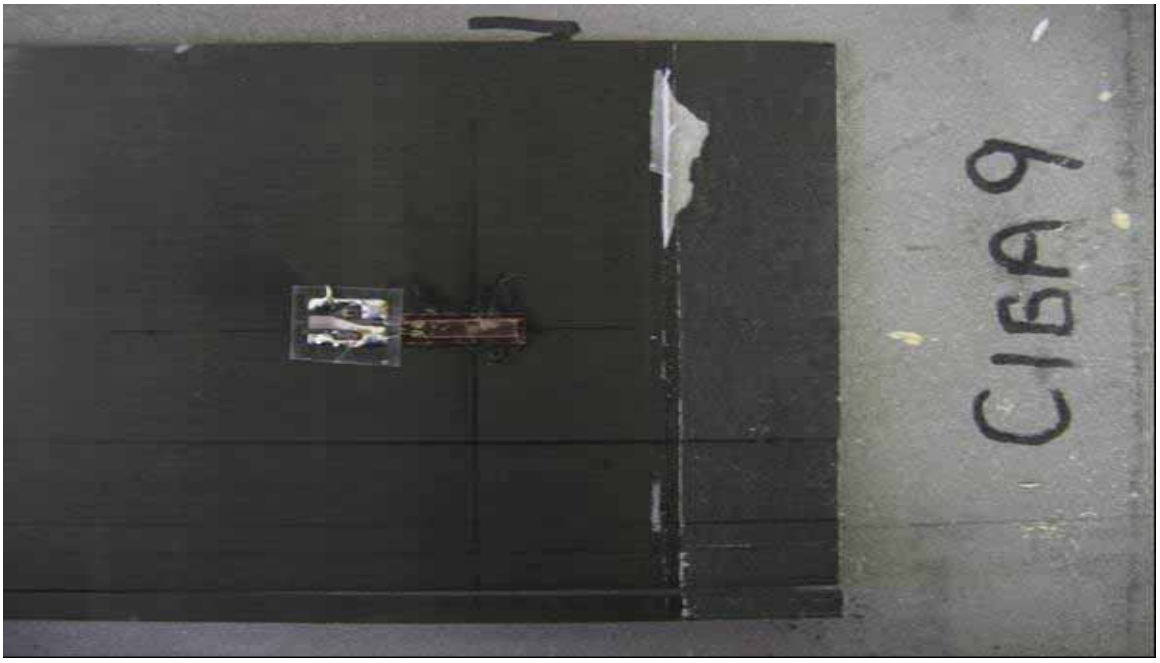

(a) FRP plate at failure

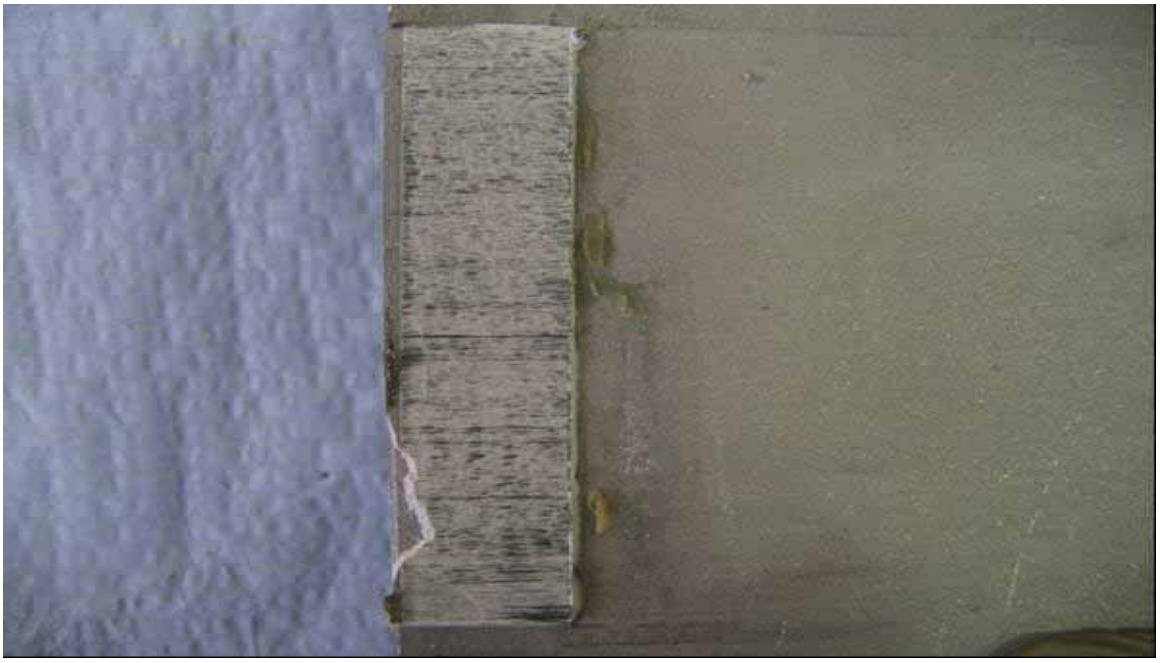

(b) Adhesive layer at failure

Figure 3.25 Failure mode of specimen CIBA 9

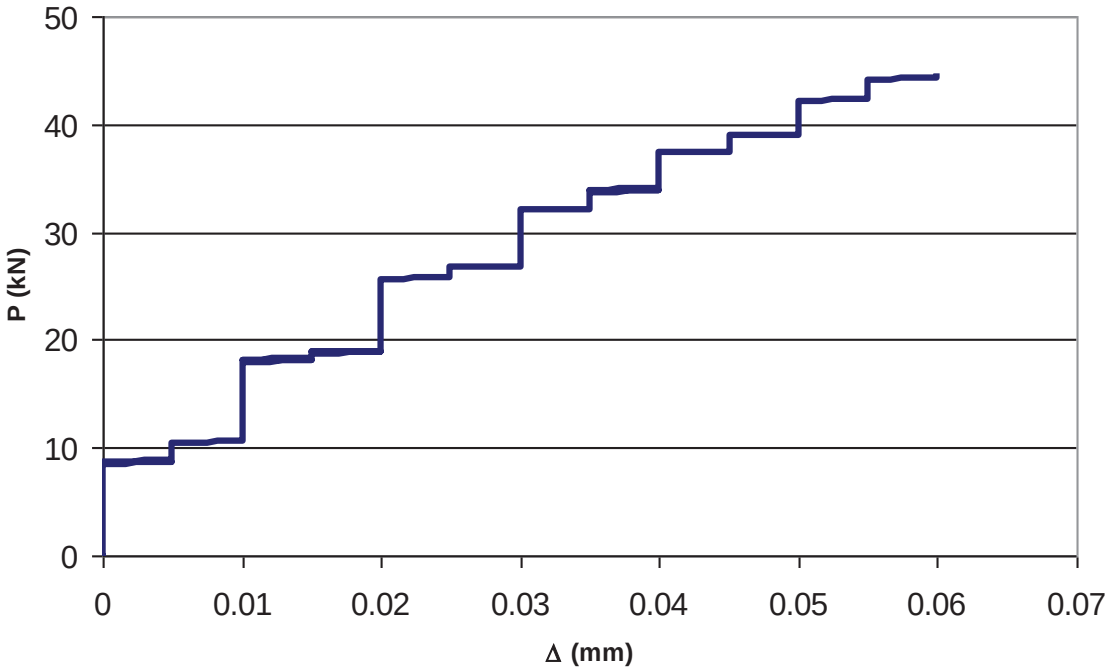

Figure 3.26 Global P-Δ for specimen CIBA 9

3.7.5 SPECIMEN CIBA 10

The test for short bond length was repeated in CIBA 10 and the failure mode is shown in Figure 3.27. The failure mode was within the FRP plate. The failure load, as shown in Figure 3.28, was 36 kN and the corresponding τ_{ave} was calculated as 18 MPa which is 20% less than CIBA 9.

(a) FRP plate at failure

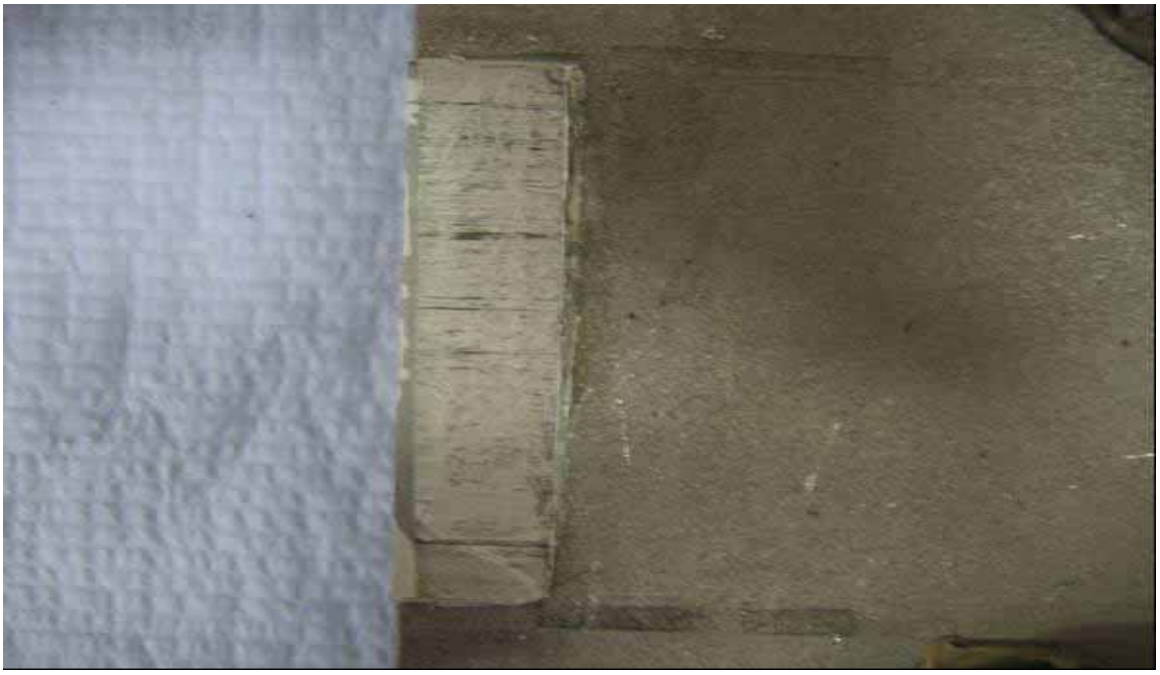

(b) Adhesive layer at failure

Figure 3.27 Failure mode of specimen CIBA 10

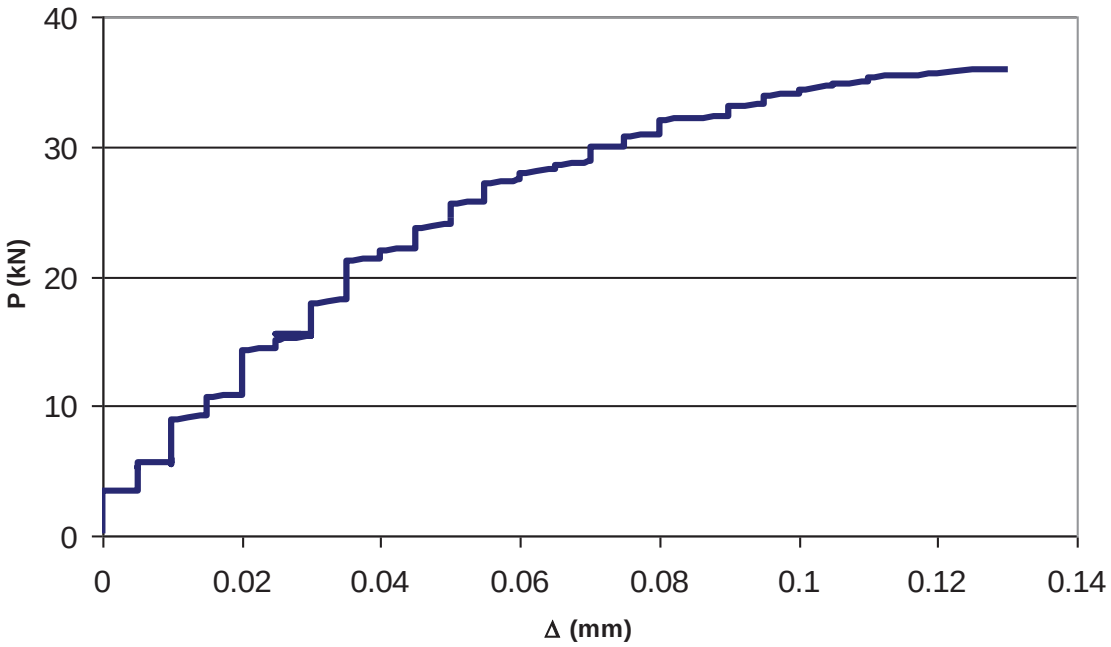

Figure 3.28 Global P-Δ for specimen CIBA 10

3.7.6 SUMMARY ON CIBA SERIES TESTS

The global *P-Δ* responses for CIBA adhesive are shown in Figure 3.29. CIBA 8 is not included in the graph due to its experimental error. The higher value of P_{IC} load for the fully anchored specimens CIBA 7 was due to the thicker FRP plate compared to CIBA 6. This observation was the same as in the comparison of SIKA 1 and SIKA 2 specimens. Similarly a shorter plateau was observed for a thicker FRP plate in CIBA 7 compared to CIBA 6.

The failure mode for the fully anchored specimens (CIBA 6, CIBA 7 and CIBA 8) shows that the debonding occurred firstly within the layer of the adhesive and then propagates within the FRP plate at the loaded end. This indicates that the bond between the adhesive-steel and adhesive-FRP can be stronger than the interfaces of the fibres and resin in the FRP plate.

For the not fully anchored specimens the value of average bond shear, τ_{ave} was 22.4 MPa and 18 MPa for CIBA 9 and CIBA 10 specimens

respectively. The failure mode for the two specimens was debonding between the adhesive-FRP layer. Since both were having the same parameter and the same failure mode, the difference of result was significant and may result in scatter in the analysis of τ_{max}. Taking this into consideration, further tests will be conducted for the not fully anchored specimens.

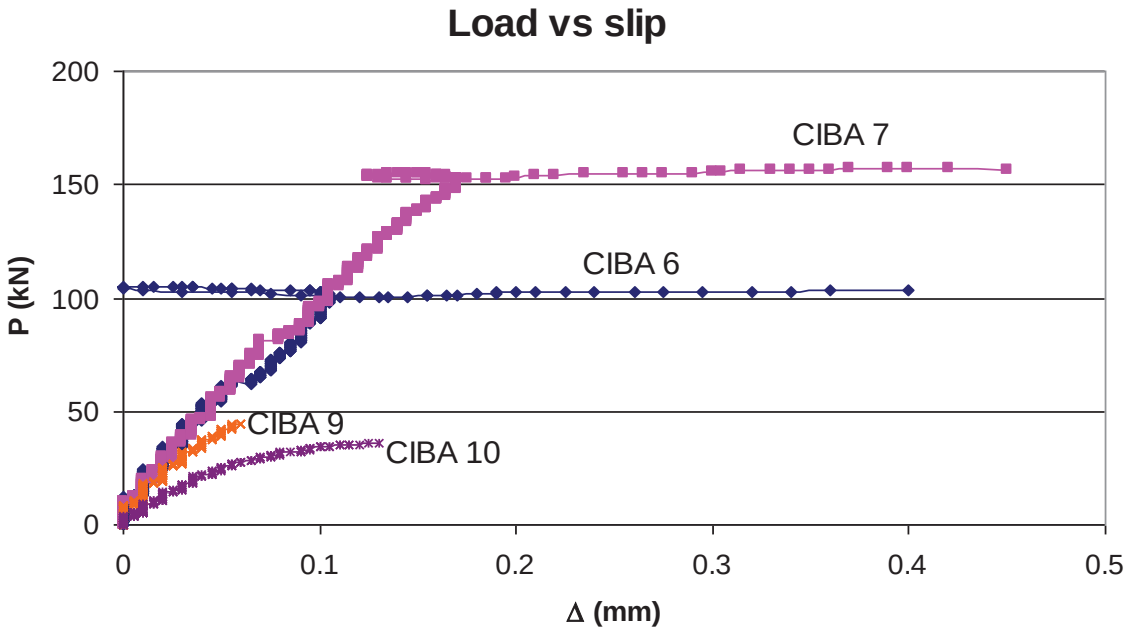

Figure 3.29 Global P-Δ for specimen CIBA series

3.8 ADDITIONAL TESTS WITH CIBA ADHESIVE

In this section, further tests using CIBA adhesive are described. The tests in this section will be presented in the sequence of not fully anchored specimens first, and then followed by the fully anchored specimens. The parameters and material properties of the FRP are tabulated in Table 3.3.

Table 3.3 Material properties of FRP for the additional CIBA tests

Test specimen	FRP thickness (mm), t_p	Bonded length (mm), L_p	Young's Modulus (MPa), E_p	Category
CIBA 11	1.2	20	153446	Not fully anchored
CIBA 12	1.2	250	159498	Fully anchored
CIBA 13	1.2	20	157264	Not fully anchored
CIBA 14	1.2	20	156926	Not fully anchored
CIBA 15	1.2	250	157132	Fully anchored
CIBA 16	1.2	250	170698	Fully anchored
CIBA 17	1.2	250	171983	Fully anchored

3.8.1 ADDITIONAL NOT FULLY ANCHORED SPECIMENS

3.8.1.1 SPECIMEN CIBA 11

Figure 3.30 shows the, *P-Δ* curve for specimen CIBA 11. The failure load was 33.5 kN and the corresponding τ_{ave} was calculated as 16.8 MPa.

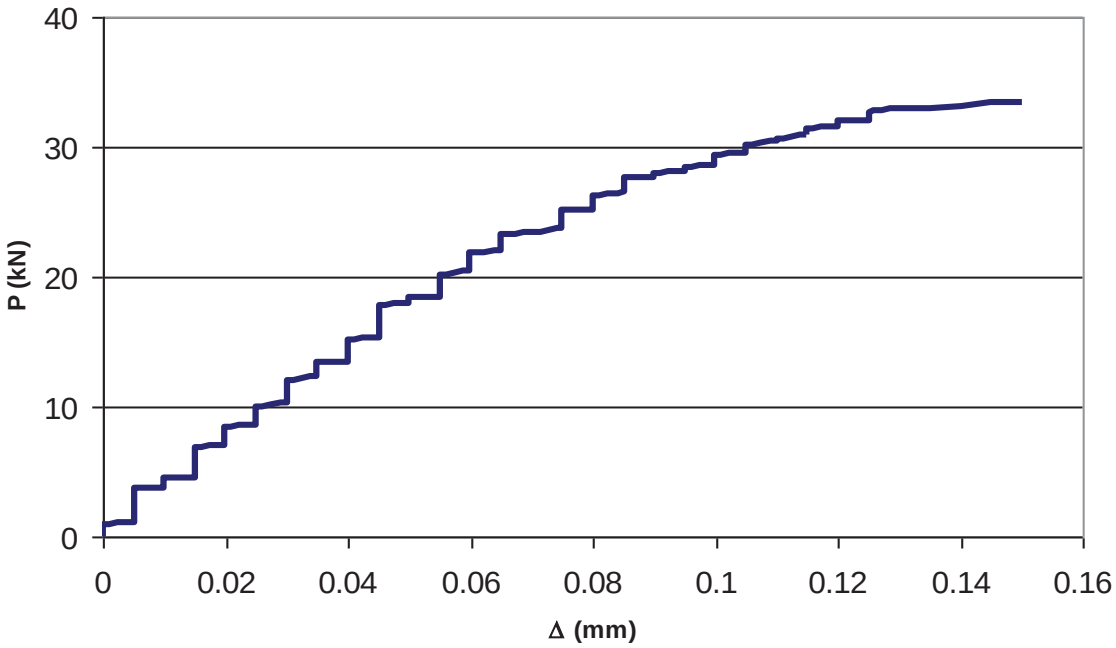

Figure 3.30 Global P-Δ for specimen CIBA 11

3.8.1.2 SPECIMEN CIBA 13

Figure 3.31 shows the, *P-Δ* curve for specimen CIBA 13. The failure load was 55.4 kN and the corresponding τ_{ave} was calculated as 27.7 MPa.

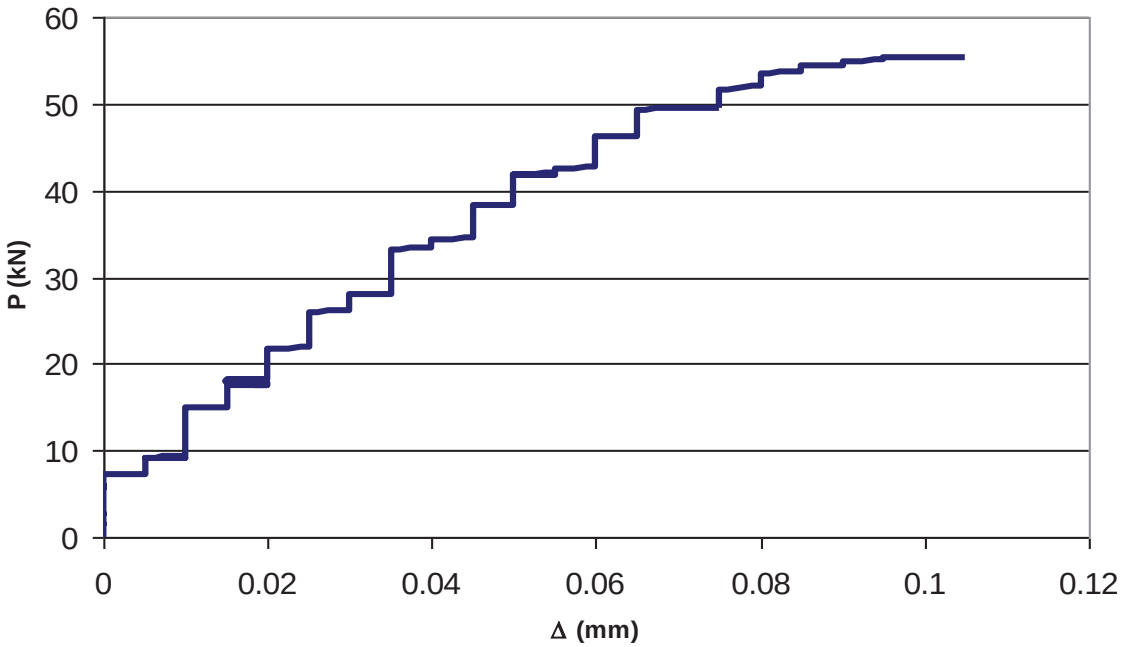

Figure 3.31 Global P-Δ for specimen CIBA 13

3.8.1.3 SPECIMEN CIBA 14

Figure 3.32 shows the, *P-Δ* curve for specimen CIBA 14. The failure load was 57.9 kN and the corresponding τ_{ave} was calculated as 28.95 MPa.

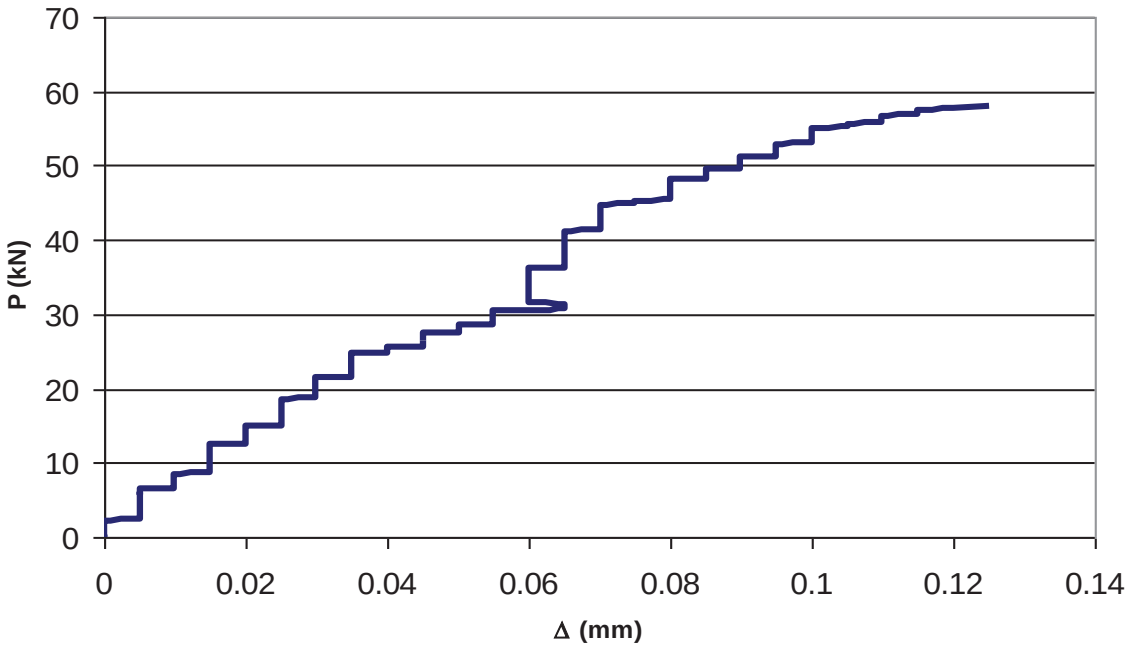

Figure 3.32 Global P-Δ for specimen CIBA 14

3.8.2 ADDITIONAL FULLY ANCHORED SPECIMEN TESTS

For the additional fully anchored specimen tests, strain gauges were glued along the FRP plate at 25 mm intervals. The instrumentation and location of the strain gauges is shown in Figure 3.33. Four specimens were tested: CIBA 12, CIBA 15, CIBA 16 and CIBA 17. A loading and unloading procedure was also implemented. The reason of this procedure was to investigate the permanent deformation that may or not may occur when the shear stress is moving on the descending branch of the bilinear τ-δ curve (Figure 2.1). All other instrumentation for the test was described in Section 0. Specimen CIBA 12 serves as the control

specimen where load was applied until failure without unloading. The loading increment, P_L for specimens CIBA 15 and 16 was at 20 kN interval and the unloading decrement, P_{UL} was conducted until reaching 0 kN. Finally for specimen CIBA 17, P_L was at 25 kN intervals and P_{UL} was at 0.5P_L. The loading and unloading procedure is summarised in Table 3.4.

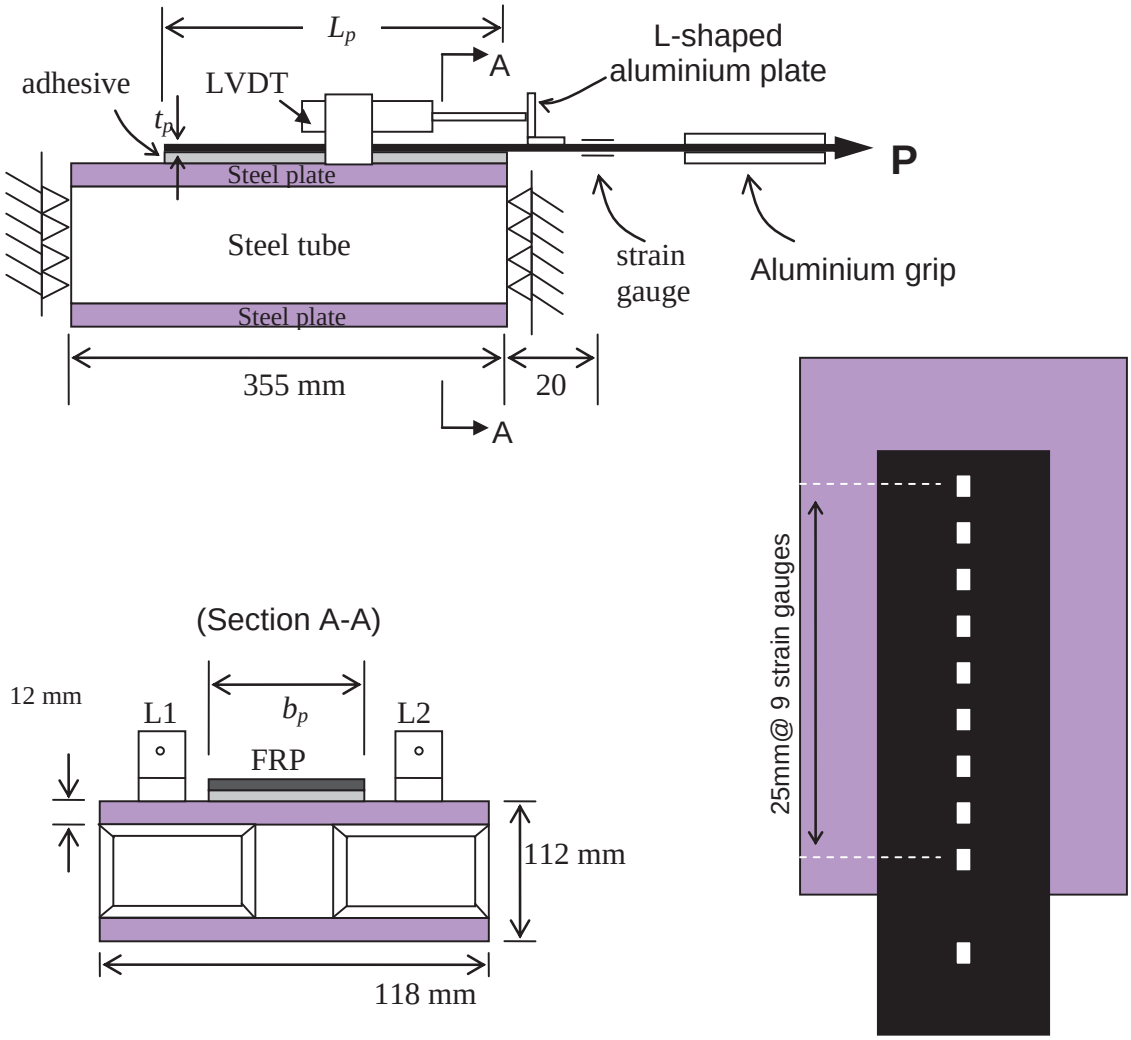

Figure 3.33 Detail instrumentations of the additional specimen

Table 3.4 Loading and unloading procedure for the additional CIBA tests

Test specimen	Loading increment, P_L (kN)	Unloading, P_{UL} (kN)
CIBA 12	-	-
CIBA 15	20	0
CIBA 16	20	0
CIBA 17	25	$0.5P_L$

3.8.2.1 SPECIMEN CIBA 12

The specimen failed prematurely by debonding at a load of 76.8 kN. Figure 3.34 shows the failure mode of the specimen. The FRP plate was split across the cross section along the bonded length as shown in Figure 3.34(a). The debonding surface of the adhesive was smooth with minimal attachment of the FRP fibre on the adhesive surface indicating a pure interfacial debonding.

Figure 3.35 shows the global *P-Δ* curve for specimen CIBA 12 where the failure load was at 76.9 kN, below the expected failure load at 100 kN from the previous result of CIBA 6. The maximum slip at debonding was 0.085 mm.

The average stress between the strain gauges were calculated as,

$$\tau_{ave} = E_p t_p \frac{\varepsilon_n - \varepsilon_{n-1}}{d_x} \qquad 3.2$$

where ε_n - ε_{n-1} is the strain difference between two locations and d_x is the distance between the two locations of the strain gauges. The slip between the strain gauges were calculated as,

$$\delta_n = \delta_{n-1} - \Delta slip \qquad 3.3$$

and the change in slip, *Δslip* is defined as,

$$\Delta slip = \frac{1}{2}\left(\varepsilon_n - \varepsilon_{n-1}\right)d_x \qquad 3.4$$

Figure 3.36 shows the local bond-slip curve for the specimen CIBA 12. Strain gauge at 25 mm was faulty and did not give a correct readings hence it was not included in the graph. The pure interfacial debonding which is observed in Figure 3.34 was reflected in the low shear stress recorded in Figure 3.36 indicates that the failure is due to insufficient bonding of the FRP plate to the adhesive.

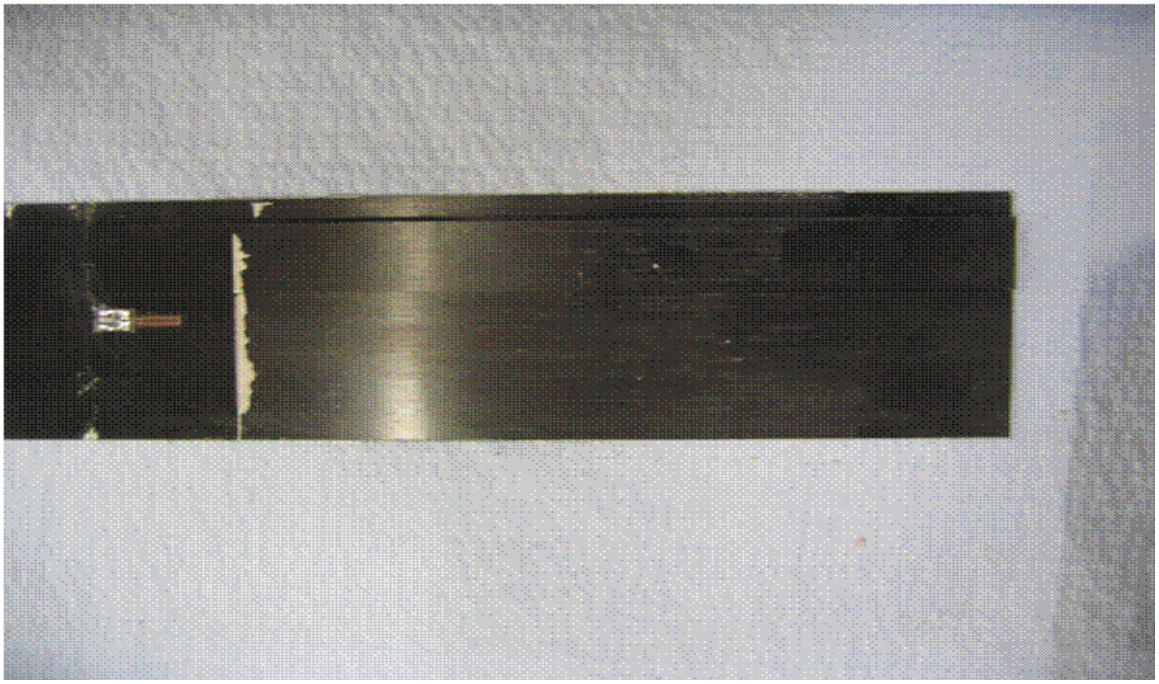

(a) FRP plate at failure

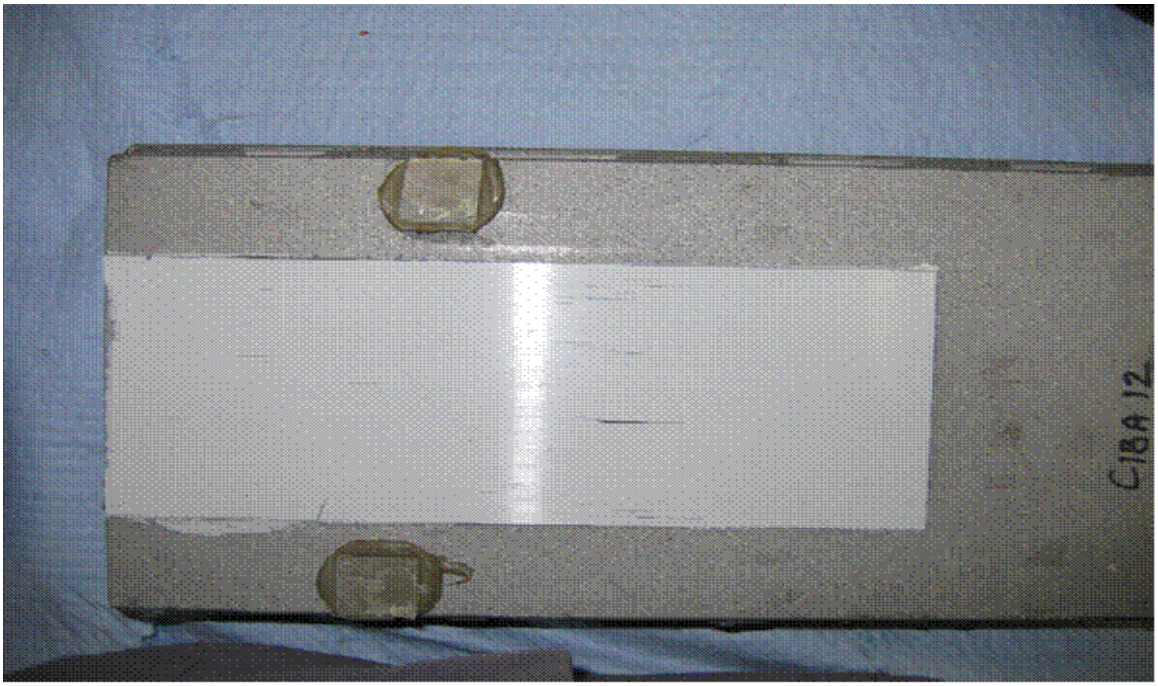

(b) Adhesive layer at failure

Figure 3.34 Failure mode of specimen CIBA 12

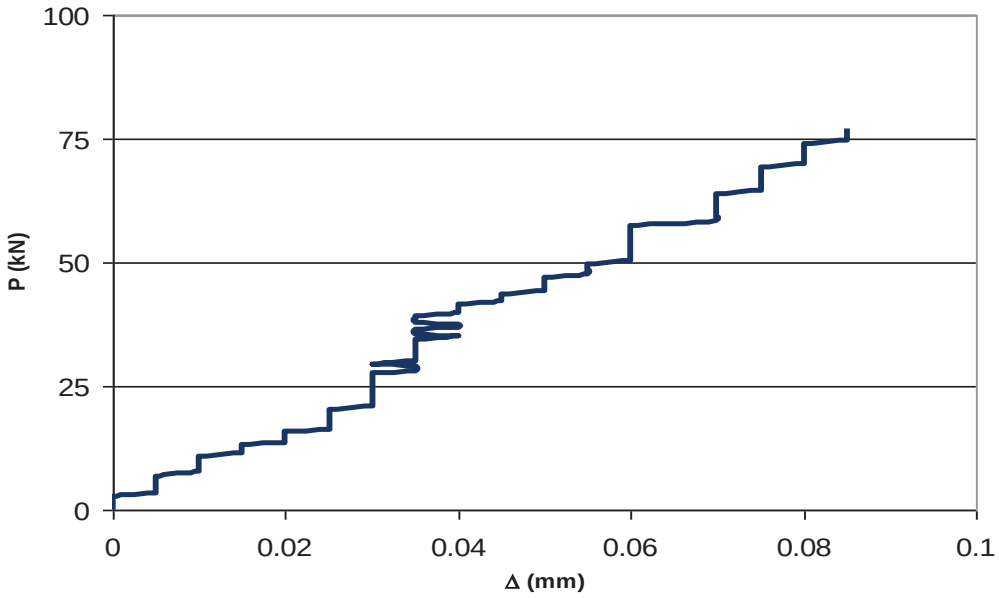

Figure 3.35 Global P-Δ for specimen CIBA 12

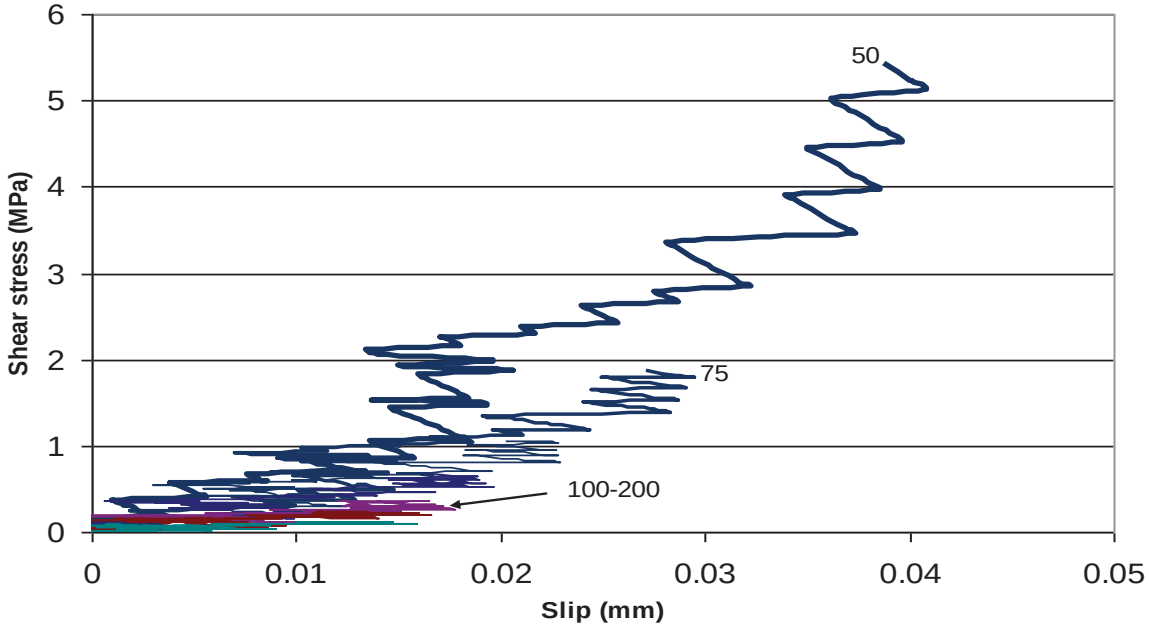

Figure 3.36 Local τ-δ for specimen CIBA 12

3.8.2.2 SPECIMEN CIBA 15

Figure 3.37 shows the failure mode of sample CIBA 15. Pure interfacial debonding was again observed in this specimen. The FRP fibres were split and there was a clean debonding between the interfaces of the FRP-adhesive. Loading and unloading were carried out at 20 kN increment. During the third increment, 59.5 kN of applied load, a loud bang was heard from the UTM machine indicating that debonding has occurred. The debonding load obtained from this test was also lower than the expected P_{IC} at 100kN. Referring to the smooth surface of adhesive attached on the steel plate, it is suggested that bond was not properly developed between the adhesive and FRP plate resulting on the premature failure.

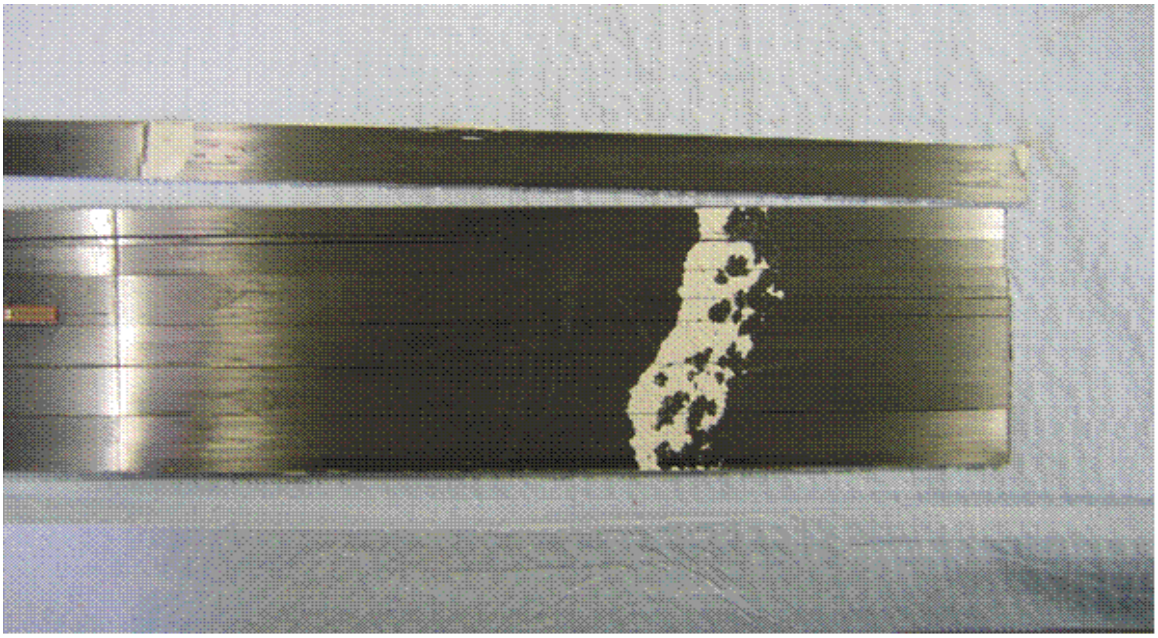

(a) FRP plate at failure

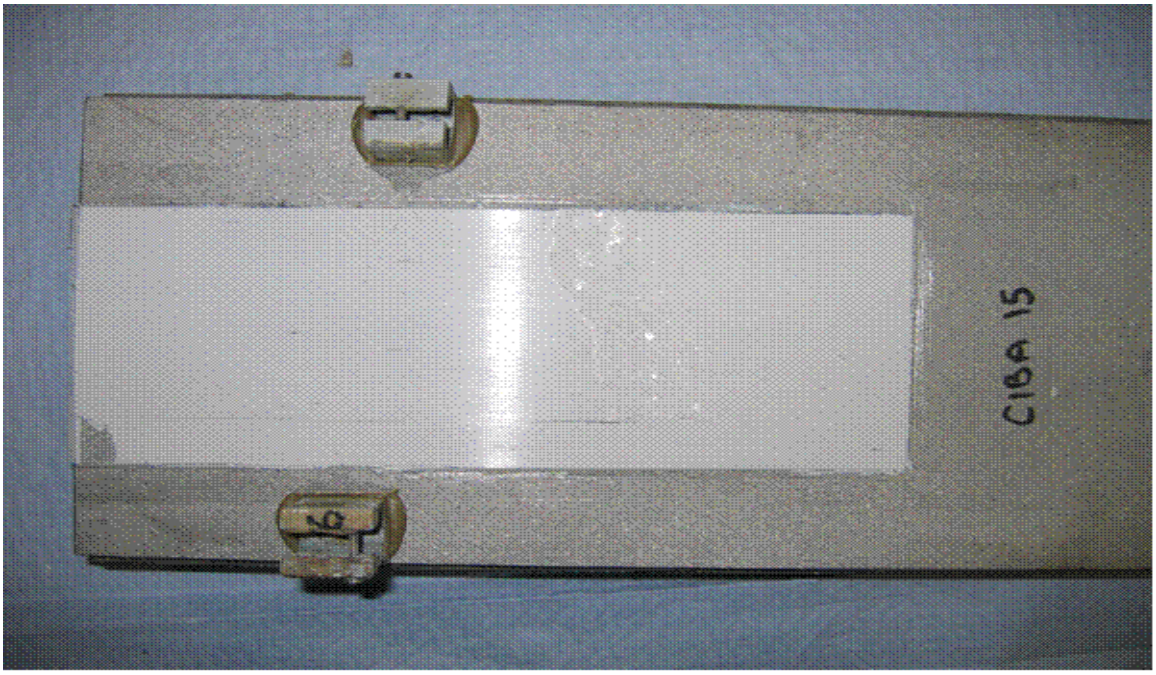

(b) Adhesive layer at failure

Figure 3.37 Failure mode of specimen CIBA 15

Figure 3.38 shows the global *P-Δ* curve for specimen CIBA 15. Loading and unloading procedure was conducted at 20 kN and unloading was down to 0 kN. As shown in Figure 3.39, the shear stresses at the strain gauges were small which is also indicated in specimen CIBA 12 in Section 3.8.2.1, due to the pure interfacial debonding that occurred in this specimen. The maximum shear stress calculated from the strain data in Figure 3.39,shows that it is still in the ascending branch when the premature debonding occurs.

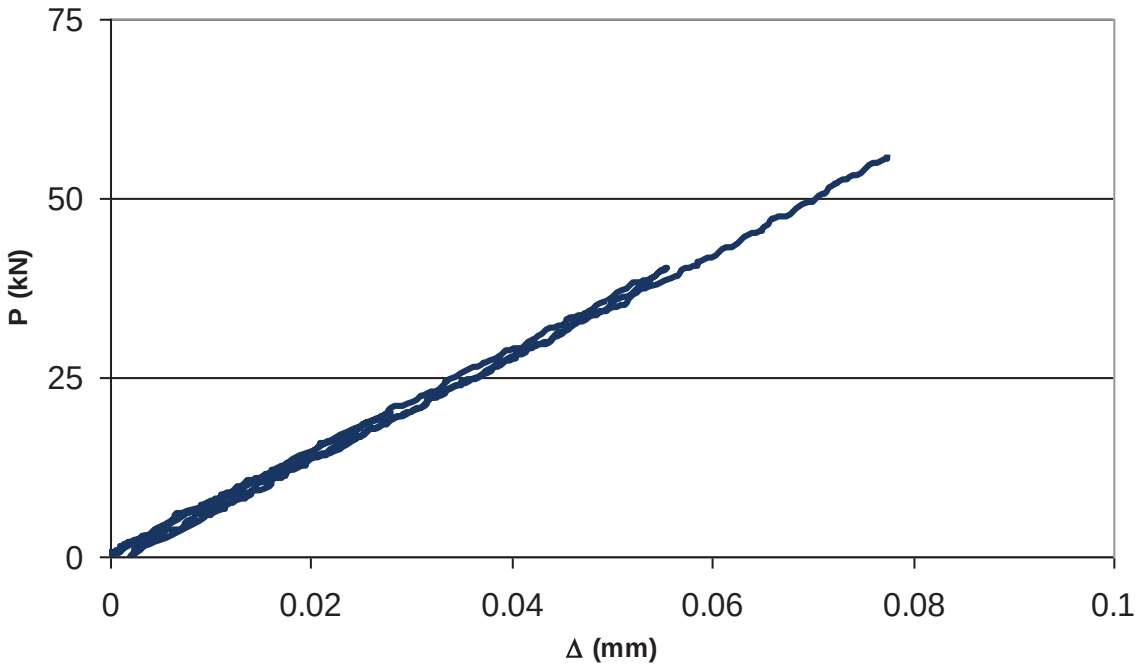

Figure 3.38 Global P-Δ for specimen CIBA 15

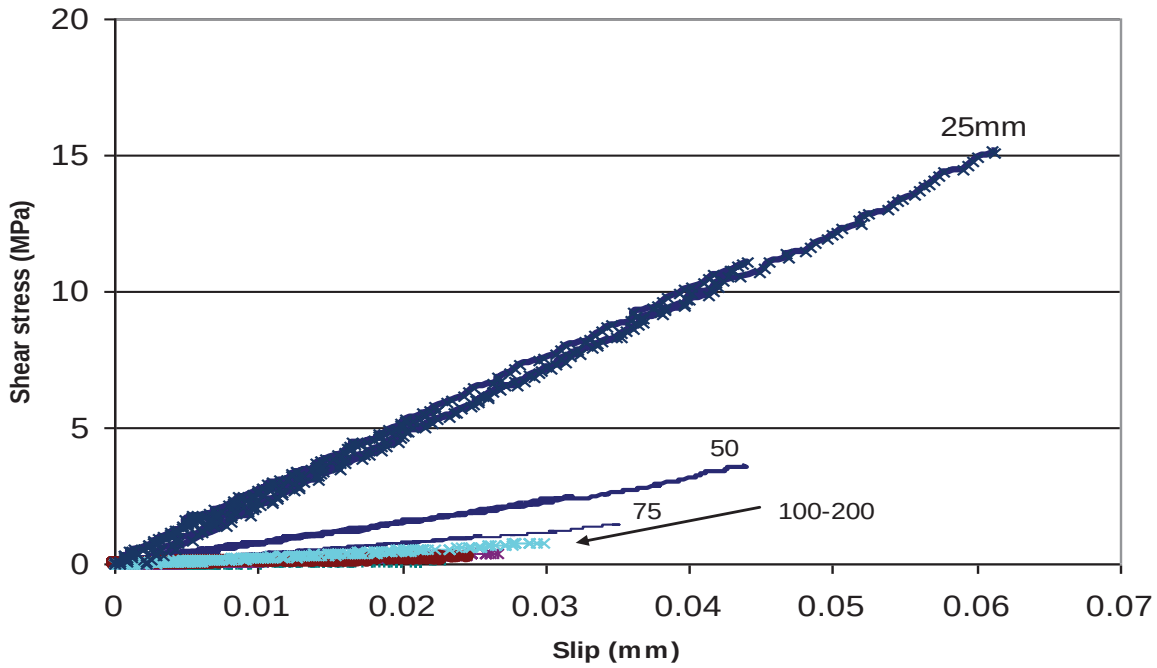

Figure 3.39 Local τ-δ for specimen CIBA 15

3.8.2.3 SPECIMEN CIBA 16

Figure 3.40 shows the failure of specimen CIBA 16. Splitting of the FRP plate was observed. Debonding firstly occurred within the adhesive layers (between 0 to 30mm from the loaded end) then moved towards the FRP plate.

The global *P*-Δ curve for specimen CIBA 16 is shown in Figure 3.41. The loading increment was conducted at 20 kN interval before unloading down to 0 kN for each iteration. Prior to 100 kN loading, the loading-unloading path remains the same which means that no permanent deformation has occurred. Initially a load control was conducted but beyond the 100 kN load, displacement control was used for loading-unloading. Since the UTM machine used in the testing did not have the mechanism for the displacement control to be applied automatically, the displacement was observed visually. Unloading was conducted at displacement increment of 0.03-0.04 mm. The P_{IC} load was 99.8 kN with a slip of 0.15 mm. The specimen failed 106.4 kN with a slip of 0.26 mm.

Figure 3.42 shows the local τ-δ curve for the specimen CIBA 16. It can be observed that the local τ-δ curve was bilinear as recorded by strain gauge 25 mm. Strain gauge 50 mm was faulty and did not give a correct reading. Strain gauges 75-200mm give a low shear stress at debonding. This indicates that while the bond between the adhesive and FRP was strong, the bond between the FRP fibres was weak. The peak shear stress τ_{max} was 23.3 MPa and the corresponding slip, δ_1 was 0.11 mm. An interpolation of the descending branch (shown by the dashed line in Figure 3.42) predicted that δ_{max} to be 0.25 mm.

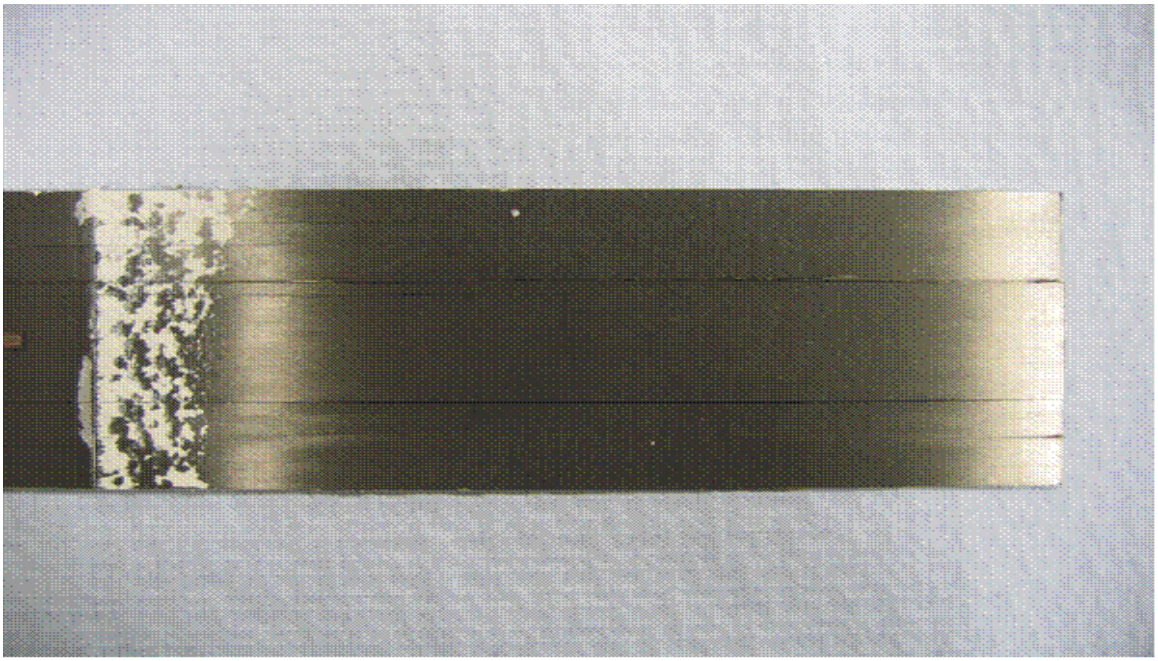

(a) FRP plate at failure

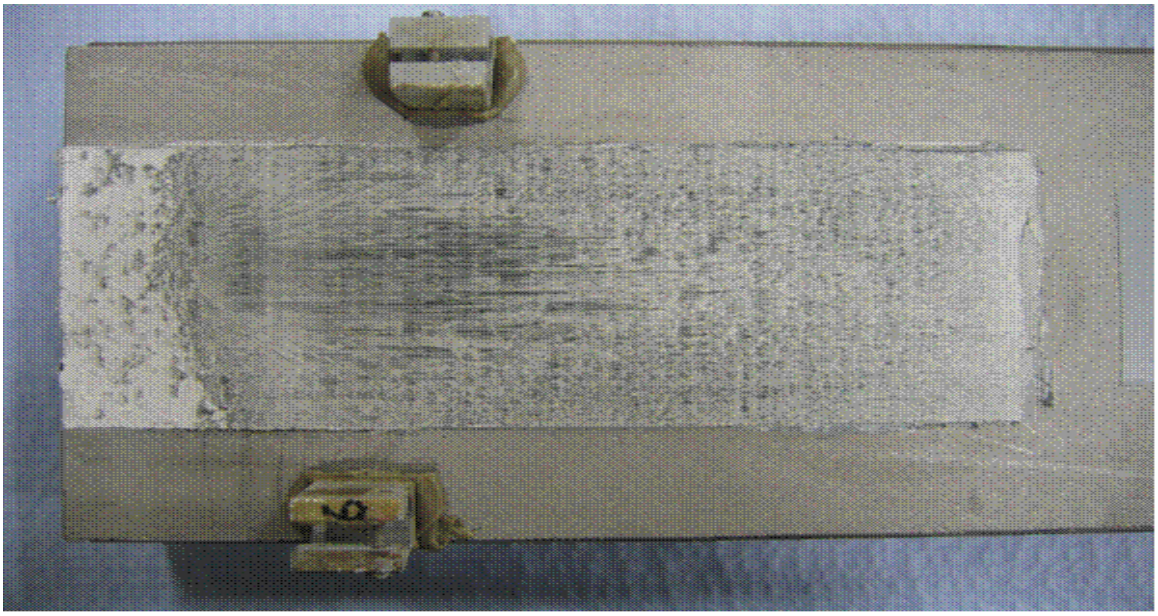

(b) Adhesive layer at failure

Figure 3.40 Failure mode of specimen CIBA 16

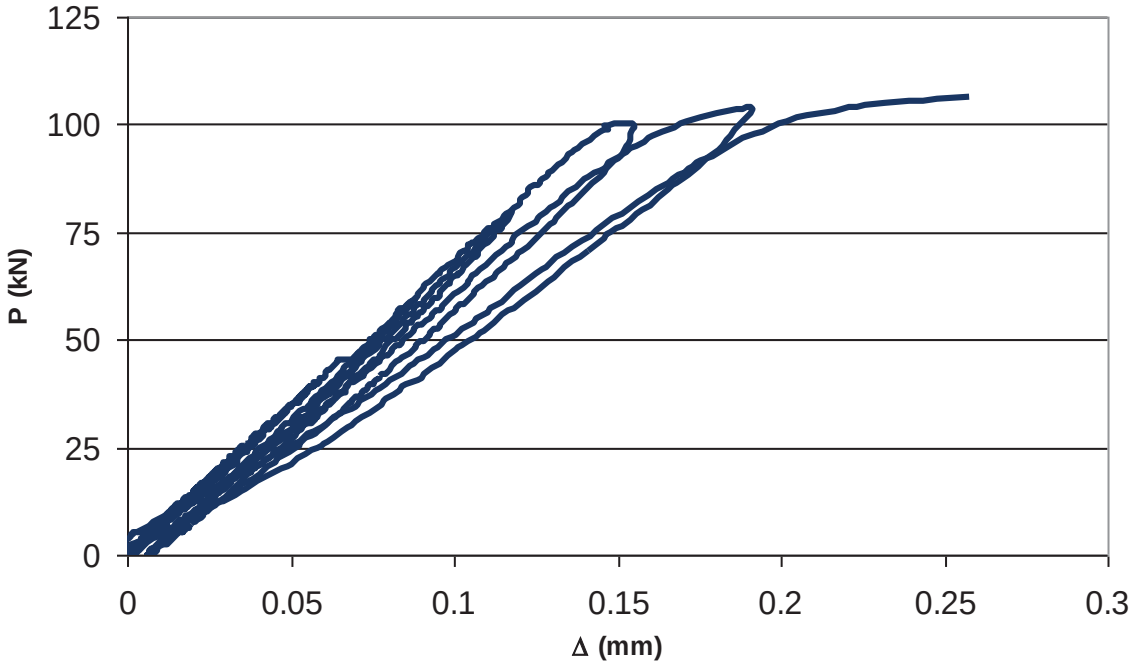

Figure 3.41 Global P-Δ for specimen CIBA 16

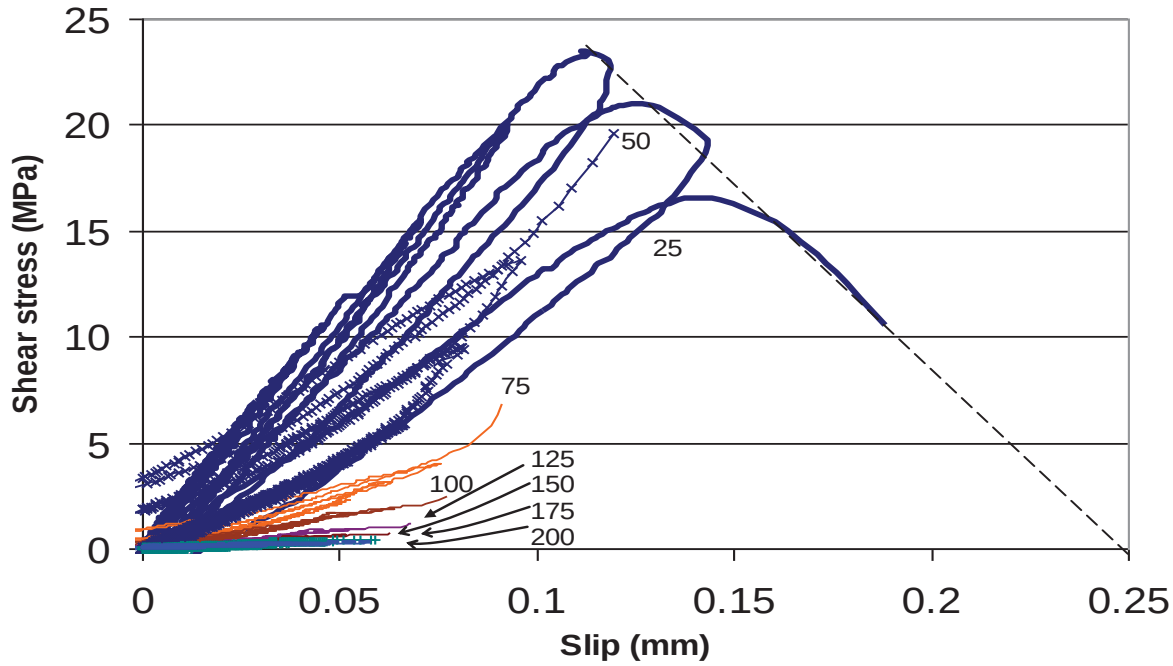

Figure 3.42 Local τ-δ for specimen CIBA 16

Permanent deformation occurred at the descending branch of the $\tau\delta$ curve for this specimen as shown by strain gauge 25 mm in Figure 3.43. On the ascending branch, unloading returns to the origin 0. After reaching the maximum shear stress, unloading to 0 MPa shear stress resulted in 0.009 mm of slip (corresponding load of 99.8 kN) which was an indication of permanent deformation. The next iteration of loading-unloading when the shear stress reached 20.9 MPa (corresponding load of 103.4 kN) shows that the slip at 0 MPa shear stress was 0.016 mm. This clearly shows that permanent deformation occurs at the descending branch of the bilinear τ-δ curve.

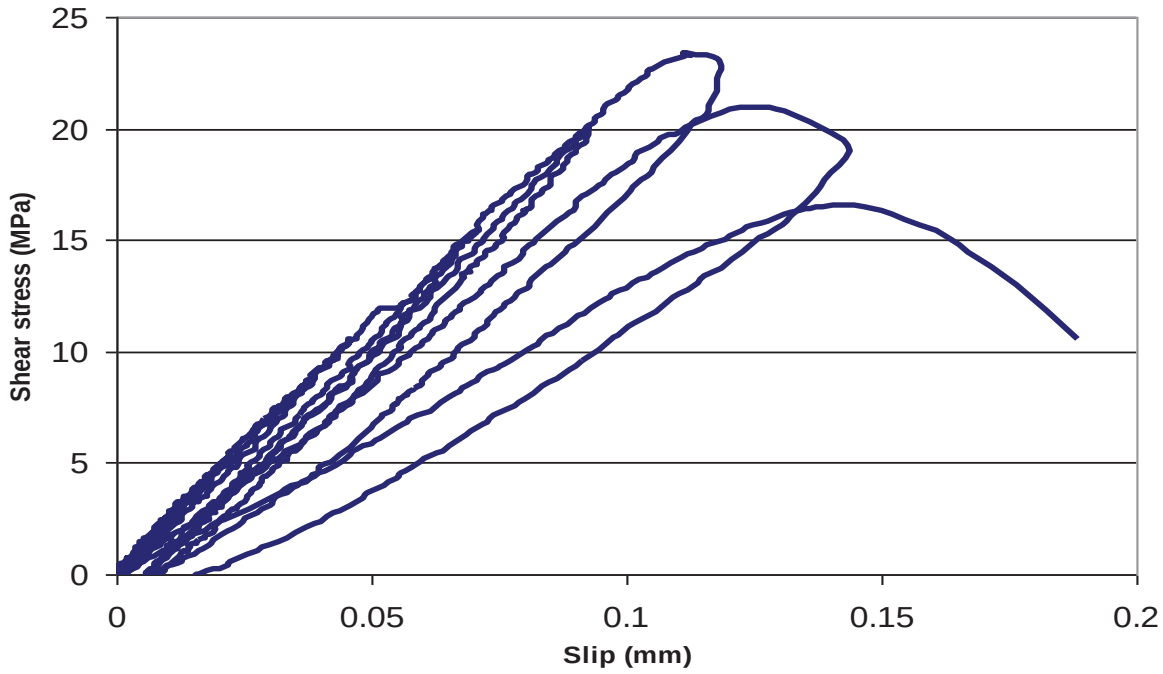

Figure 3.43 Local τ-δ for specimen CIBA 16 (strain gauge 25 mm)

3.8.2.4 SPECIMEN CIBA 17

It was shown in the test of specimen CIBA 16 that permanent deformation occurred at the descending branch of the bilinear τ-δ curve. However in that test the maximum slip, δ_{max} has not been achieved experimentally (Figure 3.43). Hence, the objective of this test was to reach the point of δ_{max} experimentally. The loading-unloading procedure for this test was by increasing the load at P_L = 25 kN increment and unloading by decreasing the load to 0.5P_L for each iteration so that the time consumed by the test can be reduced. After reaching the 100 kN load, unloading was conducted at every 0.03-0.04 mm increment of slip.

Figure 3.44 shows the failure of specimen CIBA 17. Splitting of the FRP plate occurred at failure. The debonding failure firstly occurred within the adhesive layer and then moved towards the fibres of the FRP plate. This type of failure is similar to specimen CIBA 16.

The global P-Δ curve for specimen CIBA 16 is shown in Figure 3.45. According to the P-Δ curve, P_{IC} was 100 kN with the corresponding slip of 0.25 mm. Total debonding occurred at a load of 107.3 kN with the corresponding slip of 0.34 mm.

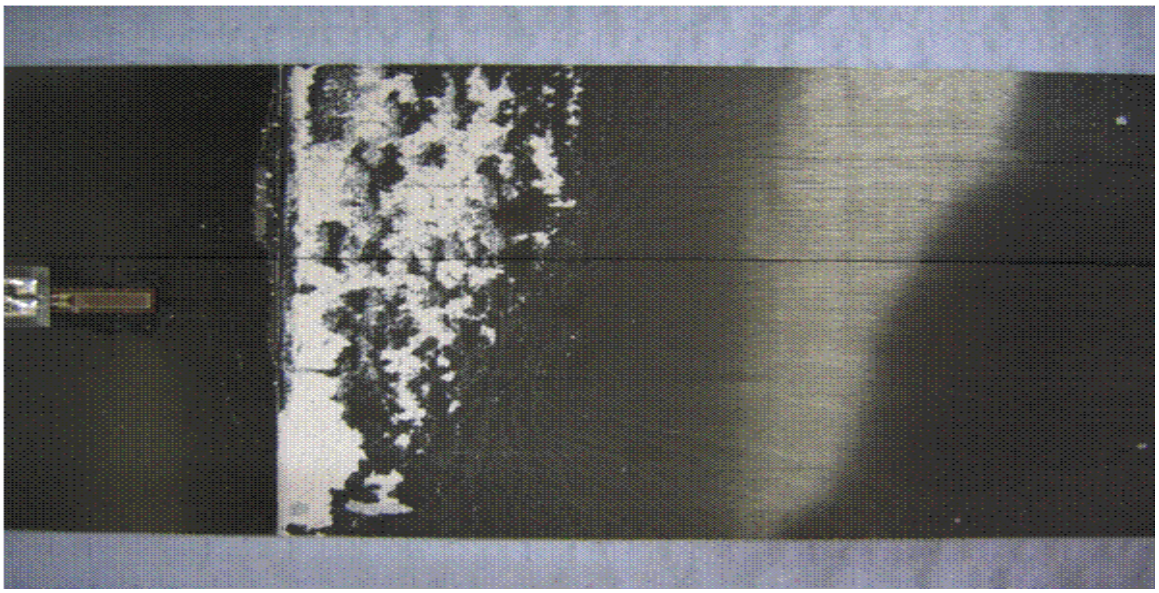

(a) FRP plate at failure

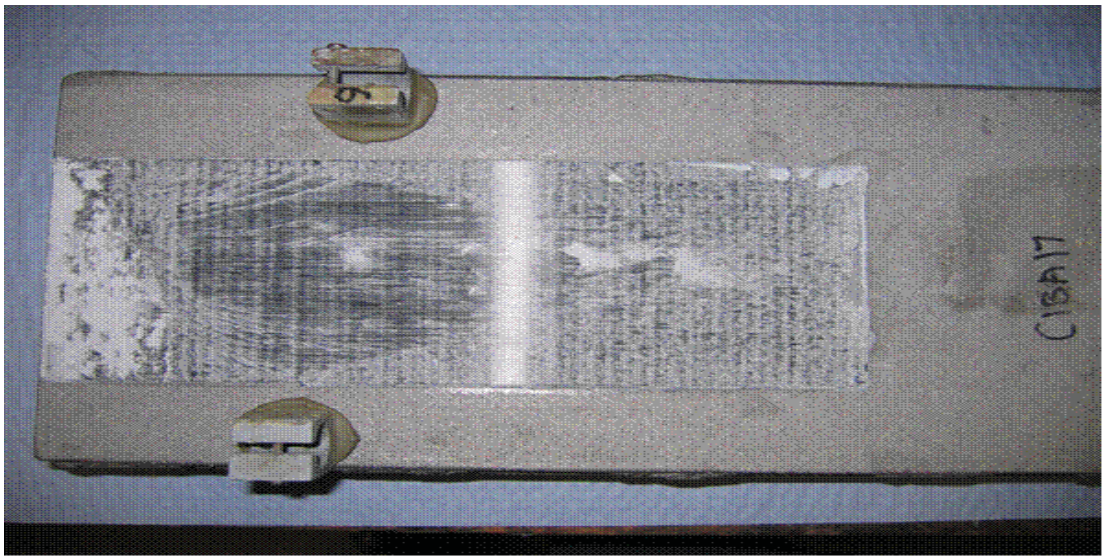

(b) Adhesive layer at failure

Figure 3.44 Failure mode of specimen CIBA 17

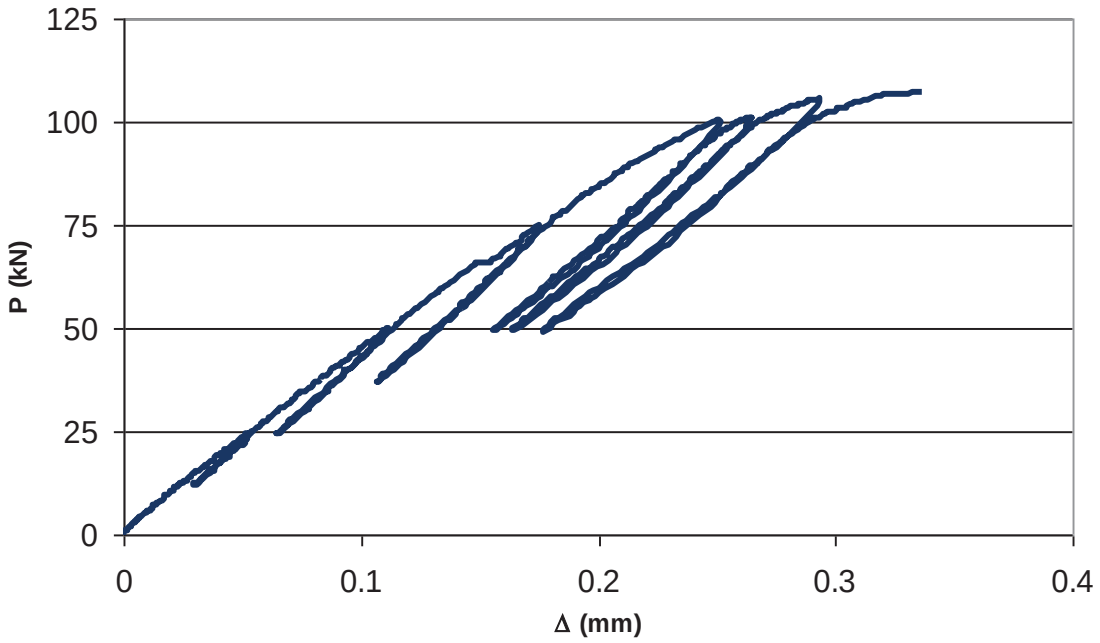

Figure 3.45 Global *P-Δ* for specimen CIBA 17

Figure 3.46 shows the local τ-δ curve for the specimen CIBA 17. From strain gauge 25 mm, τ_{max} was calculated as 22.1 MPa with the corresponding δ_1 as 0.2 mm. The τ-δ curve was in bilinear shape. However, total debonding occurred while not reaching the δ_{max}. This can be explained by the adhesive-FRP debonding which occurred at 25 mm from the loaded end (Figure 3.44) at which strain gauge 25 mm was located. An interpolation of the descending branch of the τ-δ curve in Figure 3.46 (shown by the dashed line) predicted that the value of δ_{max} is about 0.29 mm.

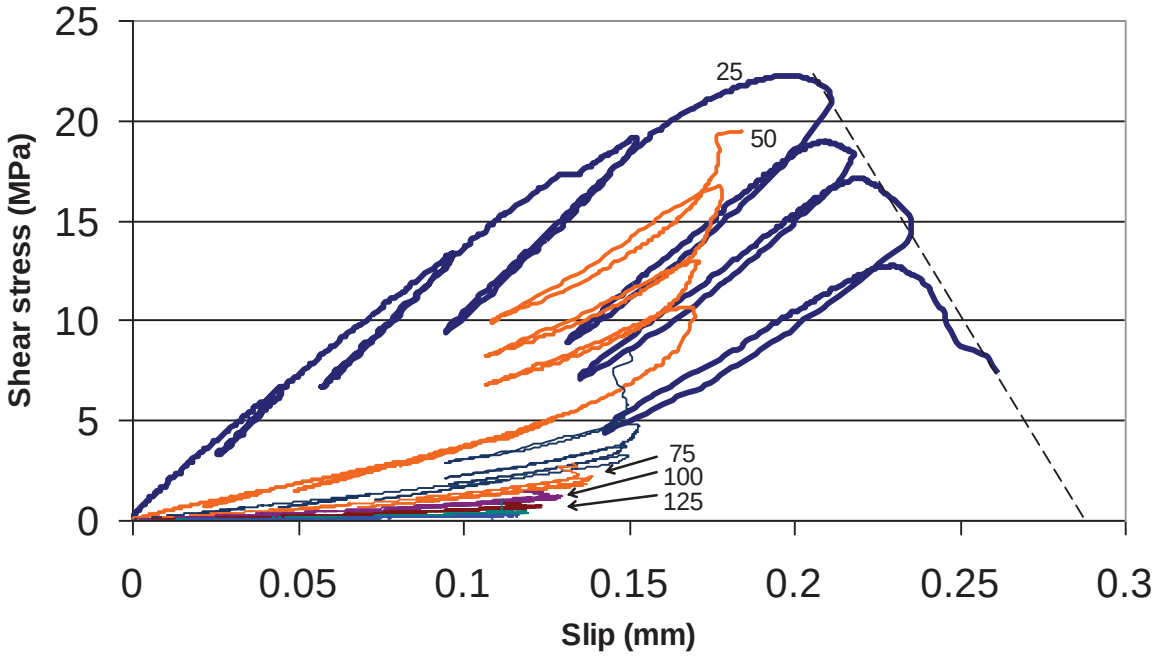

Figure 3.46 Local τ-δ for specimen CIBA 17

3.8.3 SUMMARY ON ADDITIONAL TESTS WITH CIBA SPECIMENS

An additional three specimens were developed and tested for the not fully anchored specimens. Figure 3.1 shows the *P*-Δ curve for the not fully bonded specimens tested in this chapter. It can be observed that a large scatter between the highest failure load compare to the lowest failure load. Figure 3.47 summarised the failure loads and the corresponding shear stresses. The lowest failure load was 33.5 kN with the corresponding shear stress of 16.8 MPa whereas the highest failure load was 57.9 kN with the corresponding shear stress of 28.9 MPa. The differences of 42% between the lowest and highest values were significant. The results for the not fully anchored specimens are tabulated in Table 3.5.

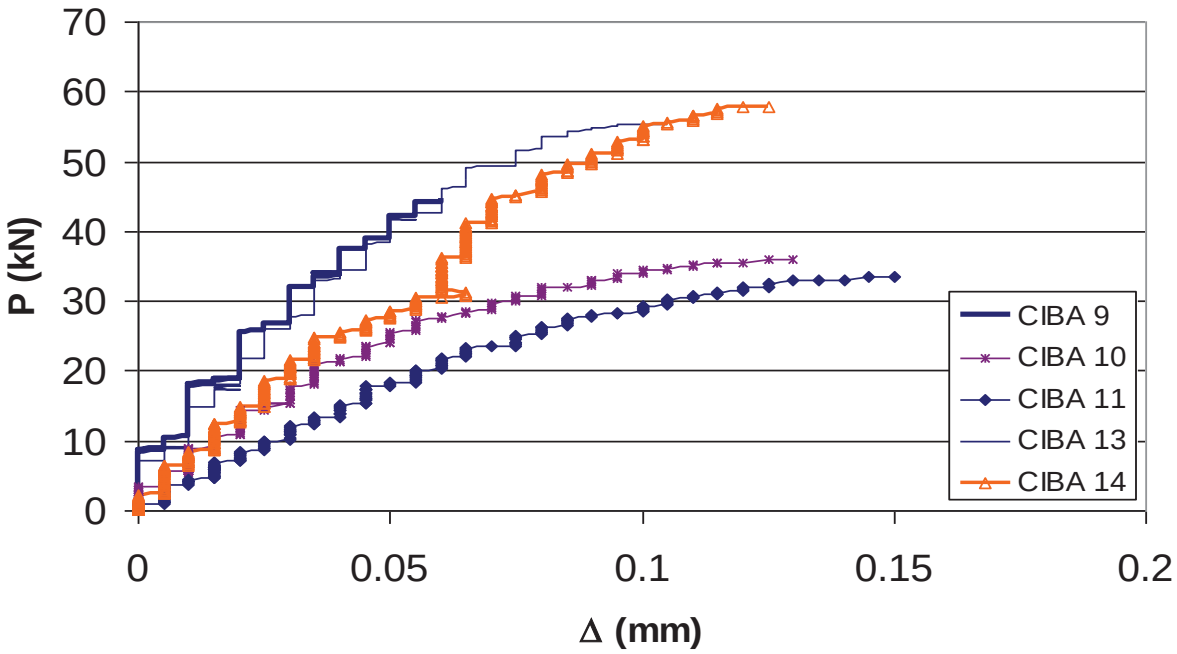

Figure 3.47 Global *P-Δ* curve for the not fully bonded specimens

Table 3.5 Failure load and shear stress for not fully bonded specimens

Test specimen	Test Failure Load (kN)	Shear stress at failure (MPa)
CIBA 9	44.7	22.4
CIBA 10	36.0	18.0
CIBA 11	33.5	16.8
CIBA 13	55.4	27.7
CIBA 14	57.9	28.9
	Average	22.9

An additional four specimens were developed and tested for the fully anchored specimens. Nine strain gauges were glued on the FRP plate on each specimen at 25 mm intervals. Loading and unloading procedure was implemented on all the specimens. Of the four specimens, only specimen CIBA

16 and CIBA 17 were tested up to the descending branch of the bilinear τ-δ curve while the other two failed without capturing the descending branch due to the abrupt debonding. Figure 3.48 shows the τ-δ curve obtained from the experiment. The difference of δ_1 was due to the different types of failure modes that the specimens experienced. For specimen CIBA 16, the failure mode was within the adhesive layer whereas for specimen CIBA 17, the failure mode was within the FRP plate at the strain gauge 25 mm. The value of the peak shear stresses of 23.3 MPa and 22.1 MPa for specimen CIBA 16 and CIBA 17 was close to the shear stresses obtained from the not fully bonded specimens, averaging at 22.9 MPa.

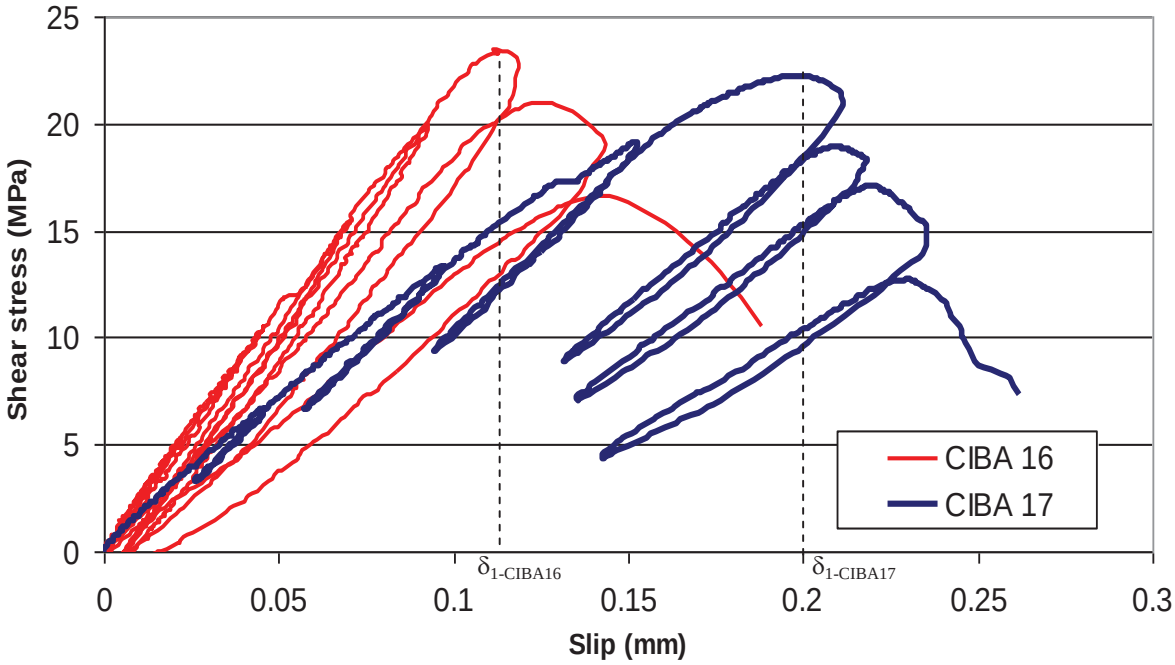

Figure 3.48 Local τ-δ for specimen CIBA 16 and CIBA 17 calculated from strain gauge 25 mm.

3.9 CONCLUSIONS

A total of 17 pull tests were conducted for the derivation of the τ-δ curve in the next chapter. The test consists of FRP plates of different length glued on two types of adhesive. Loading and unloading procedure was also conducted on some of the specimens. Data collected was the debonding load, failure load, shear stress, slip, strain and material stiffness.

The two adhesives used were to know the adhesive that is more susceptible to fail within the adhesive layer and for this CIBA adhesive was chosen. The not fully anchored specimens were tested to obtain the average shear stress that will be used in the derivation of τ-δ curve in the next chapter.

The conclusion from these test are:

- The maximum slip that occurred is small in the range of 0.25 mm. Any small movement of the specimen or machine will result in significant experimental error.
- A longer bond length on a fully anchored specimen will lead to a longer plateau on the global P-Δ curve i.e. more ductile.
- A thicker FRP plate will increase the P_{IC} value while reducing the ductility.
- Different types of failure modes may result in different values of δ_{max} as indicated by specimen CIBA 16 and CIBA 17.
- The value of shear stress obtained from the not fully anchored test which is close to the value obtained from the fully anchored test may indicate that the peak shear stress, τ_{max} can be obtained directly from the not fully anchored specimen test.

CHAPTER 4: ANALYSIS ON THE DERIVATION OF τ-δ RELATIONSHIP

4.1 INTRODUCTION

This chapter explains the derivation of the τ-δ relationship based on a structural mechanics approach. To illustrate the derivation, a numerical method is developed using FORTRAN computer language. This numerical method is based on the partial interaction theory. Test results from the experiments conducted in the previous chapter were analysed.

The structure of this chapter will be the description of the numerical modelling based on the partial interaction theory and the steps taken in deriving the τ-δ relationship based on structural mechanics approach. In this section, the values of τ_{max} and δ_{max} were established. Next, the numerical modelling was used to get the best fit curve by determining the value of δ_1. The method of derivation will also be compared with the published results by (Xia and Teng 2005). Finally, conclusions are made at the end of this chapter.

4.2 PARTIAL-INTERACTION NUMERICAL MODELLING OF LOCAL AND GLOBAL BOND CHARACTERISTICS OF FRP PLATED STEEL JOINTS

The partial-interaction numerical method developed by (Haskett, Oehlers et al. 2007) which was explained in Section 2.8 for FRP-concrete pull tests in which the cross-section of the concrete element is much greater than that of the FRP section was modified to fit the purpose of this research. The modified numerical method illustrated in Figure 4.1 is described as follows:

- At Position 0, an initial strain at the loaded end is fixed, $\varepsilon_p(0)$, and with this the force $P(0)$ is known. Hence the corresponding strain in the steel, $\varepsilon_s(0) = -P(0)/(AE)_s$
- With the corresponding initial strain and force, the slip at the loaded end $\delta(0)$ is guessed.
- The slip strain at Position 0 is calculated: $\frac{ds(0)}{dx} = \varepsilon_p(0) - \varepsilon_s(0)$
- Assuming that the segmental length d_x is very small, the slip δ is considered to be constant over the segment. Due to this, the bond stress τ which was derived from the bond-slip characteristic as in Fig. 3 is also constant.
- The bond force acting over the first segment length is calculated: $B(0) = \tau(0) dx L_{per}$.
- The load in the FRP at Position 1 can now be calculated as: $P(1) = P(0) - B(0)$,
- The corresponding strain at Position 1 in the FRP and steel are $\varepsilon_p(1) = P(1)/(EA)_p$ and $\varepsilon_s(1) = -P(1)/(EA)_s$ respectively.
- The change in slip over the first segment length is calculated by integrating the slip strain over the segment length (slip strain at Position 0 and 1), $\Delta s(0) = \int_{x=0}^{x} \frac{ds(0)}{dx} dx$
- The slip for the next segment is $\delta(1) = \delta(0) - \Delta s(0)$.
- The process is carried out throughout the bonded length until the boundary condition is achieved. There are two boundary conditions. For fully anchored plates, the boundary condition is $\delta = ds/dx = 0$ and for the not fully anchored plates, that is plates with bond lengths less than L_{crit}, the boundary condition is $\varepsilon_p = 0$ at the free end.

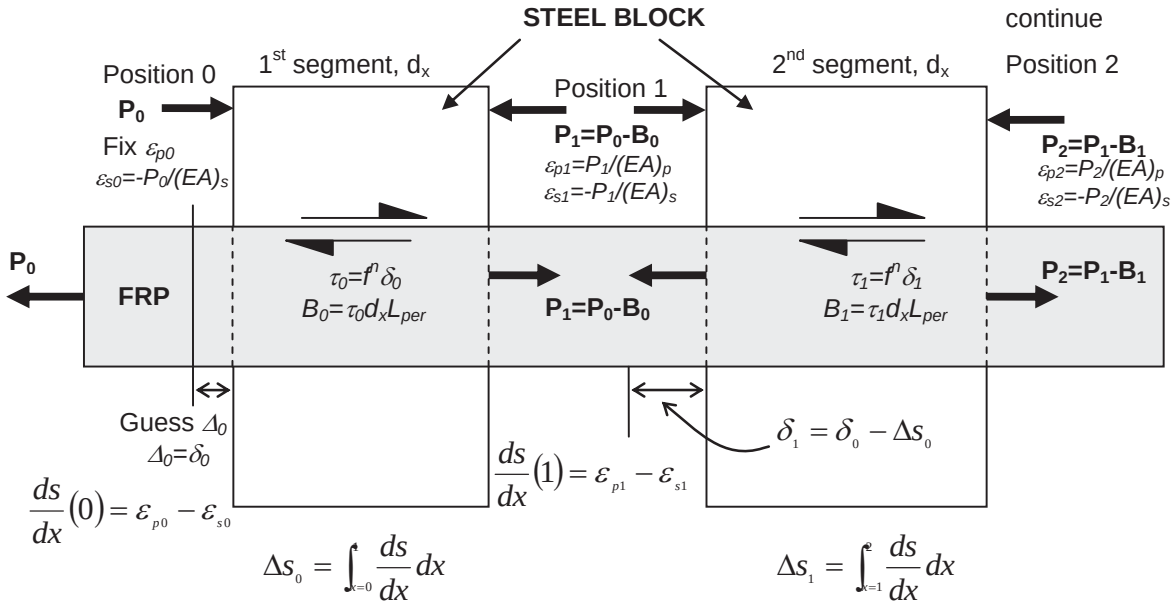

Figure 4.1 Graphical representation of the numerical analysis for FRP plated steel joints

As an example of the application of the numerical model, Figure 4.2 shows a global P-Δ curve and a numerical analysis for a fully anchored FRP-steel specimen. The values of τ_{max}-δ_{max} which can be obtained directly from the experiment were used in the numerical method. In this example, the value of δ_1 = 0.1mm, is shown to be the value that best fits the experimental *P*-Δ graph in Figure 4.2. Varying the value of δ_1 also illustrates the effect of δ_1 on the elastic part of the *P*-Δ graph without affecting the value of P_{IC}. The value of P_{IC} was not affected simply because the fracture energy G_f, which is the area below the τ-δ graph in Figure 1.1, did not change.

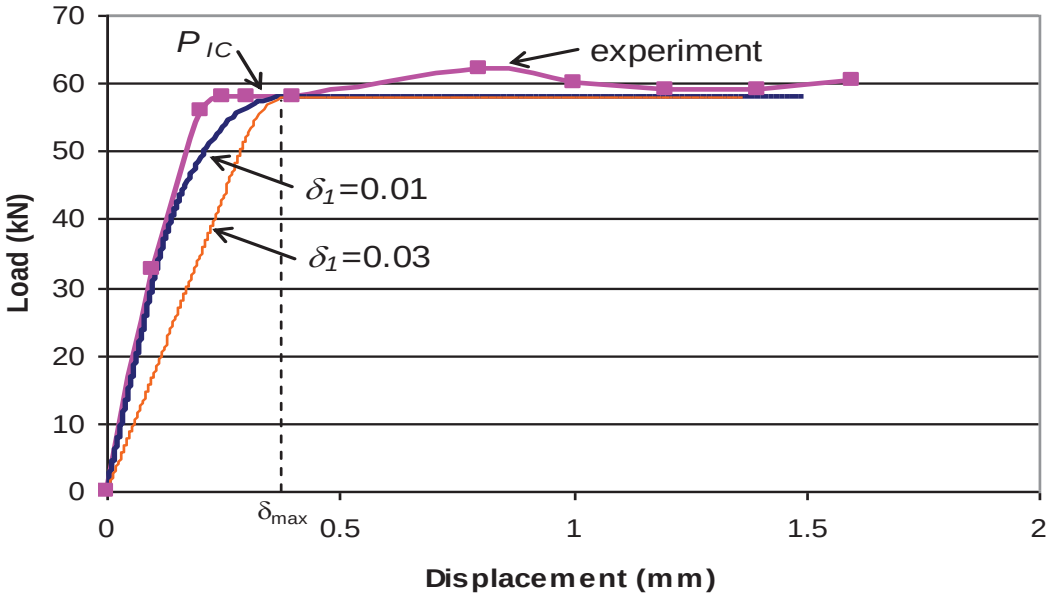

Figure 4.2 Influence of δ_1 to the global load–slip (τ-Δ) response.

4.2.1 DISCUSSION ON THE CRITICAL BOND LENGTH

The derivation of the critical bond length in Eqs. 2.9 and 2.10 were based on the bond length over which the shear stresses offer a total resistance which is at least 97% of the applied load for a joint with an infinite bond length (Yuan, Teng et al. 2004). Experimentally, the critical bond length can be obtained from the shear stress graph of the pull test as the shear stress distribution from the τ_{max} to zero over the bonded length. Using the definitions of critical bond length defined by (Yuan, Teng et al. 2004) and recorded experimentally, the critical bond for specimens CIBA 16 and CIBA 17 are shown in Table 4.1 and Figure 4.3 respectively. The values of τ_{max} and δ_{max} were obtained from the experimental τ-δ graphs in Figure 3.42 and Figure 3.46.

Table 4.1 shows the comparison of the critical bond length values obtained using Eqs. 2.9 and 2.10, experiments and numerical method from Section 4.2. It shows that the values obtained from the numerical analysis are

closer to the values obtained experimentally with difference of 3.8% and 14.5% for specimens CIBA 16 and CIBA 17 respectively compare to the values obtained using Eqs. 2.9 and 2.10.

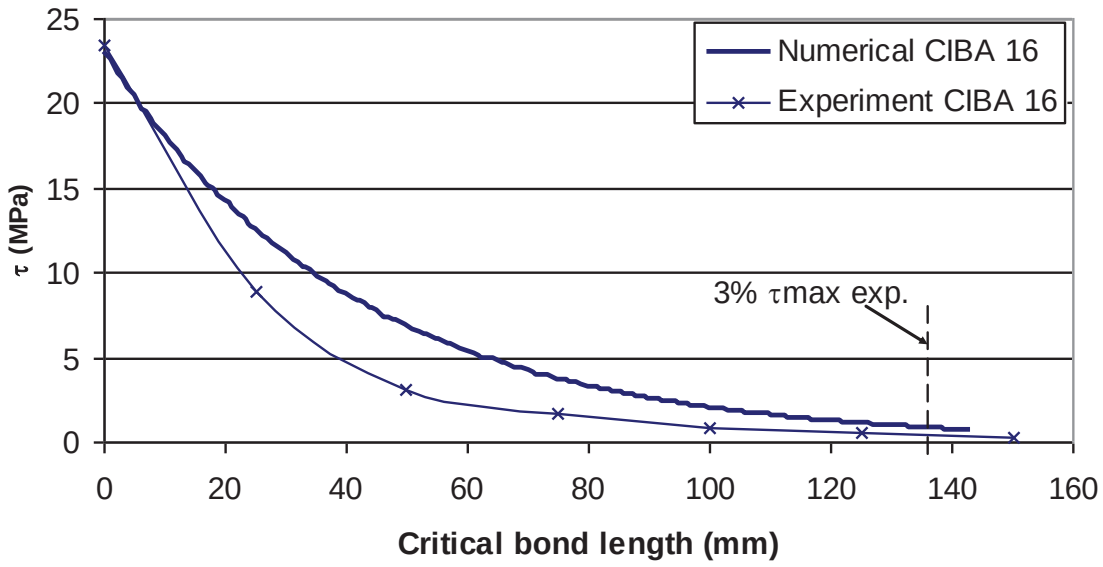

(a) CIBA 16

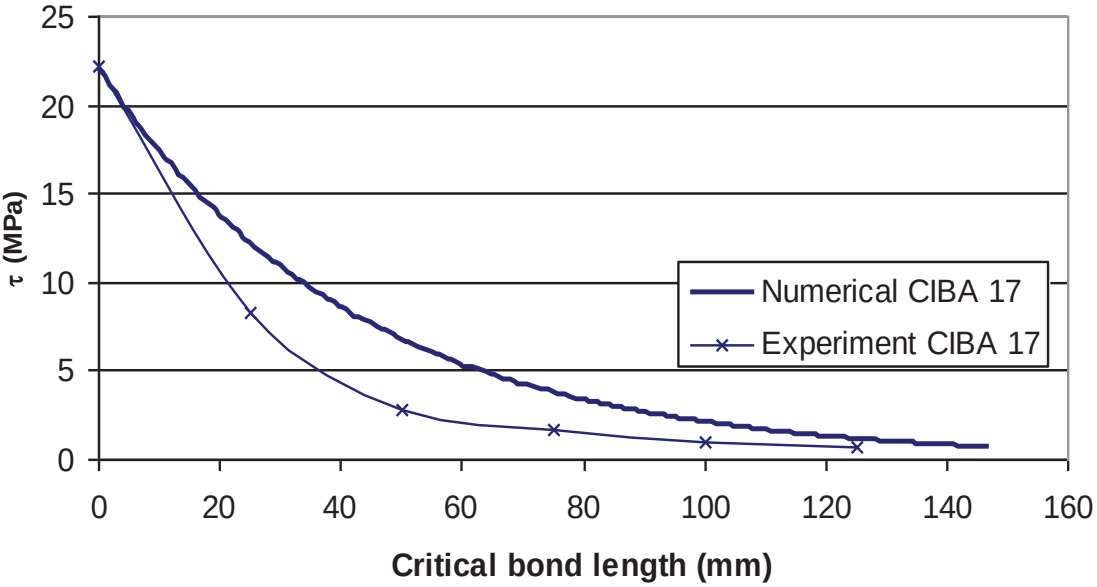

(b) CIBA 17

Figure 4.3 Critical bond length analysis of specimen CIBA

Table 4.1 Critical bond length comparison

Test specimen	L_{crit} (Yuan, Teng et al. 2004) (mm)	L_{crit} (experiment) (mm)	L_{crit} (numerical) (mm)
CIBA 16	73.5	137.5	143
CIBA 17	81.6	125.0	147

4.3 τ_{max} FROM NOT FULLY ANCHORED CIBA SPECIMENS

For a not fully anchored FRP-steel specimen, the numerical method was used to investigate the effect of bond length on the uniformity of the bond stress distribution. This is required for deciding the minimum bond length needed for obtaining the maximum bond stress τ_{max} directly for the short plate test in the following section. As described in Section 4.2.1, the critical bond length for CIBA adhesive is between 125 to 147 mm. Hence, specimens with bond length of 20 mm were chosen to be analysed as a not fully anchored specimen. Figure 4.4 shows the bond distribution obtained numerically with almost a uniform value of bond stress across the 20 mm bonded length.

The experimentally derived $\tau_{max,exp}$ and the average values for each adhesive type from the not fully anchored test results are given in Appendix D. The mean for each adhesive are 22.9 MPa and for CIBA adhesive and 22.7 MPa for SIKA adhesive.

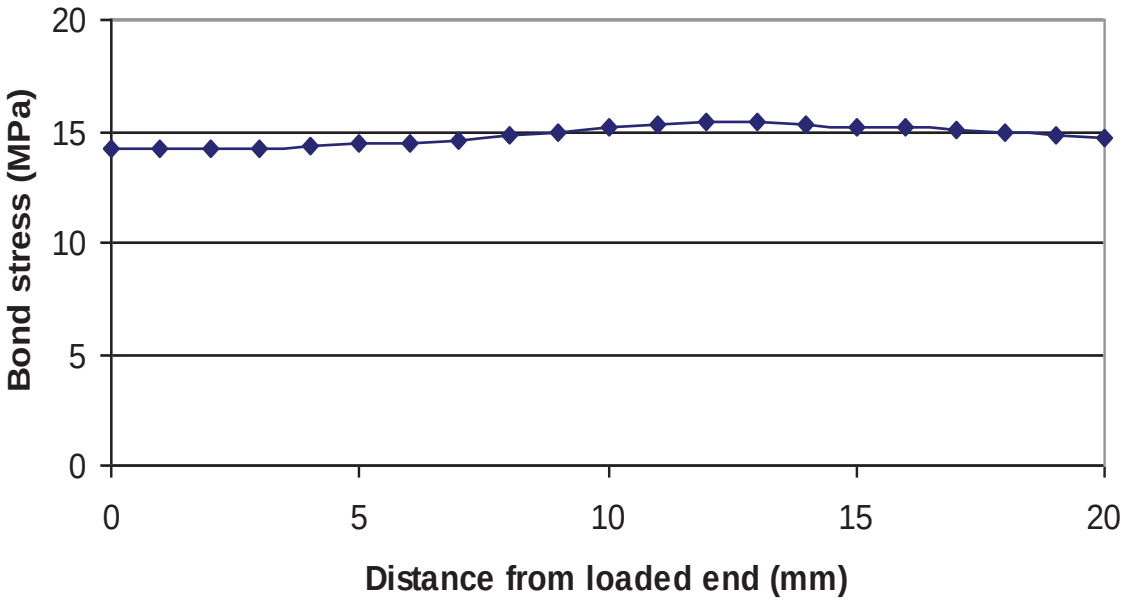

Figure 4.4 Bond stress distribution for a not fully anchored embedment

4.4 P_{IC} FROM FULLY ANCHORED SPECIMENS AND δ_{max} FROM THE GENERIC EQUATIONS

The values of $P_{IC,exp}$ were directly obtained from the P-Δ graphs whereas the values of $\tau_{max,exp}$ were obtained from the not fully anchored specimens as mentioned in Section 4.3. Hence, the values of $\delta_{max,cal}$ can be calculated using Eq. 2.11.

4.5 δ_1 FROM PARTIAL-INTERACTION NUMERICAL MODELLING

The final step in deriving the bond-slip characteristic is to establish the value of δ_1. Using the numerical method described in Section 4.2, the values of δ_1 were varied to get the best fit curve for both the fully anchored specimen and for the not fully anchored specimens. This is possible since the values of $\tau_{max,exp}$ and $\delta_{max,cal}$ were established earlier and used in the numerical method.

4.6 COMPARISON BETWEEN EXPERIMENTAL RESULT WITH NUMERICAL ANALYSIS

It is mentioned in Section 4.3 that the values of $\tau_{max,exp}$ for SIKA and CIBA adhesives were 22.9 and 22.7 MPa respectively. The values for $\delta_{max,cal}$ varies according to the corresponding values of $\tau_{max}\delta_{max}$ which were related to the experimental P_{IC} as tabulated in Appendix D. In this section, the numerical analysis was compared with the experimental results to get the best fit P-Δ curve by varying the values of δ_1.

4.6.1 SPECIMEN SIKA 1

Figure 4.5 shows the comparison between the experimental P-Δ against the numerical analysis curves for specimen SIKA 1. The best fit curve at the elastic region is when δ_1 = 0.01 mm was used. The experimental P_{IC} value was 73.9 kN. The value of the calculated maximum slip, $\delta_{max,cal}$ is 0.13 mm in comparison to 0.07 mm obtained from the experiment. The total debonding slip for the experiment was 0.77 mm whereas the numerical analysis was 0.98 mm.

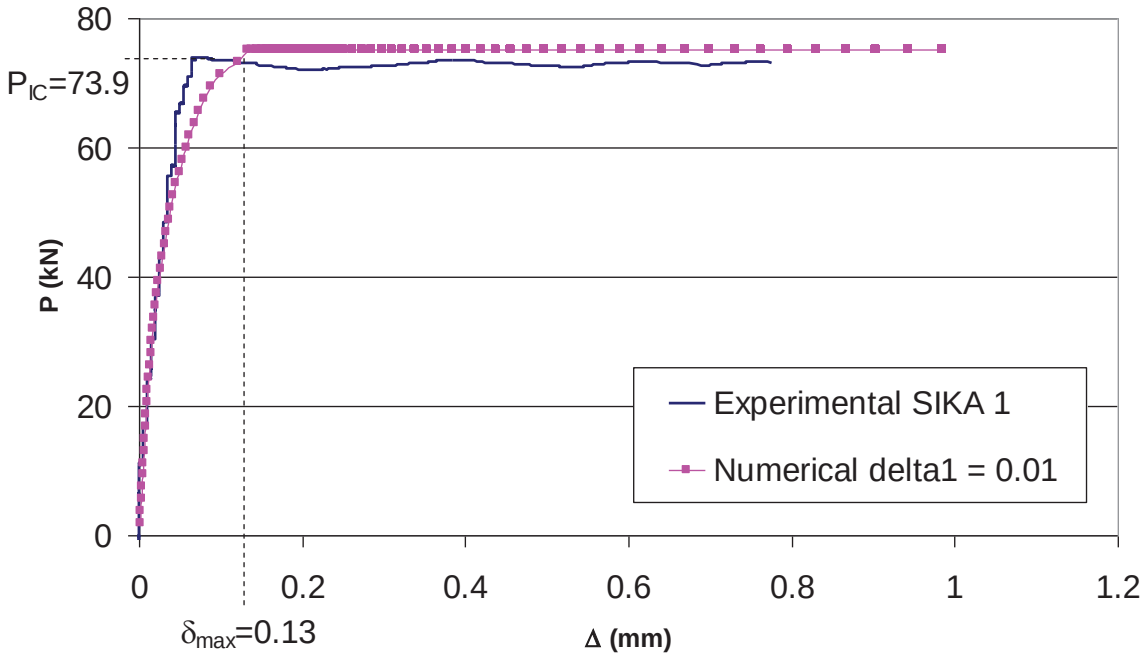

Figure 4.5 Comparison between experimental and numerical P-Δ curves of specimen SIKA 1

4.6.2 SPECIMEN SIKA 2

Figure 4.6 shows the comparison between the experimental *P-Δ* against the numerical analysis curves for specimen SIKA 2. The best fit curve at the elastic region is when δ_1 = 0.05 mm was used. The experimental P_{IC} value was 100.5 kN. The value of the calculated maximum slip, $\delta_{max,cal}$ is 0.11 mm in comparison to 0.09 mm obtained from the experiment. The total debonding slip for the experiment was 0.4 mm whereas the numerical analysis was 0.6 mm.

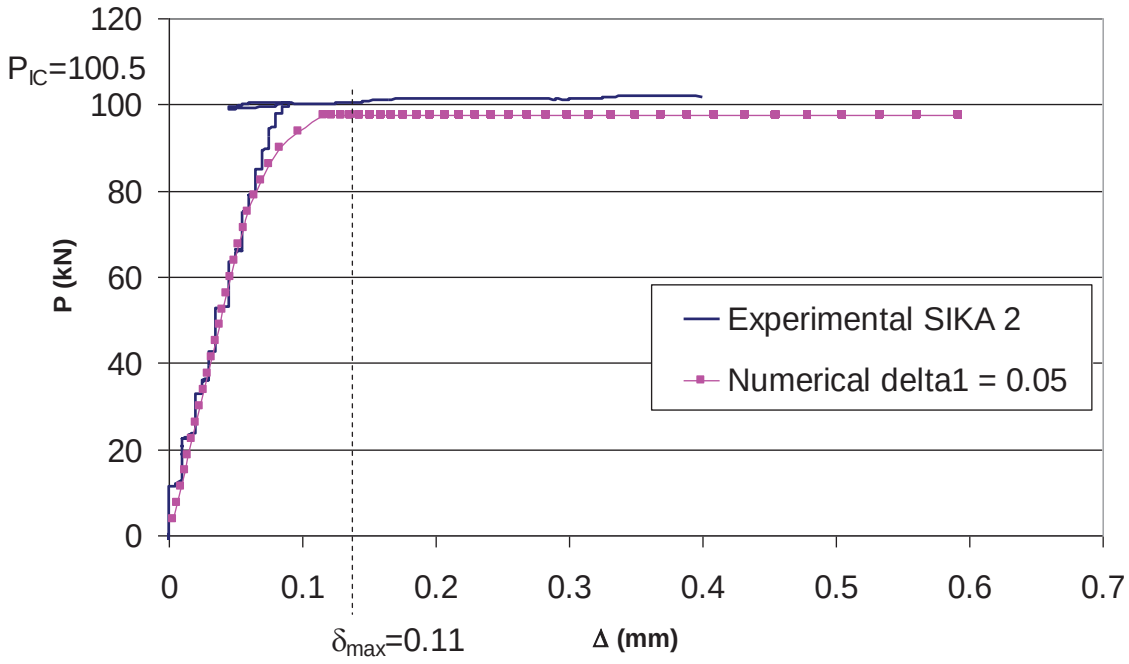

Figure 4.6 Comparison between experimental and numerical P-Δ curves of specimen SIKA 2

4.6.3 SPECIMEN SIKA 3

In Figure 4.7, the comparison between the experimental P-Δ against the numerical analysis curves for specimen SIKA 3 is shown. The best fit curve at the elastic region is when δ_1 = 0.01 mm was used. The experimental P_{IC} value was 68.7 kN. The value of the calculated maximum slip, $\delta_{max,cal}$ is 0.11 mm in comparison to 0.05 mm obtained from the experiment. The total debonding slip for the experiment was 0.12 mm whereas the numerical analysis was 0.25 mm.

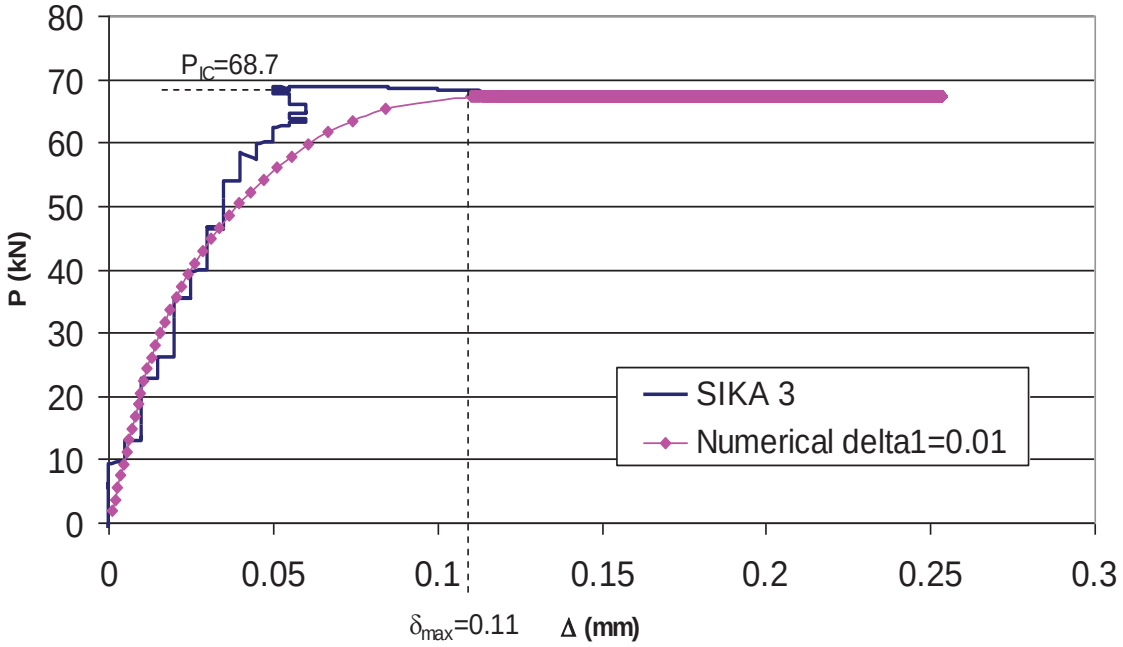

Figure 4.7 Comparison between experimental and numerical P-Δ curves of specimen SIKA 3

4.6.4 SPECIMEN SIKA 4

In Figure 4.8, the comparison between the experimental *P-Δ* against the numerical analysis curves for specimen SIKA 4 is shown. The best fit curve from the numerical analysis is when δ_1 = 0.02 mm was used. The experimental failure load was 44.8 kN. compared to 42.2 kN for the numerical analysis which is 6% difference. The total debonding slip for the experiment was 0.06 mm whereas the numerical analysis was 0.04 mm. Since SIKA 4 was a not fully anchored specimen, $\delta_{max,cal}$ cannot be calculated using Eq. 2.11.

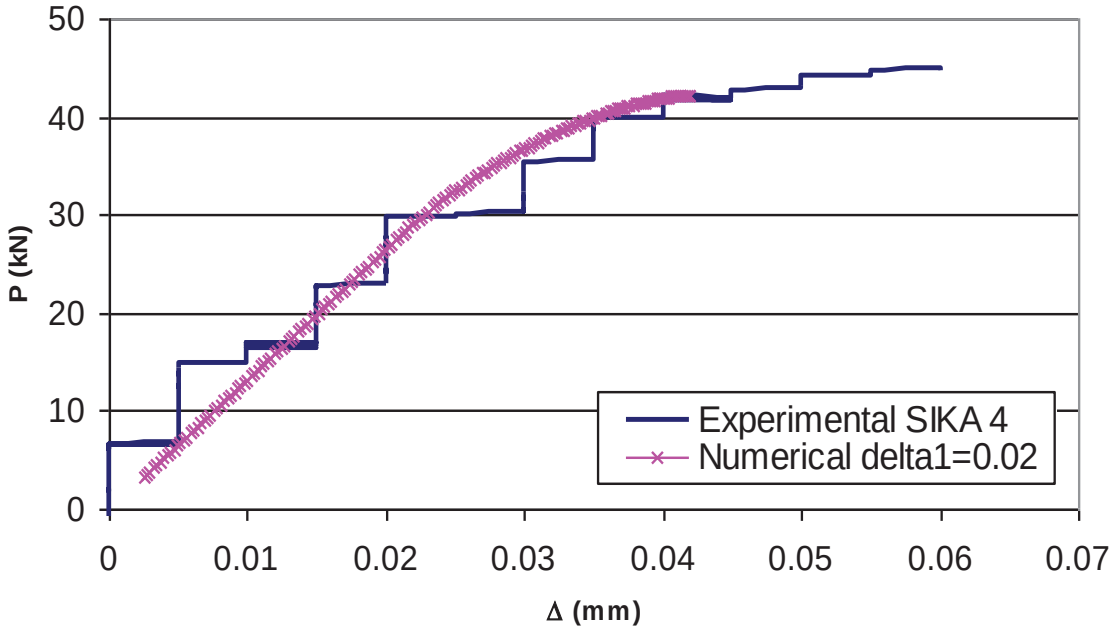

Figure 4.8 Comparison between experimental and numerical P-Δ curves of specimen SIKA 4

4.6.5 SPECIMEN SIKA 5

Specimen SIKA 5 has the same properties as specimen SIKA 4 with slight difference on the value of the failure load. Hence the same δ_1 = 0.02 mm can be used to get the best fit curve as shown in Figure 4.9. The experimental failure load was 46.8 kN compared to 42.2 kN for the numerical analysis which is 10% difference. The total debonding slip for the experiment was 0.06 mm whereas the numerical analysis was 0.04 mm. Since SIKA 5 was a not fully anchored specimen, $\delta_{max,cal}$ cannot be calculated using Eq. 2.11.

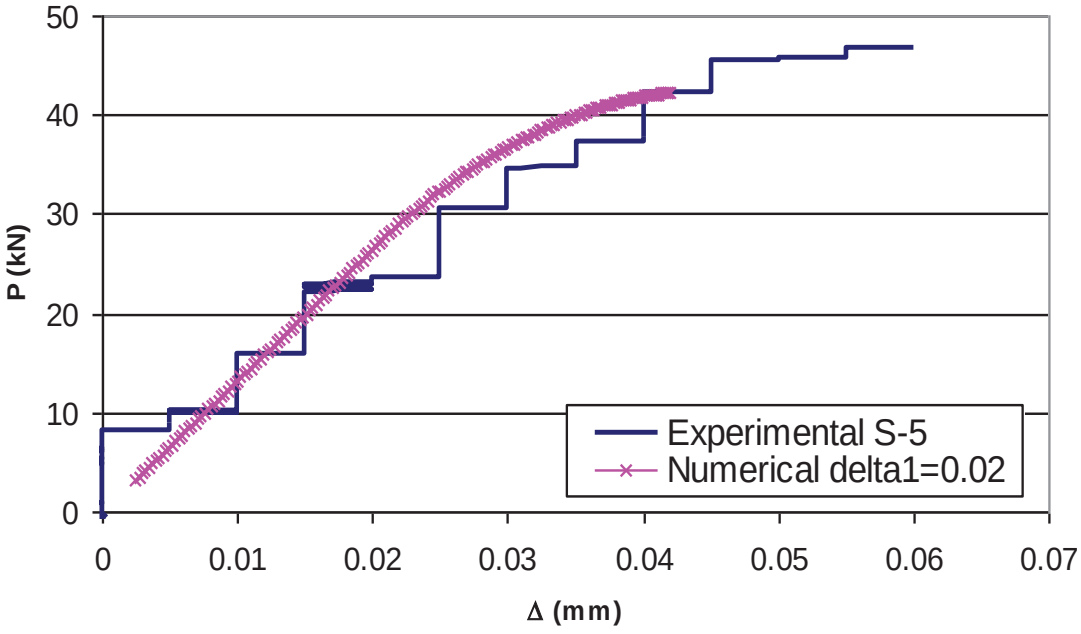

Figure 4.9 Comparison between experimental and numerical P-Δ curves of specimen SIKA 5

4.6.6 SPECIMEN CIBA 6

Figure 4.10 shows the comparison between the experimental *P-Δ* against the numerical analysis curves for specimen CIBA 6. The best fit curve at the elastic region was when δ_1 = 0.02 mm is used. The experimental P_{IC} value was 100.6 kN. The value of the calculated maximum slip, $\delta_{max,cal}$ is 0.23 mm in comparison to 0.11 mm obtained from the experiment. The total debonding slip for the experiment was 0.4 mm whereas the numerical analysis was 1.18 mm.

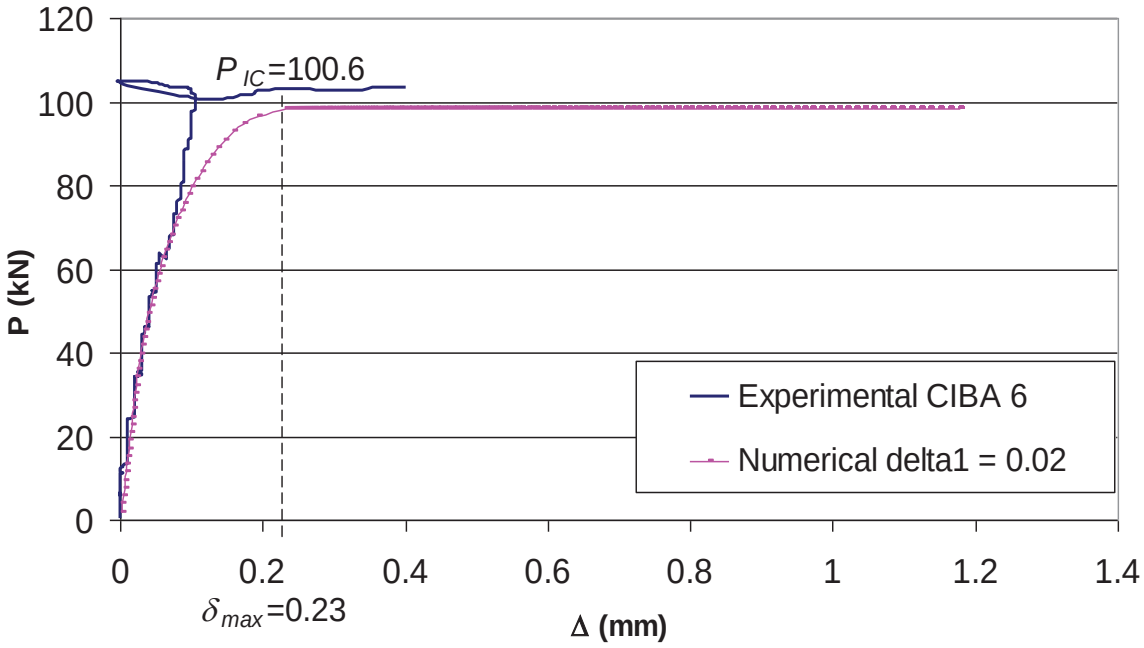

Figure 4.10 Comparison between experimental and numerical P-Δ curves of specimen CIBA 6

4.6.7 SPECIMEN CIBA 7

Figure 4.11 shows the comparison between the experimental *P-Δ* against the numerical analysis curves for specimen CIBA 7. The best fit curve at the elastic region was when δ_1 = 0.07 mm is used. The experimental P_{IC} value was 152.3 kN. The value of the calculated maximum slip, $\delta_{max,cal}$ is 0.26 mm in comparison to 0.18 mm obtained from the experiment. The total debonding slip for the experiment was 0.45 mm whereas the numerical analysis was 0.84 mm.

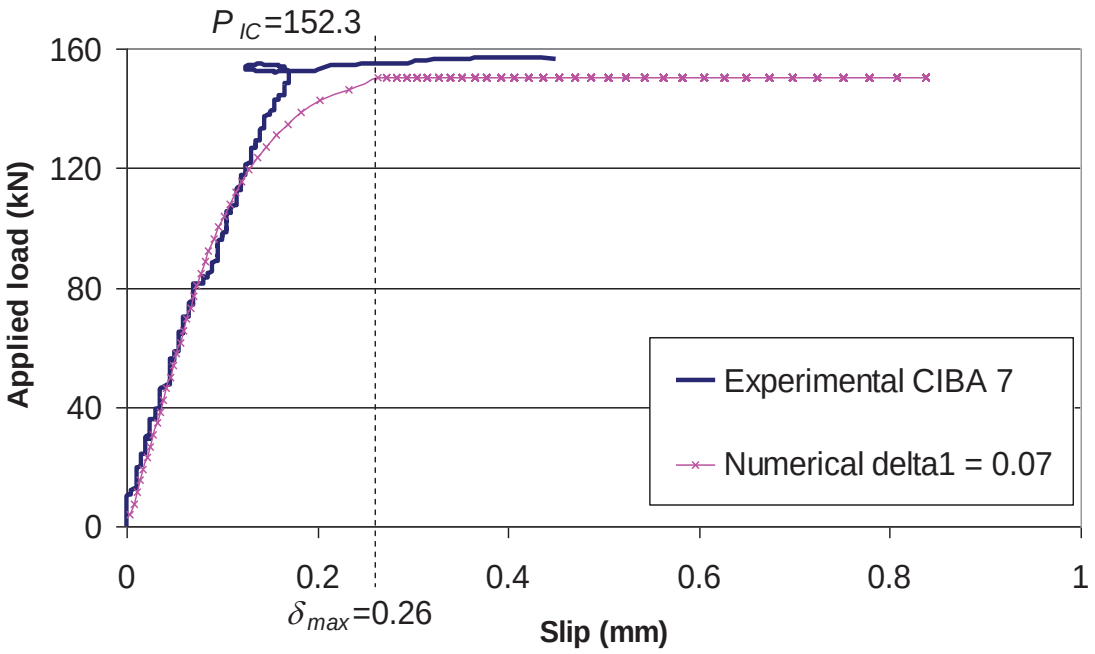

Figure 4.11 Comparison between experimental and numerical P-Δ curves of specimen CIBA 7

4.6.8 SPECIMEN CIBA 7

In Figure 4.12, the comparison between the experimental *P-Δ* against the numerical analysis curves for specimen CIBA 9 is shown. The best fit curve is when δ_1 = 0.03 mm was used. The experimental failure load was 44.7 kN compared to 44.0 kN for the numerical analysis which is 1% difference. The total debonding slip for the experiment was 0.06 mm whereas the numerical analysis was 0.05 mm. Since CIBA 9 was a not fully anchored specimen, $\delta_{max,cal}$ cannot be calculated using Eq. 2.11.

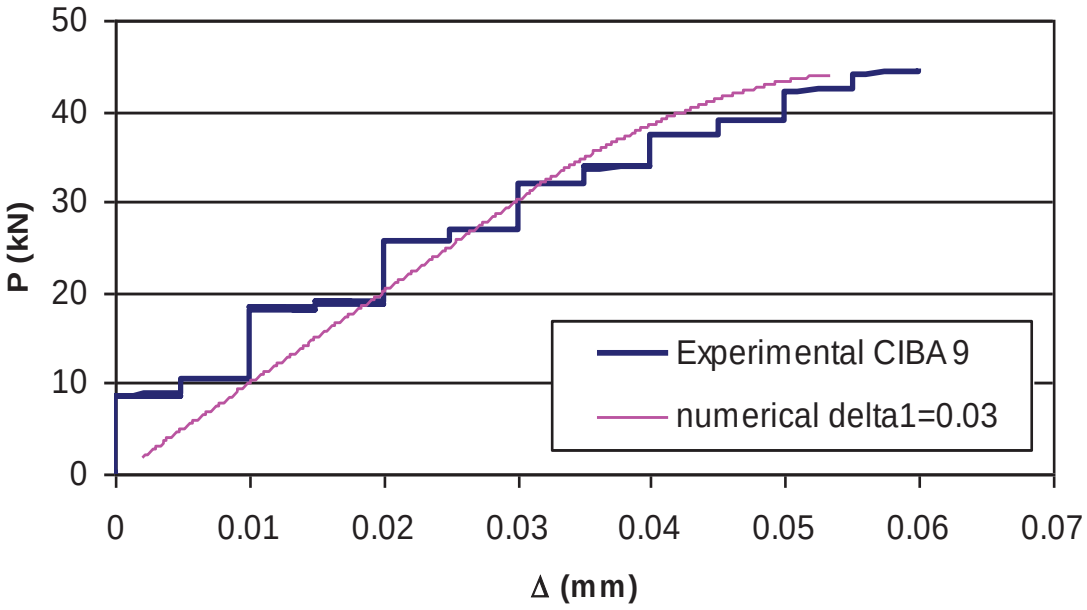

Figure 4.12 Comparison between experimental and numerical P-Δ curves of specimen CIBA 9

4.6.9 SPECIMEN CIBA 10

The failure load for specimen CIBA 10 was 36.0 kN which is much lower than specimen CIBA 9 even though both specimens have the same properties. This leads to a different value of δ_1 to get the best fit curve for CIBA 10. As shown in Figure 4.13, the value of δ_1 to get the best fit curve for CIBA 10 is 0.08 mm compare to 0.03 mm for CIBA 9. The numerical failure load was 43.7 kN which is 18% difference from the experimental. The total debonding slip for the experiment was 0.13 mm whereas the numerical analysis was 0.10 mm.

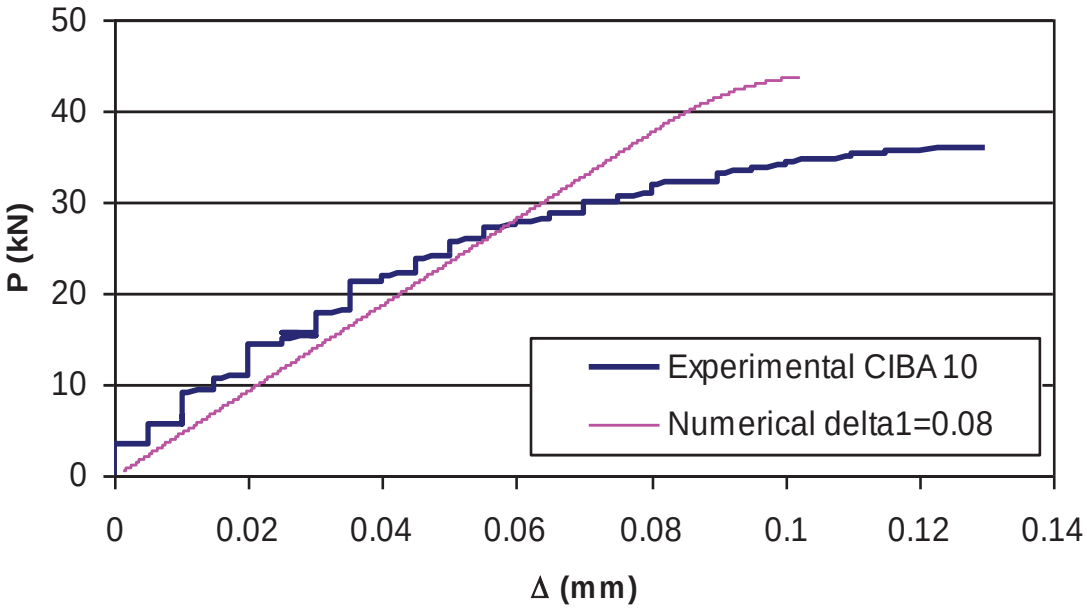

Figure 4.13 Comparison between experimental and numerical P-Δ curves of specimen CIBA 10

4.6.10 SPECIMEN CIBA 11

In Figure 4.14, the comparison between the experimental *P-Δ* against the numerical analysis curves for specimen CIBA 11 is shown. The best fit curve is when δ_1 = 0.12 mm was used. The experimental failure load was 33.5 kN compared to 43.6 kN for the numerical analysis which is 23% difference. The total debonding slip for the experiment was 0.15 mm whereas the numerical analysis was 0.14 mm.

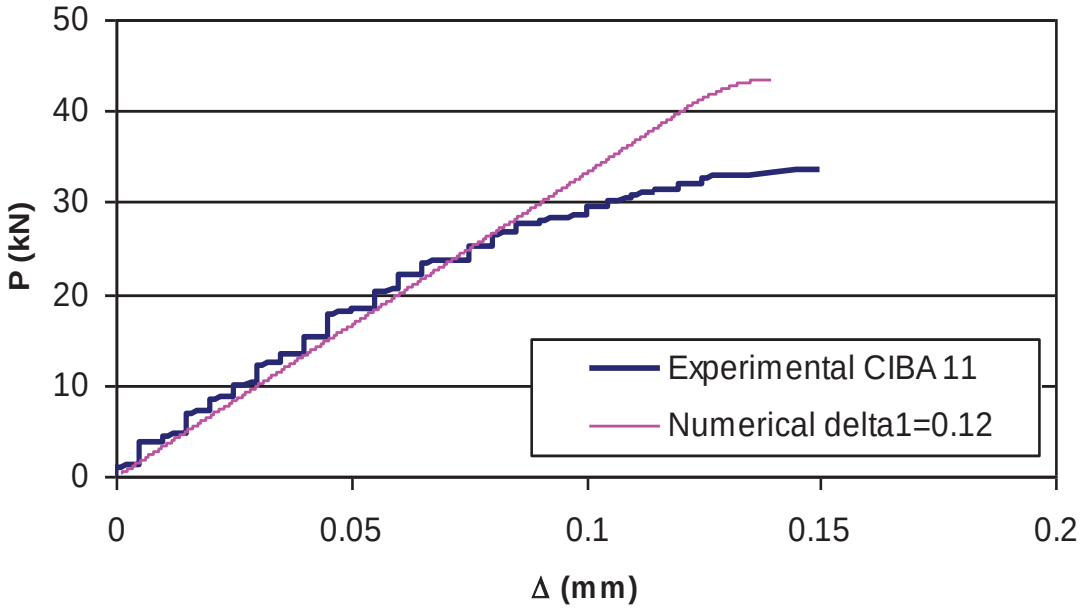

Figure 4.14 Comparison between experimental and numerical P-Δ curves of specimen CIBA 11

4.6.11 SPECIMEN CIBA 13

Figure 4.15 shows the comparison between the experimental *P-Δ* against the numerical analysis curves for specimen CIBA 13. The best fit curve is when δ_1 = 0.03 mm was used. The experimental failure load was 55.4 kN compared to 44.0 kN for the numerical analysis which is 21% difference. The total debonding slip for the experiment was 0.10 mm whereas the numerical analysis was 0.05 mm. Since CIBA 13 was a not fully anchored specimen, $\delta_{max,cal}$ cannot be calculated using Eq. 2.11.

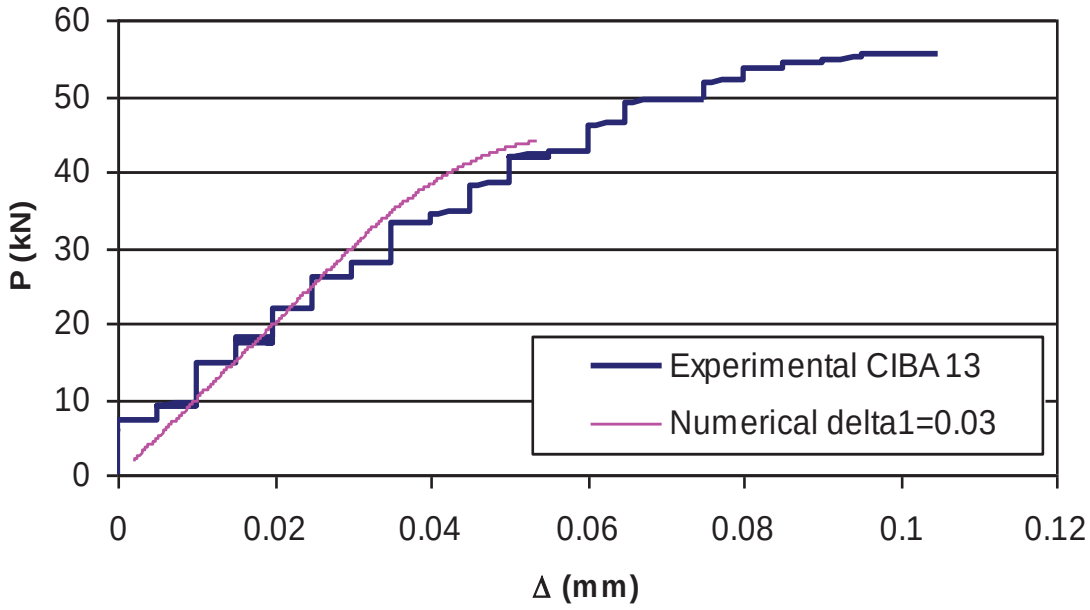

Figure 4.15 Comparison between experimental and numerical P-Δ curves of specimen CIBA 13

4.6.12 SPECIMEN CIBA 14

Figure 4.16 shows the comparison between the experimental *P-Δ* against the numerical analysis curves for specimen CIBA 14. The best fit curve is when δ_1 = 0.05 mm was used. The experimental failure load was 57.9 kN compared to 43.9 kN for the numerical analysis which is 24% difference. The total debonding slip for the experiment was 0.12 mm whereas the numerical analysis was 0.07 mm. Since CIBA 14 was a not fully anchored specimen, $\delta_{max,cal}$ cannot be calculated using Eq. 2.11.

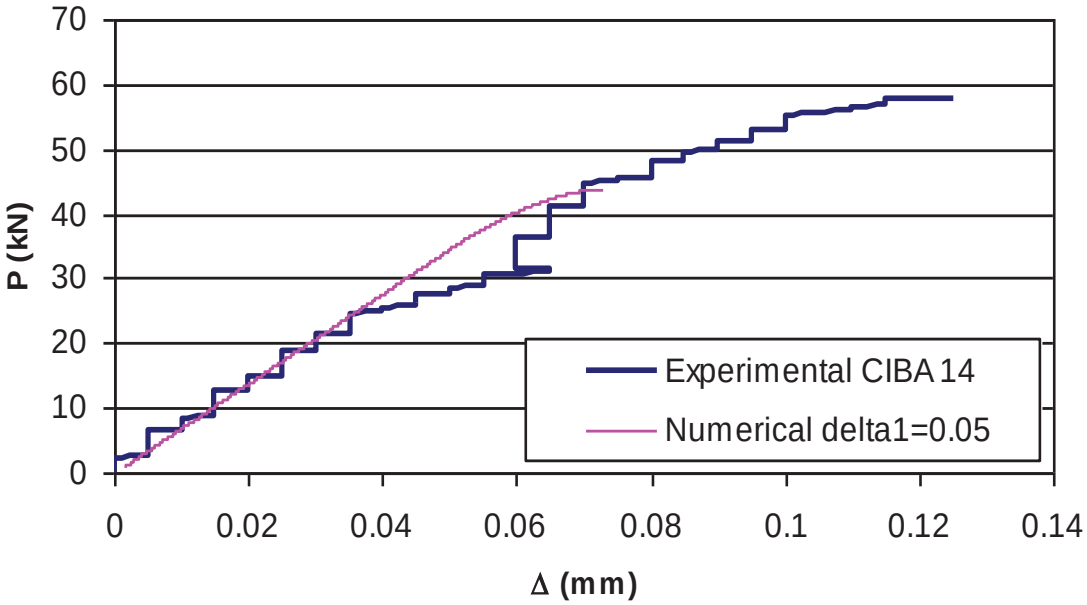

Figure 4.16 Comparison between experimental and numerical P-Δ curves of specimen CIBA 14

4.6.13 SPECIMEN CIBA 16

For the case of specimen CIBA 16 which has loading-unloading *P-Δ* curve, only the first loading path was used for the best fit assessment. As shown in Figure 4.17 the best fit curve is when δ_1 = 0.1 mm was used. The experimental failure load was 106.4 kN. The value of the calculated maximum slip, $\delta_{max,cal}$ is 0.21 mm in comparison to 0.25 mm obtained from the experiment. The total debonding slip for the experiment was 0.26 mm whereas the numerical analysis was 0.96 mm.

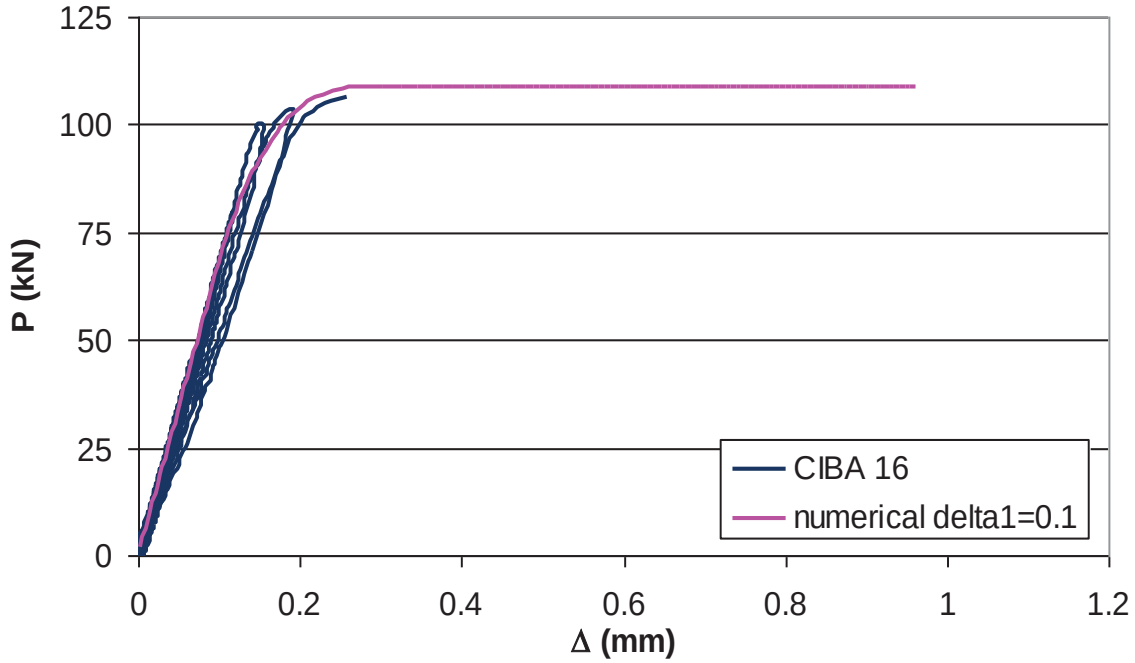

Figure 4.17 Comparison between experimental and numerical P-Δ curves of specimen CIBA 16

4.6.14 SPECIMEN CIBA 17

In Figure 4.18, the comparison between the experimental and numerical analysis *P-Δ* curve is shown. The best fit curve is when δ_1 = 0.2 mm was used. The experimental failure load was 107.3. The value of the calculated maximum slip, $\delta_{max,cal}$ is 0.21 mm in comparison to 0.29 mm obtained from the experiment. The total debonding slip for the experiment was 0.33 mm whereas the numerical analysis was 0.74 mm.

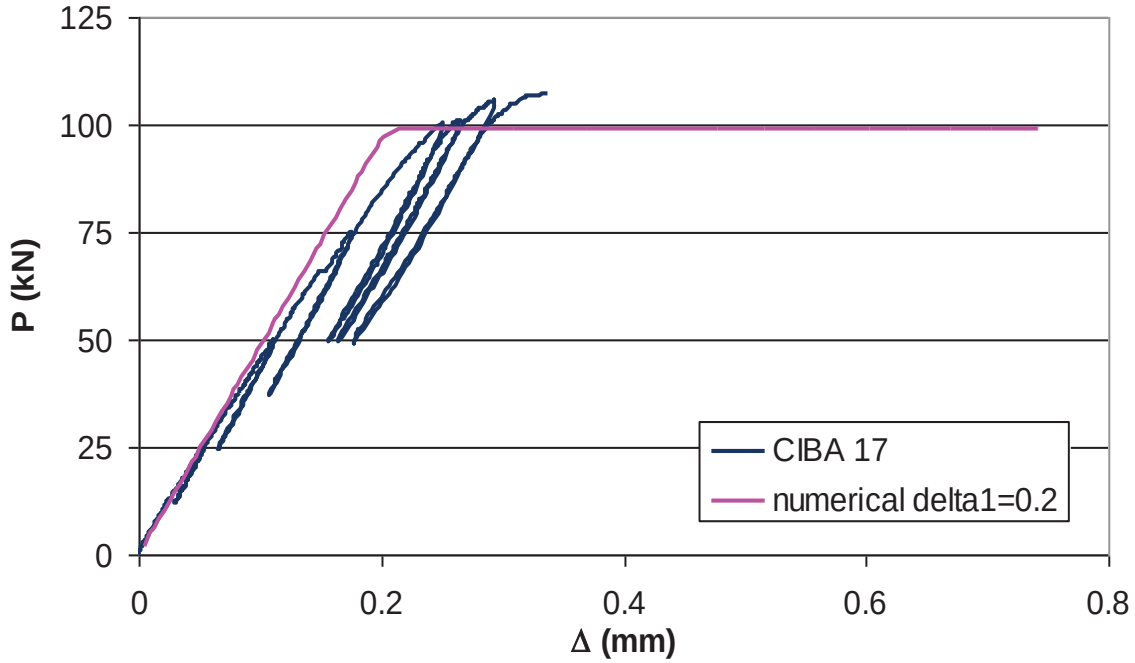

Figure 4.18 Comparison between experimental and numerical P-Δ curves of specimen CIBA 17

4.7 ANALYSIS OF PUBLISHED RESULTS (XIA AND TENG 2005)

In the research carried out by by Xia and Teng (2005), the values of τ_{max} and δ_{max} were obtained experimentally. It is an exhaustive and costly expecially during the preparation of the samples. Large number of strain gauges needs to be glued across the FRP length. Furthermore, strain gauges only give average stresses over the strain gauge length and consequently can miss the peak stresses. As the strain gauges are only placed on the outer surface of the FRP plate, the readings may be affected by local distortion of the plate whilst debonding.

In this section, the experimental values of τ_{max} from the current research in Section 4.3 will be used to obtain the values of δ_{max} and δ_1 from Xia and Teng (2005). This is possible since the adhesive in specimens A and B by Xia and

Teng (2005) was the same adhesive used in specimens CIBA and SIKA in the current research. The values of δ_{max} can be calculated using Eq. 2.11 since τ_{max} is known whereas the values of δ_1 is the best fit curve obtained using the numerical method developed in Section 4.2.

4.7.1 τ_{max}-δ_{max} FROM EXPERIMENT RESULTS

In the published results by Xia and Teng (2005), the values of τ_{max} and δ_{max} were obtained from the experimental results. As shown in Figure 4.19 (a), the published results for the values of τ_{max} and δ_{max} for adhesive A are 18.5 MPa and 0.34 mm respectively. The published results for the values of τ_{max} and δ_{max} for adhesive B are 15.5 MPa and 0.23 mm respectively as shown in Figure 4.19 (b). These values of the τ_{max} were obtained by processing the data from the strain gauges which were glued on the FRP plate. This only give average stresses over the strain gauge length and consequently can miss the peak stresses and as the strain gauges are only placed on the outer surface of the FRP plate the readings may be affected by local distortion of the plate whilst debonding. In order to avoid these problems, the method in obtaining the values of τ_{max} from the not fully anchored specimen, calculating δ_{max} from Eq. 2.11 and varying the values of δ_1 using the numerical method as described in the current research will be carried out to analyse the published results.

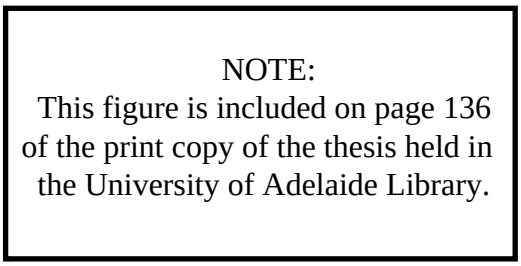

Figure 4.19 Shear stress distributions from Xia and Teng (2005) experiments

4.8 COMPARISON OF XIA AND TENG (2005) EXPERIMENTAL RESULT WITH CURRENT RESEARCH

In this section, the numerical analysis was compared with the experimental results to get the best fit *P-Δ* curve by varying the values of δ_1. As mentioned in Section 4.3, the values of $\tau_{max,exp}$ for specimens CIBA and SIKA from the current research are 22.7 MPa and 22.9 MPa respectively. Instead of using the values of τ_{max} obtained from the published results, the current values of $\tau_{max,exp}$ from specimens CIBA and SIKA will be used for specimens A and B in the published results.

4.8.1 SPECIMEN A-1

The experimental P_{IC} value was 58.5 kN and is obtained directly from the *P-Δ* graph in Figure 4.20. The value of $\tau_{max,exp}$ is 22.9 MPa as mentioned in Section 4.8. Since the value of P_{IC} and $\tau_{max,exp}$ are known, the value of the calculated maximum slip, $\delta_{max,cal}$ is 0.30 mm. Using these values of $\tau_{max,exp}$ and $\delta_{max,cal}$, the numerical method is used to obtain the best fit curve by varying the value of δ_1. The best fit curve is obtained when δ_1 = 0.1 mm is used as shown in Figure 4.20.

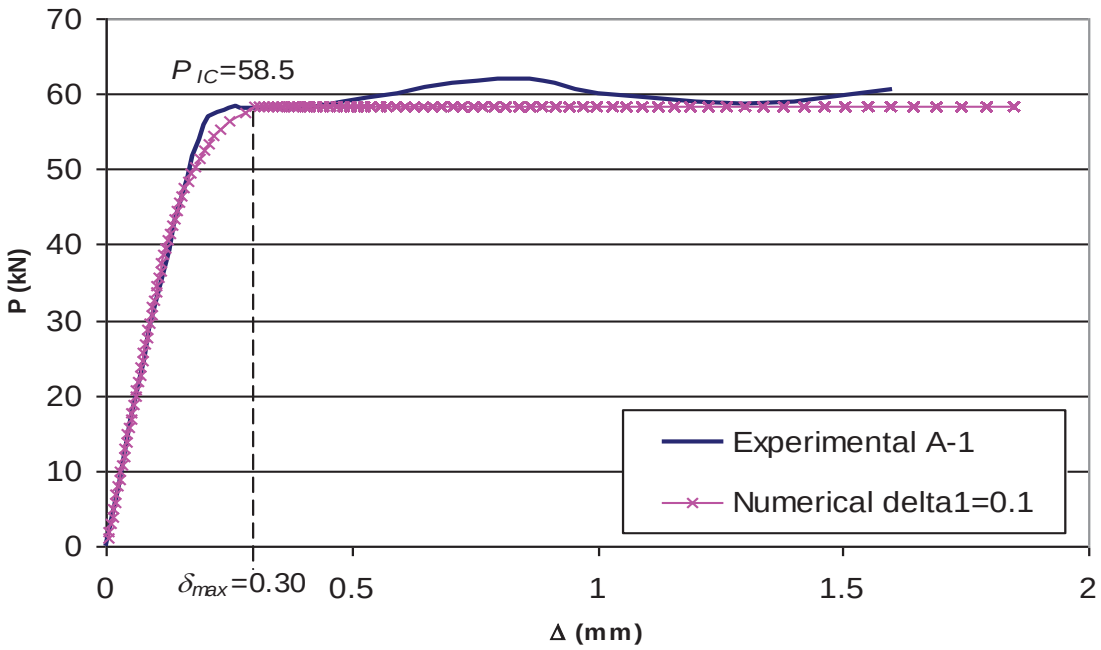

Figure 4.20 Comparison between experimental and numerical P-Δ curves of specimen A-1

4.8.2 SPECIMEN A-2A

In Figure 4.21, the comparison between the experimental *P-Δ* against the numerical analysis curves for specimen A-2A is shown. The best fit curve is when δ_1 = 0.1 mm was used. The experimental P_{IC} value was 60.0 kN and is obtained directly from the *P-Δ* graph in Figure 4.21. The value of $\tau_{max,exp}$ is 22.9 MPa as mentioned in Section 4.8. Since the value of P_{IC} and $\tau_{max,exp}$ are known, the value of the calculated maximum slip, $\delta_{max,cal}$ is calculated as 0.30 mm.

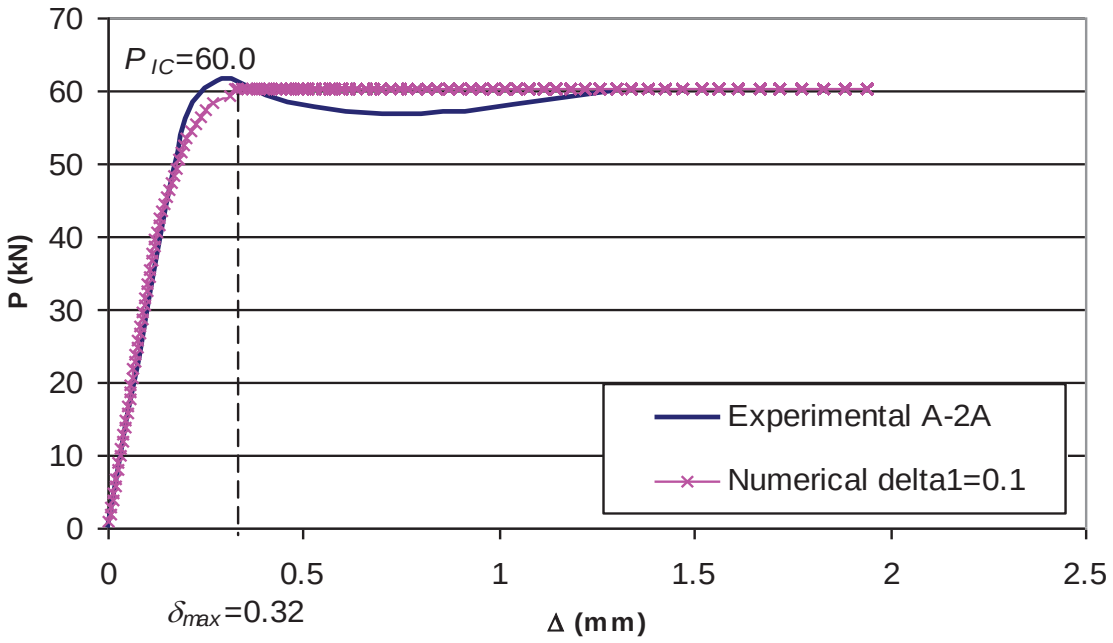

Figure 4.21 Comparison between experimental and numerical P-Δ curves of specimen A-2A

4.8.3 SPECIMEN B-1

Figure 4.22 shows the comparison between the experimental *P-Δ* against the numerical analysis curves for specimen B-1. The best fit curve at the elastic region was when δ_1 = 0.05 mm is used. The experimental P_{IC} value was 39.0 kN compared to 38.6 kN for the numerical analysis. The total debonding slip for the experiment was 1.20 mm whereas the numerical analysis was 1.28 mm.

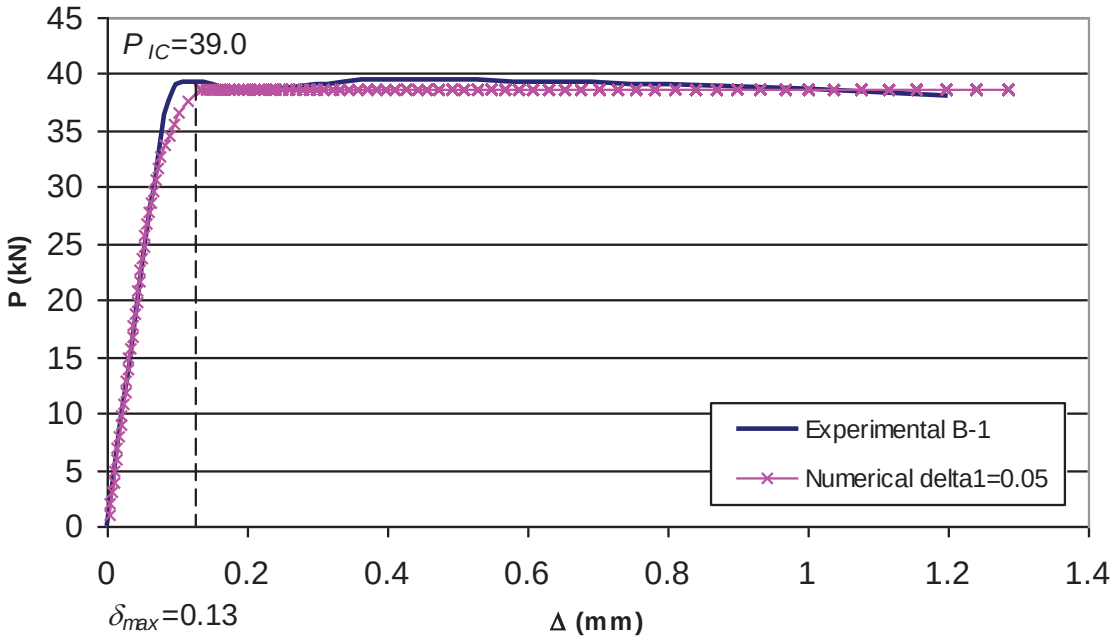

Figure 4.22 Comparison between experimental and numerical P-Δ curves of specimen B-1

4.8.4 SPECIMEN B-2A

In Figure 4.23, the comparison between the experimental *P-Δ* against the numerical analysis curves for specimen B-2A is shown. The best fit curve is when δ_1 = 0.09 mm was used. The experimental failure load was 42.2 kN compared to 42.6 kN for the numerical analysis. The total debonding slip for the experiment was 1.20 mm whereas the numerical analysis was 1.33 mm.

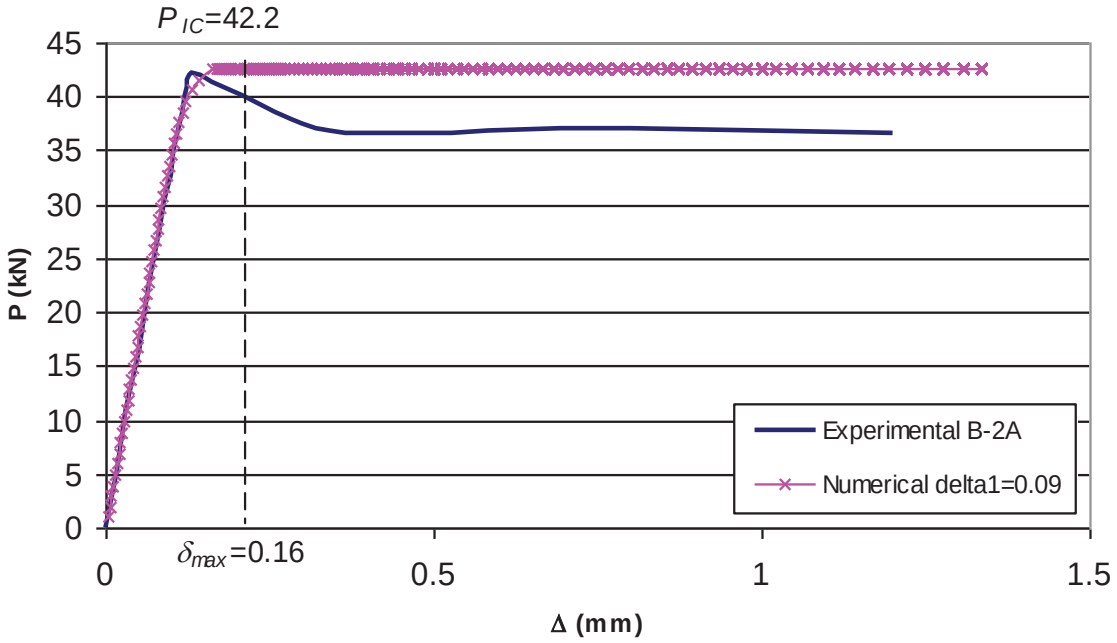

Figure 4.23 Comparison between experimental and numerical P-Δ curves of specimen B-2A

4.9 SUMMARY ON THE NUMERICAL ANALYSIS BEST FIT CURVE

The numerical method developed in this research has been proven to be able to predict the values of P_{IC} correctly. The role of δ_1 in influencing the elastic region of the global *P-Δ* curve was also established. From the current research, the values of $\delta_{max,cal}$ for CIBA adhesive are 0.23 mm and 0.26 mm for Specimen CIBA 6 and CIBA 7 respectively. For specimens CIBA 16 and CIBA 17, the $\delta_{max,cal}$ was 0.21 mm. Similarly, the values of $\delta_{max,cal}$ for SIKA adhesive were close with 0.13 mm for specimen SIKA 1 and 0.11 mm for specimens SIKA 2 and SIKA 3 respectively. This show that the results of $\delta_{max,cal}$ show small scatters in both CIBA and SIKA specimens. The experimental slip $\delta_{max,exp}$, obtained from the *P-Δ* graph as tabulated in Appendix D, shows larger scatters between the same types of adhesive, which indicates that slip data from the experiment may be susceptible to experimental errors. The final step in deriving the bond-slip characteristics is to establish the value of δ_1. Using the numerical method described in Section 4.2, the values of δ_1 were varied to get the best fit curve. The results of this analysis are tabulated in Appendix D.

In the published results by Xia and Teng (2005), the values of $\tau_{max,exp}$ and $\delta_{max,exp}$ for specimens A-1 and B-1 are described in Figure 4.19. However, these values are susceptible to experimental errors as explained in Section 4.7.1. Hence, the values of $\tau_{max,exp}$ from the current research were used. The values of P_{IC} were directly obtained from the *P-Δ* graph and is used to calculate $\delta_{max,cal}$ using Eq. 2.11. $\delta_{max,cal}$ for specimens A-1 is 0.30 mm which is close to the the value of the averaged $\delta_{max,cal}$ from specimen CIBA at 0.23 mm. Similarly, the value of $\delta_{max,cal}$ for specimens B-1 is 0.13 mm is in good comparison with the value of $\delta_{max,cal}$ from specimen SIKA at 0.12 mm. Finally, the best fit curve is obtained by varying the value of δ_1 using the numerical method. The results of this analysis are tabulated in Appendix E.

The length of the plateau, after P_{IC} was reached was influenced by the mode of failure. For example, the plateau for specimens SIKA 1 and SIKA 2 in

Figure 4.5 and Figure 4.6 were predicted by the numerical analysis correctly if compared to specimens CIBA 6 and CIBA 7 (Figure 4.9 and Figure 4.10). This is because for specimen SIKA 1 and SIKA 2, the failure mode was within the adhesive layer. Even though the failure mode for specimens CIBA 6 and CIBA 7 was initially within the adhesive layer, the major part of the debonding failure was within the FRP plate which was a weaker mode of failure resulting in a shorter plateau in the figures. Hence, the numerical analysis was correct in predicting the failure mode within the adhesive layer correctly.

4.10 CONCLUSIONS

It has been shown that the bond-slip characteristics of the adhesive joint between FRP and steel is difficult to measure directly through experiments because of the very small slips and steep stress gradients. An alternative approach to quantifying the bond-slip characteristics has been proposed using a combination of structural mechanics principles as well as measurable experimental data. The steps of the approach are as follows:

- Obtain the value of the peak shear stress τ_{max} from short pull tests where the anchorage length is much smaller than the critical length L_{crit} that can be determined from partial interaction structural mechanics.
- Obtain the value of the intermediate crack debonding resistance P_{IC} from fully anchored samples.
- From partial interaction structural mechanics, the fracture energy ½ $\tau_{max}\delta_{max}$ is a function of P_{IC}, hence, $\tau_{max}\delta_{max}$ can be obtained and as τ_{max} is known δ_{max} can be determined.
- Obtain δ_1 the slip at τ_{max} from curve fitting using a partial interaction numerical analysis.

CHAPTER 5: FRP PLATED STEEL COUPON TESTS

5.1 INTRODUCTION

The objective of the experimental program in this chapter is to understand the steel and FRP strain development specifically for a steel flange under the influence of axial load only. For this purpose, two sets of samples were prepared. The first set was prepared so that plate end debonding was the main failure criteria. On other hand, the second set was prepared so that debonding will occur at the tapered area of the steel, representing yielding of steel at the bonded length.

5.2 SPECIMENS

Four samples were tested. Figure 5.1 shows the specimen for the first set of testing which consisted of two samples. The samples consisted of steel plates with a constant width of 30 mm, bonded with FRP of 40 mm or 80 mm length. The thickness of FRP plate is 1.2 mm.

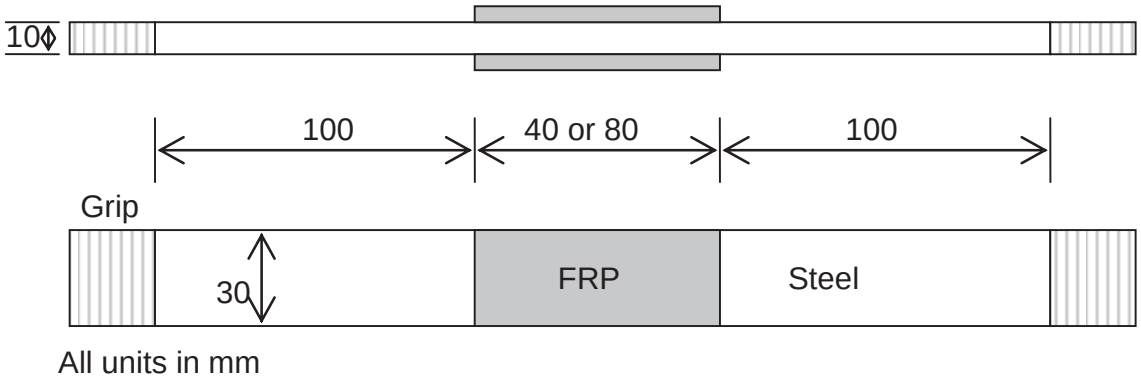

Figure 5.1 Shape and dimension of test specimen with a constant width (CW) steel plate

Figure 5.2 shows the shape and dimension of the second set of specimens which also consisted of two samples. This specimen was based on the experiment conducted by Al-Emrani and Kliger (2006). The steel plates were tapered so that yielding of steel will occur on the middle section. The steel plate was varied in width from 100 mm at the widest and 30 mm at the thinnest. The constant width of 30mm that ran for 50 mm in length was designed to provide spaces for strain gauges. The FRP that was bonded on to the steel plate was 250 mm long. However the first sample was bonded with one layer of FRP and the other with two layers of FRP. The thickness of FRP plate is 1.2 mm.

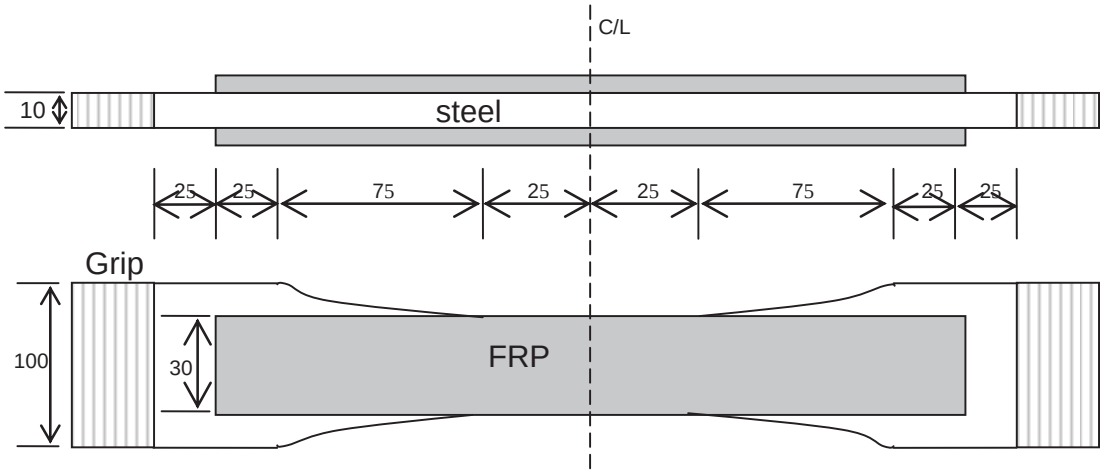

Figure 5.2 Shape and dimension of test specimen with a varying width (VW) steel plate

All of the steel plate was cut to size using a steel cutter. The steps taken for the preparations of the samples which include the preparation of the adhesive and bonding the FRP to the steel are similar to what has been described in Section 3.2, so it will not be repeated here. Table 5.1 shows the geometrical properties of the specimens after they were constructed.

Table 5.1 Geometrical properties of test specimens

Test specimen	Steel thickness, t_s (mm)	FRP width, b_p (mm)	FRP FRP layer	Bonded length, L_p (mm)	Category
CW 1	9.49	30.0	1	40	Constant width
CW 2	9.51	30.0	1	80	Constant width
VW 1	11.95	30.0	1	250	Varying width
VW 2	11.96	30.0	2	250	Varying width

5.3 TEST SETUP

The testing rig used in the experiment was similar to the earlier series (Chapter 3) as shown in Figure 3.4. The bottom part of the sample is clamped while the pulling was conducted on the upper part of the sample. The applied load was under the combination of load and displacement control as explained in Section 3.3.

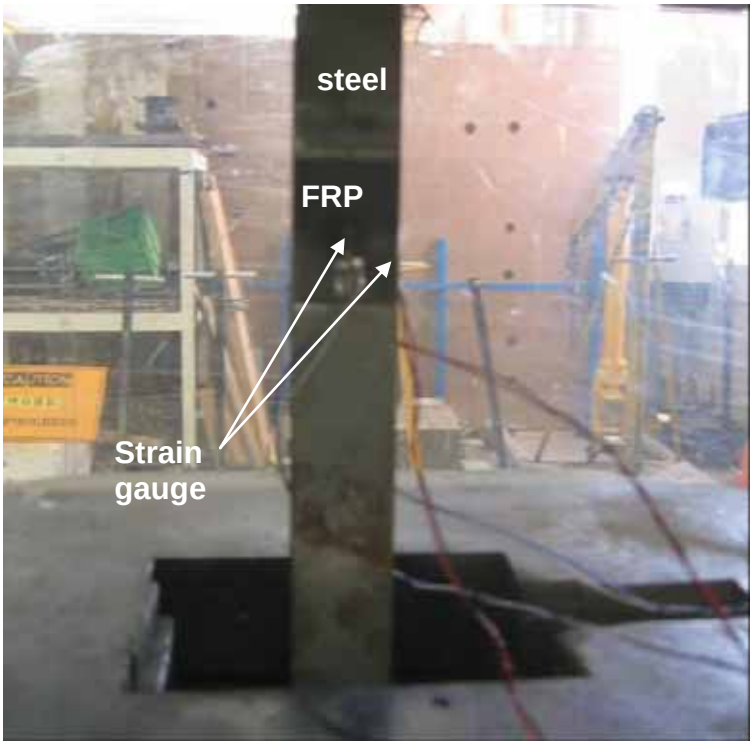

Figure 5.3 Test setup

5.4 INSTRUMENTATION

For the CW specimens, two 5 mm strain gauges were glued at the top of the FRP plate and two 5 mm strain gauges were glued at the sides of the steel plate as shown in Figure 5.4. For the VW specimens, 16 mm strain gauges were glued at the top of the FRP plate and ten 5 mm strain gauges were glued at the sides of the steel plate as shown in Figure 5.5. Strains were recorded from these strain gauges and the load applied was recorded from the UTM machine.

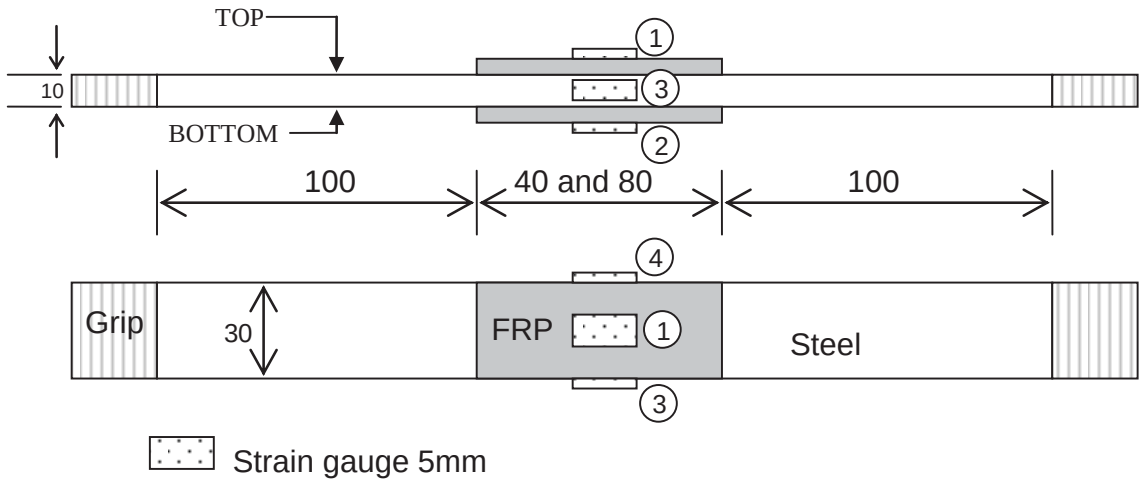

Figure 5.4 Strain gauges location of test specimen with a constant width (CW) steel plate

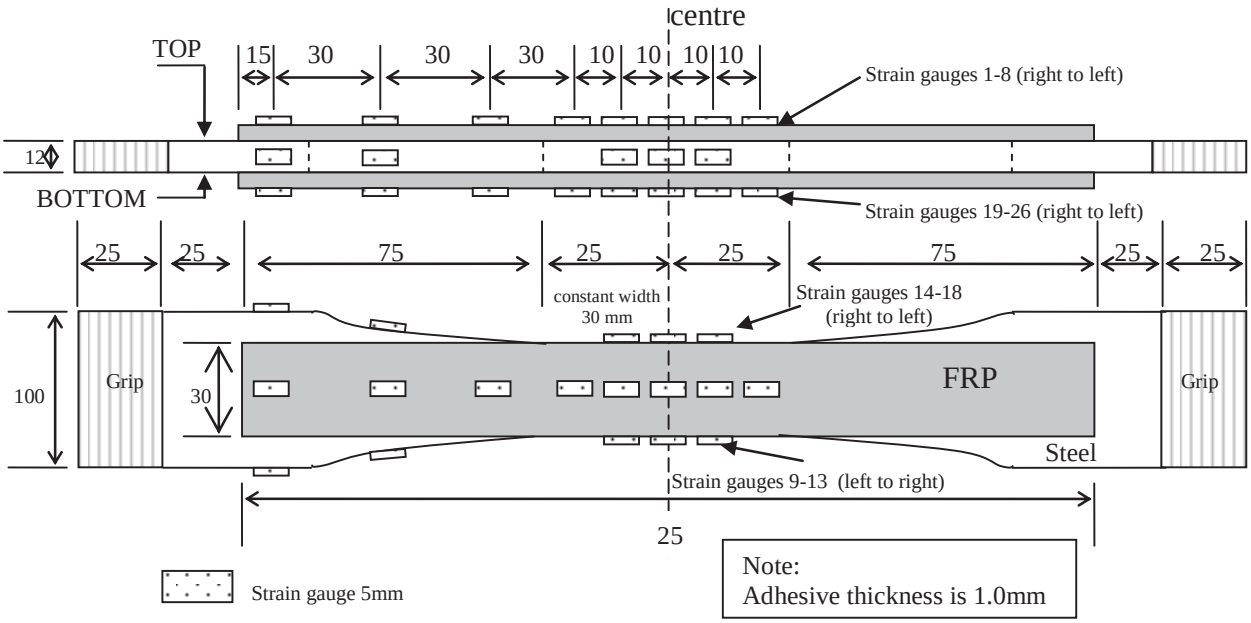

Figure 5.5 Strain gauges location of test specimen with a varying width (VW) steel plate

5.5 MATERIAL PROPERTIES

CIBA adhesive was used in the experiments. The CIBA adhesive and the FRP plate used in these experiments were similar from the previous experiments and are detailed in Section 3.5. Pull tests were conducted on the steel plate to get the stress-strain relationship. Three samples were tested. The geometry of the steel plate for the pull tests was similar to the FRP plated steel plate as shown in Figure 5.5. The stress-strain relationship of the steel is shown in Figure 5.6. From this relationship, the yield stress and the ultimate stress of the steel were extracted and tabulated in Table 5.2. The averaged value of the steel material properties will be used in the numerical scheme in Chapter 6.

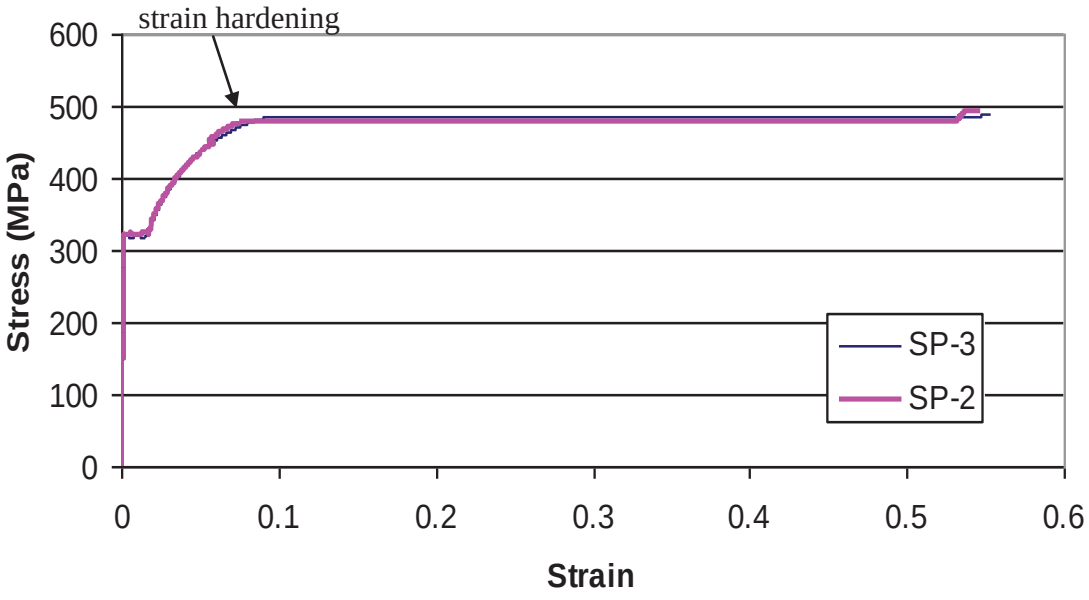

Figure 5.6 Stress-strain relationship of the steel.

Table 5.2 Material properties of the steel plate

Test specimen	SP-1	SP-2	SP-3	Averaged
Yield load, P_y (kN)	116.5	115.7	115.4	115.9
Yield stress, f_y (MPa)	307	313	305	308
Yield strain, ε_Y	0.00151	0.00155	0.00150	0.00152
Young's Modulus, E_s (MPa)	201943	201836	203265	202348
Strain hardening stress, f_{sh} (MPa)	-	486	486	486
Strain hardening, ε_{sh}	-	0.095	0.095	0.095

5.6 TEST RESULTS OF CW SPECIMENS

5.6.1 SPECIMEN CW1

Figure 5.7 shows sample CW1 at failure. It can be observed that the debonding occurred between the adhesive and steel layers (the top and bottom surfaces refers to Figure 5.4). The breaking point of the steel plate was near the plate end where the strength of the steel plate was its weakest. Figure 5.8 shows the load-strain relationship of CW1. Debonding occurs at approximately 85 kN load and almost abruptly. This is due to the shortness of the bonded FRP. Immediately after the FRP debonded, the steel plate yielded before finally breaking at 98 kN load.

It can be observed in Figure 5.8 that there was an increment or strain difference between the steel and the FRP. The strain difference was calculated as 62% at the point just before debonding occurred. This strain difference indicated the partial interaction behaviour between the steel and FRP.

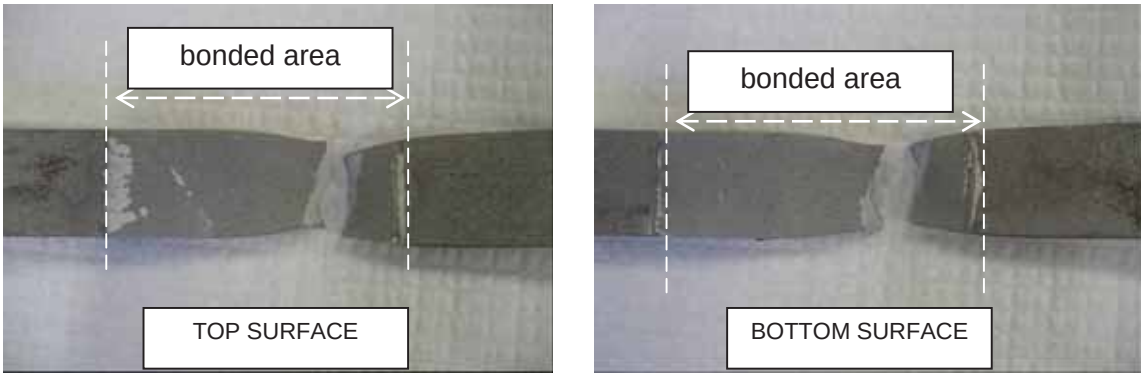

(a) steel plate

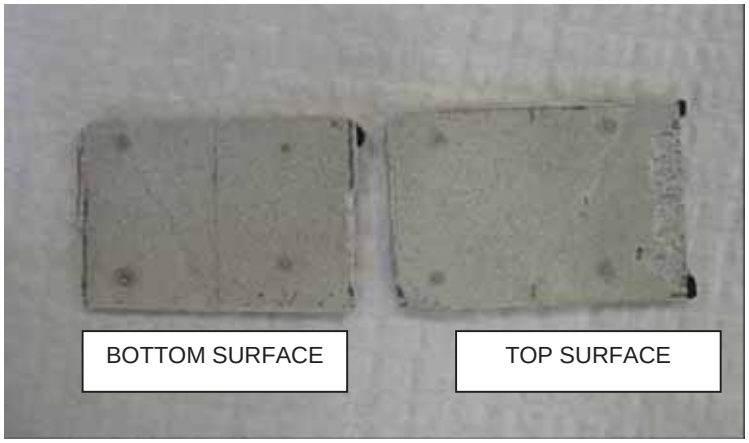

(a) FRP

Figure 5.7 Failure mode of CW1.

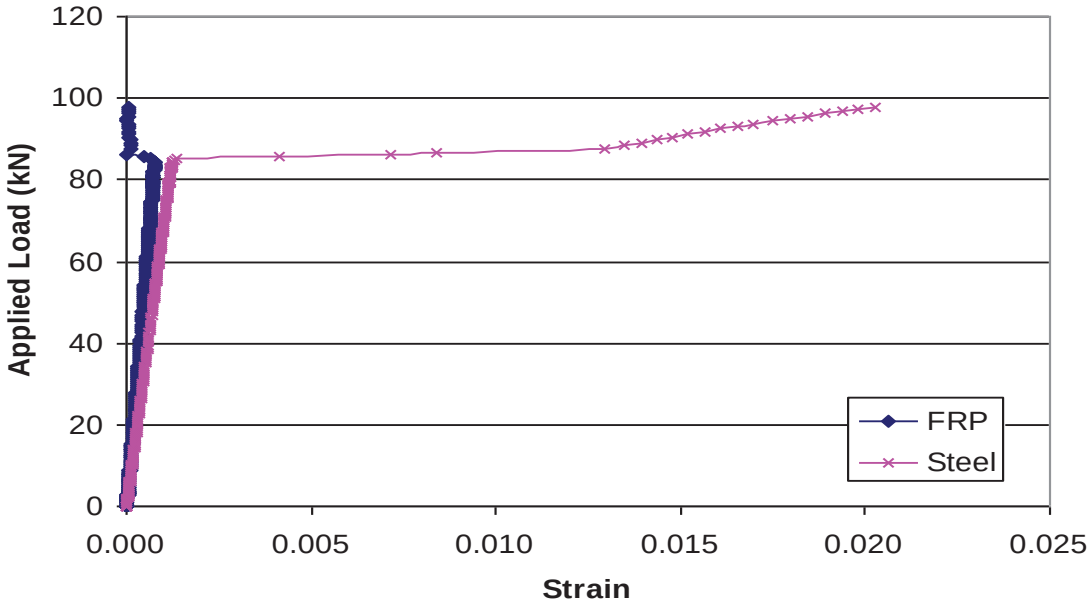

Figure 5.8 Experimental result for CW1.

5.6.2 SPECIMEN CW2

Breaking point for sample CW2 was clearly outside the bonded area as shown in Figure 5.9. The smooth surface of the steel plate indicates that the debonding failure occurred at the steel-FRP layer which is similar to CW1. Total debonding occurs at a load of 86.4 kN at which the sample behaved as a bare steel plate.

Figure 5.10 shows the experimental results. The strain difference between the FRP and steel strains was calculated as 12% which is smaller compare to specimen CW1.

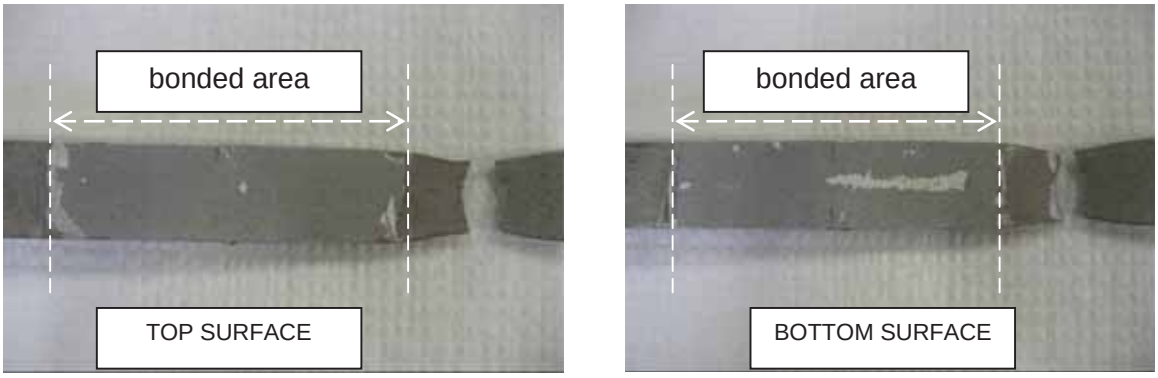

(a) steel plate

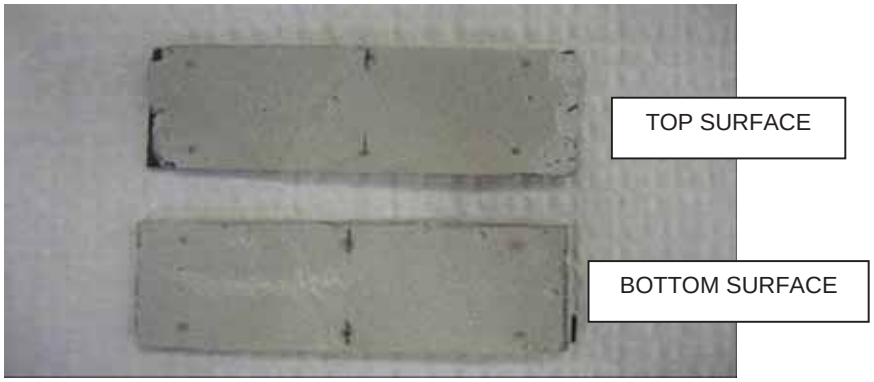

(a) FRP

Figure 5.9 Failure mode of CW2.

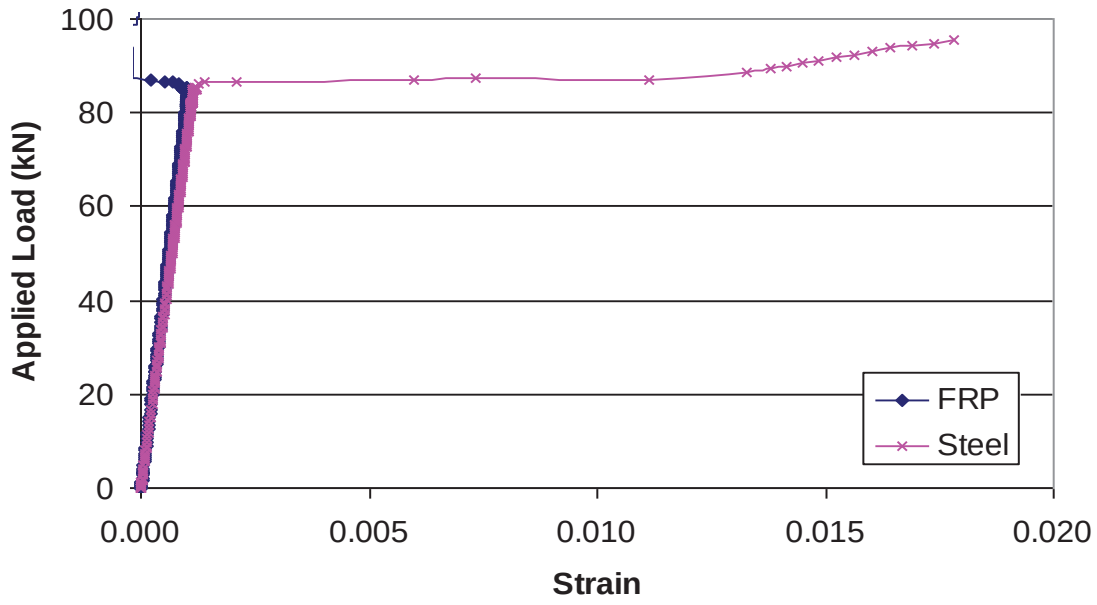

Figure 5.10 Experimental result for CW2.

5.6.3 COMPARISONS BETWEEN SPECIMENS CW1 AND CW2

Figure 5.11 shows the strain comparisons between the 40 mm and 80 mm bonded length specimens. It is clear from the graph that as the bonded length was increased, the strain difference between the steel plate and FRP becomes smaller. It is expected that as the bonded length becomes longer, the partial interaction behaviour shifted to the full interaction behaviour where there are no longer differences between the strains in the steel plate and FRP.

The other observation from this comparison is that the strains in the FRP were more affected by the change of the bonded length compare to the strains of the steel plate. As shown in the same graph, the reduction of slope for the FRP strains was bigger than that in the steel. Finally, the debonding point for both bond lengths was equal at about 86 kN. It is difficult to point the debonding mechanism, whether debonding occurs before or after steel has yielded since only one strain gauge is attached on a specific length of the bond length on the specimen. Attaching more strain gauge is not possible due to lack of spacing on

the FRP plate. A short bond length also does not show any increase of strength for the specimen.

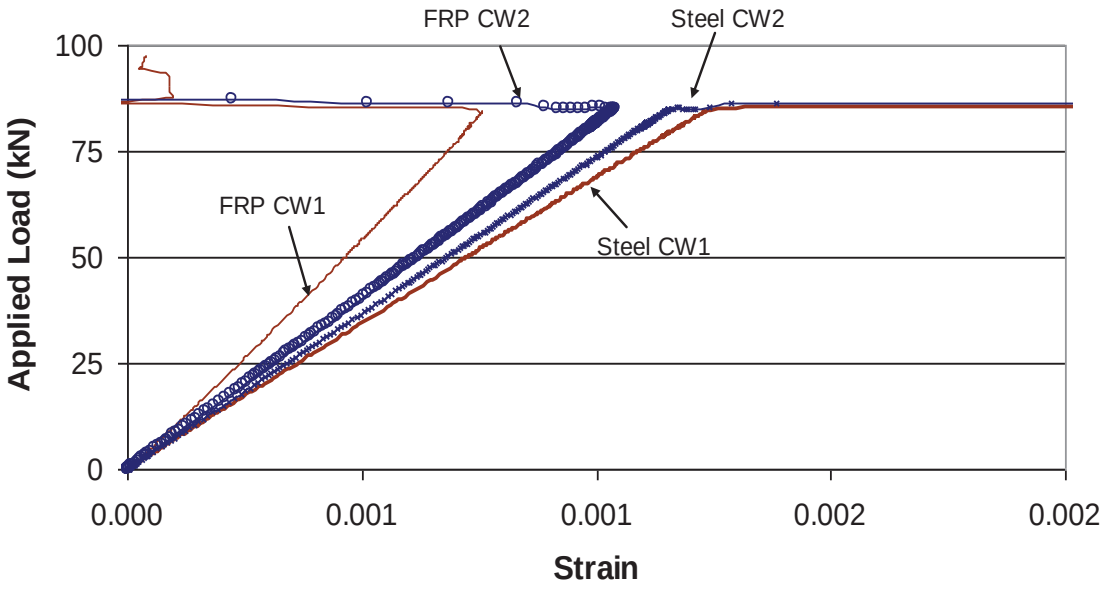

Figure 5.11 Comparison of strains between CW1 and CW2.

5.7 TEST RESULTS OF VW SPECIMENS

5.7.1 SPECIMEN VW1

Sample VW1 was bonded with a 125 mm FRP on top and bottom faces of the steel plate as shown in Figure 5.5, including all the numbering and locations of the strain gauges. Since the sample was symmetrical, the strain gauges were attached more on one side. However, the middle section was considered to be of importance hence the concentration of strain gauges attached is more.

Figure 5.12 shows the specimen at failure. The debonding failures were a mix of steel-adhesive, FRP-adhesive and FRP layer. At the top surface as shown in Figure 5.12 (a), the debonding failure occurred on the steel-adhesive layer at the middle part of the steel plate, whereas, FRP-adhesive layer failure mainly occurred close to the plate end. At the bottom surface as shown in Figure 5.12

(b), the debonding failure occurs at the steel-adhesive layer in the middle of the specimen, whereas, at the plate end debonding occurred at the FRP-adhesive and within the FRP layers as shown in Figure 5.16 (b). The FRP itself did not break. The steel plate breaks only after the FRP has been totally debonded.

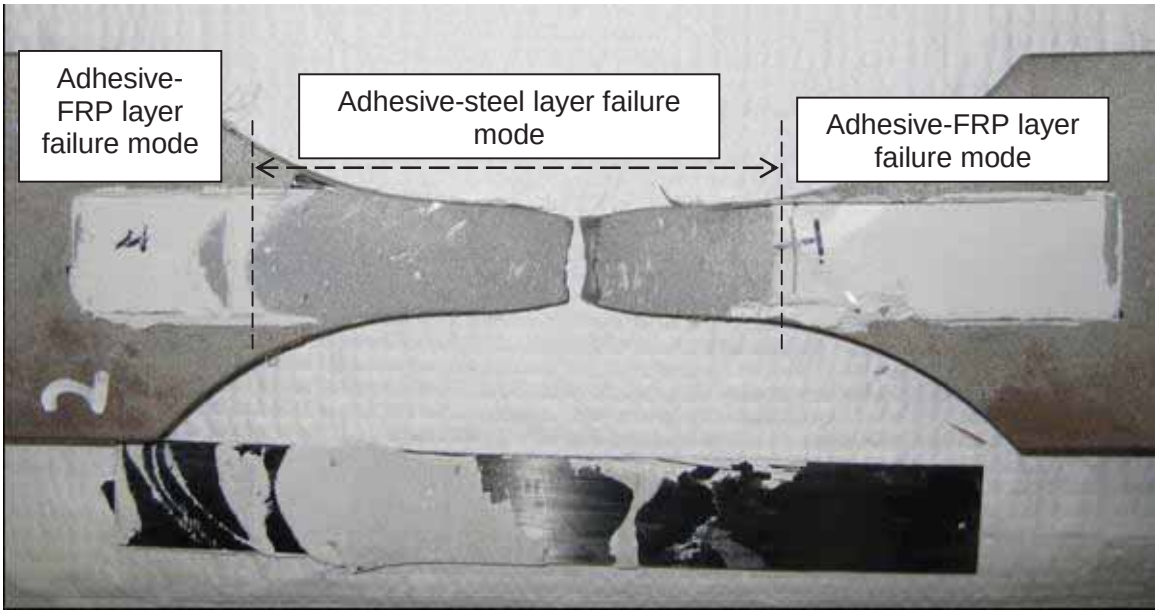

(a) top surface

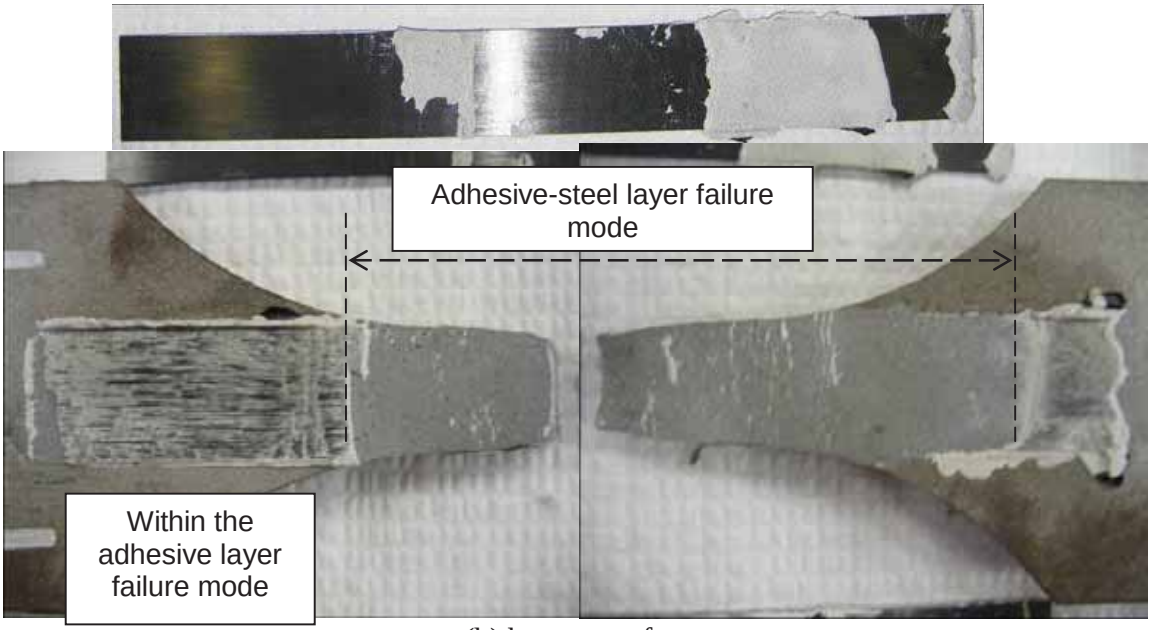

(b) bottom surface

Figure 5.12 Failure mode of VW1.

5.7.1.1 MIDDLE SECTION (0 mm)

It can be observed in Figure 5.13 that after the FRP debonded, a drop-off of the applied load occurs indicating an increase of strength when FRP was still bonded with the steel plate. After debonding, the specimen behaved as a plain steel plate. The steel yielded progressively after that to a maximum applied load of 168.5kN compare to the peak of 177 kN just before FRP debonded.

Figure 5.14 shows the experimental result of VW1 around the stage where debonding occurred. At the elastic stage, both FRP and steel strains follow the same curve indicating full interaction between the steel and FRP plates. In the inelastic range, the FRP strain was higher than the steel strain. There are three stages of behaviour for the specimen: during elastic, steel yielding and debonding as illustrated in Figure 5.14. Initially, the steel plate behaved elastically up until 158 kN of applied load with the recorded 0.001845 and 0.001991 strains on the steel and FRP plates respectively. Then the steel starts to yield until the applied load of 177 kN with the strain readings of 0.005108 and 0.004723 strains for the steel and FRP respectively. Beyond the 177 kN applied load, debonding occurred and the strength of the specimen was reduced.

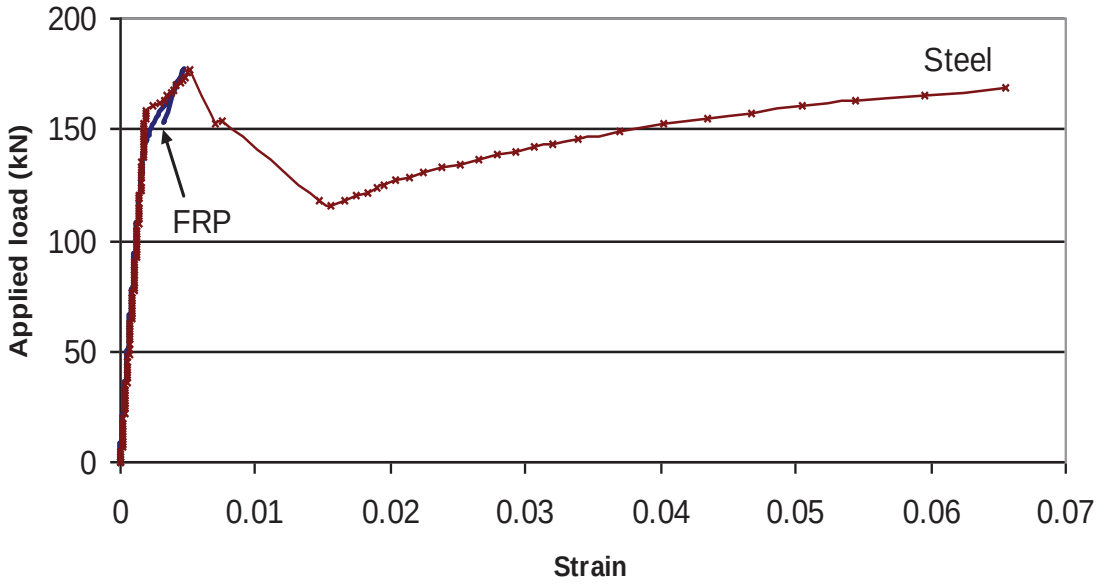

Figure 5.13 Experimental result for VW1 at 0mm.

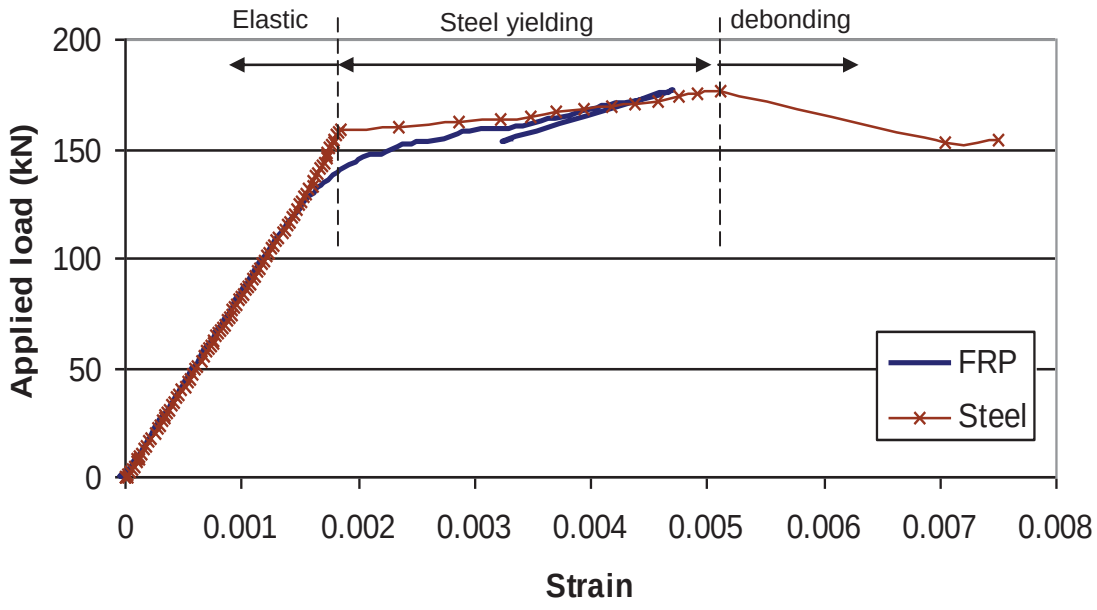

Figure 5.14 Experimental result for VW1 at 0mm at debonding.

5.7.1.2 10 mm FROM THE MIDDLE

Figure 5.15 shows the averaged strain result at 10 mm from the middle of specimen VW1. Referring to Figure 5.5, the strain results were taken from the left and right positions. An increased of strength was also observed prior to debonding. After debonding, the specimen behaved as a plain steel plate.

Figure 5.16 shows the strain results at the right position. At the elastic range, full interaction behaviour is observed. The elastic stage occurred up to the applied load of 165.1 kN with the corresponding strains of 0.001965 and 0.004526 for the steel and FRP respectively. Yielding stage starts after the 165.1 kN of applied load and continued until debonding occurred. During the stage of steel yielding and debonding, the strains in the FRP were always larger than the strain in the steel plate. Debonding occurred when the strain of the steel plate reaches 0.005181.

Figure 5.17 shows the strain results at the left position. Similar to the results obtained in the right position, full interaction behaviour is observed at the elastic range. The elastic stage occurred up to the applied load of 157.7 kN with the corresponding strains of 0.001810 and 0.003435 for the steel and FRP respectively. Yielding stage starts after the 165.1 kN of applied load and continued until debonding occurred. Similar to the right position during the stage of steel yielding and debonding, the strains in the FRP were always larger than the strain in the steel plate. Debonding occurred when the steel plate reaches 0.004206 of strain.

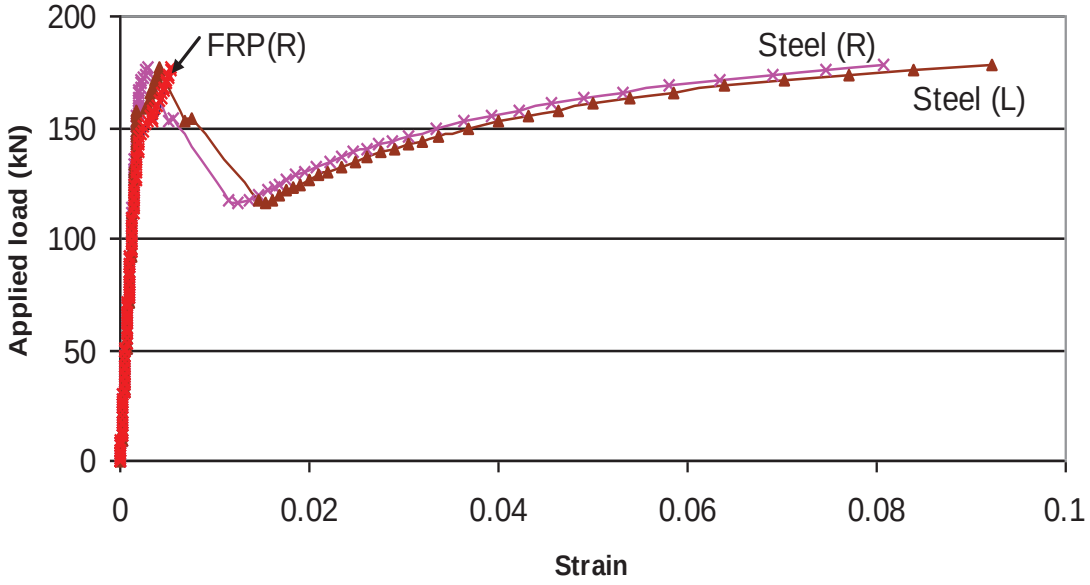

Figure 5.15 Experimental result for VW1 at 10mm from the middle

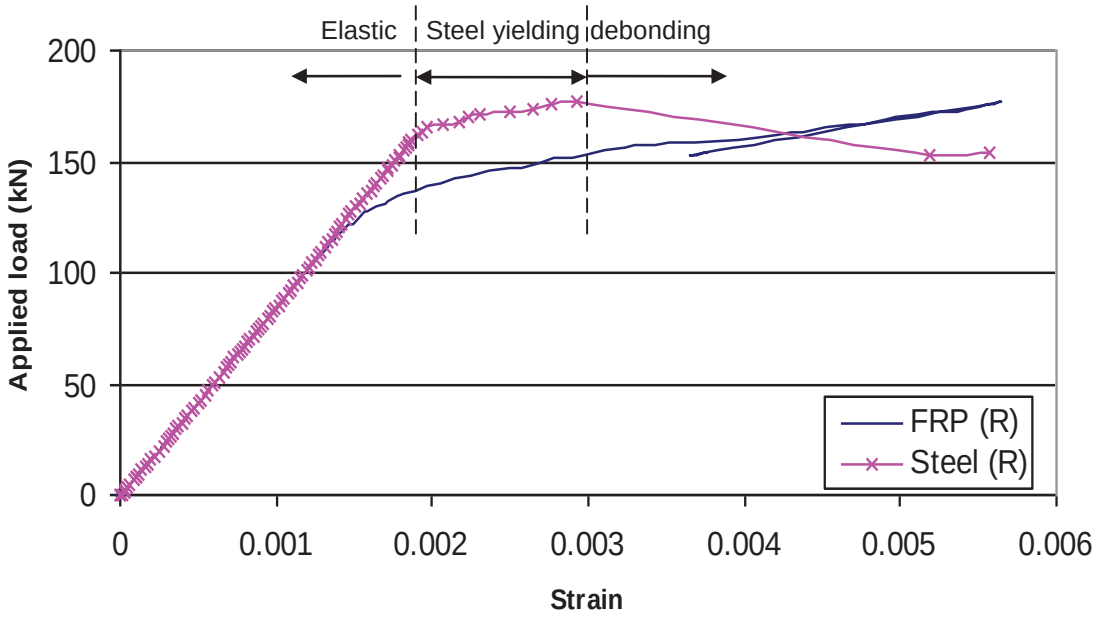

Figure 5.16 Experimental result for VW1 at 10mm from the middle at debonding (right)

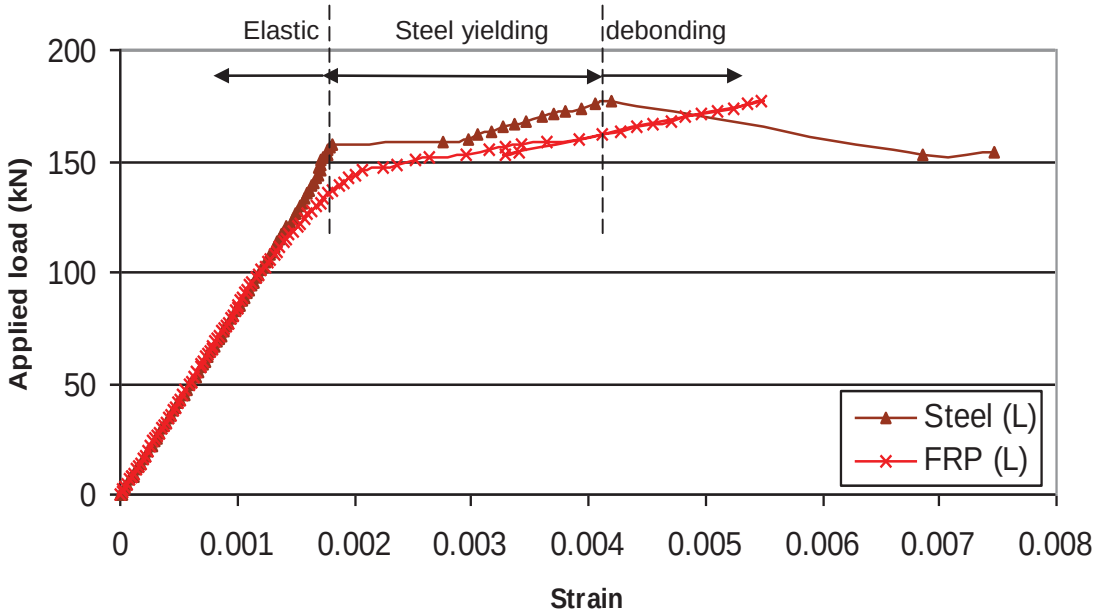

Figure 5.17 Experimental result for VW1 at 10mm from the middle at debonding (left)

5.7.1.3 80 mm AND 110 mm FROM THE MIDDLE

Figure 5.18 and Figure 5.19 show the strain result for sample VW1 at 80 mm and 110 mm from the middle section respectively. It is obvious that the steel has not yielded at these sections. At 80 mm, full interaction was observed until the load of 100 kN when the FRP strain becomes larger than the steel strain. The recorded strain of steel at debonding was 0.001162 with the applied load of 175.5 kN. However, at 110 mm, there is a large variation on the strains which may caused by experimental error.

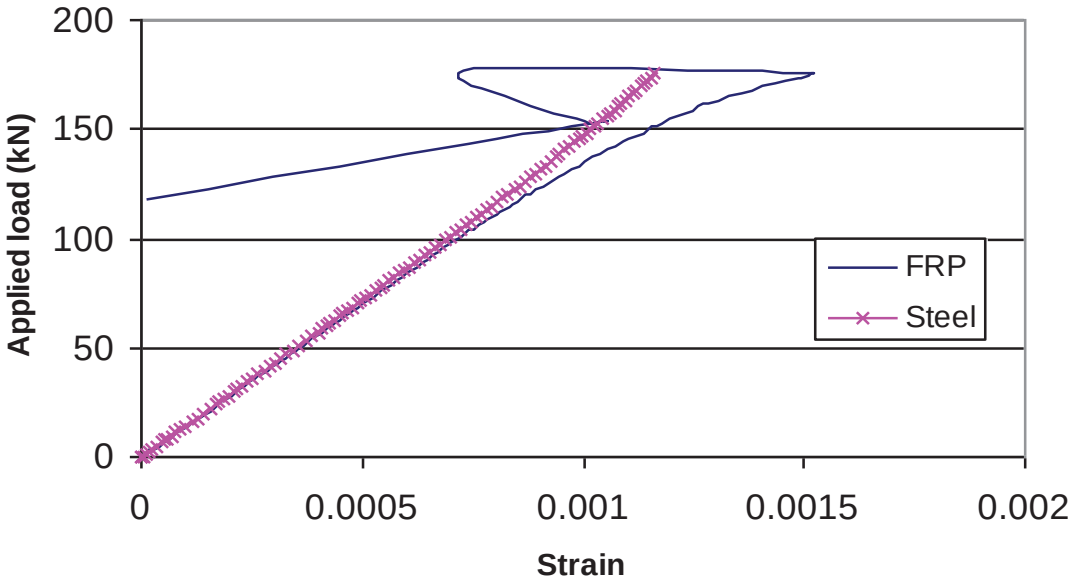

Figure 5.18 Experimental result for VW1 at 80mm from the middle at debonding

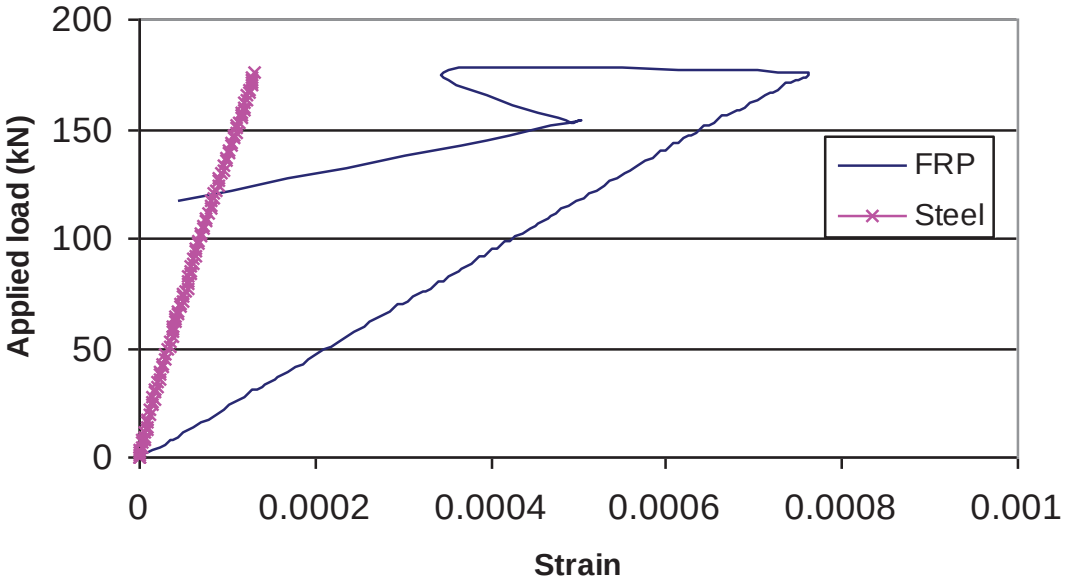

Figure 5.19 Experimental result for VW1 at 110mm from the middle at debonding

5.7.1.4 STRAINS ACROSS THE BOND LENGTH

Figure 5.20 shows the strain distributions of steel and FRP plates at three different stages described in Section 5.7.1.1. At the elastic stage, the strain for the steel was in the elastic range throughout the bonded length. The values of the FRP strain at this stage were close to the values of the steel strain which indicates full interaction behaviour. The yielding strain of the steel plate is 0.00152 as stated in Table 5.2.

At the steel yielding stage, the steel has yielded 70 mm towards the bonded length. In comparison from the FRP strain results of the same stage, there was a jump of strains between the 10 mm and 80 mm of the bond length. Finally at the debonding stage as shown in Figure 5.20 (c), there was a huge jump in the strain of the steel compared to the previous stages. The steel plate has yielded up to 80 mm of the bond length.

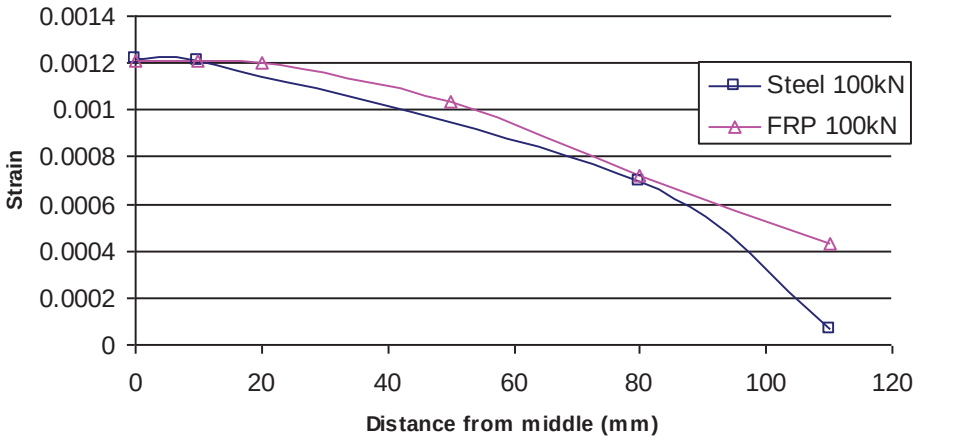

(a) elastic

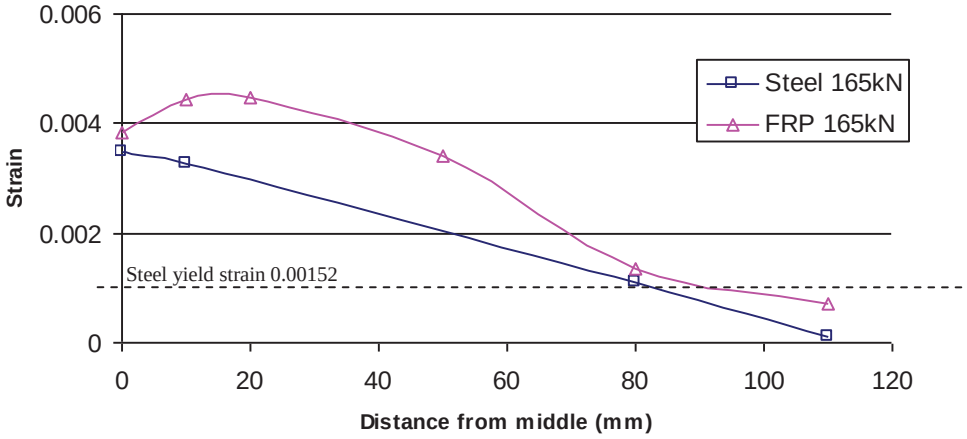

(b) steel yielding

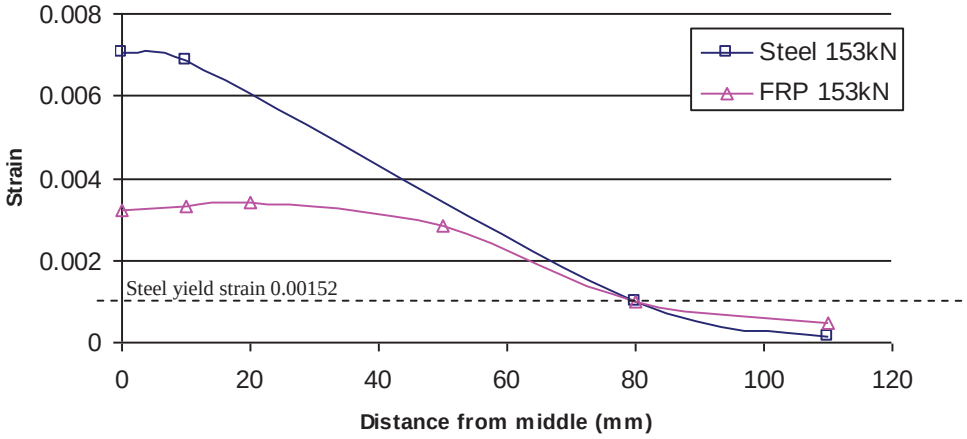

(c) debonding

Figure 5.20 Strains across the bonded length at different stages (VW1).

5.7.2 SPECIMEN VW2

Sample VW2 was bonded with two layers of 125 mm FRP on top and bottom faces of the steel plate. The rest of the experimental setup was the same as in sample VW1. Figure 5.21 shows the specimen at failure. At the top surface as shown in Figure 5.21 (a), the debonding failure occurred on the steel-adhesive layer at the middle part of the steel plate, whereas, FRP-adhesive layer failure mainly occurred close to the plate end. At the bottom surface, debonding failure occurs at the steel-adhesive layer in the middle of the specimen whereas part of the FRP plate is still bonded to the steel plate as shown in Figure 5.21 (b). The FRP plate at the top surface debonded at the load of approximately 175 kN. However, the FRP plate at the bottom surface was still glued onto the steel plate when the steel plate broke.

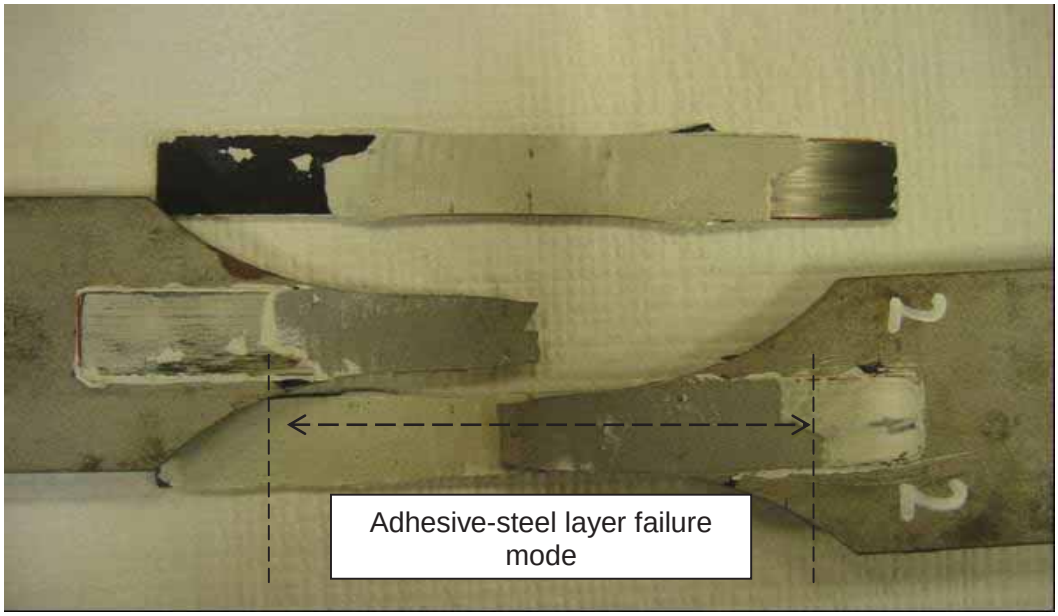

(a) top surface

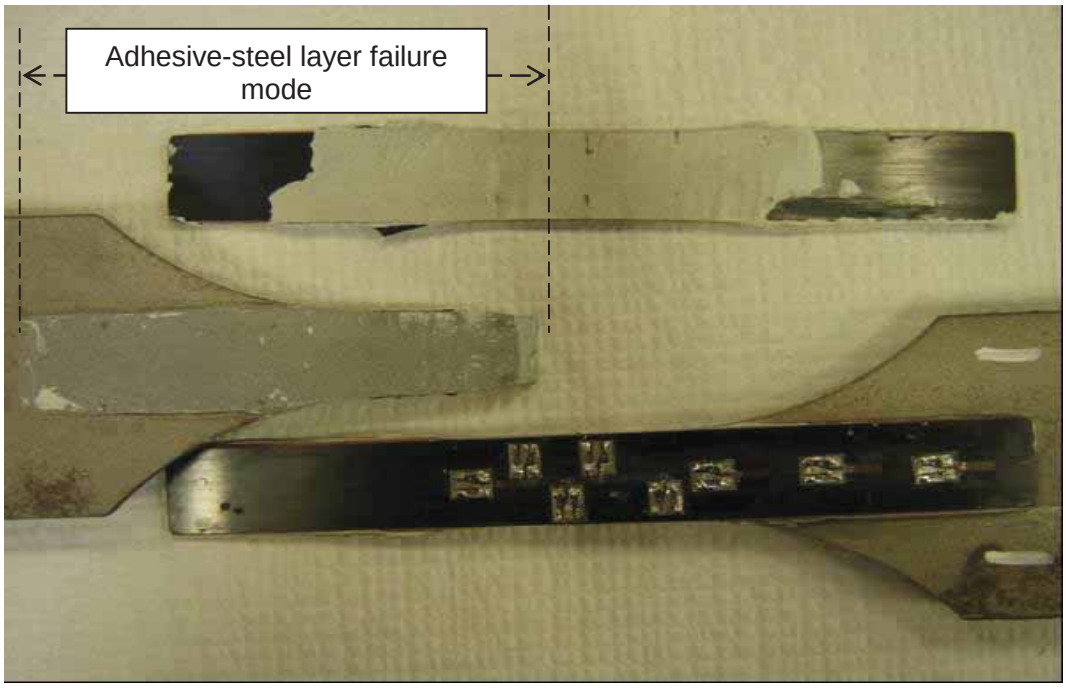

(b) bottom surface

Figure 5.21 Failure mode of VW2.

5.7.2.1 MIDDLE SECTION (0 mm)

The experimental result is shown in Figure 5.22. Similar to the trend observed in VW1, the steel yielded as soon as the FRP debonded. The peak load prior to debonding was 177.1kN. Then a drop of the applied load occurred to 115 kN after which the steel yielded progressively after that to a maximum applied load of 173.5kN. This indicates an increase of strength of the steel in the linear range when FRP was still bonded to the steel plate.

Figure 5.23 shows the load-strain result at debonding which shows the same three stages of behaviour observed in specimen VW1. At a lower load, the strain in the FRP was relatively smaller than the strain in the steel. Steel yielded at 0.001738 strain with the corresponding strain in the FRP of 0.001586. However at debonding, the strain in the FRP was higher than the strain in the steel. The difference in strains indicates the partial interaction behaviour of the specimen. Debonding occurred at 177.1 kN of applied load with the corresponding strains of 0.003634 and 0.002476 for the steel and FRP plates respectively.

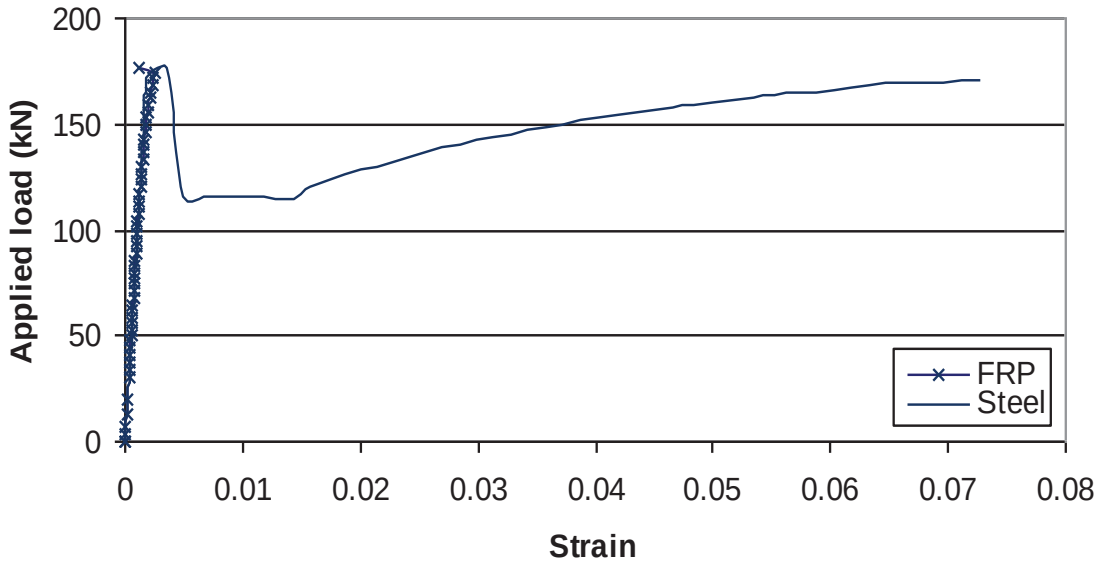

Figure 5.22 Experimental result for VW2 at 0mm.

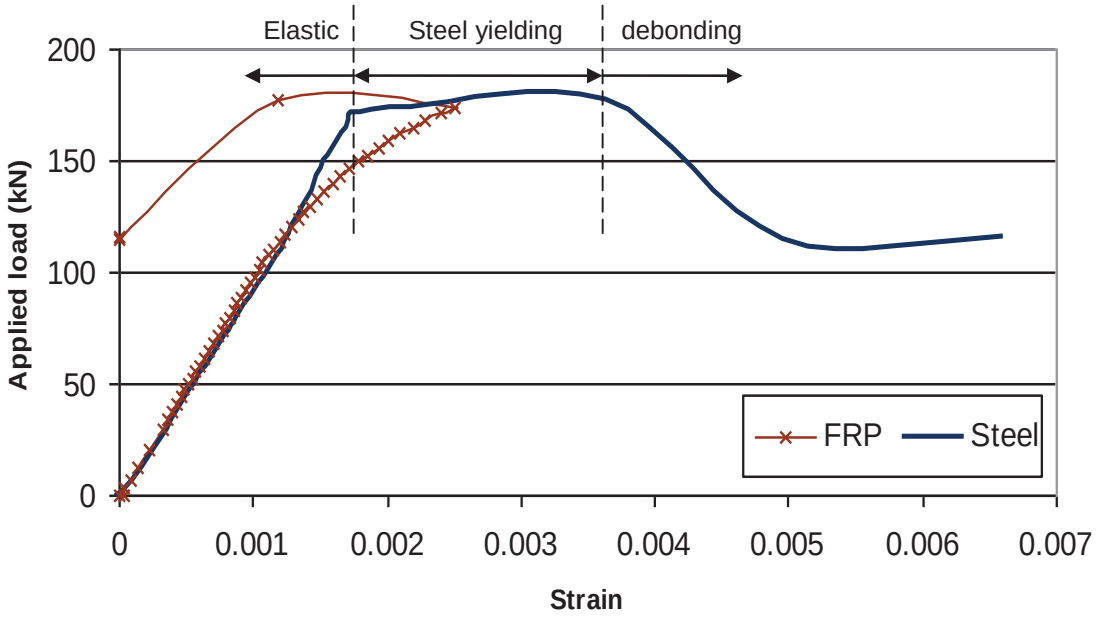

Figure 5.23 Experimental result for VW2 at 0mm at debonding.

5.7.2.2 10 mm FROM THE MIDDLE

Figure 5.24 shows the strain result at 10 mm from the middle. The elastic strength of the steel was significantly increased as indicated by the load drop off after debonding. As soon as the FRP debonded, the steel yielded. The peak applied load at the elastic range was at approximately 175 kN for both sides of the specimen. Load drop-off occurred after debonding to about 115 kN before increasing again as a result of strain hardening to a peak of 181.8 kN.

The strain result at the debonding stage is shown in Figure 5.25 for strain gauges glued at the right side of the specimen. Debonding occurred at an applied load of 174.2 kN with the corresponding strains of 0.002726 and 0.002025 for the steel and FRP plates respectively.

Figure 5.26 shows the strain results at the left side of the specimen. Debonding is more abrupt compared to the right side as indicated by the sudden

load drop-off. Debonding occurred at an applied load of 174.2 kN with the corresponding strains of 0.001732 and 0.002522 for the steel and FRP plates respectively.

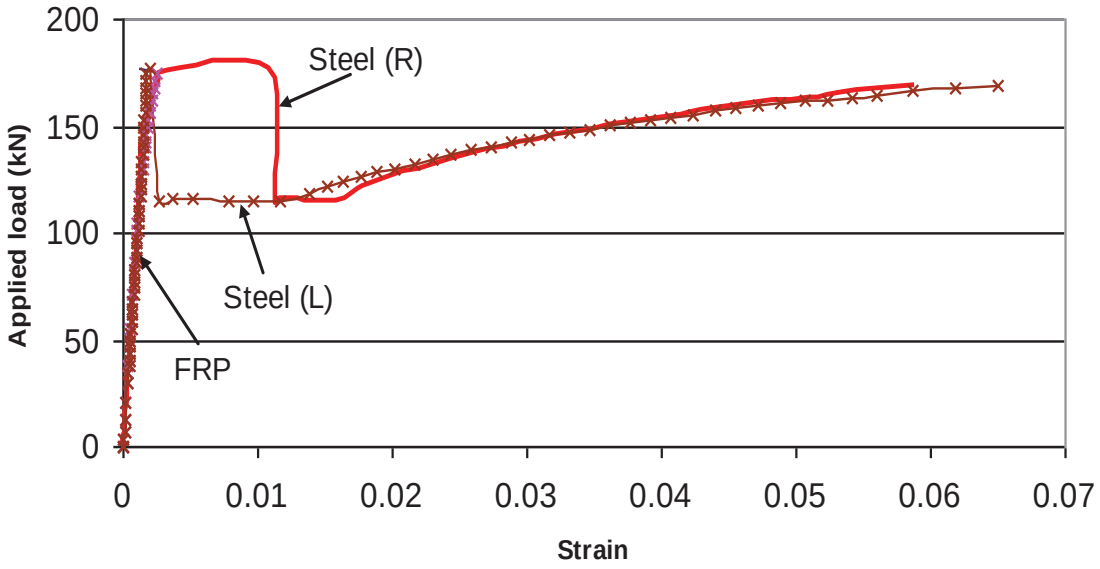

Figure 5.24 Experimental result for VW2 at 10mm.

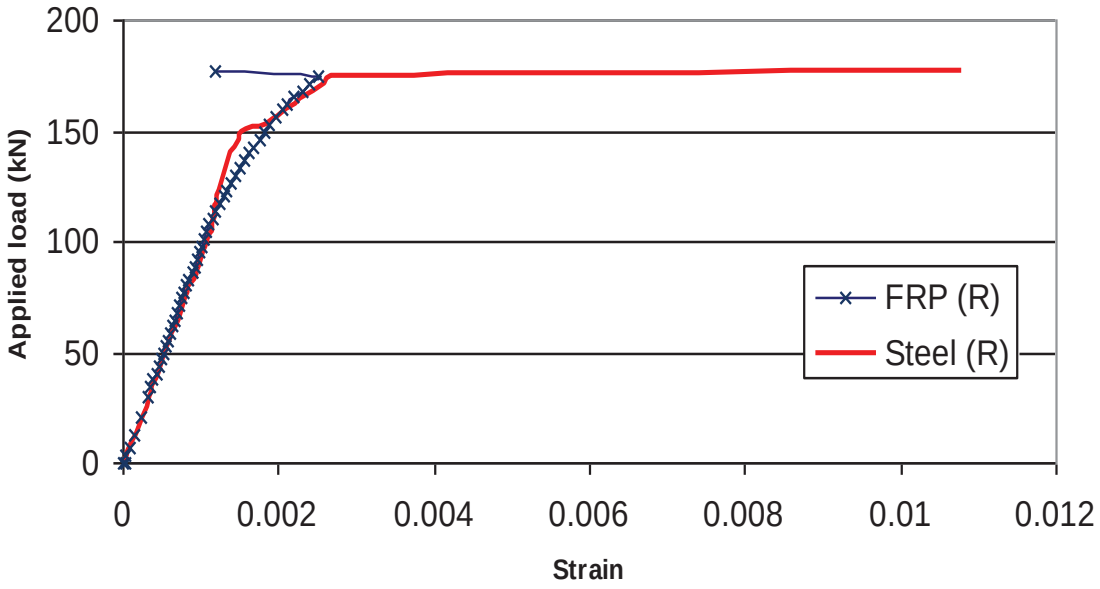

Figure 5.25 Experimental result for VW2 at 10mm at debonding (right).

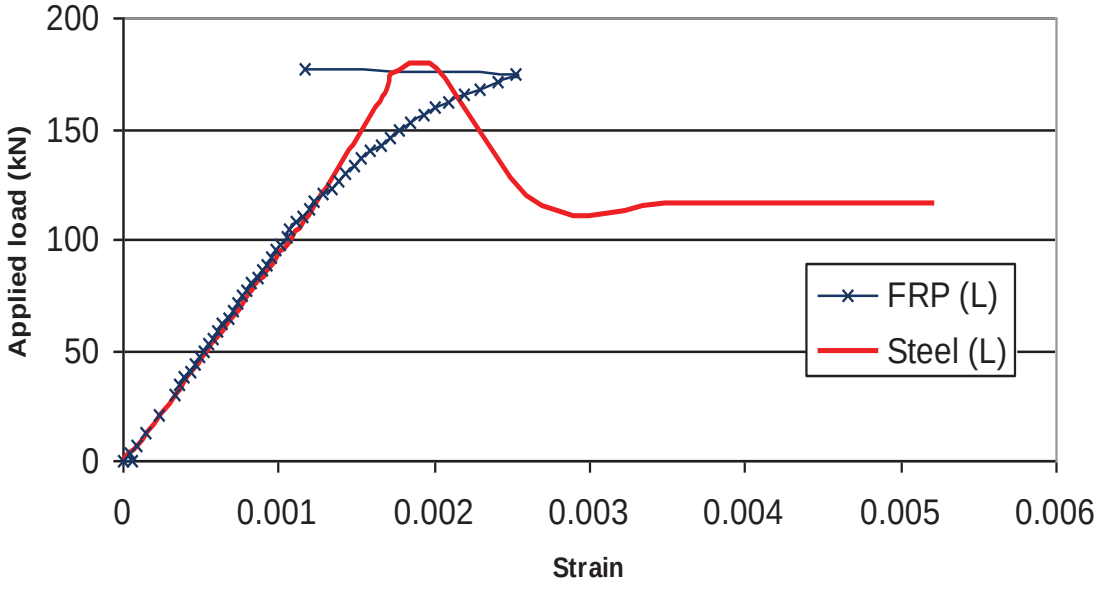

Figure 5.26 Experimental result for VW2 at 10mm at debonding (left).

5.7.2.3 80 mm AND 110 mm FROM THE MIDDLE

Figure 5.27 and Figure 5.28 shows the load-strain results at 80 mm and 110 mm from the middle respectively. Obviously, experimental error may have occurred at the 110 mm strain gauge. According to the strain reading at 80 mm, full interaction behaviour was observed at the lower load level until the applied load reached 101.2 kN. Debonding occurred at the applied load of 174.2 kN with the corresponding strain reading of 0.001099 and 0.000911 for the steel and FRP plates respectively.

There are a few possible errors that may occur during the preparation of the surface where the strain gauges are to be glued. For example, when applying the strain gauges, the surfaces of the steel/FRP plates were not smoothed properly. Another possibility is when using solvent to remove the dirt from the surfaces, the solvent must be fully removed and strain gauges must be applied immediately. For both examples provided above, the bond between the strain gauges to the surfaces it attached may be weakened, hence the errors in the strain reading as shown in Figure 5.18, Figure 5.19, Figure 5.27 and Figure 5.28.

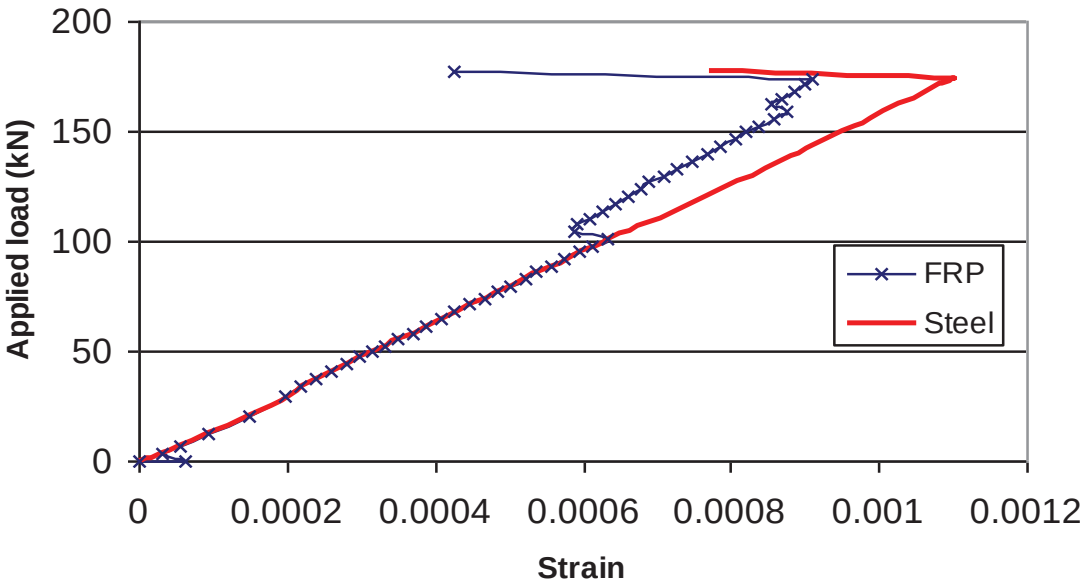

Figure 5.27 Experimental result for VW2 at 80mm at debonding.

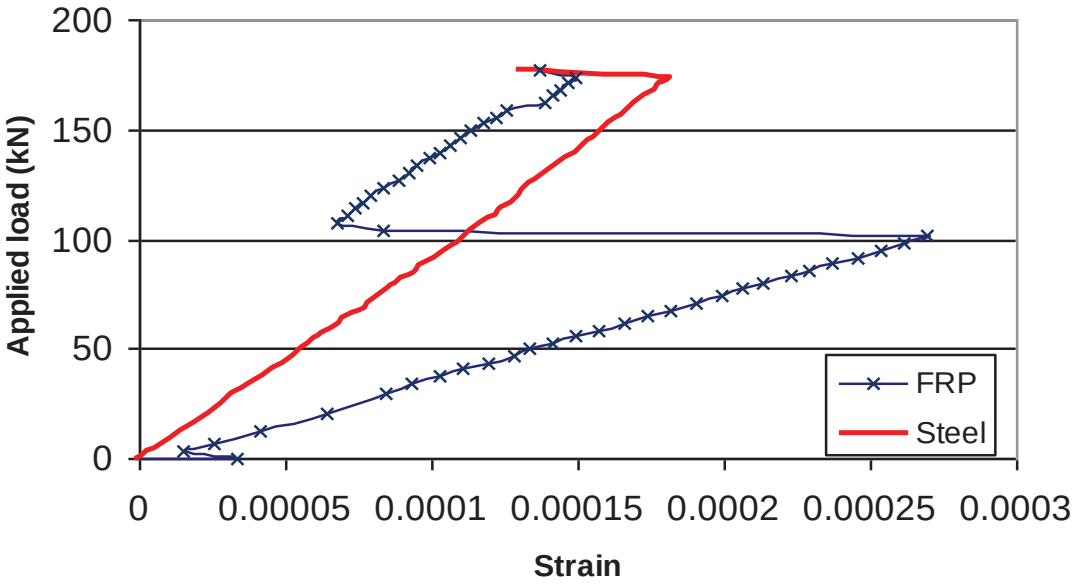

Figure 5.28 Experimental result for VW2 at 110mm at debonding.

5.7.2.4 STRAINS ALONG THE BOND LENGTH

Figure 5.29 shows the strain distributions of steel and FRP plates at three different behavioural stages. At the elastic stage, the strain for the steel was in the elastic range throughout the bonded length, which is similar to the behaviour of specimen VW1. The strain of the steel at the middle is 0.001110 compared to 0.001041 for the FRP strain. At the plate end, the strain in the steel is 0.000111 compared to 0.000269 for the FRP strain.

At the steel yielding stage, the steel has yielded 40 mm along the bonded length. It is observed that instead of the FRP strains that were larger in values along the bonded length in specimen VW1, the strain in the steel was larger in specimen VW2. This inconsistency may be the result of experimental error. At the middle section, the strain of the steel is 0.003633 compare to 0.001185 for the FRP strain. At the plate end, the strain in the steel is 0.000129 compare to 0.000137 for the FRP strain.

Finally at the debonding stage as shown in Figure 5.29 (c), there was a huge jump in the strain of the steel compared to the previous stages. The FRP has debonded totally from the steel plate as indicated by the zero values of the FRP strains. The steel plate has yielded up to 80 mm of the bond length. The strain of the steel at the middle is 0.004965 compare to 0.000127 at the plate end.

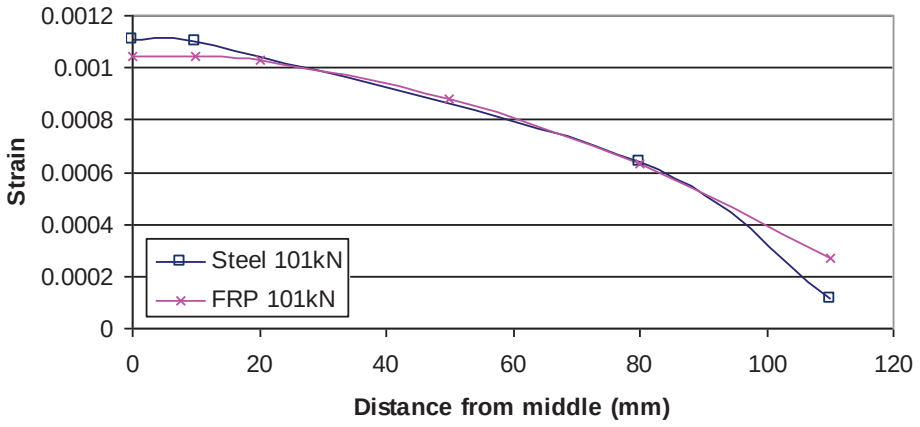

(a) elastic

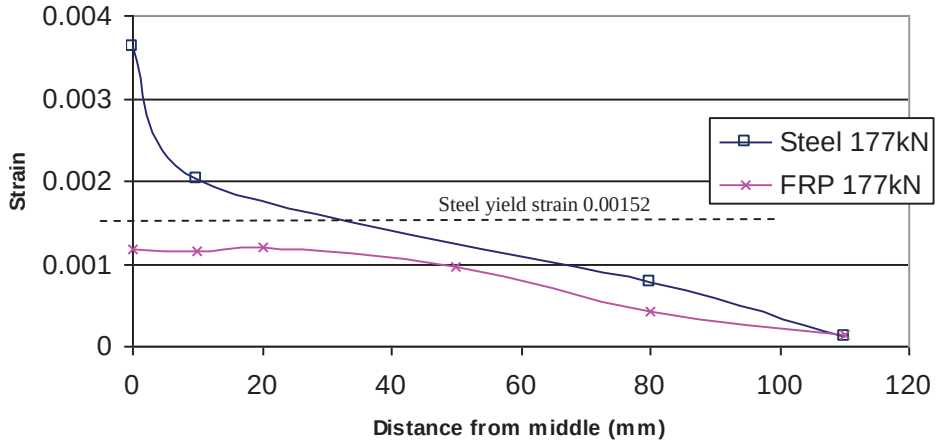

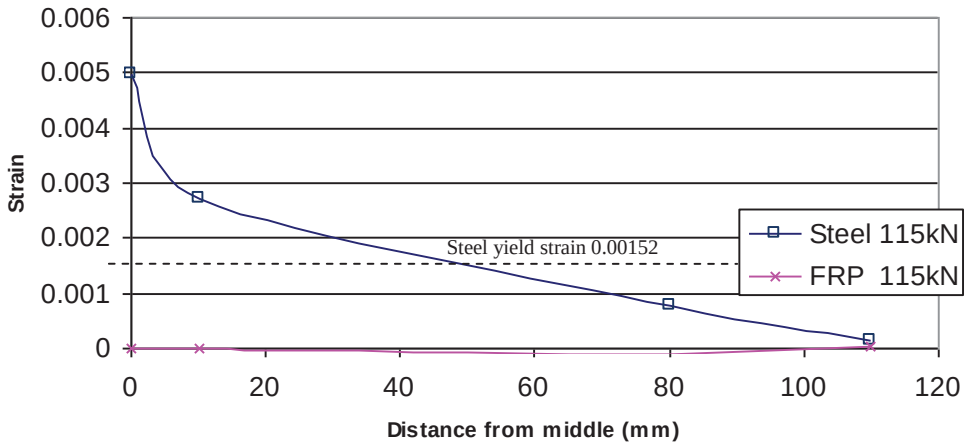

(c) debonding

Figure 5.29 Strains across the bonded length at different stages (VW2).

5.8 CONCLUSIONS

A total of 4 pull tests were conducted in this chapter. The test consists of FRP plates glued on steel plates with varying geometry. The first set of steel plates consisted of constant width (CW) plates to investigate the partial interaction behaviour at different bond lengths. The second set of specimens were steel plates with varying width (VW) to allow steel yielding at the centre to investigate the effect of debonding at steel yielding.

The conclusions from these tests are:

- For the CW test results, the strain difference indicating partial interaction behaviour reduces as the bond length is increased.
- The FRP strain is always lower than the steel strain at any applied load in the CW results.
- For VW test results, the strength of the specimen was increased while FRP is still bonded to the steel plate.
- Two distinct failure modes were observed in the VW specimens. At the middle section, debonding occurred at the steel-adhesive layer. At the plate end, debonding occurred either at the FRP-adhesive or within the FRP layers.
- The strain in the FRP was always lower than the strain in the FRP at the elastic range. However prior to debonding, the strain in the FRP is higher.
- It is difficult to observe the debonding mechanism experimentally since debonding can occur at either the middle or end of the FRP plate although initially debonding initiation starts at the plate end.

CHAPTER 6: ANALYSIS OF THE DEBONDING MECHANISM IN FRP PLATED STEEL MEMBERS

6.1 INTRODUCTION

In this chapter, numerical analyses were carried out to investigate the debonding mechanisms of FRP plated steel members based on the experimental works conducted in Chapter 5. This numerical method was then compared with the experimental and FEM results conducted by Al-Emrani and Kliger (2006). At the end of this chapter, the debonding mechanisms in FRP plated steel members based on these experimental and numerical works are discussed.

6.2 PARTIAL-INTERACTION NUMERICAL METHODS FOR STEEL DUE TO AXIAL FORCE ONLY

The following section will explain how the theory is developed and integrated into the numerical method. It is based on a steel plate glued with FRP as in the experiments conducted in Chapter 5. Theoretically, the debonding mechanisms obtained from this analysis, simulate the failure mode of a steel beam glued with FRP plate (Al-Emrani and Kliger 2006).

6.2.1 MATERIAL PROPERTIES

The bilinear bond-slip characteristic for the glue is taken from Chapter 4 and integrated into the numerical method. The idealised stress-strain relationship of steel and FRP is shown in Figure 6.1 which allows nonlinearity in the steel plate was used in the numerical method to simplify the mathematical function used in the computer programming.

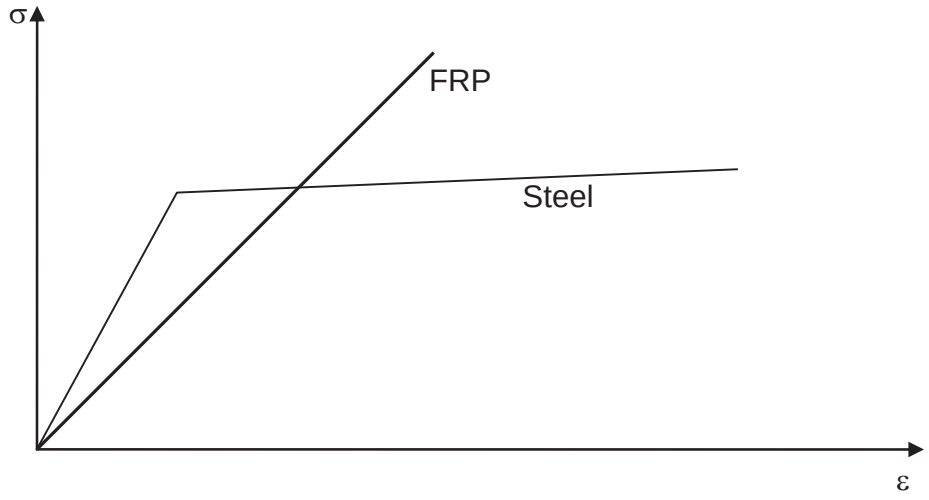

Figure 6.1 Stress-strain relationship of steel and FRP

6.2.2 THE FORCES IN THE STEEL PLATE AND FRP

The differences of strain between the steel and FRP due to an applied force develops a change of slip. According to the local τ-δ relationship, the bond stress increased or reduced. The bond force developed, which is a direct presentation of the bond stress, will affect the distribution of the steel and FRP forces. The relationship between these forces; steel, FRP and bond was integrated in the numerical method. Graphically, the change in the forces of steel and FRP plates in the numerical method is shown in Figure 6.2. Consider an element of steel, FRP and adhesive as shown in Figure 6.2. As load is applied, the forces of steel and FRP at the middle section; $(P_s)_0$ and $(P_p)_0$ can be calculated. The shear reaction of the adhesive is such that it will increase the force in the steel and decrease the force in the FRP on subsequent element as shown in Figure 6.2.

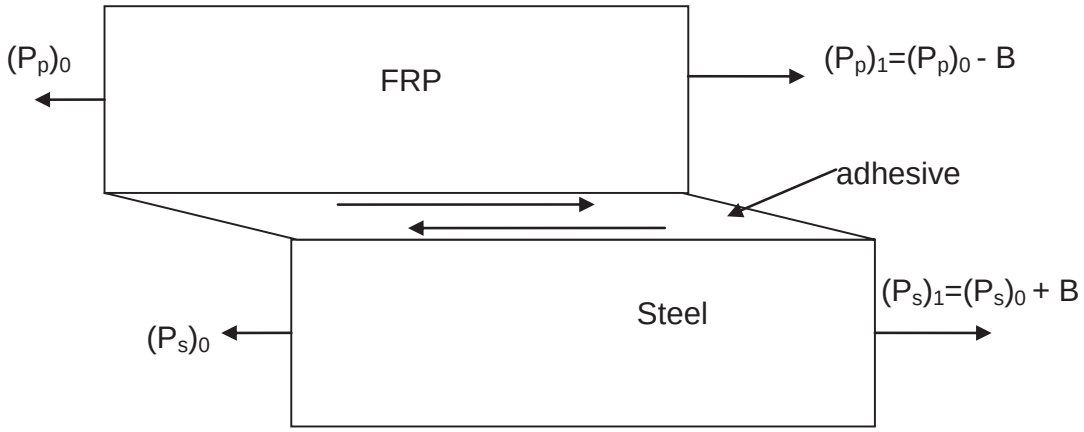

Figure 6.2 Forces in steel and FRP

6.2.3 BOUNDARY CONDITION σ_p=0 AT THE END OF THE FRP PLATE

At the end of the FRP plate, the stress of the plate σ_p is 0. The force in the FRP must always reduce to 0 as it reaches the plate end. At the same time, the force in the steel keeps increasing all the time. The distribution of the steel and FRP strains, ε_s and ε_p respectively are shown graphically in Figure 6.3.

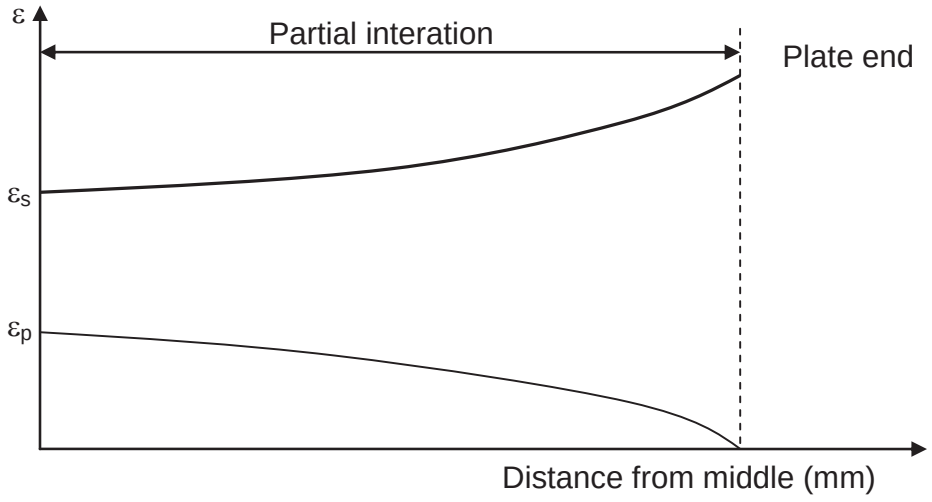

Figure 6.3 Strain distribution of steel and FRP

6.2.4 BOUNDARY CONDITION ds/dx=s=0 ALONG THE FRP PLATE

Another boundary condition can be established if the geometry of the steel plate is varied at the middle section. For example if a tapered steel plate is considered with the smaller geometry at the centre compare to at the end (as shown in Figure 5.2), then higher stress will occur at the centre plate when the steel plate yields. The distribution of strains,ε, slipstrain, *ds/dx*, and slip, *s*, are shown in Figure 6.4. The point where *ds/dx=s=0* occur at the same point is the boundary condition. The area enclosed by the boundary condition is experiencing partial interaction whereas the area beyond that is experiencing full interaction.

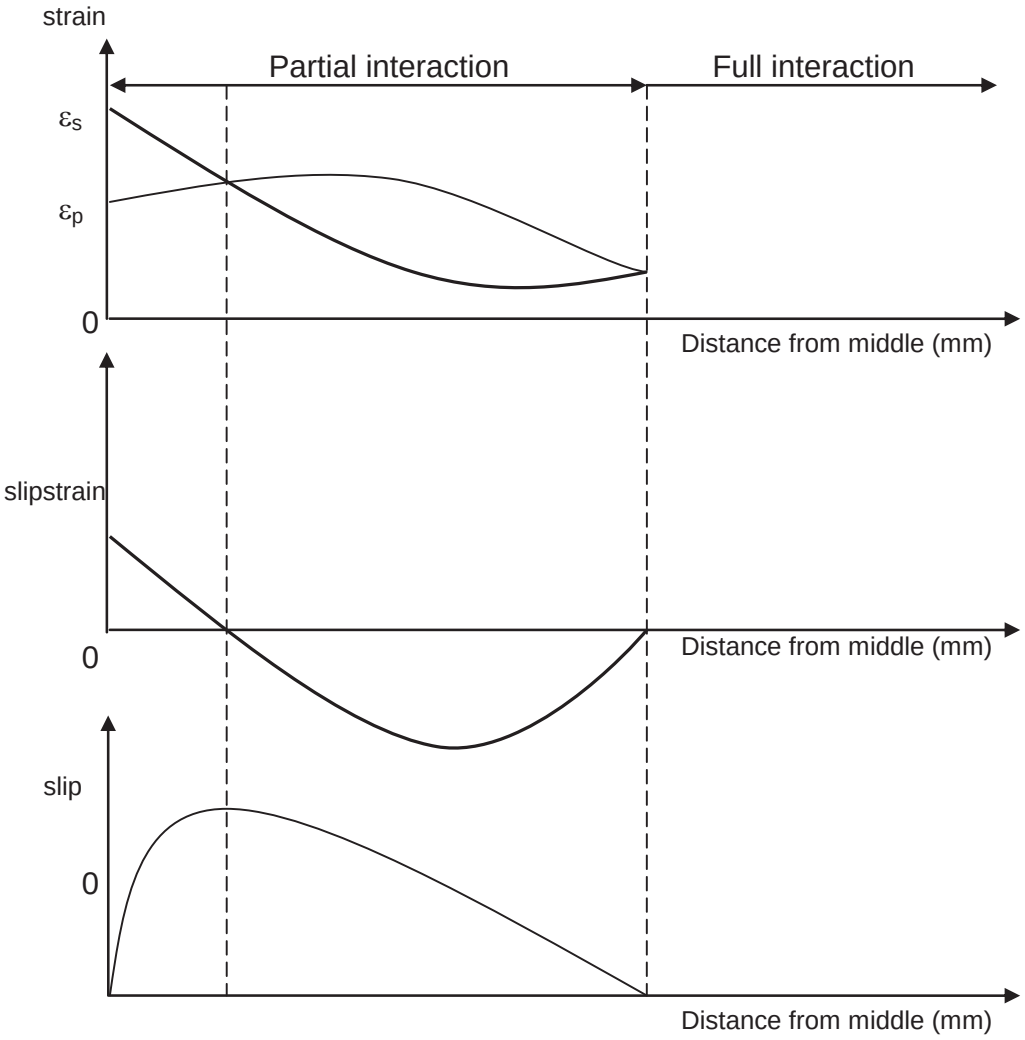

Figure 6.4 Strain, slipstrain and slip distributions of FRP plated steel member

6.2.5 PARTIAL-INTERACTION NUMERICAL METHOD FOR DEBONDING MECHANISM

Consider a sample of steel plate with a constant width glued with FRP as shown in Figure 6.5 (a). Due to symmetry, the sample can be idealised as in Figure 6.5 (b). Only half of the length is taken into consideration. The idealisation is developed to accommodate any local τ-σ relationship, failure plane (L_{per}), bonded length (L_p), cross section of the steel (A_s) and FRP (A_p) and stress-strain profile of the steel plate and FRP. The numerical methods are as follows:

- Strain of steel is fixed at the middle $\varepsilon_s(0)$ and the strain of FRP is guessed $\varepsilon_p(0)$.
- According to the stress-strain profile of the steel and FRP, the load at the centre, $P_s(0)$ and $P_p(0)$ are calculated.
- The load in the steel and FRP are calculated at the end of the first segment : $P_s(0) = \varepsilon_s E_s t_s L_{per}$ and $P_p(0) = \varepsilon_p E_p t_p b_p$
- Due to symmetry at the centre, slip at this section is zero.
- The assumed slip at the centre corresponds to the local slip over the first segment length. Corresponding to this assumed slip, $\delta(0)$, the bond stress, $\tau(0)$, acting over the first segment length is calculated according to the local τ–δ relationship assumed.
- The bond force acting on the first segment is $B(0) = \tau(0) d_x b_b$.
- The load in the steel and FRP is calculated at the end of the first segment : $P_s(1) = P_s(0) + B(0)$ and $P_p(1) = P_p(0) - B(0)$,
- The corresponding strain for the steel and FRP are calculated: $\varepsilon_s(1) = \dfrac{P_s(1)}{(A_s E_s)}$ and $\varepsilon_p(1) = \dfrac{P_p(1)}{(A_p E_p)}$
- The slip strain is calculated: $\dfrac{ds(0)}{dx} = \varepsilon_s(0) - \varepsilon_p(0)$

- The change in slip over the first segment length is calculated by integrating the slip strain over the segment length: $\Delta s(0) = \int \frac{ds(0)}{dx} dx$.
- According to the change in slip over the segment length, the slip at the beginning of the second segment is calculated: $\delta(1) = \delta(0) - \Delta s(0)$.
- According to this slip the bond force acting over the second segment is calculated, with the numerical process repeating itself over the subsequent segments.
- If the boundary condition is not met, then change the assumed $\varepsilon_p(0)$.
- If the boundary condition is met, then increase the fixed $\varepsilon_s(0)$.

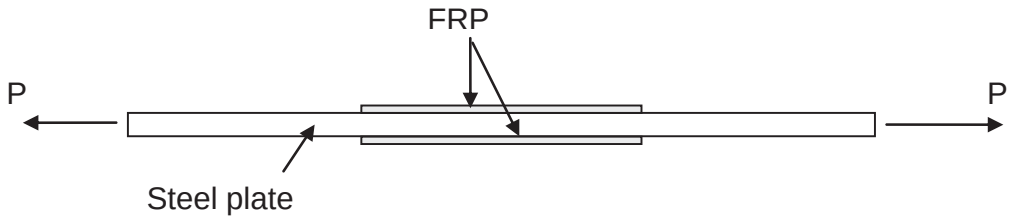

(a) laboratory specimen

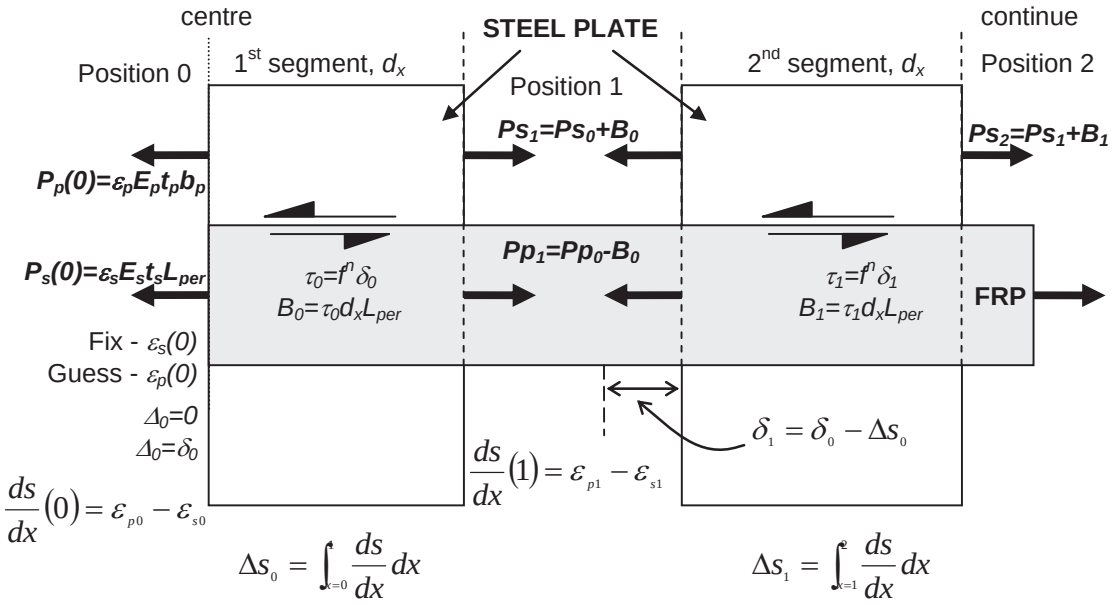

(b) numerical idealisation

Figure 6.5 Graphical representation of the numerical analysis for FRP plated steel members

6.3 DEBONDING MECHANISM

The debonding mechanism at the plate end and between the plate ends due to the yielding of steel are explained in the following sections.

6.3.1 PLATE END DEBONDING

For the purpose of demonstrating plate end debonding, the following analyses were conducted at a range where the steel was in the linear elastic range at an applied load of 50 kN. Consider a constant width steel plate glued with FRP plate as shown in Figure 5.1. By varying the FRP bonded length, the strain distribution of steel and FRP plates are shown in Figure 6.6. At a 20 mm bond length, the difference between the strains at the middle of the specimen was the largest compared to 120 mm bond length. As the bond length increases, the differences between the strains at the middle reduced.

The slip-strain distribution, which is the difference of the two strains in Figure 6.6, is shown in Figure 6.7. It shows that the slip-strain value at the middle of the specimen reduces to zero as the bond length is increased. The slip-strain values increased towards the plate end. Corresponding to the slip-strain distribution, the slip distribution can also be seen in Figure 6.8. The slip starts zero at the middle and increases as the slip-strain increases.

It is important to note that two conditions of the steel affect the behaviour of the FRP plated steel member. First, when the steel was at the linear elastic range and second, when the steel has yielded. As demonstrated earlier when the steel was in the linear elastic range, plate end debonding will occur.

For the FRP plated steel member with constant width throughout the length, the weakest point was at plate end hence yielding will occur here first. At steel yielding, the strain of the steel increased rapidly compare to the strain of the FRP. Corresponding to this, the slip-strain and slip will also increased rapidly and eventually debonding will occur first at the plate end. Hence, the trend provided by the strain, slip-strain and slip distributions for the FRP plated steel member

with a constant width, regardless whether the steel has yielded or not, shows that debonding will occur at the plate end.

Figure 6.6 to Figure 6.8 also show that at any point along the bonded length, the boundary condition *s=ds/dx=0* can never be found. The only boundary condition that can be found was when the FRP stress, σ_p, at the plate end is zero as shown in Figure 6.6 (the FRP strain converted to stress will also gives zero at the plate end). It is also important to note that the starting value of ε_s was always bigger than ε_p at the middle of the section in the numerical method so that the boundary condition σ_p=0 can be met.

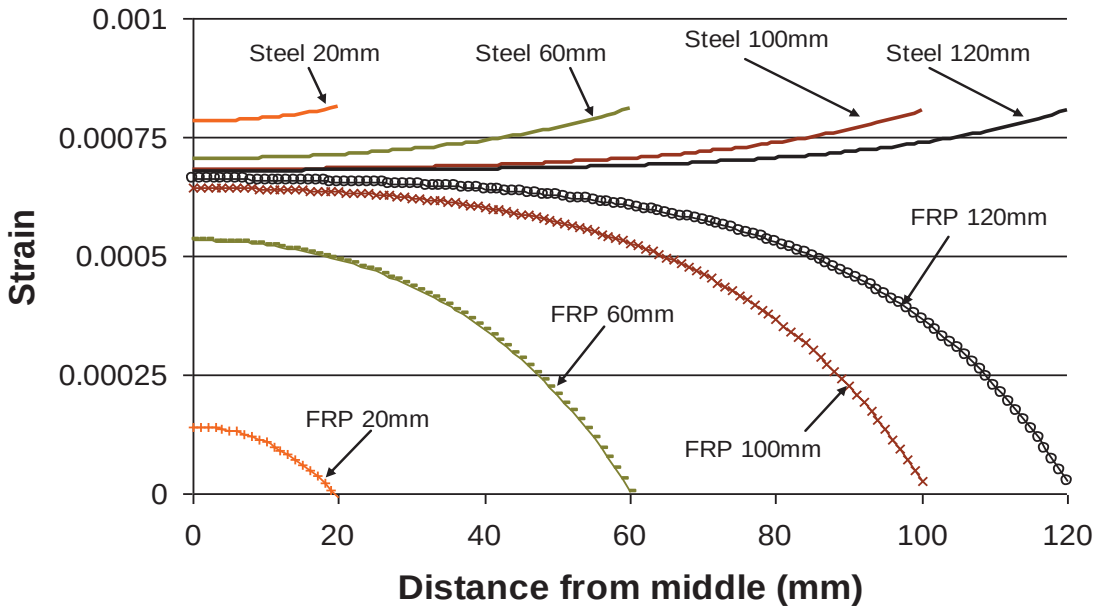

Figure 6.6 Strain distribution of steel and FRP for plate end debonding.

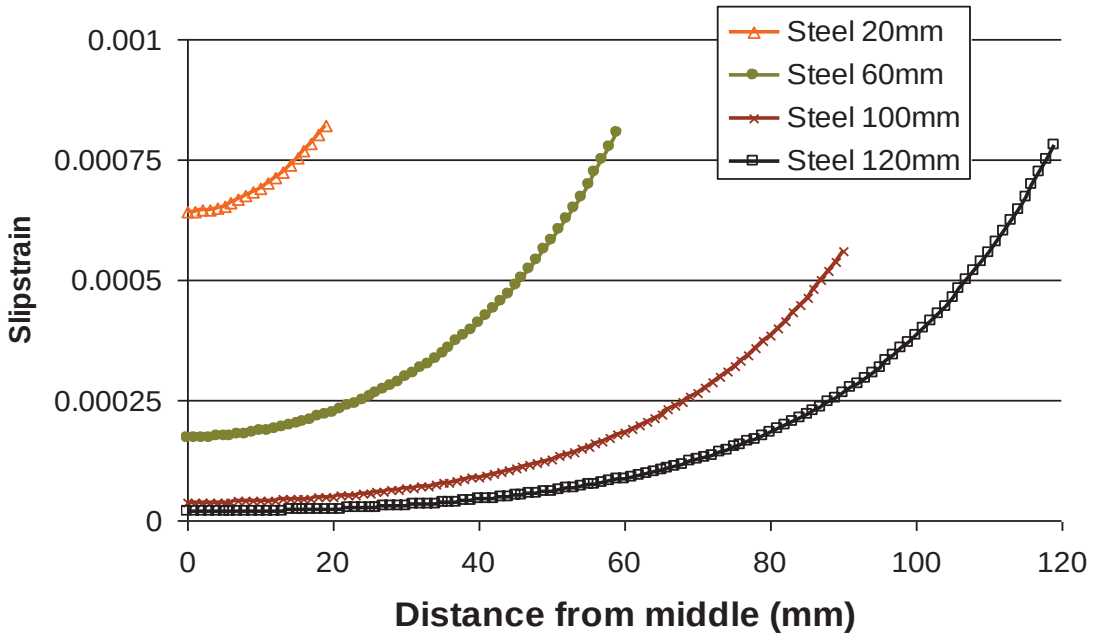

Figure 6.7 Slipstrain distribution of steel and FRP for plate end debonding.

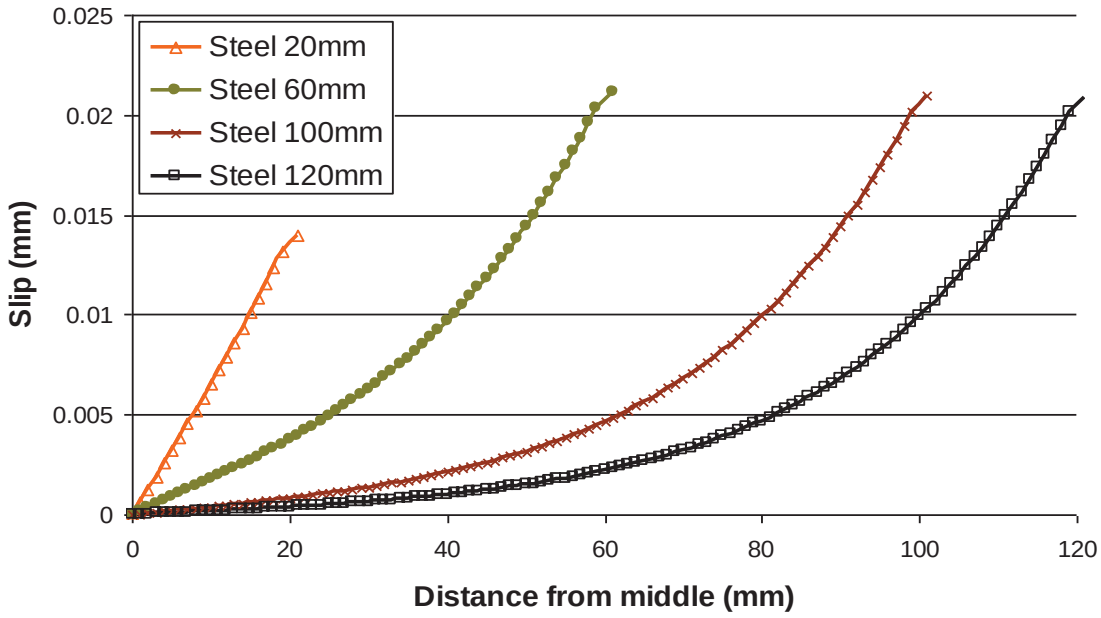

Figure 6.8 Slip distribution of steel and FRP for plate end debonding.

If the bond length was increased further, then $\varepsilon_s = \varepsilon_p$ at the middle which corresponds to s=ds/dx=0 which means no solution for the numerical method to be found. If $\varepsilon_s < \varepsilon_p$ at the middle, then according to the numerical method, ε_p will always be increasing towards the plate end, hence, no solution of the boundary condition σ_p=0 will be found as well as shown in Figure 6.9.

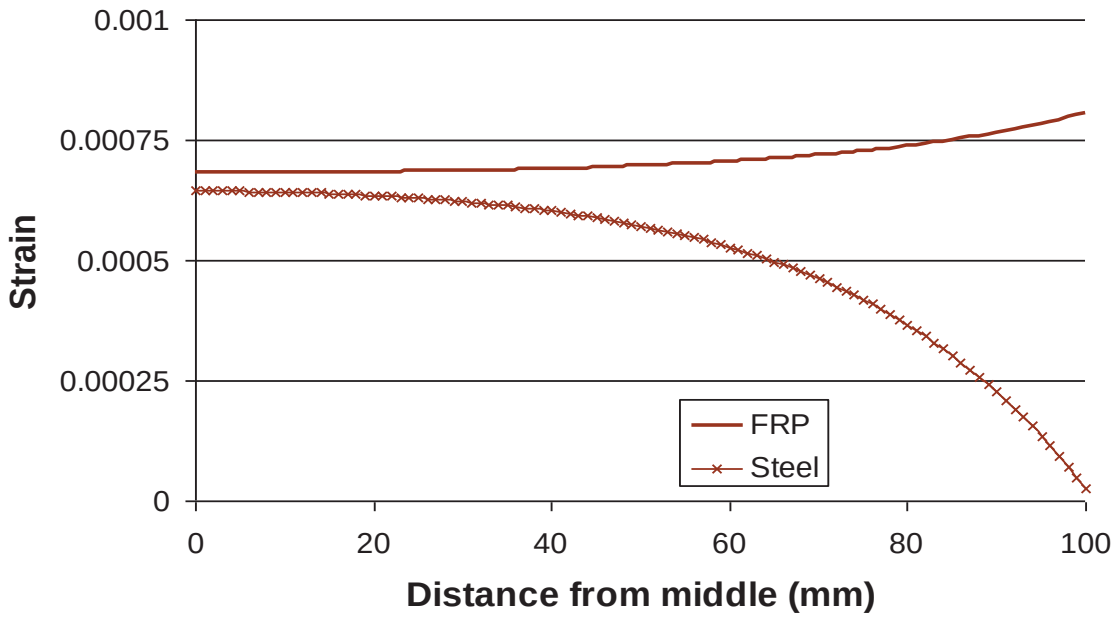

Figure 6.9 Strain distribution of steel and FRP when $\varepsilon_x < \varepsilon_p$ at the middle.

6.3.2 DEBONDING BETWEEN PLATE ENDS DUE TO STEEL YIELDING

In this section, the debonding mechanism of FRP plated steel members is explained when the steel has yielded along the bonded length. For the purpose of demonstrating the debonding mechanism, the FRP plated steel member with varying widths in Figure 5.2 (Chapter 5) with infinite bond length was used.

Figure 6.10 shows the distribution of steel strain on a bonded length on an increased loading (the label (a) being the lowest and (c) the highest). It can be observed that the region where the steel has yielded was confined to the region where the area of the steel was the smallest (0-30 mm from the middle section). Beyond the yield region, there is almost no increase of strains as the applied load is increased. The corresponding FRP strain distribution is shown in Figure 6.11.

The slip-strain was calculated from the differences of the steel and FRP strains and is shown in Figure 6.12. The corresponding slip distribution is shown in Figure 6.13. Both figures show that the $s=ds/dx=0$ boundary condition was achieved at the same point at about 200 mm from the middle section, which means the second boundary condition was met. At a lower load (labelled (a)), the slip has just reached its peak value. As the load was increased, the slip at that point increased to (c) as shown in Figure 6.13. From the graph it can be observed that the slip increment only occurred at a range from 0 to 200 mm from the middle. The corresponding bond stress distribution in Figure 6.14 shows the debonding propagation. At maximum slip, the bond-stress is equal to 0 which is clearly depicted in the graph labelled (a). As the slip keep on increasing, the maximum slip propagates to the left and right ride with the corresponding graph (b) of the bond-stress propagation. The 0 value of bond-stress between the peak bond-stress indicate that debonding has already occurred. From this observation, it can be concluded that debonding starts at the peak slip and then propagates left and right of the bonded length.

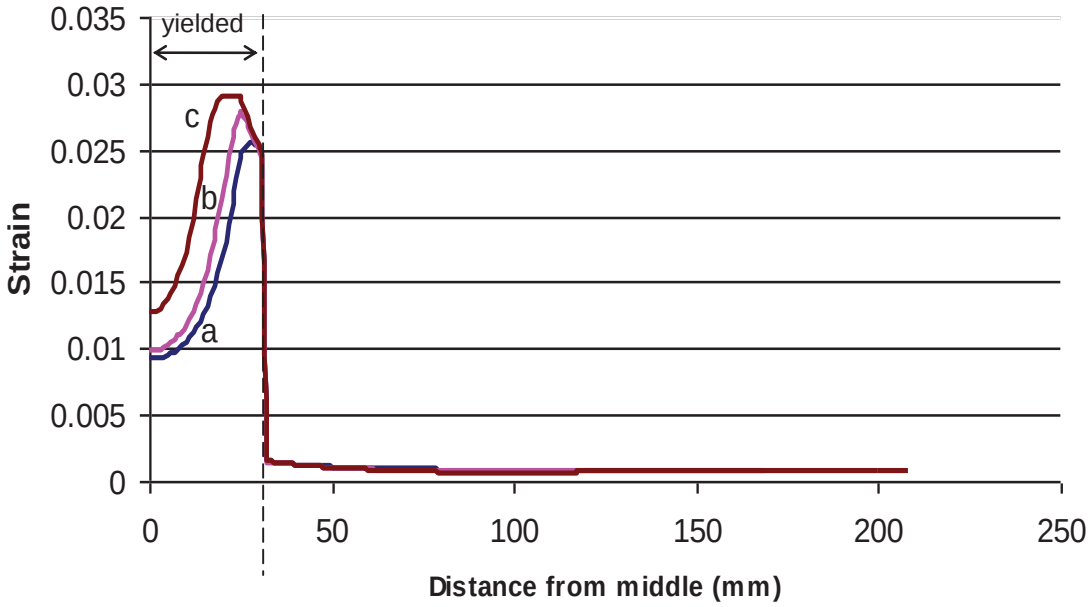

Figure 6.10 Steel strain distribution after steel yielding

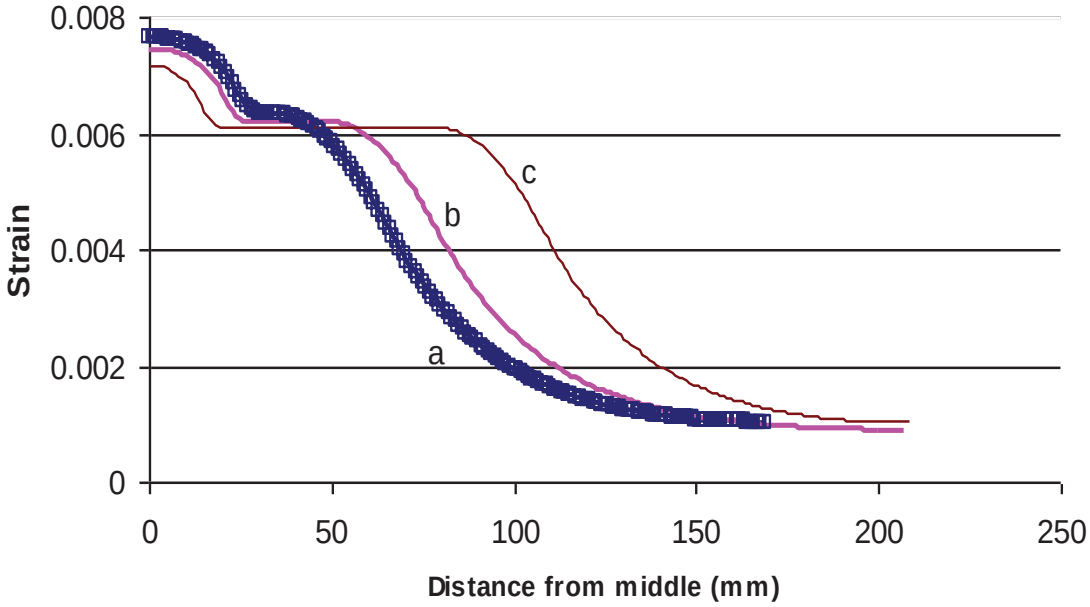

Figure 6.11 FRP strain distribution after steel yielding

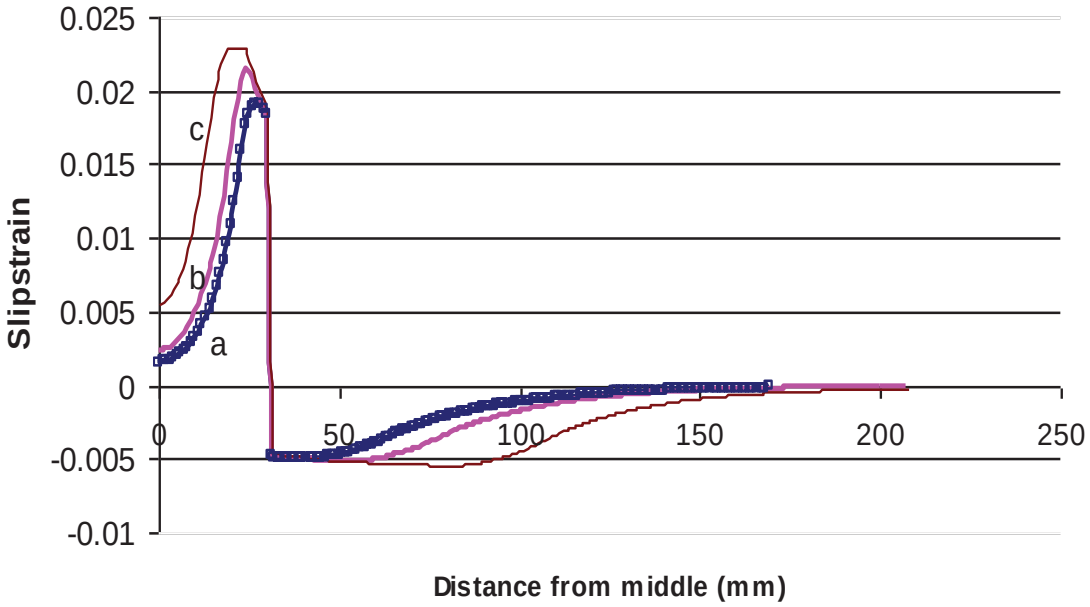

Figure 6.12 Slipstrain distribution after steel yielding

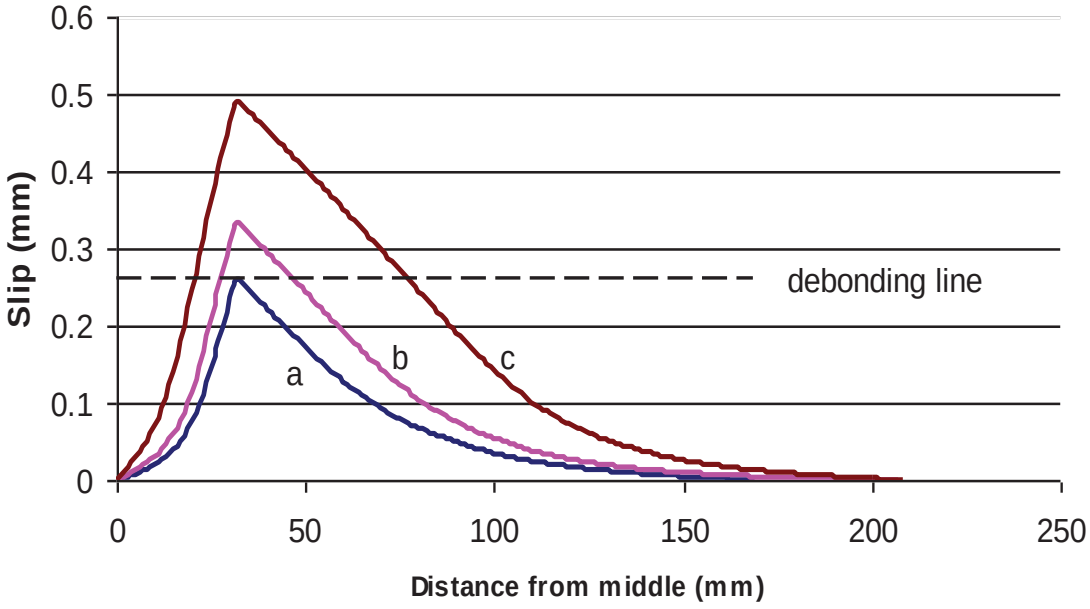

Figure 6.13 Slip distribution after steel yielding

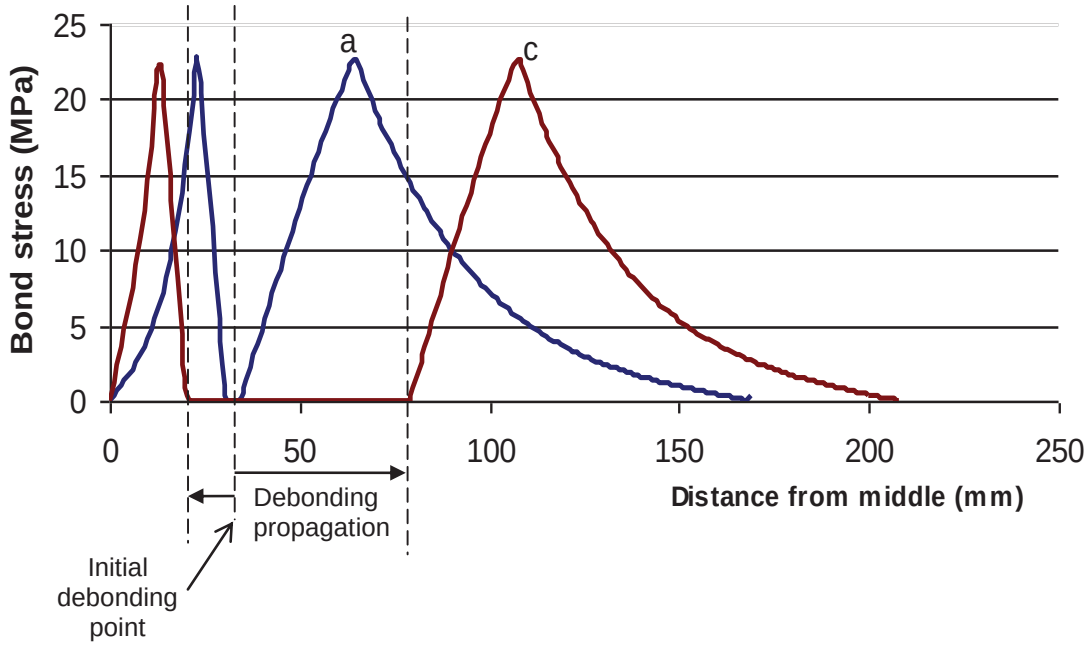

Figure 6.14 Bond stress distribution after steel yielding

6.3.3 COMBINATION OF PLATE END DEBONDING AND DEBONDING DUE TO YIELDING OF STEEL

Sections 6.3.1 and 6.3.2 explained the two debonding mechanisms on an FRP plated steel plate. The first debonding mechanism occurred at the plate end whereas the other occurred at the length where the steel has yielded. In the case of plate end debonding, there was a point when the strains in the steel and FRP were equal which resulted in zero slip-strain and slip. The area where the slip-strain and slip were not zero is shown in the partial interaction region at the right side of Figure 6.15.

The second debonding mechanism occurred where the steel has yielded between the plate ends. The point where the slip-strain and slip were zero along the bond length was demonstrated in Section 6.3.2 (refer Figure 6.12 and Figure 6.13) which was also the boundary condition in the numerical method. Hence,

partial interaction region also occurred at the region where the steel has yielded and is shown at the left side of Figure 6.15.

The two debonding mechanisms existed at a certain length at which either one of two boundary conditions, σ_p=0 and s=ds/dx=0 are met. These are also the partial interaction regions as shown in Figure 6.15. Extending the length of the bond length will only extend the length of the full interaction region.

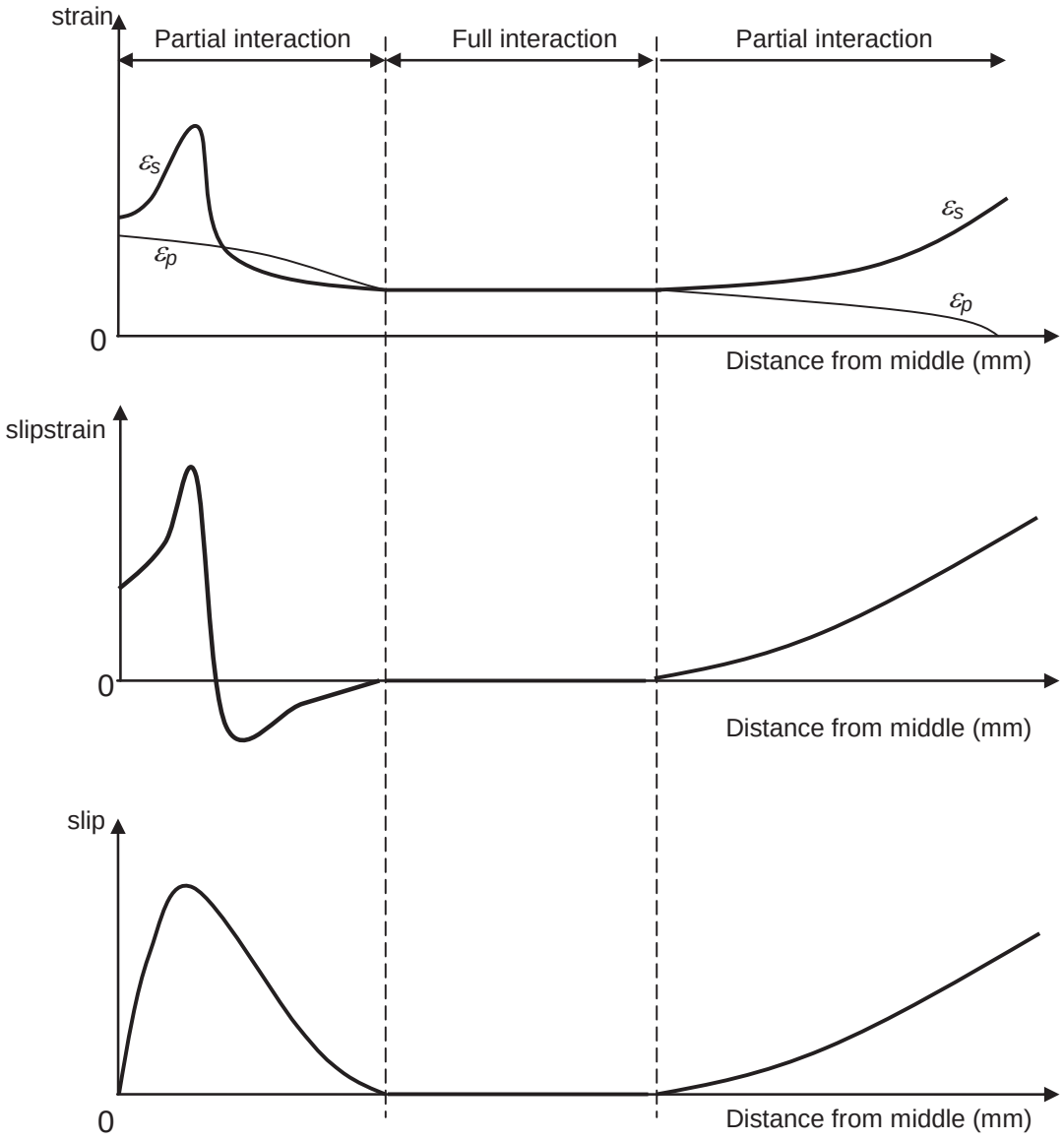

Figure 6.15 Full and partial interaction regions of FRP plated steel member

6.4 ANALYSIS OT TEST RESULTS

In this section, the numerical method will be used to analyse the results obtained from the experimental work in Chapter 5.

6.4.1 SPECIMENS CW1 AND CW2

Figure 6.16 shows the numerical strains for the 40 mm and 80 mm bond lengths respectively. It can be observed from Figure 6.16 that as the bond length is increased, the strain difference between the steel and FRP reduced. The reduction of slope for the FRP strain was bigger than the steel strain when comparing the bond length. These two trends observed in the numerical results were similar with the experimental results in Figure 5.11.

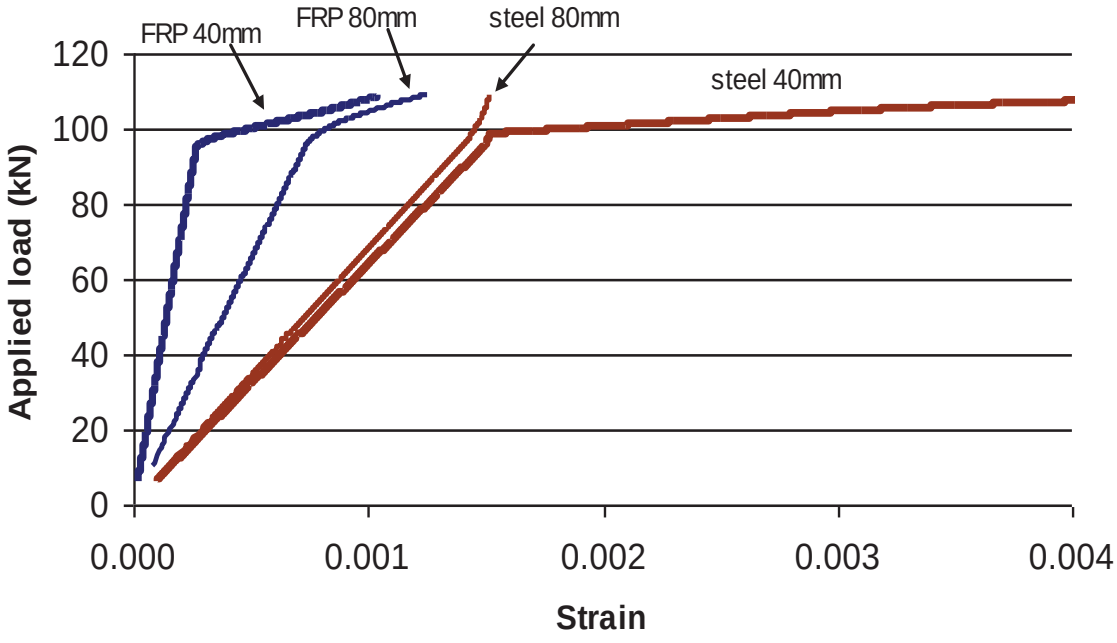

Figure 6.16 Numerical load-strain for CW1 and CW2.

The change of FRP strain slope due to steel yielding is shown in Figure 6.17. The change of slope occurred due to the yielding of steel at approximately 94 kN of applied load. The yielding of steel started from the plate end since it was the weakest point and gradually propagated to the middle of the specimen. This trend was not observed in the experimental result as illustrated in Figure 5.11 so it can be derived that debonding occurred abruptly as soon as the steel plate yielded during the experiment.

The rapid increase in bond stresses from the linear elastic to the nonlinear stages is shown in Figure 6.18 to illustrate the development of bond stresses during the change of slope in Figure 6.17. During the linear elastic stage, the maximum bond stress developed was about 5 MPa up until 94 kN of load. The bond stress distribution at the linear elastic stage is illustrated as the shaded area in Figure 6.18. Once the steel has yielded, the bond stress increased rapidly up to the maximum of 25 MPa which started from the plate end. This peak bond stress will propagate towards the middle of the specimen and eventually debonding starts at the plate end. The ascending and descending branch of the bilinear τ-δ relationship applied in this analysis is evident as shown in Figure 6.18. The bond stress propagation in the numerical analysis agrees well with the study conducted by Yuan et al. (2004).

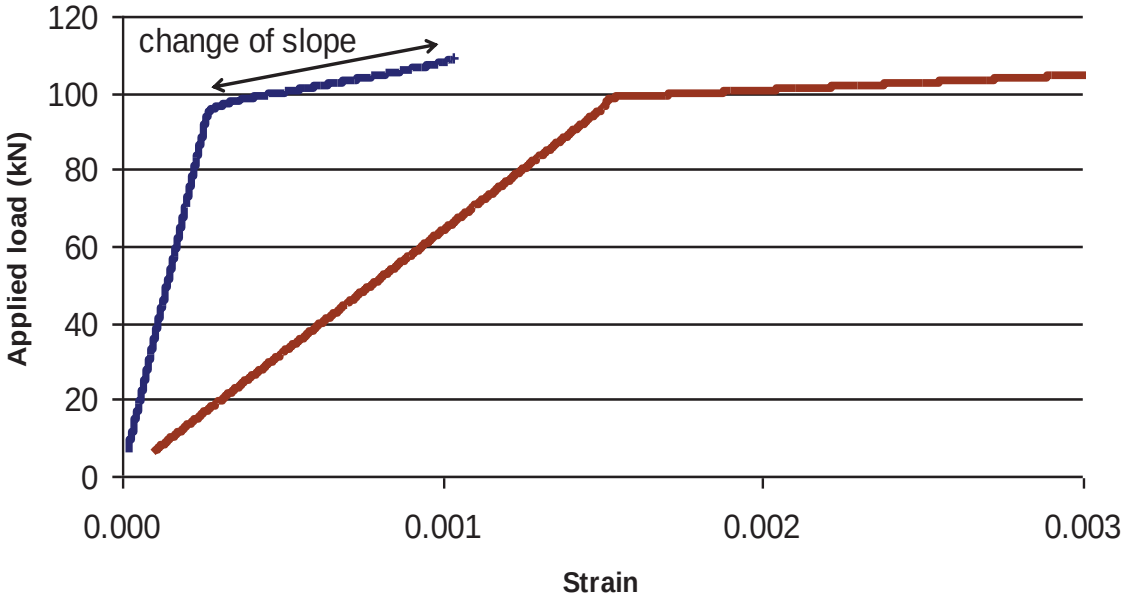

Figure 6.17 Numerical load-strain for CW1.

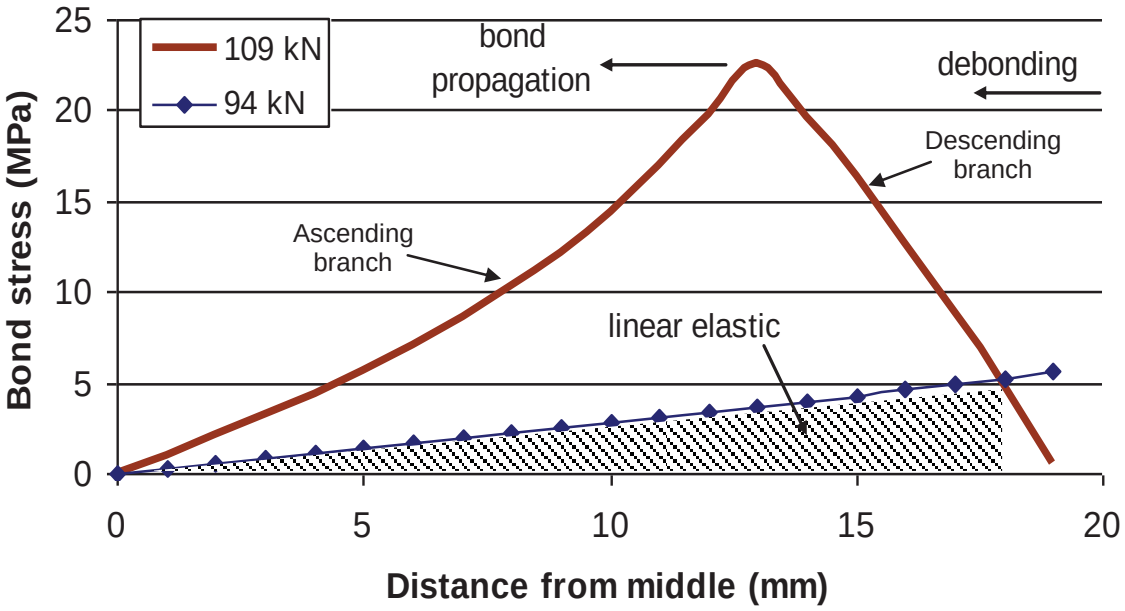

Figure 6.18 Numerical bond stress for CW1 at steel yielding.

6.4.2 SPECIMEN VW1

Figure 6.19 shows the experimental and numerical load-strain of steel plate comparison for specimen VW1. The corresponding comparison for load-strain of the FRP plate is shown in Figure 6.20. There are three stages of behaviour experienced by the specimen as illustrated in Figure 6.19; linear elastic, steel yielding and debonding. The three behavioural stages were correctly predicted by the numerical analysis.

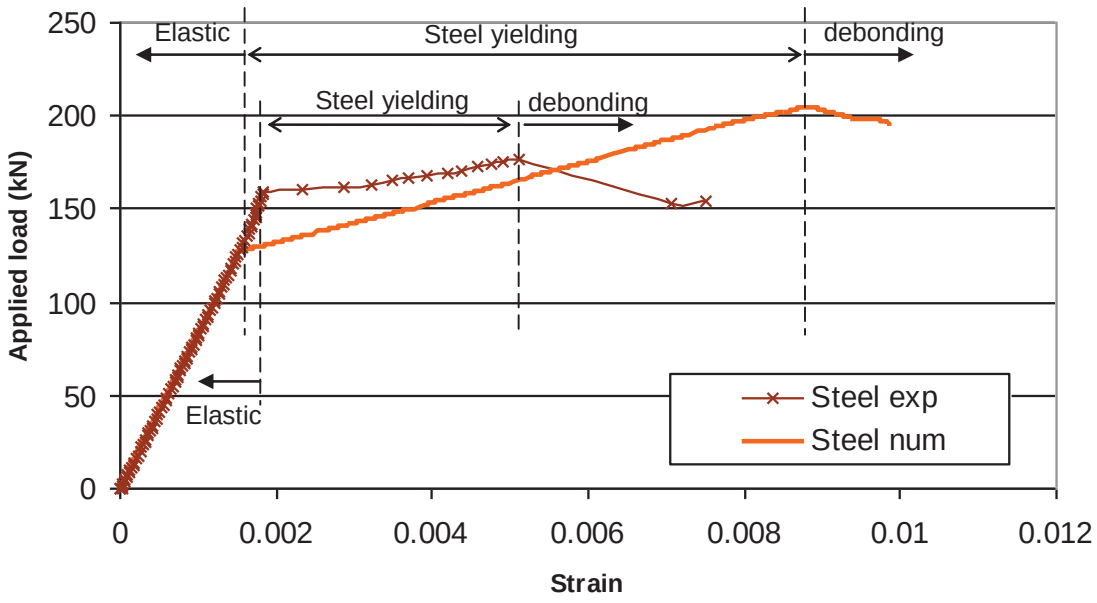

Figure 6.19 Steel load-strain comparison for VW1

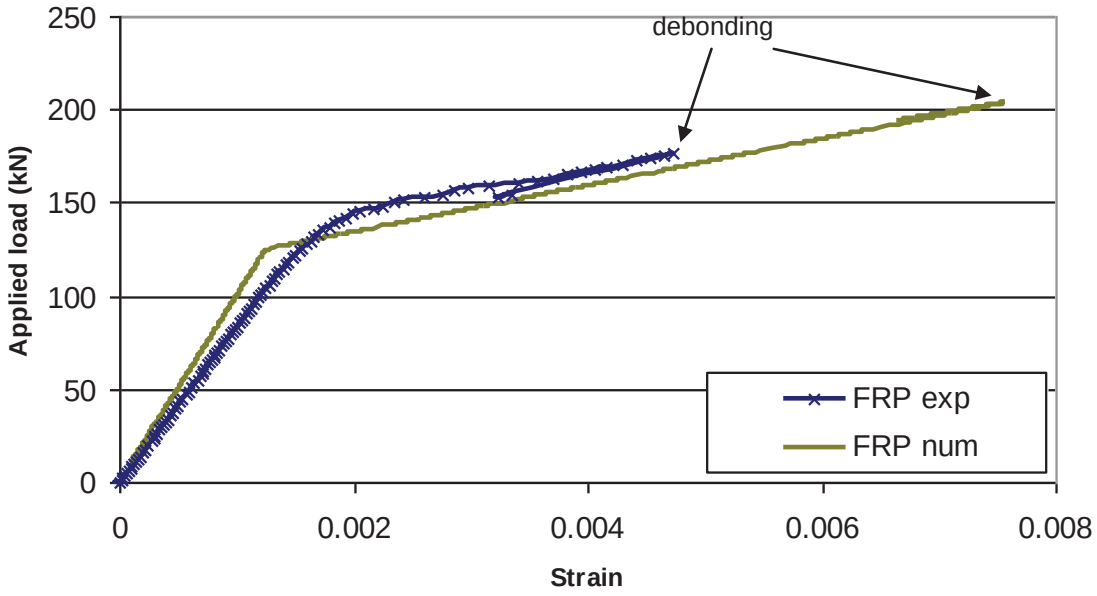

Figure 6.20 FRP load-strain comparison for VW1

From the comparison shown in Figure 6.19 and Figure 6.20, the numerical slip and bond stress distribution can be extracted. The linear elastic range ends at 128 kN. At this stage the slip and bond stress developed was low as shown in the linear graph in Figure 6.21 and Figure 6.22. After that, the steel plate yielded until 177 kN of applied load. During this stage, the bond stress reached its peak at about 30 mm from the middle as shown in Figure 6.22. Debonding started at 177 kN at which the bond stress is reduced to zero as shown in the same figure. It can be observed that the debonding occurs at the region where the steel has yielded. The corresponding slip is shown in Figure 6.21 and it is observed that the maximum slip is reached at the same point of 30 mm from the middle. The value of slip which exceeds the maximum slip of 0.25 mm means that debonding has occurred which is clearly shown in the figure.

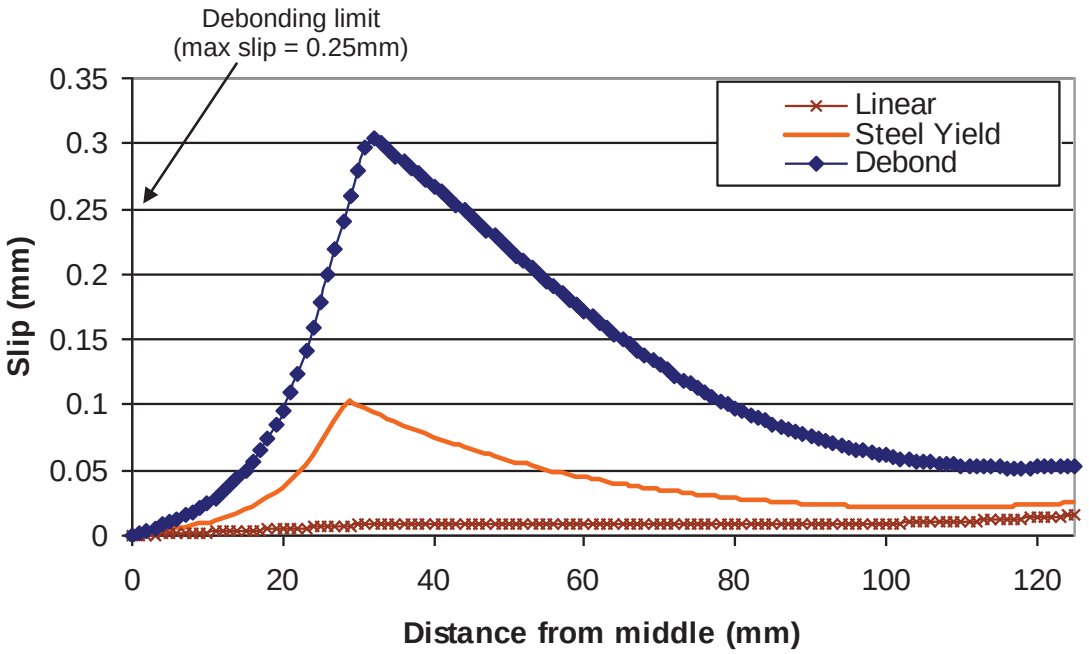

Figure 6.21 Numerical slip at different stages of loading (VW1)

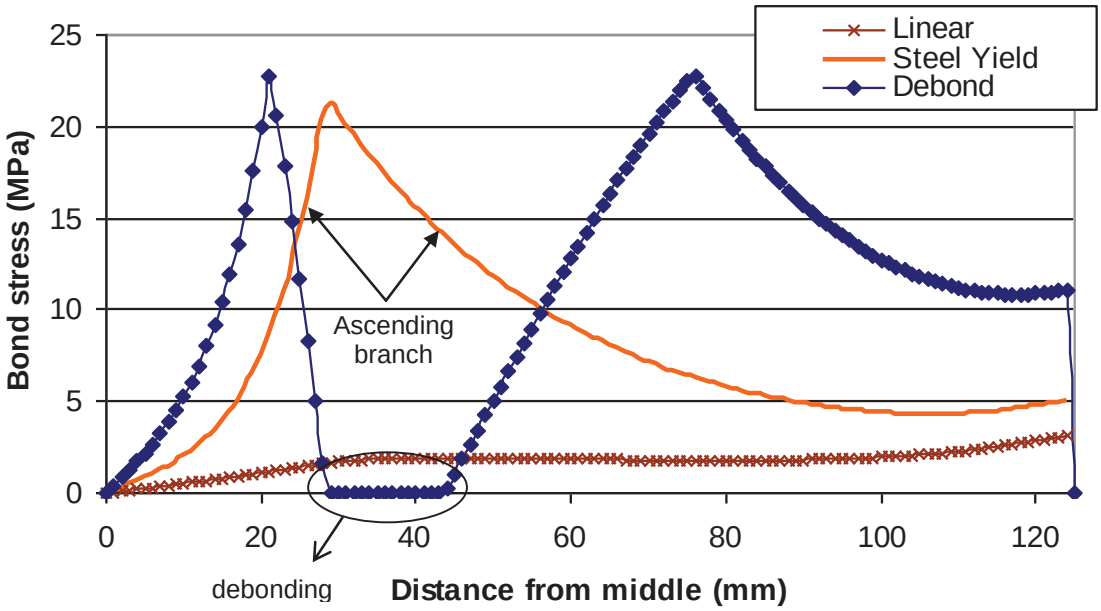

Figure 6.22 Numerical bond stress at different stages of loading (VW1)

Figure 6.23 shows the numerical bond stress distribution at the debonding for specimen VW1. Initially, the peak bond stress occurred at 30 mm from the middle of the specimen as described earlier. As the debonding propagates in both directions left and right of the bonded length, the peak bond stress propagates in the same direction as the debonding propagates. The ascending and descending branches of the bond stress at debonding which corresponds to the bilinear τ-δ relationship applied in the analysis are shown in Figure 6.23. This indicates that both branches of the bond stress distribution prior to debonding are the ascending branch as shown in Figure 6.22 and not necessarily ascending-descending branch as described earlier for the case of plate end debonding.

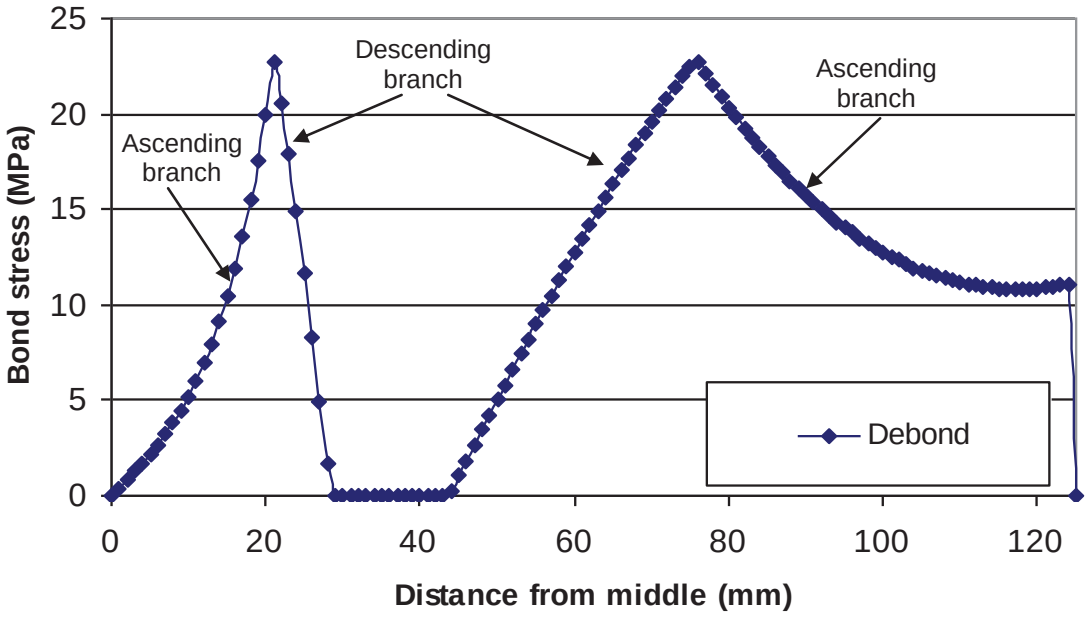

Figure 6.23 Peak numerical bond stress at debonding (VW1)

6.4.3 SPECIMEN VW2

Figure 6.24 shows the experimental and numerical load-strain of steel plate comparison for specimen VW2. The corresponding comparison for load-strain of the FRP plate is shown in Figure 6.21. The three stages of behaviour which were earlier described in specimen VW1 were also experienced by specimen VW2. However at the debonding stage, the failure mode is more abrupt in specimen VW2 as shown by the amount of strain generated by the steel plate in Figure 6.24 compared to specimen VW1 (Figure 6.19). This is because the FRP plate glued to the steel plate was doubled in specimen VW2. The three behavioural stages were correctly predicted by the numerical analysis. The difference between the test and theory at the large strain levels (after yielding) is simply because idealised stress-strain diagram was used in the theory.

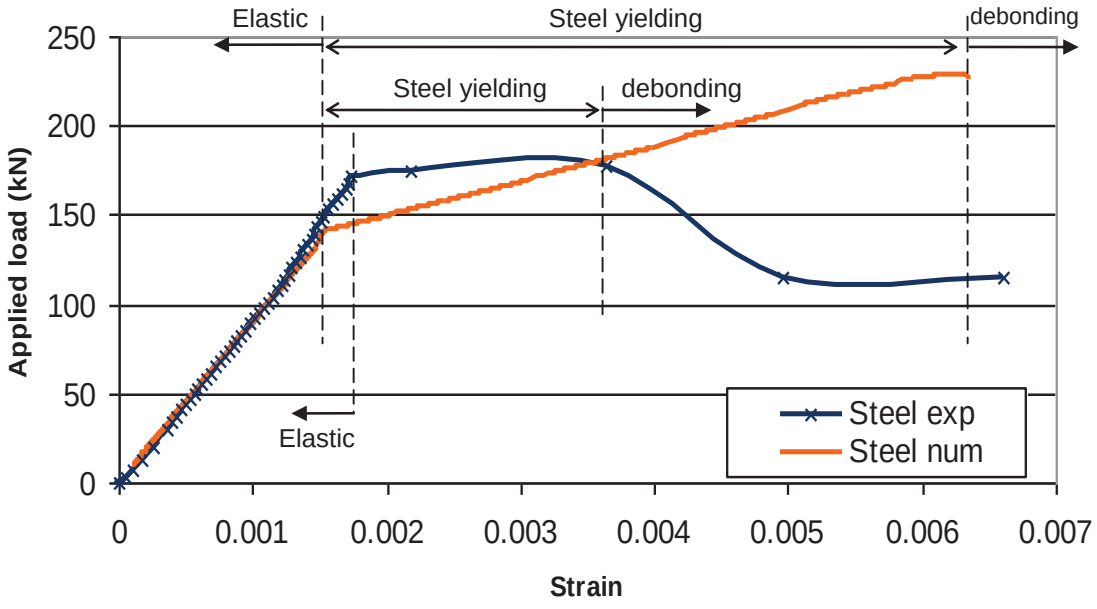

Figure 6.24 Steel load-strain comparison for VW2

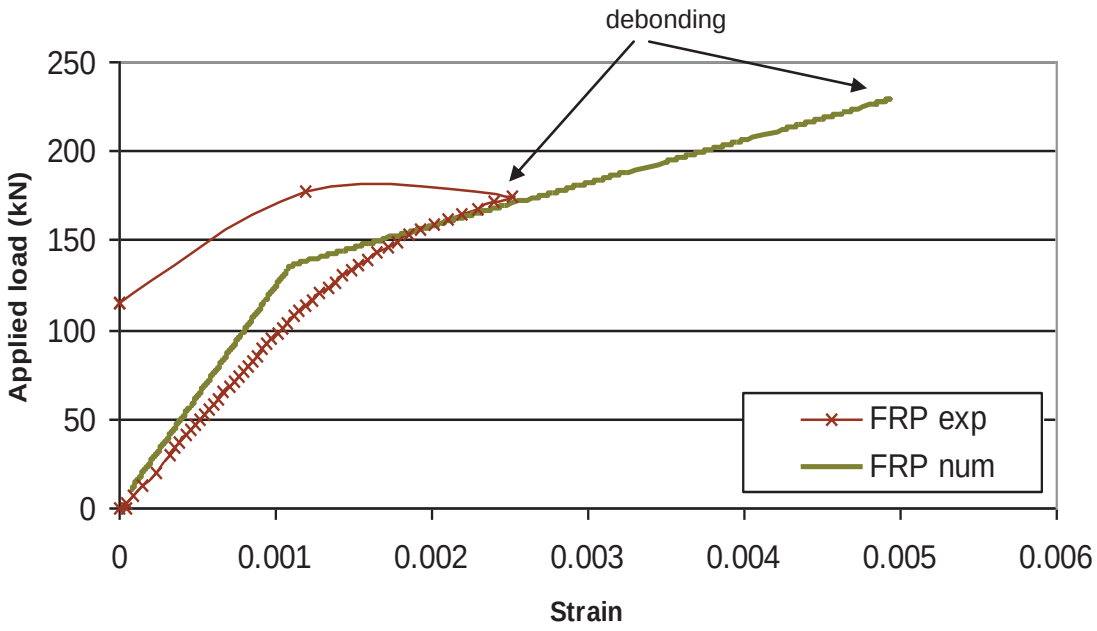

Figure 6.25 FRP load-strain comparison for VW2

6.5 COMPARISON WITH PUBLISHED RESULTS

Al-Emrani and Kliger (2006) experimented on FRP plated tapered steel members with varying FRP thicknesses. The schematic drawing of the specimen is shown in Figure 2.18 and the relevant measured material properties of the FRP plate are given in Appendix B. The objectives of the published report were detailed in Section 2.6.3.3 so it will not be repeated here.

The τ-δ relationship of the adhesive was not available from the published report, hence, the one obtained from this thesis will be used. Due to this, the objective of this comparison was to analyse the debonding mechanism and not to compare the accuracy of the results in terms of the 'numbers'. Three specimens were compared, A12, B12 and B17 which have different types of adhesive and FRP thicknesses. Experimental and FEM results were reported in the published report and reproduced in this section. These published results were then compared with the numerical analyses developed from this chapter.

Figure 6.26 to Figure 6.28 show the comparison of applied load-axial stress from the experiment and numerical analyses on the three different specimens A12, B12 and B17 based on the strain readings on the FRP plate at the middle of the section. According to the experimental report by Al-Emrani and Kliger (2006), specimens B12 and B17 failed as a result of tensile rupture of the FRP plate whereas specimen A12 failed due to debonding in the middle of specimen after the steel plate yielded.

In the numerical analysis, the decrease of the FRP stresses as shown in Figure 6.26 and Figure 6.27 after the steel has yielded suggested that successive yielding of steel leads to the debonding. This is also the type of failure occurred on sample VW1 as reported in Sections 5.7.1 and 6.4.2. The stress recorded by the numerical analysis for specimen A12 was 1117 MPa prior to debonding in comparison with 1553 MPa from the experiment. Both values were below the ultimate stress of 1932 MPa, indicating a good correlation by the numerical analysis to predict the failure.

For the specimen which failed due to FRP rapture as shown in Figure 6.28, the stress propagation of the FRP in the numerical analysis does not have the decrease of stresses. The stress recorded by the numerical analysis for specimen B17 was 1106 MPa prior to debonding in contrast to 1384 MPa from the experiment which exceeded the ultimate tensile stress of 1252 MPa. The final tensile stress calculated by the numerical analysis was lower than the ultimate tensile stress because at rupture, no solution was to be found. The 12% difference of the numerical final tensile stress compare to the ultimate tensile stress, suggested that the FRP has ruptured.

For specimen B12, the stress recorded by the numerical analysis was 1357 MPa prior to debonding in comparison to 1892 MPa from the experiment which exceeded the ultimate tensile stress of 1855. Incorrect values of the τ-δ and steel plate σ-ε relationships may be the cause of these discrepancies.

Figure 6.29 shows the bond stress distribution along the bonded length from the experiment and numerical for specimen A12. At 150 kN (149 kN for the numerical analysis), the steel plate has yielded, creating a high bond stress at the middle of the specimen. It was suggested by Al-Emrani and Kliger (2006) that debonding may occur first at the middle section before at the plate end based on the high bond stress which also occurred at the plate end. In the numerical analysis as shown in Figure 6.29 (b), it is suggested that debonding occurred at the middle section and then propagates toward the plate end as indicated by the debonding propagation of specimen VW1 in Section 6.4.2.

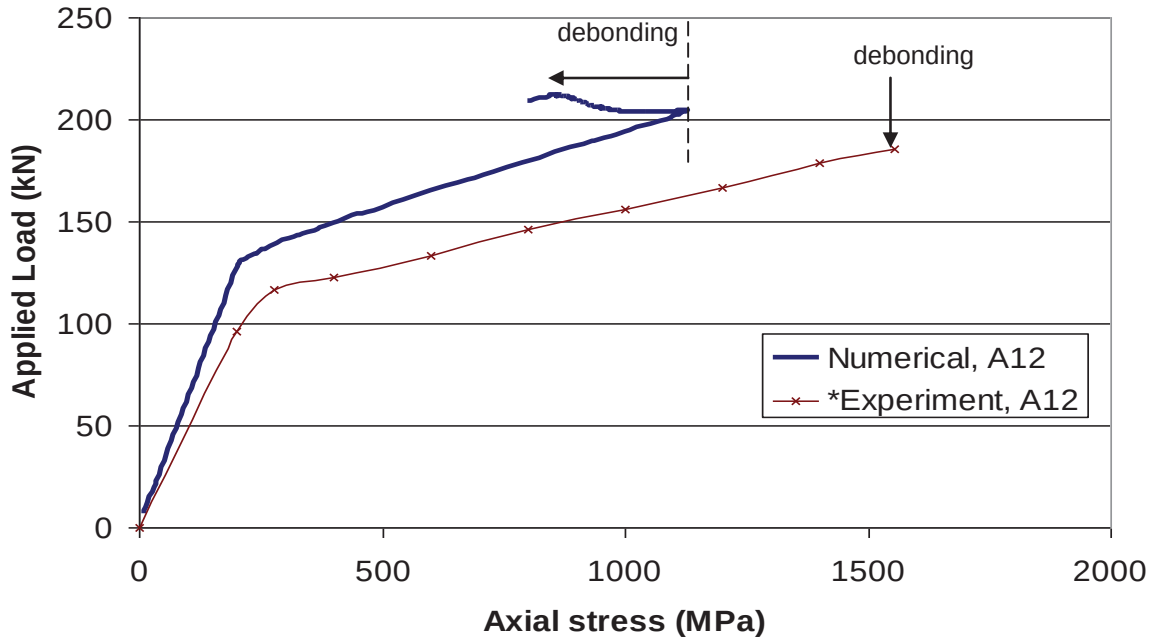

Figure 6.26 Numerical and experimental load-axial stress comparison for specimen A12

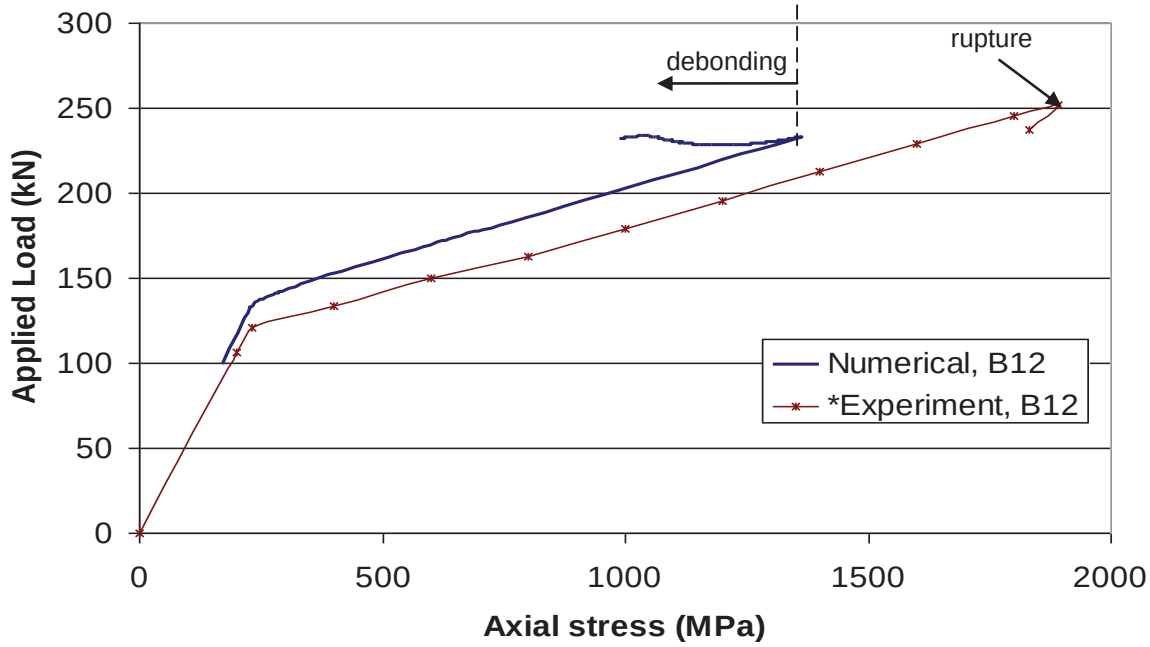

Figure 6.27 Numerical and experimental load-axial stress comparison for specimen B12

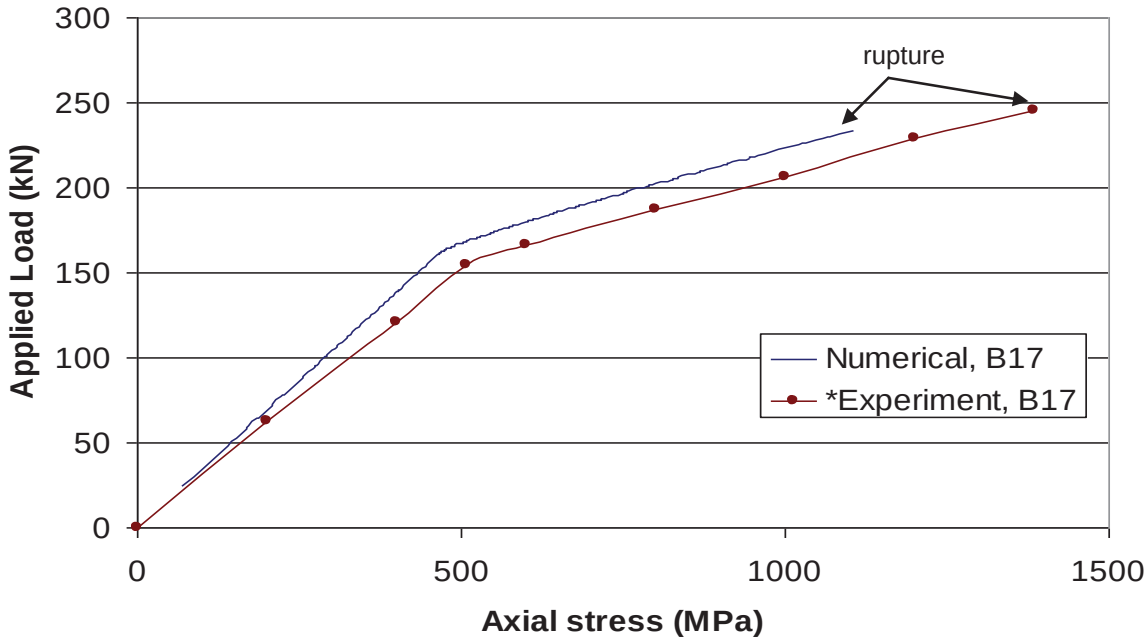

Figure 6.28 Numerical and experimental load-axial stress comparison for specimen B17

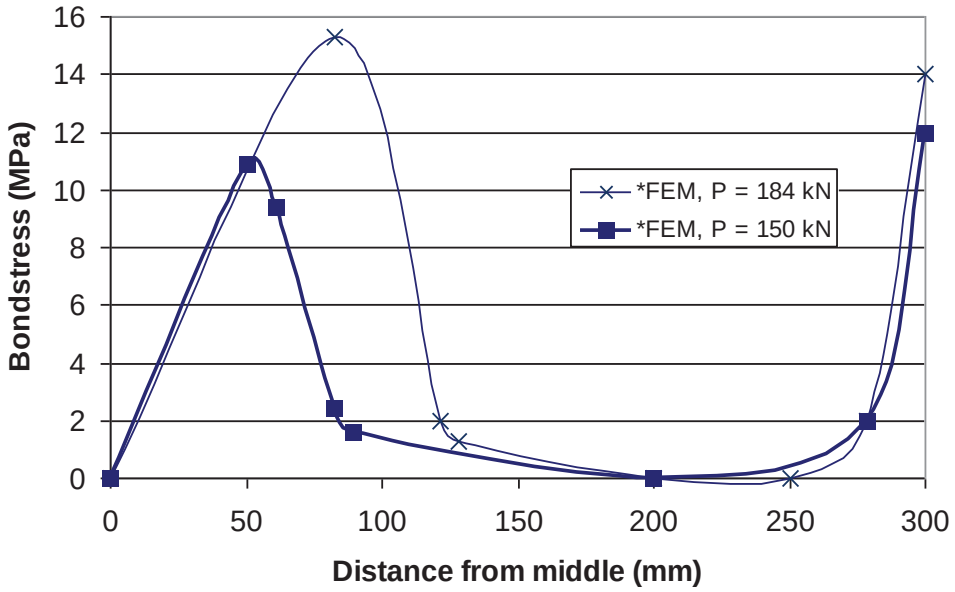

(a) FEM

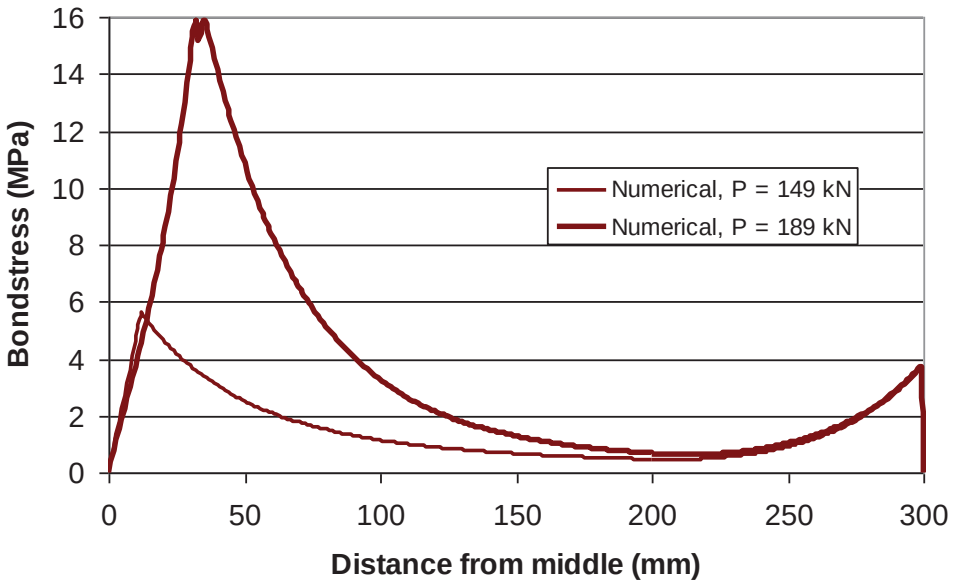

(b) numerical analysis

Figure 6.29 Numerical and FEM shear stress comparison across the bonded length.

Figure 6.30 shows the comparison of bond stress-load from the experiment and numerical on two different specimens A12 and B12 at the plate end. Experimentally, A12 failure was due to progressive debonding due to the yielding of steel whereas for specimen B12, rupture occurred at the middle section of the specimen. As indicated earlier in the numerical analysis, both specimens debonded progressively due to the yielding of the steel plate at the middle section. The debonding in the numerical analysis is indicated by the huge increment of bond stress after the applied load of 200 kN as shown in Figure 6.30. The same trend was shown by specimen A12 experimentally.

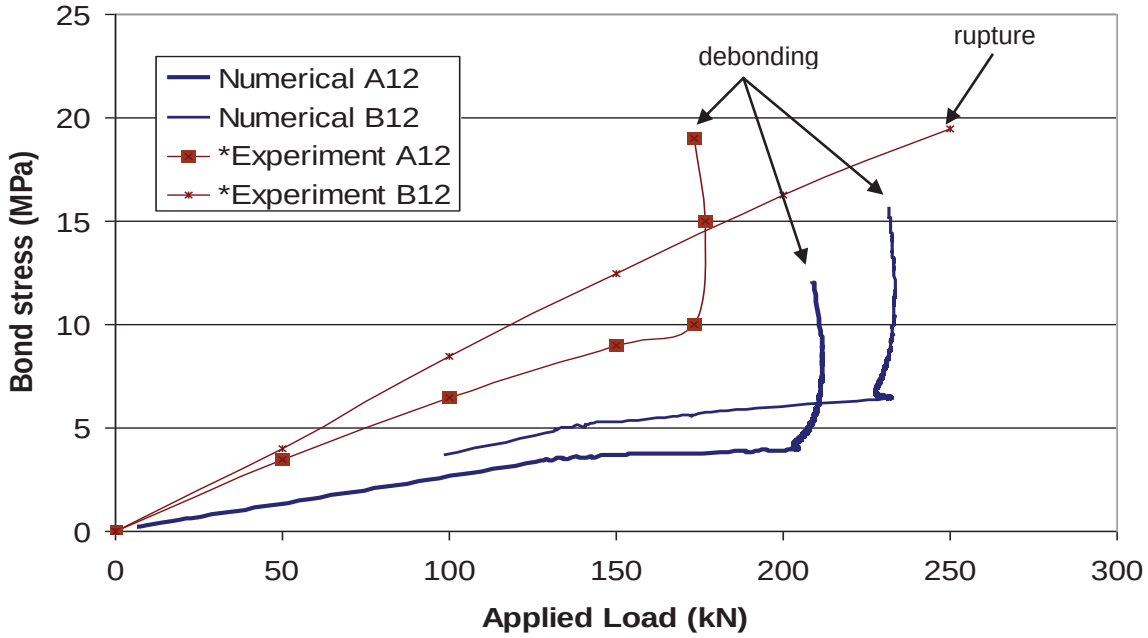

Figure 6.30 Numerical and experimental shear stress comparison at plate end.

6.6 CONCLUSIONS

A numerical method was developed to study the debonding mechanism of FRP plated steel members based on partial and full interaction theory. This numerical method was able to show the debonding mechanism for the plate end debonding and debonding due to the yielding of steel. The numerical analysis results were compared with the experiments conducted in Chapter 5 and the experiments published by Al-Emrani and Kliger (2006). From this study, a few conclusions can be made:

- For the plate end debonding to occur, the steel plate along the bonded length must not yield. The yielding of steel at the plate end will encourage debonding at the plate end by increasing the steel strain compared to the FRP strain. Corresponding to this huge difference of strains, huge slip will follow with a subsequent debonding at the plate end.
- If the steel yielded between the plate ends, the huge difference of steel and FRP strains will create huge slip with subsequent debonding. Debonding will start at the middle section and then propagate towards the middle section and the plate ends.

CHAPTER 7: DEVELOPMENT OF MOMENT-ROTATION CAPACITY NUMERICAL METHOD FOR FRP PLATED STEEL BEAM

7.1 INTRODUCTION

The importance of the moment-rotation capacity is obvious in the plastic design where the member should be able to form plastic hinges which must rotate in order for the collapse mechanism to occur without losing the moment capacity. Cost savings by reducing the use of the steel material can also be achieved due to the redistribution of the moments via the plastic hinges. Furthermore, in the seismic design, the rotation capacity is important in order for the seismic energy to be dissipated by the plastic behaviour (Gioncu and Petcu 1997). Extensive research has also been conducted on the moment-rotation capacity of steel members in particular the connection rigidity (Yee and Melchers 1986; Chen and Kishi 1989; Kishi and Chen 1990; Emmanuel Attiogbe 1991; Foley and Vinnakota 1995; Shi, Chan et al. 1996; Li, Nethercot et al. 2000; Alan R. Kemp 2001; Sang-Sup Lee 2002; Darko Beg 2004; Ali Abolmaali 2005; Shi, Shi et al. 2007).

7.2 DEFINITION OF ROTATION CAPACITY

One of the definitions of the rotation capacity can be defined as,

$$R = \theta_h/\theta_p \tag{7.1}$$

where θ_p is the elastic rotation at the point of the plastic moment M_p while θ_h is the plastic rotation at the point where the moment drops below M_p (Cevik 2007). The other definition of rotation capacity is,

$$R = \theta_{hm}/\theta_p \quad (7.2)$$

where θ_{hm} is the plastic rotation up to the maximum moment on the rotation curve (Kemp 1985). However, the rotation capacity defined by the American Society of Civil Engineers (ASCE) is more common. Rotation capacity is defined as,

$$R = \theta_2/\theta_1 \quad (7.3)$$

where θ_1 is the theoretical rotation when full plastic capacity is achieved and θ_2 is the rotation when the moment capacity drops below M_p as shown in Figure 7.1 (Cevik 2007).

Eurocode 3 (2003) defines the role of cross section classification in identifying the extent to which the resistance and rotation capacity of cross sections is limited by its local buckling resistance (Figure 7.2):

- Class 1 cross-sections are those which can form a plastic hinge with the rotation capacity required from plastic analysis without reduction of the resistance.
- Class 2 cross-sections are those which can develop their plastic moment resistance, but have limited rotation capacity because of local buckling.
- Class 3 cross-sections are those in which the stress in the extreme compression fibre of the steel member assuming an elastic distribution of stresses can reach the yield strength, but local buckling is liable to prevent development of the plastic moment resistance.
- Class 4 cross-sections are those in which local buckling will occur before the attainment of yield stress in one or more parts of the cross-section.

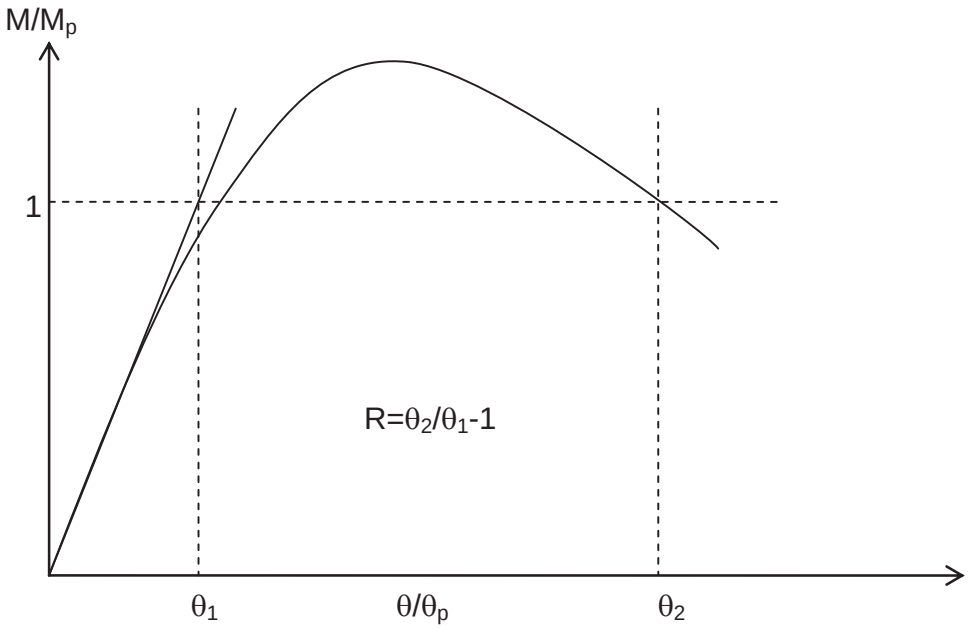

Figure 7.1 Rotation capacity definition by ASCE.

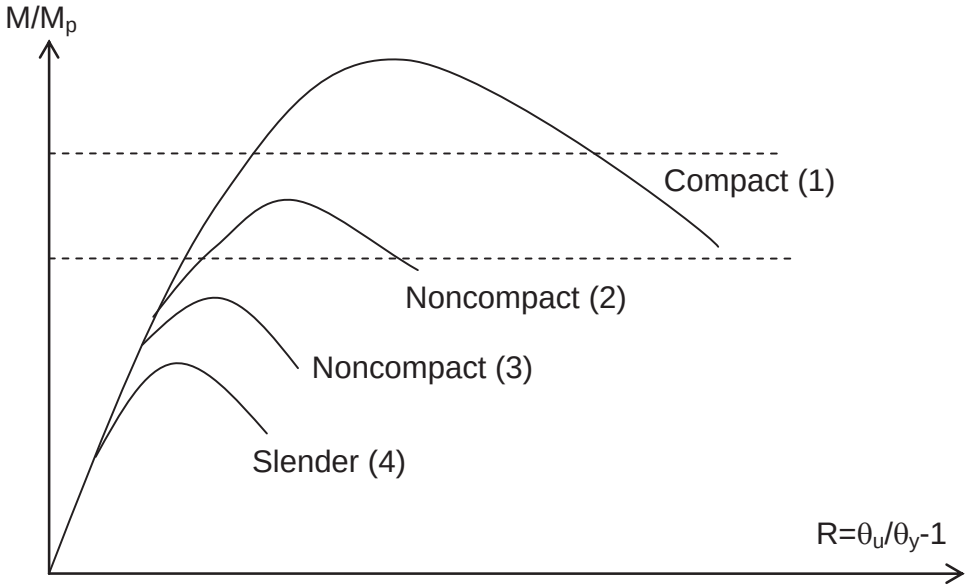

Figure 7.2 Definition of rotation capacity based on normalized moment-rotation relationship

7.3 PLASTIC MOMENT OF CONTINUOUS BEAMS

Due to the complexity in determining the rotation capacity in a structure, Gioncu and Petcu (1997) simplified the analysis of a continuous beam in Figure 7.3 (a) by tranforming it into a standard beam (SB) in Figure 7.3 (c) without changing the beam's behaviour. In the study, the top flange is wider than the bottom in the aim of studying the influence of tension flange on the rotation capacity. The standard beams are categorised into two, the first with a central concentrated load (SB_1) which resulted in a gradient moment and the second with two concentrated loads (SB_2) which resulted in a uniform moment. The inflection points in Figure 7.3 (b) divide the members into positive (SB_1) and negative (SB_2) bending moments. The theoretical studies and experimental tests of the standard beams were reported in literature which added to the advantage of simplifying the continuous beam. The corresponding collapse mechanisms are shown in Figure 7.3 (d).

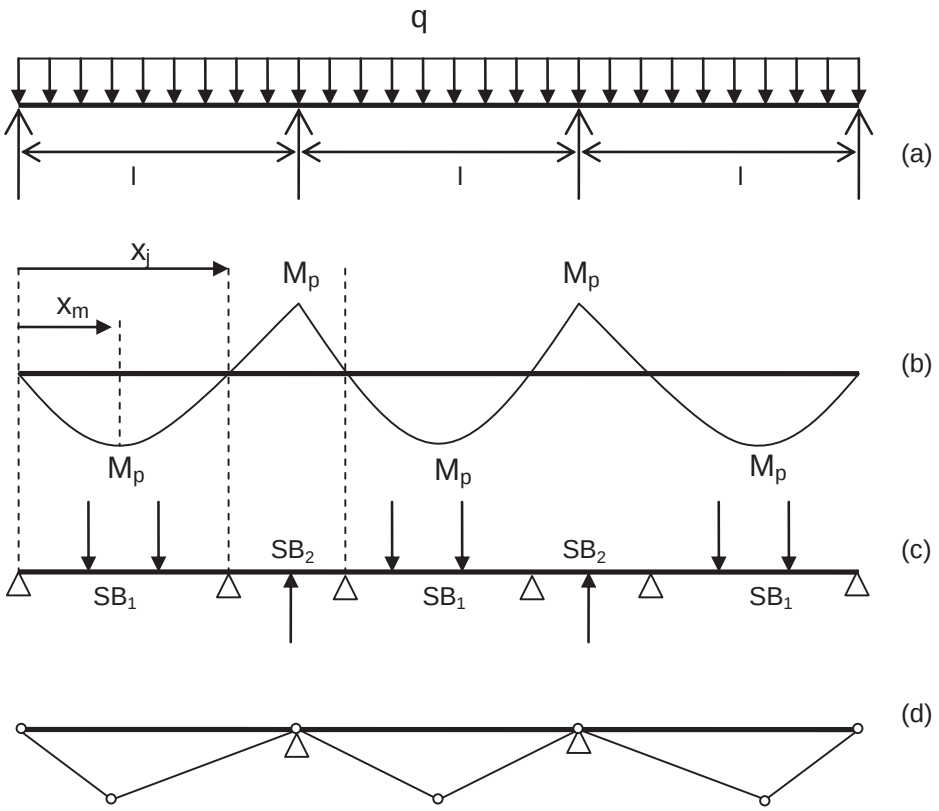

Figure 7.3 Standard beams for a continuous beam

The positions of the inflection points and the maximum moments are as follows (Figure 7.4). The position of the maximum moment is given by,

$$x_m = \left(1 - 2\frac{M_a + M_b}{ql^2}\right)\frac{1}{2}, \tag{7.4}$$

and the inflection point is,

$$x_i = \left\{1 - 2\frac{M_a + M_b}{ql^2} \pm \left[\left(1 - 2\frac{M_a + M_b}{ql^2}\right)^2 + \frac{8M_a}{ql^2}\right]^{\frac{1}{2}}\right\}\frac{1}{2}, \tag{7.5}$$

where M_a and M_b are the end moments.

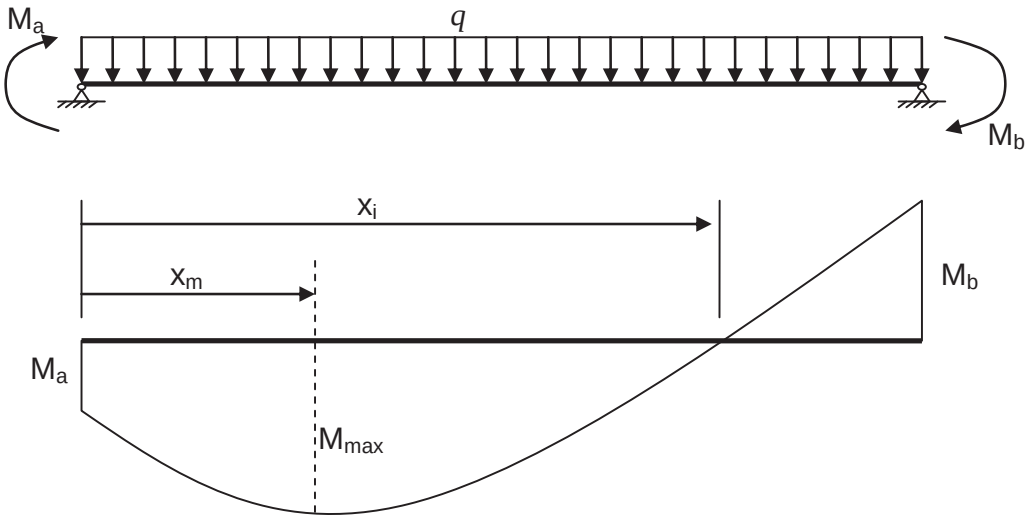

Figure 7.4 Characteristic points in a beam.

Eqs. 7.4 and 7.5 are now used for the calculations of the positions of inflection points and the maximum moments. The moment distribution of a continuous beam in Figure 7.3 (b) can be separated into three situations as shown in Figure 7.5 (Gioncu and Petcu 1997).

I. Marginal beam in Figure 7.5 (a), where M_a = 0, M_{max} = -M_b = M_p and for $M_p < \frac{ql^2}{8}$, the position of the maximum moment and inflection points are given as,

$$x_m = \left(1 - \frac{2M_p}{ql^2}\right)\frac{1}{2} \tag{7.6}$$

$$x_i = 2x_m \tag{7.7}$$

II. Central beam in Figure 7.5 (b), where M_{max} = -M_a = -M_b = M_p and for $M_p \leq \frac{ql^2}{8}$, the position of the maximum moment and inflection points are given as,

$$x_m = \frac{1}{2} \tag{7.8}$$

$$x_{i1,2} = \left[1 \pm \left(1 - \frac{8M_p}{ql^2}\right)^{\frac{1}{2}}\right]\frac{1}{2} \tag{7.9}$$

III. Beam with left plastic hinge at a distance from the extremity in Figure 7.5 (c), where $M_a \neq M_p$, M_{max} = M_p = M_b and for $M_p < \frac{ql^2}{8}$, the position of the maximum moment and inflection points are given as,

$$x_m = \left[1 - 2\left(\frac{M_p}{ql^2}\right)^{\frac{1}{2}}\right]\frac{1}{2} \tag{7.10}$$

$$x_i = \left[1 - \left(2 - \sqrt{2}\right)\left(\frac{M_p}{ql^2}\right)^{\frac{1}{2}}\right]l \tag{7.11}$$

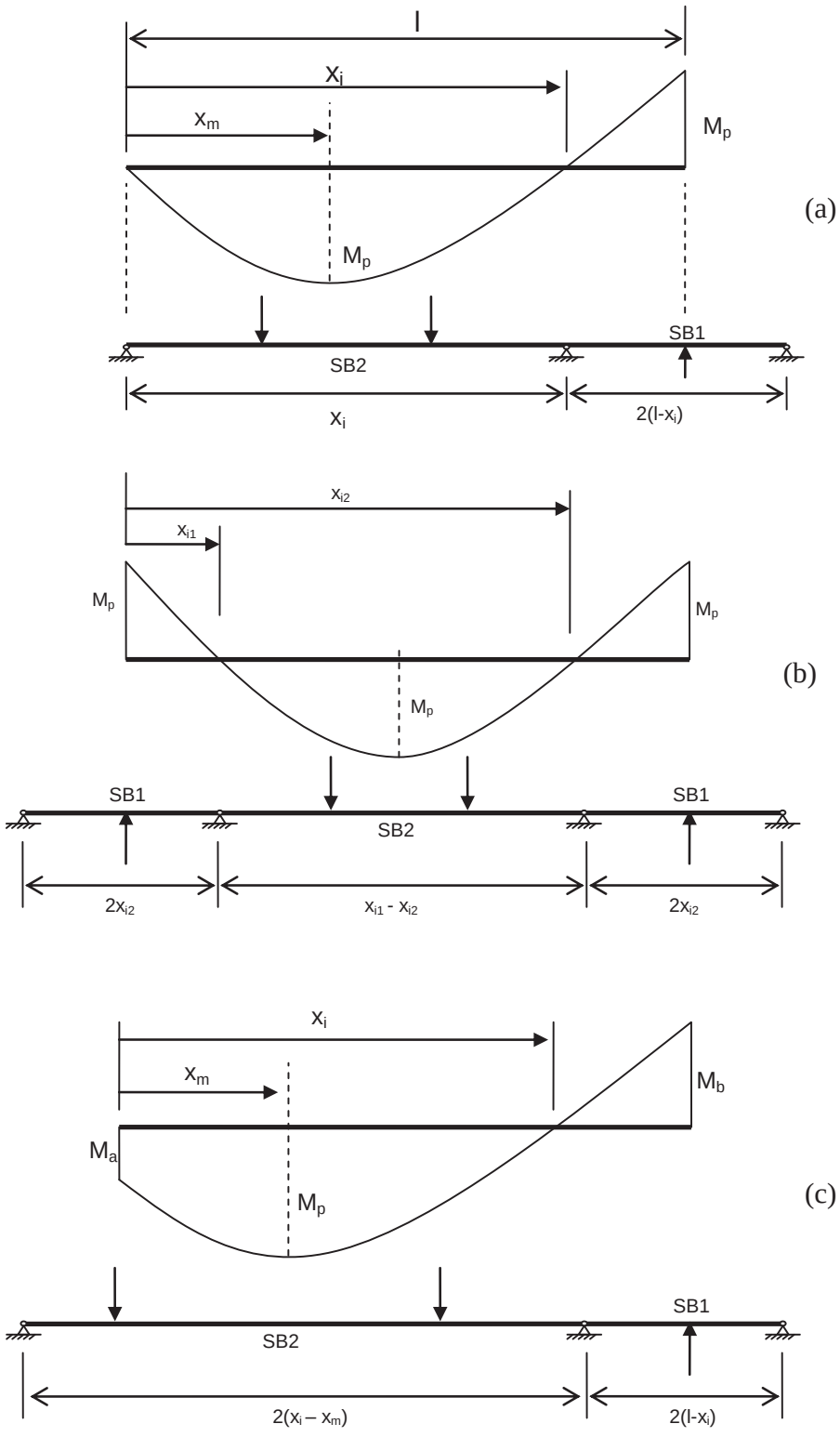

Figure 7.5 Locations of inflection and maximum moment points in standard beams.

7.4 ROTATION CAPACITY OF BEAMS

As explained in Section 7.3, a continuous beam can be simplified as standard beams (SB) and the associated varying bending moment diagrams are presented. These variations of bending moment affect the behaviour of the standard beams. Gioncu and Petcu (1997) described the behaviour of the two standard beams, SB1 and SB2 as follows:

I. For SB1, two possible failures may occur; crack or local buckling. In both cases, the steel beam will reach its flange yielding, M_{pf} and M_p as shown in Figure 7.6. If crack occurs at the tension zone, the moment will reached its ultimate capacity as shown in Figure 7.6 (a). The ultimate moment is given by,

$$M_u = \frac{1}{4}\left(1+3\frac{f_u}{f_y}\right)M_p \qquad (7.12)$$

where f_u and f_y are the ultimate and yield tensile stress of the steel member and $M_u \approx (1.33 – 1.40)M_p$. The corresponding ultimate rotation is given by,

$$\theta_u = 2\varepsilon_u \qquad (7.13)$$

where ε_u is the steel strain in the range of 0.4 to 0.5.

If local buckling occurs in the compression flange, a maximum value of bending is reached and a drop in moment capacity is produced without reaching M_u as shown in Figure 7.6 (b).

There are three zones in the moment diagram; the elastic range, elasto-plastic range and full-plastic range as shown in Figure 7.6 (c). The length

of the full plastic zone (elasto-plastic range plus full-plastic range) is given by,

$$l_p = \frac{1}{2}\left(1 - \frac{M_p - M_0}{M_{\max} - M_0}\right)l \qquad (7.14)$$

and the length of the flange plastic zone (full-plastic range) is given by,

$$l_{pf} = \frac{1}{2}\left(1 - \frac{M_{pf} - M_0}{M_{\max} - M_0}\right)l \qquad (7.15)$$

where M_0 is the moment due to eccentricity.

II. For SB2, only local buckling failure is to occur. The ultimate moment will not be reached by the steel member. However, a plateau of the moment-rotation curve is to be expected as shown in Figure 7.7 (a). A uniform moment is expected in the moment distribution as shown in Figure 7.7 (b). In obtaining the same plastic moment in SB1, the concentrated load applied on SB2 is 3P/4. The plastic hinge can occur in both full-plastic zone ($M_{max} = M_p$) or in hardening range ($M_{max} > M_p$).

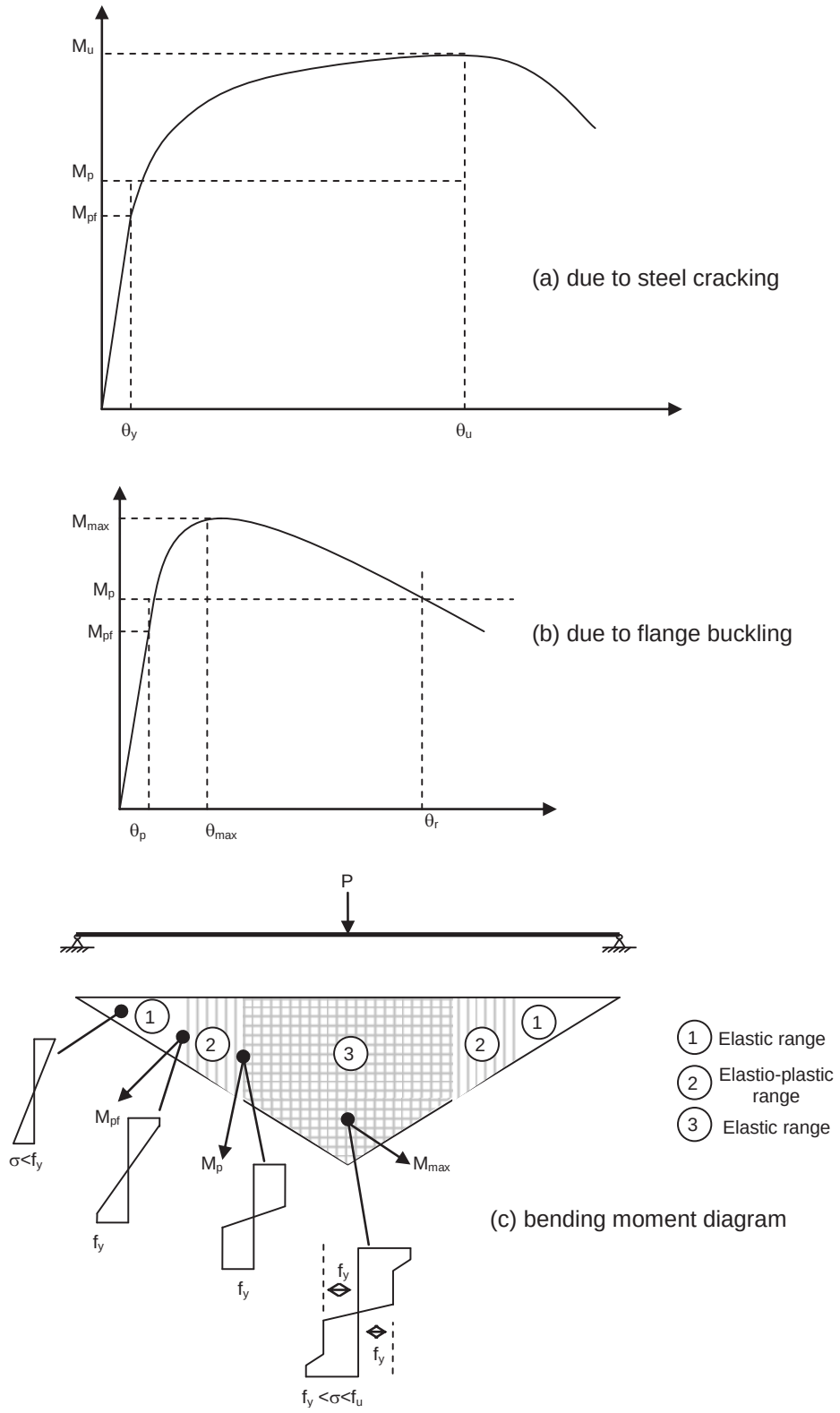

Figure 7.6 Moment rotation curve for SB1

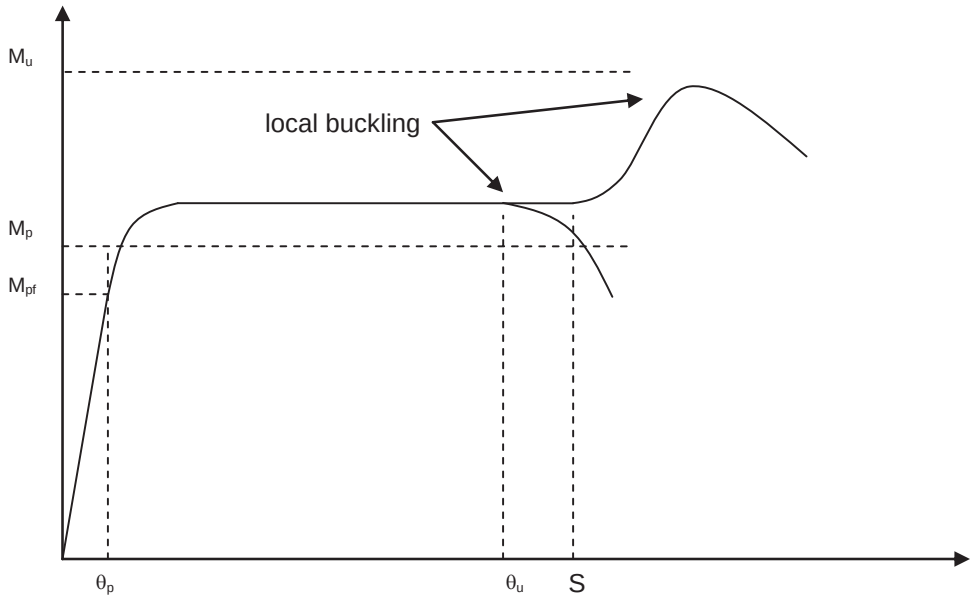

(a) due to flange buckling

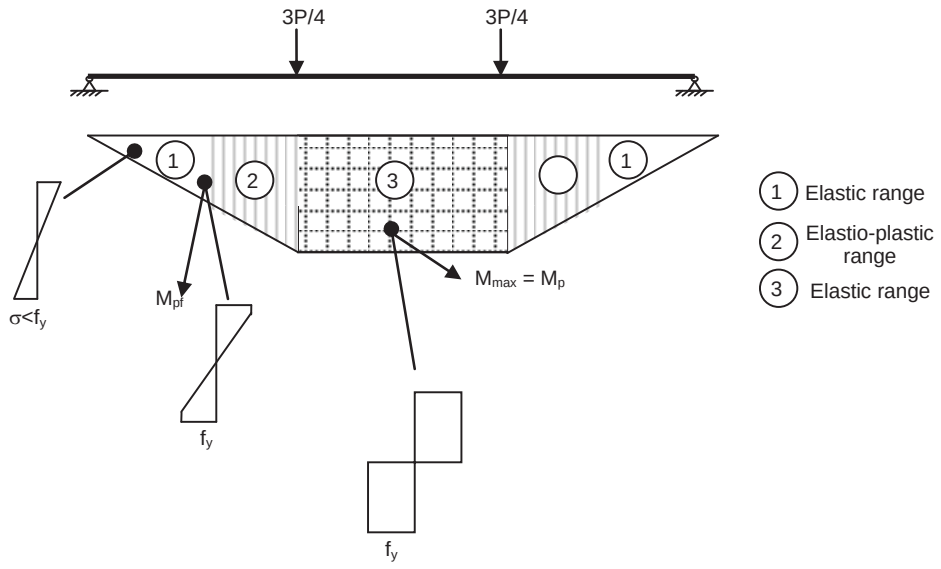

(b) bending moment diagram

Figure 7.7 Moment rotation curve for SB2

7.5 PARTIAL-INTERACTION NUMERICAL METHOD FOR FRP PLATED I-SECTION STEEL BEAM

The bilinear bond-slip characteristic for the glue is taken from Chapter 4 and integrated into the numerical method. The stress-strain relationship of steel and FRP is similar to the one used in Section 6.2.1. The force relationship in the steel and FRP at the bottom flange of the I-section is similar to the one explained in Section 6.2.2. There are two boundary conditions that are to be expected which is similar to the one observed in Section 6.2.3 and Section 6.2.4. The additional analysis to be included into the numerical method is the summation of forces in the I-section, the distance of neutral axis and the curvature at a specific load. The steps in solving this will be explained in the next section.

7.6 NUMERICAL METHOD PROCEDURE

The objective of the partial-interaction numerical method developed in this research is to quantify the moment and rotation of a steel I-section. The numerical method illustrated in Figure 7.8 is described as follows:

- At Position 0, strain of FRP is fixed at the middle ε_{p0} and the curvature is guessed χ_0. The strain in the steel, ε_{s0} and the distance to the neutral axis d_{NA0} can be calculated from χ_0.
- According to the stress-strain profile of the steel and FRP, the load at the centre, P_{s0} and P_{p0} are calculated.
- Due to symmetry at the centre, slip at this section is zero.
- The assumed slip at the centre corresponds to the local slip over the first segment length. Corresponding to this assumed slip, δ_0, the bond stress, τ_0, acting over the first segment length is calculated according to the local τ–δ relationship assumed.
- The bond force acting on the first segment is $B_0 = \tau_0 d_x L_{per}$.

- The stresses and forces of the steel, σ_{sy} and P_{sy} can be calculated at that position.
- The tension and compression forces, F_T and F_C can be calculated respectively.
- Vary d_{NA0} until the sum of forces, $\sum F = F_T + F_C = 0$.
- Calculate the moment at Position 0, M_0 which is also the maximum moment, $M_{\max}$ from the distribution of moment along the span. The subsequent moment along the span, M_D can be calculated.
- The load in the FRP is calculated at the end of the first segment: $P_{p1} = P_{p0} - B_0$ and the subsequent FRP strain is $\varepsilon_{p1} = \frac{P_{p1}}{(A_s E_s)}$.
- The slip strain is calculated: $\frac{ds_0}{dx} = \varepsilon_{s0} - \varepsilon_{p0}$
- The change in slip over the first segment length is calculated by integrating the slip strain over the segment length: $\Delta s_0 = \int \frac{ds_0}{dx} dx$.
- According to the change in slip over the segment length, the slip at the beginning of the second segment is calculated: $\delta_1 = \delta_0 - \Delta s_0$.
- χ_1 is guessed at the end of the first segment, where ε_{s1} and d_{NA1} can be calculated.
- Vary d_{NA1} until the sum of forces, $\sum F = F_T + F_C = 0$
- Calculate the moment at Position 1, M_1 and compare with M_{D1}.
- If $M_1 \neq M_{D1}$, then vary χ_1.
- The process is carried out throughout the bonded length until the boundary condition is achieved. There are two boundary conditions. For fully anchored beams, the boundary condition is $\delta = ds/dx = 0$ and for the not fully anchored beams, that is plates with bond lengths less than L_{crit}, the boundary condition is $\varepsilon_p = 0$ at the free end.

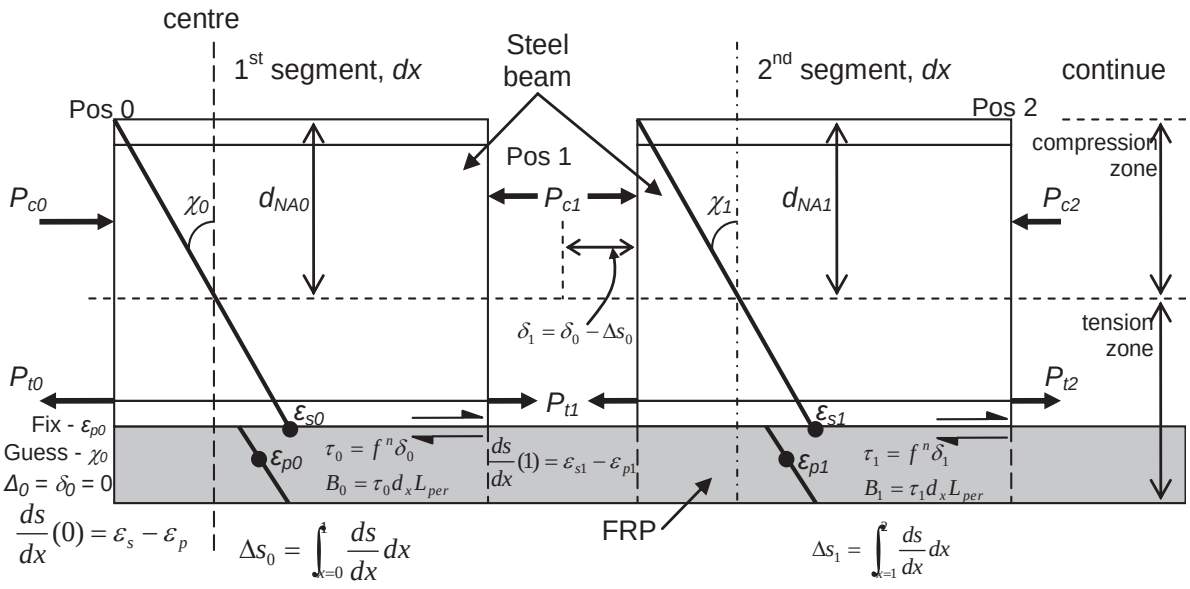

Figure 7.8 Graphical representation of the numerical analysis for FRP plated steel section

7.7 DEBONDING MECHANISM

For the purpose of demonstrating the plate end debonding, the I-section in Figure 7.9 is used. The beam is 2000 mm long with a total depth of 150 mm. The FRP plate is 1.2 mm thick with a varying length up to 200 mm. The beam is loaded at the centre resulting in a gradient moment distribution.

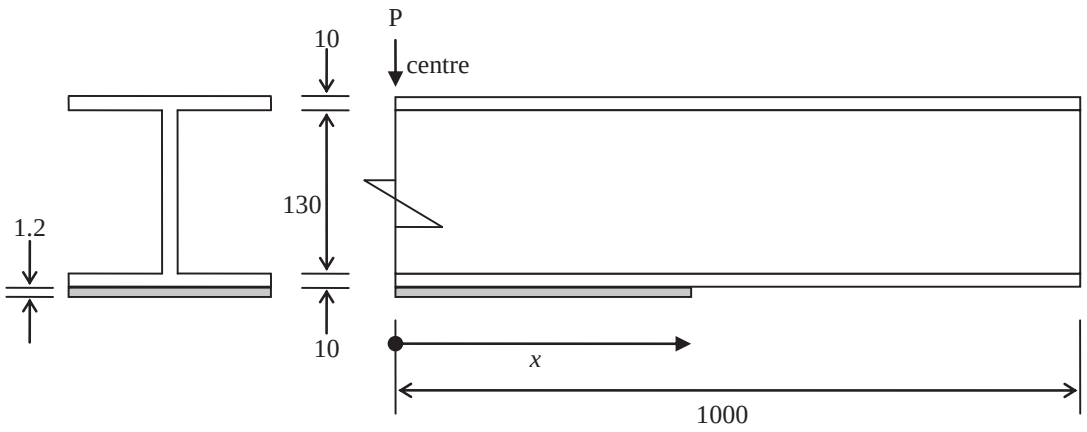

Figure 7.9 Specimen for the numerical procedure

7.7.1 PLATE END DEBONDING

Figure 7.10 shows the steel and FRP strain distributions at the bottom flange along a varied length. There is a significant difference of steel and FRP strains between the 50 mm and 150 mm bond length at the middle section. This pattern is similar to the case of FRP plated steel plate in Section 6.3.1. As the bonded length is varied, the difference of strains at the middle section becomes smaller and eventually leads to zero slip-strain. Figure 7.11 shows the slip-strain distribution at varying bonded lengths. The bonded length of 150 mm shows a value close to zero at the middle section. Consequently the slip distribution in Figure 7.12 shows an increment of slip at the plate end which eventually will lead to a maximum slip hence debonding.

The plate end debonding as shown in the Figure 7.10 to 7.12 is the expected debonding when the critical bond length of the FRP is not exceeded. The small drops in the curve shown in Figure 7.11 is due to numerical iteration in achieving the solution. Yielding of the steel may occur at the middle section of the I-section but it does not necessarily means that debonding may occur at the middle since the difference of strains between the FRP and steel that is needed

is relatively high. Figure 7.13 shows that debonding occurs at the plate end as the maximum slip has been exceeded. Since debonding has occurred, the plastic moment needed for the calculation of moment-rotation is not reached.

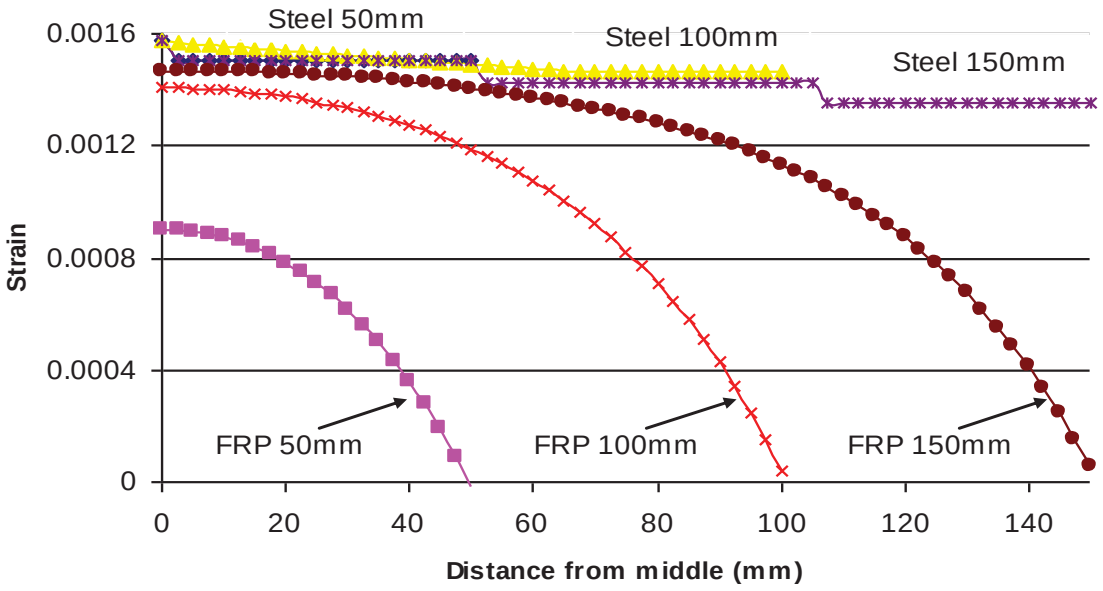

Figure 7.10 Strain distribution of steel and FRP at bottom flange

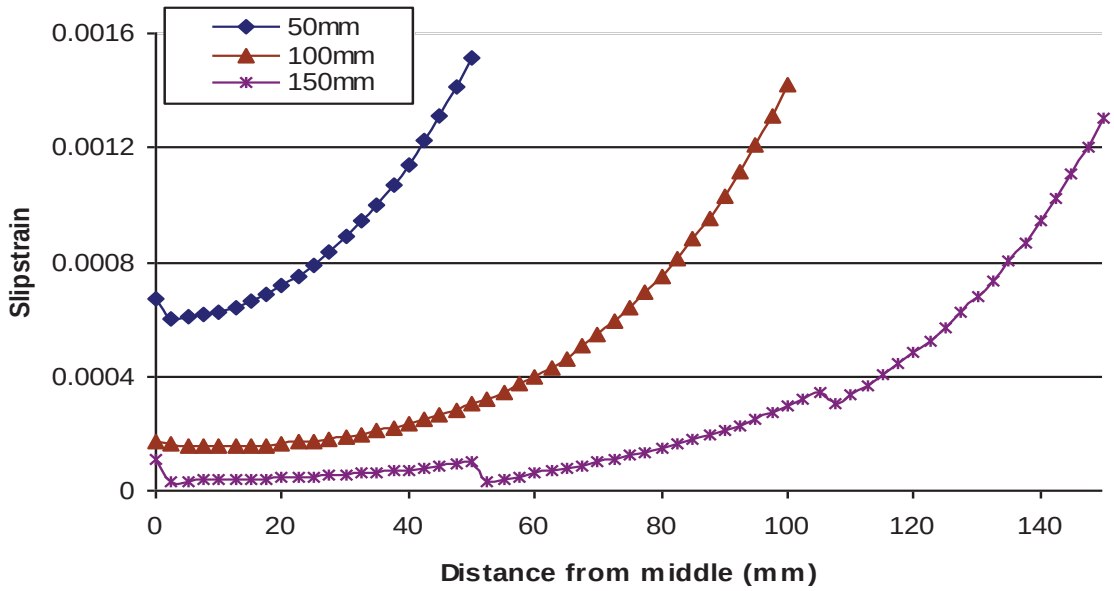

Figure 7.11 Slipstrain distribution of steel and FRP at bottom flange

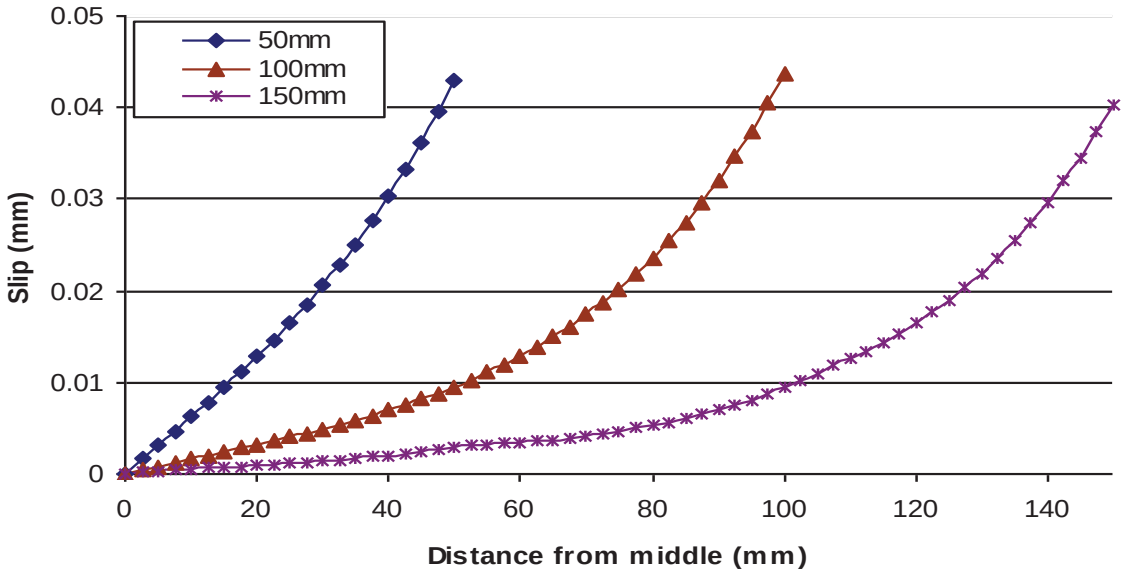

Figure 7.12 Slip distribution of steel and FRP at bottom flange

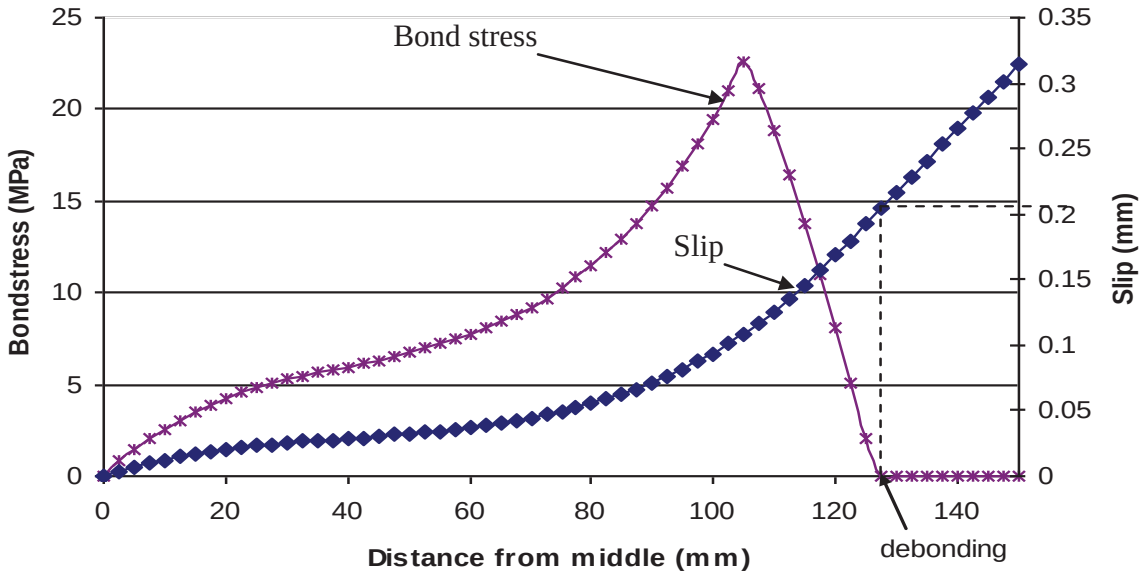

Figure 7.13 Plate end debonding at 150 mm bond length

7.7.2 DEBONDING AT CENTRE DUE TO STEEL YIELDING

Section 7.3 has shown that the analysis of moment-rotation for a steel section can be done by transforming a continuous beam into the respective standard beams which are simply supported beams. Both SB1 and SB2 cases can be analysed using the numerical method stated in Section 7.6 by applying the load at specific point as shown in Figure 7.5.

7.8 CONCLUSIONS

A numerical method was developed to study the debonding mechanism of FRP plated steel sections based on partial and full interaction theory. For the plate end debonding, it is shown that debonding occurs before the plastic moment can develop. However, using the standard beam analysis, the plastic moment may occur with subsequent debonding at the middle section in a fully anchored FRP length. The numerical analysis presented in this chapter cannot be solved due to the problems determining the solutions in the iterative procedure. Hence, improvement in the iterative method should be implemented in the numerical analysis to obtain the results required for the purpose of moment-rotation capacity analysis.

CHAPTER 8: SUMMARY AND CONCLUSIONS

8.1 INTRODUCTION

A total of 21 specimens were tested and three numerical methods are developed to study the debonding mechanism of FRP plated steel members. In the first experiment, steel blocks glued with FRP plates are tested. In the second experiment, steel plates glued with FRP plates are tested.

The first numerical method developed was used in the derivation of the τ-δ relationship. The second numerical method was developed to investigate the debonding mechanism of FRP plated steel member due to the yielding of steel. Finally, a numerical method for moment-rotation capacity of FRP plated steel beam is presented for future work.

8.2 CONCLUSIONS ON THE PUSH PULL TESTS AND NUMERICAL METHOD

A total of 17 push pull specimens were tested by varying the anchored length. The summary of the experimental works are as follows:

- The slip recorded from the LVDT in the experiment is prone to error.
- A longer bond length on a fully anchored specimen will lead to a longer plateau on the global P-Δ curve i.e. more ductile.
- A thicker FRP plate will increase the P_{IC} value while reducing the ductility.
- Different types of failure modes may result in different values of δ_{max} as indicated by specimen CIBA 16 and CIBA 17
- The value of shear stress obtained from the not fully anchored test which is close to the value obtained from the fully anchored test may indicate that the peak shear stress, τ_{max} can be obtained directly from the not fully anchored specimen test.

A numerical method based on the partial interaction theory was also developed. This analysis contributes in the derivation of the bond-slip characteristics of the FRP plated steel members by following the steps as summarized:

- Obtain the value of the peak shear stress τ_{max} from short pull tests where the anchorage length is much smaller than the critical length L_{crit} that can be determined from partial interaction structural mechanics.
- Obtain the value of the intermediate crack debonding resistance P_{IC} from fully anchored samples.
- From partial interaction structural mechanics, the fracture energy ½ $\tau_{max}\delta_{max}$ is a function of P_{IC}, hence, $\tau_{max}\delta_{max}$ can be obtained and as τ_{max} is known δ_{max} can be determined.
- Obtain δ_1 the slip at τ_{max} from curve fitting using a partial interaction numerical analysis.

8.3 CONCLUSIONS ON THE STEEL COUPON TESTS AND NUMERICAL METHOD

Four specimens were prepared and tested. Two of the specimens were designed so that debonding would occur at the plate end. The other two specimens were designed to that debonding will occur as the steel has yielded. The conclusion from these test are:

- For CW test results, the strain difference indicating partial interaction behaviour reduces as the bond length is increased.
- The FRP strain is always lower than the steel strain at any applied load in the CW results.
- For VW test results, the strength of the specimen was increased while FRP is still bonded to the steel plate.
- The strain in the FRP was always lower than the strain in the FRP at the elastic range. However prior to debonding, the strain in the FRP is higher.
- Two distinct failure modes were observed in the VW specimens. At the middle section, debonding occurred at the steel-adhesive layer. At the plate end, debonding occurred either at the FRP-adhesive or within the FRP layers.

A corresponding numerical method based on the partial interaction theory was also developed. This analysis contributes in the analysis of debonding mechanism. Based on the numerical analysis, these conclusions are made:

- For the plate end debonding to occur, the steel plate along the bonded length must not yield. The yielding of steel at the plate end will encourage debonding at the plate end by the higher increment of the steel strain compare to the FRP strain. Corresponding to this huge difference of strains, huge slip will follow with a subsequent debonding at the plate end.
- If the steel yielded between the plate ends, the huge difference of steel which has yielded and FRP strains will create huge slip with subsequent debonding. Debonding will starts at the middle section and then

propagates towards the middle section and the plate ends. Hence, debonding will likely to occur at the region where the steel has yielded due to the huge slipstrain.

8.4 SUGGESTION FOR FUTURE WORK

In Chapter 7, a numerical method was developed to study the debonding mechanism of FRP plated steel section based on partial and full interaction theory. For the plate end debonding, it is shown that debonding occurs before the plastic moment can developed. However, using the standard beam analysis, the plastic moment may occur with subsequent debonding at the middle section in a fully anchored FRP length. The numerical analysis presented in the chapter can be improved further by applying iterative method such as Jacobi method or Gauss-Seidel method to obtain the results required for the purpose of moment-rotation capacity analysis.

REFERENCES

(2003). Eurocode 3: Design of steel structures - Part1-1: General rules and rules for buildings. Brussels.

Al-Emrani, M. and R. Kliger (2006). "Experimental and numerical investigation of the behaviour and strength of composite steel-CFRP members." Advances in Structural Engineering **9**(6): 819-831.

Al-Saidy, A. H., F. W. Klaiber and T. J. Wipf (2005). "Strengthening of steel–concrete composite girders using carbon fiber reinforced polymer plates." Construction and Building Materials **21**(2): 295-302.

Alan R. Kemp, D. A. N. (2001). "Required and available rotations in continuous composite beams with semi-rigid connections." Journal of Constructional Steel Research **57**(4): 375-400.

Ali Abolmaali, J. H. M., Mohammed Farooqi, Yeol Choi (2005). "Development of moment–rotation model equations for flush end-plate connections." Journal of Constructional Steel Research **61**(12): 1595-1612.

Ali, M. S. M., D. J. Oehlers and M. A. Bradford, Eds. (2001). Shear peeling of steel plates adhesively bonded to the sides of reinforced concrete beams. Proc. Institution Civ. Eng. Struct. Build.

Ali, M. S. M., D. J. Oehlers and R. Seracino (2006). "Vertical shear interaction model between external FRP transverse plates and internal steel stirrups." Engineering Structures **28**(3): 381-389.

Buyukozturk, O., O. Gunes and E. Karaca (2003). "Progress on understanding debonding problems in reinforced concrete and steel members strengthened using FRP composites." Construction and Building Materials **18**(1): 9-19.

Cevik, A. (2007). "Genetic programming based formulation of rotation capacity of wide flange beams " Journal of Constructional Steel Research **63**(7): 884-893

Chen, J. F. and J. G. Teng (2001). "Anchorage Strength Models for FRP and Steel Plates Bonded to Concrete." Journal of Structural Engineering **127**(7): 784-791.

Chen, W.-F. and N. Kishi (1989). "Semirigid Steel Beam-to-Column Connections: Data Base and Modeling." Journal of Structural Engineering **115**(1): 105-119.

Colombi, P. and C. Poggi (2006). "Strengthening of tensile steel members and bolted joints using adhesively bonded CFRP plates." Construction and Building Materials **20**(1-2): 22-33.

Damatty, A. A. E. and M. Abushagur (2003). "Testing and modeling of shear and peel behavior for bonded steel/FRP connections." Thin-Walled Structures **41**(11): 987-1003.

Darko Beg, Z., Ioannis Vayas (2004). "On the rotation capacity of moment connections." Journal of Constructional Steel Research **60**(3-5): 601-620.

Deng, J. and M. M. K. Lee (2005a). "Behaviour under static loading of metallic beams reinforced with a bonded CFRP plate." Composite Structures **78**(2): 232-242.

Deng, J. and M. M. K. Lee (2005b). "Fatigue performance of metallic beam strengthened with a bonded CFRP plate." Composite Structures **78**(2): 222-231.

Deng, J., M. M. K. Lee and S. S. J. Moy (2003). "Stress analysis of steel beams reinforced with a bonded CFRP plate." Composite Structures **65**(2): 205-215.

Emmanuel Attiogbe, G. M. (1991). "Moment-Rotation Functions For Steel Connections." Journal of Structural Engineering **117**(6): 1703-1718.

Fawzia, S., R. Al-Mahaidi, X. L. Zhao and S. Rizkalla (2007). "Strengthening of circular hollow steel tubular sections using high modulus CFRP sheets." Construction and Building Materials **21**(4): 839-845.

Foley, C. M. and S. Vinnakota (1995). "Toward design office moment-rotation curves for end-plate beam-to-column connections " Journal of Constructional Steel Research **35**(2): 217-253.

Gioncu, V. and D. Petcu (1997). "Available rotation capacity of wide-flange beams and beam-columns Part 1. Theoretical approaches " Journal of Constructional Steel Research **43**(1-3): 161-217

Haskett, M., D. J. Oehlers and M. S. M. Ali (2007). "Local and global bond characteristics of steel reinforcing bars." Engineering Structures **30**(2): 376-383.

Jones, S. C. and S. A. Civjan (2003). "Application of Fiber Reinforced Polymer Overlays to Extend Steel Fatigue Life." Journal of Composites for Construction **7**(4): 331-338.

Kemp, A. R. (1985). "Interaction of Plastic Local and Lateral Buckling." Journal of Structural Engineering **111**(10): 2181-2196.

Kishi, N. and W.-F. Chen (1990). "Moment-Rotation Relations of Semirigid Connections with Angles." Journal of Structural Engineering **116**(7): 1813-1834.

Lam, A. C. C., J. J. R. Cheng, M. C. H. Yam and G. D. Kennedy (2007). "Repair of steel structures by bonded carbon fibre reinforced polymer patching: experimental and numerical study of carbon fibre reinforced polymer – steel double-lap joints under tensile loading." Canadian Journal of Civil Engineering **34**(12): 1542-1553.

Lenwari, A., T. Thepchatri and P. Albrecht (2006). "Debonding Strength of Steel Beams Strengthened with CFRP Plates." Journal of Composites for Construction **10**(1).

Li, T. Q., D. A. Nethercot and R. M. Lawson (2000). "Required rotation of composite connections." Journal of Constructional Steel Research **56**(2): 151-173.

Lu, X. Z., J. G. Teng, L. P. Ye and J. J. Jiang (2005). "Bond–slip models for FRP sheets/plates bonded to concrete." Engineering Structures **27**(6): 920-937.

Miller, T. C., M. J. Chajes, D. R. Mertz and J. N. Hastings (2001). "Strengthening of a Steel Bridge Girder Using CFRP Plates." Journal of Bridge Engineering **6**(6): 514-522.

Nozaka, K., C. K. Shield and J. F. Hajjar (2005). "Effective Bond Length of Carbon-Fiber-Reinforced Polymer Strips Bonded to Fatigued Steel Bridge I-Girders." Journal of Bridge Engineering **10**(2): 195-205.

Oehlers, D. and R. Seracino (2004). Design of FRP and Steel Plated RC Structures. Oxford, Elsevier.

Sang-Sup Lee, T.-S. M. (2002). "Moment–rotation model of semi-rigid connections with angles." Engineering Structures **24**(2): 227-237.

Sebastian, W. M. (2003a). "Nonlinear influence of contraflexure migration on near-curtailment stresses in hyperstatic FRP-laminated steel members." Computers & Structures **81**(16): 1619-1632.

Sebastian, W. M. (2003b). "Nonlinear proportionality of shear-bond stress to shear force in partially plastic regions of asymmetric FRC-laminated steel members." International Journal of Solids and Structures **40**(1): 25-46.

Sen, R., L. Liby and G. Mullins (2001). "Strengthening steel bridge sections using CFRP laminates." Composites Part B: Engineering **32**(4): 309-322.

Seracino, R., M. R. Raizal Saifulnaz and D. J. Oehlers (2007). "Generic Debonding Resistance of EB and NSM Plate-to-Concrete Joints." Composite for Constructions **11**(1): 62-70.

Shi, Y., G. Shi and Y. Wang (2007). "Experimental and theoretical analysis of the moment–rotation behaviour of stiffened extended end-plate connections " Journal of Constructional Steel Research **63**(9): 1279-1293.

Shi, Y. J., S. L. Chan and Y. L. Wong (1996). "Modeling for Moment-Rotation Characteristics for End-Plate Connections." Journal of Structural Engineering **122**(11): 1300-1306.

Smith, S. T. and J. G. Teng (2002). "FRP-strengthened RC beams. II: assessment of debonding strength models." Engineering Structures **24**(4): 397-417.

Tavakkolizadeh, M. and H. Saadatmanesh (2003a). "Fatigue Strength of Steel Girders Strengthened with Carbon Fiber Reinforced Polymer Patch." Journal of Structural Engineering **129**(2): 186-196.

Tavakkolizadeh, M. and H. Saadatmanesh (2003b). "Repair of damaged steel-concrete composite girders using Carbon Fiber-Reinforced Polymer sheets." Journal of Composites for Construction **7**(4): 311-322.

Xia, S. H. and J. G. Teng, Eds. (2005). Behaviour of FRP-to-steel bonded joints. Proceedings of the International Symposium on Bond Behaviour of FRP in Structures. Hong Kong, International Institute for FRP in Construction.

Yee, Y. L. and R. E. Melchers (1986). "Moment-Rotation Curves for Bolted Connections." Journal of Structural Engineering **112**(3): 615-635.

Yuan, H., J. G. Teng, R. Seracino, Z. S. Wu and J. Yao (2004). "Full-range behavior of FRP-to-concrete bonded joints." Engineering Structures **26**(5): 553-565.

Zhao, X.-L. and L. Zhang (2007). "State-of-the-art review on FRP strengthened steel structures." Engineering Structures **29**(8): 1808-1823.

APPENDIX A

Specimen details, test results and predictions from Xia and Teng (2005) experimental testing.

NOTE:
These figures are included on page 237 of the print copy of the thesis held in the University of Adelaide Library.

Material properties of adhesive from Xia and Teng (2005)

APPENDIX B

Material properties of adhesive from Al-Emrani and Kliger (2006)

NOTE:
These figures are included on page 238 of the print copy of the thesis held in the University of Adelaide Library.

Measured strength and stiffness of the FRP plate from Al-Emrani and Kliger (2006)

APPENDIX C

Specimen details and test results for not fully anchored samples

Test specimen	FRP thickness, t_p (mm)	FRP width, b_p (mm)	Bonded length, L (mm)	Test Failure Load (kN)
SIKA 4	1.2	100	20	44.8
SIKA 5	1.2	100	20	46.8
CIBA 9	1.2	100	20	44.7
CIBA 10	1.2	100	20	36.0
CIBA 11	1.2	100	20	33.5
CIBA 13	1.2	100	20	55.4
CIBA 14	1.2	100	20	57.9

Specimen details and test results for fully anchored samples

Test specimen	FRP thickness, t_p (mm)	FRP width, b_p (mm)	Bonded length, L (mm)	Debonding Load, P_{IC} (kN)	Failure Mode *
SIKA1	1.2	100	250	73.9	1
SIKA 2	2.4	100	250	100.5	1
SIKA 3	1.2	100	100	68.7	1
CIBA 6	1.2	100	250	100.6	1+2
CIBA 7	2.4	100	250	152.3	1+2
CIBA 8	1.2	100	100	-	1+2
CIBA 12	1.2	100	250	-	2
CIBA 15	1.2	100	250	-	2
CIBA 16	1.2	100	250	99.8	1+2
CIBA 17	1.2	100	250	100.0	1+2

- * 1 = adhesive, 2 = delamination

APPENDIX D

Not fully anchored specimens test results

Test specimen	Test Failure Load (kN)	$\tau_{max,exp}$ (MPa)	Averaged $\tau_{max,exp}$ (MPa)	δ_1 (mm)
SIKA 4	44.8	22.4	22.9	0.02
SIKA 5	46.8	23.4	22.9	0.02
CIBA 9	44.7	22.3	22.7	0.03
CIBA 10	36.0	18.0	22.7	0.08
CIBA 11	33.5	16.8	22.7	0.12
CIBA13	55.4	27.7	22.7	0.03
CIBA14	57.9	28.9	22.7	0.05

Fully anchored specimens test results

Test specimen	Debonding Load, $P_{IC,\ exp}$ (kN)	$\tau_{max}\delta_{max}$ (N/mm)	$\tau_{max,exp}$ (MPa)	$\delta_{max,cal}$ (mm)	$\delta_{max,exp}$ (mm)	δ_1 (mm)
SIKA 1	73.9	2.91	22.9	0.13	0.07	0.01
SIKA 2	100.5	2.61	22.9	0.11	0.09	0.05
SIKA 3	68.7	2.53	22.9	0.11	0.05	0.01
CIBA 6	100.6	5.34	22.7	0.23	0.11	0.02
CIBA 7	152.3	6.01	22.7	0.26	0.18	0.07
CIBA 8	-	-	22.7	-	-	-
CIBA 12	-	-	22.7	-	-	-
CIBA 15	-	-	22.7	-	-	-
CIBA 16	99.8	4.86	22.7	0.21	0.25	0.1
CIBA 17	100.0	4.85	22.7	0.21	0.29	0.2

APPENDIX E

Xia and Teng (2005) test results